AD NUMBER
AD803525
LIMITATION CHANGES

TO:

Approved for public release; distribution is unlimited.

FROM:

Distribution authorized to U.S. Gov't. agencies and their contractors; Administrative/Operational Use; OCT 1966. Other requests shall be referred to Air Force Materials Lab., Wright-Patterson AFB, OH 45433.

AUTHORITY

AFML per DTIC form 55

AFML-TR-66-310
PART I

INTEGRATED RESEARCH ON CARBON COMPOSITE MATERIALS

UNION CARBIDE CORPORATION
CARBON PRODUCTS DIVISION
-IN ASSOCIATION WITH-
CASE INSTITUTE OF TECHNOLOGY
BELL AEROSYSTEMS COMPANY, A TEXTRON COMPANY

TECHNICAL REPORT AFML-TR-66-310, PART I
OCTOBER 1966

AIR FORCE MATERIALS LABORATORY
RESEARCH AND TECHNOLOGY DIVISION
AIR FORCE SYSTEMS COMMAND
WRIGHT-PATTERSON AIR FORCE BASE, OHIO

5

BLANK PAGE

NOTICES

INTEGRATED RESEARCH ON
CARBON COMPOSITE MATERIALS

Union Carbide Corporation
Carbon Products Division
in Association with
Case Institute of Technology
Bell Aerosystems Company, a Textron Company

FOREWORD

The work reported herein was performed under the sponsorship of the Advanced Research Project Agency, Department of Defense, through a contract with the Air Force Materials Laboratory, MAP, Research and Technology Division, Wright-Patterson Air Force Base, Ohio, Contract No. AF 33(615)-3110, ARPA Order No. 719, Program Code No. 5950. Dr. A. M. Lovelace, MAX, is the Air Force Program Manager.

The prime contractor is Union Carbide Corporation, Carbon Products Division; the subcontractors are the Case Institute of Technology and Bell Aerosystems Company, a Textron Company. The program is administered by a committee composed of: J. C. Bowman (Chairman), R. M. Bushong, and G. B. Spence (Program Supervisor) from Union Carbide; R. H. Thomas and L. A. Schmit (Program Supervisor) from Case Institute; and W. H. Dukes and F. M. Anthony (Program Supervisor) from Bell Aerosystems. Technical personnel participating in the program are indicated as authors of their portions of the report. The manuscript was released by the authors August 1966 for publication as an RTD Technical Report.

This report covers work performed from May 17, 1965, to May 16, 1966.

This technical report has been reviewed and is approved.

A. M. Lovelace
Chief Scientist
Air Force Materials Laboratory

ii

ABSTRACT

Both resin and metal matrix composites with high modulus carbon fibers are being developed. Chemical etchants which roughen the fiber surface have approximately doubled the compressive strength of resin rings. Contact angle and wicking rate tests are used to evaluate surface treatments. Various coatings (best: Ta) improve wetting with aluminum, but brittle intermetallic phases degrade composite properties. Nickel matrix composites have near theoretical modulus and 1/2 theoretical strength. The effect of random fiber spacing on calculated composite moduli is being studied. Curing stresses and stress concentrations at fiber ends have been measured photoelastically. Improved test concepts have been formulated for uni- and bidirectional composites. Discrete element methods of structural analysis, a transient temperature analysis capability, and a statistical theory of strength have been extended to include material anisotropy. New structural synthesis algorithms are being investigated. Work is reported on a method for nonlinear, multiaxial stress analysis. Preliminary minimum weight estimates have been made for a fiber composite component representative of a fuselage section. The use of structural synthesis methods to select the best material from within a class of materials is being investigated on a series of particulate composites similar to grade JTA. Material property data, analyses of a hollow cylinder and a flat plate, and the design of a rocket throat insert are reported.

TABLE OF CONTENTS

ILLUSTRATIONS

ILLUSTRATIONS (Cont'd)

ILLUSTRATIONS (Cont'd)

ILLUSTRATIONS (Cont'd)

ILLUSTRATIONS (Cont'd)

ILLUSTRATIONS (Cont'd)

ILLUSTRATIONS (Cont'd)

TABLES

TABLES (Cont'd)

SECTION I

INTRODUCTION

The present program is a novel approach designed to fulfill three different but clearly interdependent needs of the Department of Defense: a material need, a structural design capability need, and a need for more scientists and engineers trained in applied materials problems and advanced design methods. The Carbon Products Division of Union Carbide Corporation, Case Institute of Technology, and Bell Aerosystems Company have formed an Association through which a joint effort can be made to meet these needs.

The Association has formulated a broad program which includes the development of new materials, generation of advanced analyses and design methods, and education of graduate students. In brief, the major objectives are (1) to develop high modulus carbon fiber composites, (2) to extend the methods of structural mechanics, (3) to identify DOD applications toward which the program efforts should be directed, (4) to educate engineers capable of developing and using modern materials, and (5) to integrate materials research with the needs of the designer by extending the technique of structural synthesis to include material variables.

A number of existing or planned aerospace and hydrospace systems of the Department of Defense would perform more efficiently if made from a lighter and stiffer material than any presently available. One of the most promising classes of materials for these applications is carbon fiber composites made from high modulus carbon yarn recently developed by Union Carbide. A major objective of this program is to develop resin and metal matrix composite materials containing these new high modulus carbon fibers.

Composite materials, most graphites, and many advanced aerospace materials are moderately-to-strongly anisotropic in their physical properties, show nonlinear and nonconservative stress-strain behavior to varying degrees, and exhibit brittle failure. The efficient utilization of these materials in DOD applications requires that these properties be accurately treated by the designer. A second major objective of this program is to extend and, where necessary, to develop new methods of structural mechanics to cope with anisotropy, with nonlinearity, and, to the extent possible, with nonconservatism. The accuracy of the analytical methods is to be evaluated by tests on simple but representative structural components. The structural mechanics work is to be supported by experimental and theoretical studies of the specification of the fracture surface and the statistical aspects of fracture in anisotropic brittle materials.

It is essential that the fundamental work conducted here be applicable to current DOD needs. A third major objective of this program is to

identify DOD applications toward which the program efforts should be directed. Components which represent specific hardware items and the thermal and mechanical loading conditions for these components are to be considered.

The steadily increasing use of materials which exhibit complex behavior (anisotropy, nonlinearity, nonconservatism, and nonhomogeneity) has created a demand for more engineers and scientists who are interested in and prepared for the continued development and use of these materials. A fourth major objective of this program and a prime reason for the formation of this Association is the education of these engineers and scientists. This education is to be done directly by the involvement of graduate students with various aspects of this program and by developing a greater awareness at the academic institution of current DOD material and design problems.

One of the program supervisors (Prof. L. A. Schmit) has pioneered in the development of a branch of structural mechanics known as structural synthesis. Structural synthesis has been defined as the rationally directed evolution of a structural component which, in terms of a defined objective, efficiently performs a set of specified functional purposes, i.e., sustains the load conditions without violating any of the constraints. Desirable objectives for aerospace applications are minimum weight or cost or maximum reliability. A logical extension of existing structural synthesis methods would be to add material variables to the design variables treated in the optimization process. The material variables might include composition, density, or fiber winding angle. The output of the structural synthesis process would be the specification not only of the best geometrical shape of the component to carry a certain load but also of the best material from which to make the component. The designer would then be able to tell the materials supplier which material within a given class of materials would be best for a specific application. In this way, the material needs of the designer and the development of new materials by the materials supplier would be integrated into one overall process. A fifth major objective of this program is to develop workable methods for carrying out this Integrated Approach to Applied Materials Research.

In the following three paragraphs, the general areas of responsibility of each member of the Association are defined. The overall technical program and the way in which the activities of the three members of the Association are coupled together are discussed in Section II A. The overall program can be divided into six parts, and a brief description of each part is outlined in Section II B. In Section III, a general summary is given of the work accomplished during the first year. In Section IV, two specific applications, an airframe component and a rocket nozzle insert, are identified; these applications form the objective of much of the applied work. The remaining six sections of the report present in greater detail the results of the work of the first year for each of the six parts of the program.

The primary areas of responsibility of Union Carbide Corporation, Carbon Products Division, are to develop and produce composite materials and to measure on certain materials those mechanical and thermal properties needed for the structural design work of the other members of the Association. The technical program at Union Carbide consists of: (1) materials research, a basic research program to develop new, improved composites of high modulus carbon fibers in both resin and metal matrices; (2) materials fabrication, an applied research program to produce materials for the joint research programs of the Association and to seek new ways of fabricating components which better utilize the superior properties of composite materials; (3) properties evaluation, the measurement of the mechanical and thermal properties of certain composites to provide data for the joint research programs of the Association; and (4) failure criteria, a basic research program to determine experimentally adequate failure criteria for anisotropic materials under multiaxial stress states and to find ways of representing the failure surface which can be used by the designer in practical calculations.

The primary objective of the work at Case Institute of Technology is to advance the basic structural mechanics technology required for rational design with composite materials. Composite materials offer the structural design engineer the prospect of being able ultimately to carry on simultaneously the design of the structural configuration and material. To bring this about will require fundamental advances in structural synthesis as well as a substantially improved understanding of the behavior of composite materials. The objectives of the research program at Case are: (1) the quantitative formulation and efficient solution of the structural synthesis problem, including material variables, for elementary, but representative, components fabricated from composite materials; (2) experimental stress analysis studies and theoretical investigations in micromechanics with the objective of improving the measurement and calculation of stiffness properties and failure mode criteria for composite materials; and (3) the development of improved analysis methods for anisotropic, nonlinear, and nonconservative materials.

The primary purposes of Bell Aerosystems Company's participation in this program are to interject user requirements into the applied material research efforts; to apply, at the prototype design level, the advanced analytical procedures and improved understanding of material behavior which will result from the research; and to establish application-related property specifications for materials research activities. To attain these objectives, the following seven-part technical program is to be performed: (1) application selection, the objective of which is to define representative configurations and environmental conditions which reflect DOD requirements; (2) recognition of failure modes, which involves the overall structural behavior such as elastic instability, deformation limits, and fracture and the material failure modes; (3) determination of the nature of and methods for the application of analytical tools, which are needed to cope with the anisotropic, anelastic, and nonconservative material property behavior and the multiaxial stress distributions

anticipated in structural configurations associated with the use of the subject materials; (4) definition of objective function, which is required for the assessment of performance of the components of interest in light of achieving their design objectives; (5) structural synthesis, which involves the application of structural synthesis techniques at the practical level to define the most desirable material compositions within a particular class of composites; (6) study of creative design concepts, which are certain to be necessary for a material class which is as complex as composites; and (7) testing, which is necessary to verify the value of analysis procedures used to design composite materials and the components which utilize them.

SECTION II

PROGRAM PLAN

In a project involving separate organizations, an attempt is usually made to divide the work so that each organization has separate and well-defined jobs. In the present case, a deliberate attempt has been made to do the opposite, that is, to have close coupling (1) between the materials laboratory and the structural design groups and (2) between the applied work in industry and the basic work at the university. In order to ensure this close coupling and to achieve the technical objectives set forth in the Introduction, a rather detailed program plan has been formulated. In Section II A, this plan is presented in a manner which shows how the activities at one organization interrelate with the activities at the other two organizations. In Section II B, a more detailed description is given of the technical projects which make up the total program. For brevity, the interrelatedness of these individual projects will not be pointed out here, although these connections have been established on a program plan network diagram which is more detailed than that given later in Figure 1.

A. Conceptual Approach

Turning to new materials has often been the design engineer's response to challenging design tasks. The advent of high performance composite materials makes it possible to think of tailoring materials and designing structures simultaneously in order to arrive at an optimum design. To make this promise a reality will require dramatic improvement in communication between material scientists, engineers skilled in structural mechanics, and designers. The dialogue among these three groups has often been primitive, and, even at best, it has been largely qualitative.

The concept of the Association Research Plan is to bring into existence a quantified approach to specifying (at the engineering properties level) goals for composite materials development based on representative component applications. This task requires broad capabilities ranging from basic materials science through structural mechanics to the practical design and fabrication of representative structural components. The conceptual approach underlying the Association Research Program Plan is outlined in the block diagram shown in Figure 1. Note that the Association member principally responsible for the activity represented by a block is designated in the upper left-hand corner. The category numbers following the organization designations are assigned to Union Carbide (UCC) activities beginning with 1, to Case Institute activities beginning with 20, and to Bell Aerosystems activities beginning witn 40.

The iterative cycle begins with research on new composite materials (Block UCC 1) and leads to the study of fabrication methods (Block UCC 2). The needs for high performance structural composites are assessed and the selection of appropriate representative components (Block Bell 46)

influences the materials research and fabrication techniques. The inter-relations among activities are depicted in Figure 1 by the lines connecting the blocks. The output of the materials fabrication activity provides composite materials for physical property evaluation and multiaxial stress testing (Block UCC 3) as well as for tests on structural components (Block Bell 45). The physical properties evaluation and multiaxial testing effort tie in with research concerned with the obtaining of reliable design data (Block UCC 5 and Case 27). This effort in obtaining reliable design data involves the development of test procedures and other experimental work aimed at providing the designer with stiffness and strength information on which to base structural design decisions. In parallel with the reliable design data activity, fundamental studies in micromechanics will be pursued. The micromechanics activity is thought of as having two major subdivisions. Studies aimed at predicting the stiffness properties of carbon-fiber, resin-matrix composites are represented by Block Case 25. Research on failure mechanisms for strength predictions in carbon-fiber, resin-matrix composites is depicted by Block Case 26. The outputs of micromechanics studies are shown feeding into the reliable design data activity (Block UCC 5 and Case 27). This relationship is meant to indicate that, in the beginning, these studies can be expected to provide guidance in evolving semiempirical methods for predicting stiffness and strength data. The long-range goal of micromechanics research will continue to be the establishment of experimentally verified analytical procedures for predicting stiffness and strength properties of a composite based on input describing the constituents and the process employed to create the composite. It should also be noted that the results of component testing activities (Block Bell 45) will be fed back into the reliable design data research program (Block UCC 5 and Case 27). The output of the physical properties evaluation (Block UCC 3) is seen to feed into an effort aimed at establishing approximate analytical representations for the physical properties of composites as a function of composition and processing variables (Block UCC 4). Information from the physical properties evaluation and multiaxial stress testing activity (Block UCC 3) is also drawn upon by research studies which seek generalized constitutive equations and generalized failure criteria (Block Case 24) for composite materials. The results of this research activity (Block Case 24) may provide insights useful in constructing analytical representations for physical properties. The fact that analytical representations of physical properties can be constructed which are independent of the success of the high-risk studies represented by Block Case 24 is indicated by the line connecting Block UCC 3 directly to Block UCC 4.

The analytical representation of physical properties (Block UCC 4) and the reliable design data (Blocks UCC 5 and Case 27) provide basic input information for stress analyses. Research on methods of structural analysis for composite materials is represented by Block Case 20 and Block Bell 40. The work on structural analysis at Case will be aimed at dealing with complex structural behavior (anisotropy, nonlinearity, nonconservatism) but will be limited to somewhat idealized geometric configurations (Block Case 20). The development of an advanced structural analysis capability
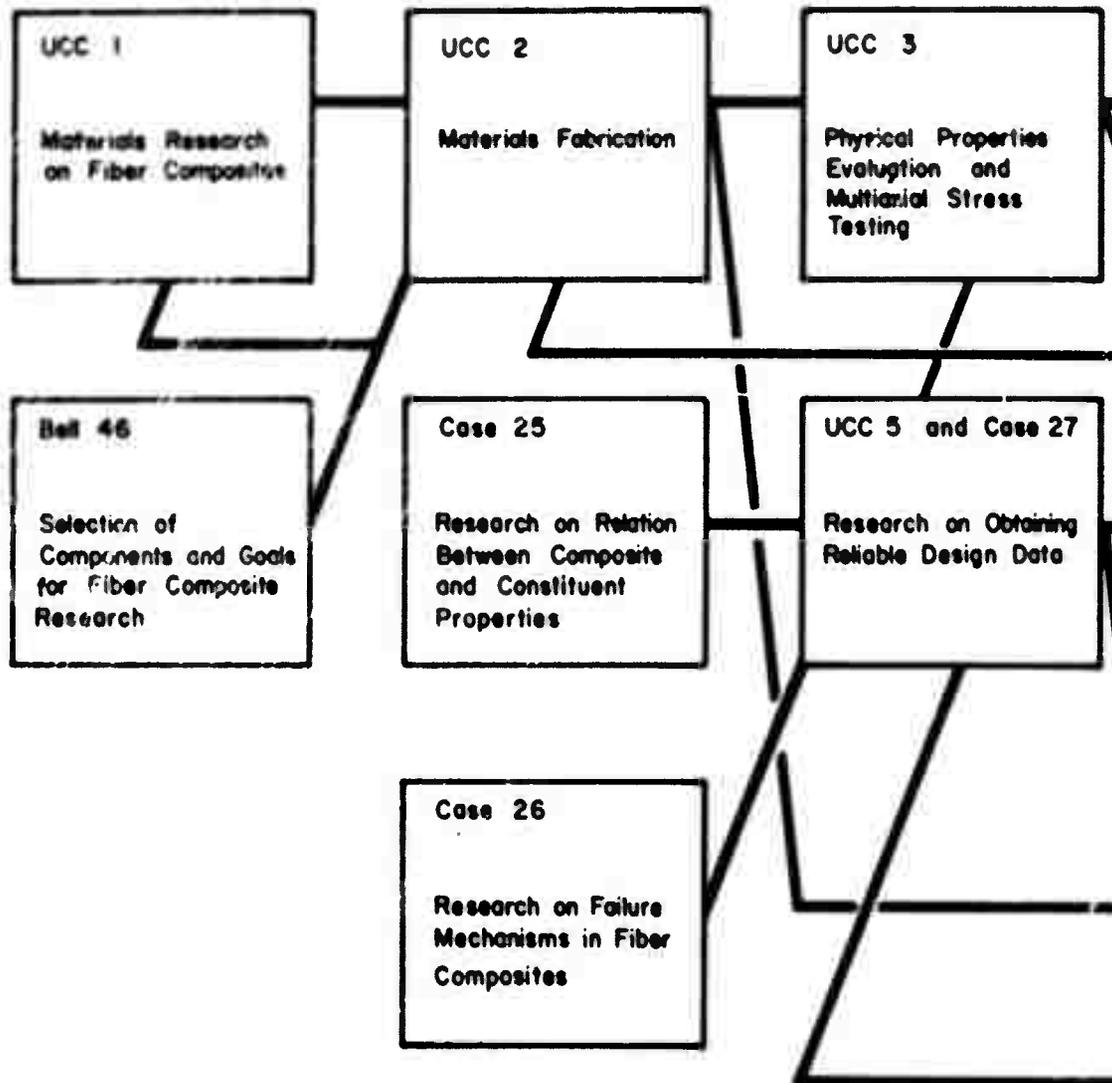
Figure 1. Conceptual Approach of Association
Research Program.

-7-

A

| Properties ... and Stress | Case 24 — Generalization of Constitutive Equations and Failure Criteria | UCC 4 — Analytical Representations of Physical Properties |

... and Case 27 — ... on Obtaining ... Design Data

Case 20 — Generation of Stress Analysis Methods

Case 21 — Extension and Evaluation of Structural Synthesis Methods

Case 2... — Generate... Capabilit... Simple ... Without ...

Bell 45 — Testing of Components

Bell 44 — Definition of Objective Function and Load Conditions

Bell 43... — Research... Statistica... of Stre...

Bell 40 — Generalization of Discrete Element Analysis Methods

Bell 41 — Extension of Structural Synthesis Methods

Bell 42 — Generatio... Synthesis... Calculatio... Represent...

β

Case 22

Generation of Structural Sythesis Capability and Calculations of Simple Components With and Without Materials Variables

Case 23

Research on Materials Evaluation Function for a Given Component

Bell 44

Definition of Objective Function and Load Conditions

Bell 43

Research on Statistical Theories of Strength

Bell 41

Extension of Structural Synthesis Methods

Bell 42

Generation of Structural Synthesis Capability and Calculations of Representative Components

C

represented by Block Bell 40 will be based on extending discrete element methods of structural analysis to composite materials. These methods are known to be especially well suited to dealing with complex geometry and irregular loading. Transient temperature response analyses and thermal stress analyses will be generated as required in both Block Case 20 and Block Bell 40. Experimental verification of some of these structural analysis studies will be undertaken: this work is indicated by the lines joining Block Case 20 and Block Bell 40 to the component testing activity (Block Bell 45). The selection and evaluation of modern algorithms for efficient structural synthesis is represented by Block Case 21. The innovations and modular procedures that evolve as a consequence of these studies will be drawn upon in generating automated optimum design capabilities for simple components with and without material variables (Block Case 22), and they will also provide a basis for studying modifications and extensions (Block Bell 41) needed to successfully apply these structural synthesis methods to actual structural components (Bell Block 42). The generation of the structural synthesis capabilities and their application to representative components (Block Bell 42) will draw upon the following: (1) research efforts aimed at defining improved objective functions and load conditions (Block Bell 44), (2) studies extending structural synthesis methods to actual structural systems (Block Bell 41), and (3) research on the statistical nature of strength theories for composite materials (Block Bell 43). The results of the research on statistical strength theories (Block Bell 43) as well as the identification of improved objective function and load condition information (Block Bell 44) will be considered wherever possible in the generation of structural synthesis capabilities for simple components (Block Case 22). It should be emphasized that initially the structural synthesis studies for simple components will be carried out for specific composite materials. Several specific materials within a class can be selected and employed. For each discrete material, an optimum design can then be sought. These results can be used to construct a materials evaluation function. The materials evaluation function expresses the dependence of the desirability of a material (with respect to a stated objective function, say, minimum weight) upon the variables which determine the engineering properties (for example, composition and processing variables). Minimizing the material evaluation function, subject to constraints on the range of values that the independent variables can assume, will yield a quantitative recommendation for a new material in the class which is expected to be better suited to the engineering task at hand. The quantitative recommendations that emerge from material evaluation function studies (Block Case 23) can then be used to close the loop (i.e., make specific recommendations to guide the fabrication of improved composite materials within the class considered). Alternatively, when the structural synthesis capabilities are extended to include as design variables those quantities which determine the material engineering properties, it will be possible to use the results of structural synthesis calculations to close the loop. Inclusion of the composition and processing variables within the structural synthesis process will represent a significant advance in design, whereby the structural configuration and the material are designed simultaneously. Structural synthesis calculations carried out for

representative components (Block Bell 42) will also provide insight which can be used to guide the fabrication of new composite materials within a class. The application of the materials evaluation function or the incorporation of material variables into large-scale structural synthesis capabilities for actual representative components is thought to represent a potentially attainable goal.

B. Technical Approach

For convenience of presentation, the program plan has been divided into six parts. In the following paragraphs, the long-range objectives of the work of each part are discussed.

1. Particulate Composite Studies (See Section V for results of the first year.)

It was decided to carry through all aspects of the Integrated Approach to Applied Materials Research at an early stage of the program in order to gain experience in how to introduce material variables into the synthesis procedure and to establish a working relationship between the materials laboratory and the structural designer. Because high modulus carbon fiber composites were not available in sufficient quantities at the start of the program, the first pass had to be made with another class of materials; in addition, the calculations had to be based on the best currently available analysis procedures, failure mode criteria, and structural synthesis algorithms. These disadvantages are more than offset by the fact that much of the experience gained and many of the techniques developed will be applicable to later passes of the integrated approach which will utilize carbon fiber composites.

The material selected for the first pass is a class of particulate composites designated the JT-series materials. These composites combine the good thermal shock resistance of graphite with oxidation resistance provided by incorporating ZrB_2 and Si into the graphite matrix. When this material is exposed to oxygen at elevated temperatures, a protective oxide coating is formed on the exposed surface by oxidation of the bulk material, thereby providing oxidation protection in depth. One member of this series is the commercial product JTA, which is currently being used for rocket nozzle inserts and is being evaluated by the Air Force for additional applications.

The JT-series materials are being produced and their physical properties measured by Union Carbide. At Case Institute, two structural synthesis problems are being investigated with the objective of determining the optimum material for each application (a thick-walled cylinder and a flat plate). For at least one application, the optimum material will actually be made, its properties determined, and its performance calculated, thus providing a means of evaluating the entire integrated approach concept. The design of a more complicated component, a rocket nozzle insert of JTA material, is being carried out at Bell Aerosystems. The analysis

-10-

procedures at Case and Bell (for linearly elastic, orthotropic materials with temperature dependent properties) will be evaluated by tests at Bell on simple components. The analysis work will be supported by studies of failure under multiaxial stress conditions at Union Carbide and Case and by studies of statistical theories of failure for anisotropic composites at Bell.

2. Materials Research on Carbon-Fiber, Resin-Matrix Composites (See Section VI for results of the first year.)

Prior to the start of this program, carbon-fiber, resin-matrix composites had been fabricated by the same methods used for glass fiber composites. Therefore, the objective of this work, which is being conducted at Union Carbide, is to improve the existing processes through studies of the surface treatment of the carbon fiber and the use of finishes. Progress is to be evaluated by mechanical tests of unidirectional composite rings. Concurrently, larger resin matrix components will be fabricated by filament winding and molding techniques, using the best state-of-the-art. These components will include samples for the reliable design data studies, simple components for testing analysis procedures, and the more complicated component representative of a fuselage section.

3. Micromechanics and Design Data Studies for Fiber Composites (See Section VII for results of the first year.)

The best use of fiber composite materials has been hampered in the past by lack of reliable measurements or, preferably, calculations of composite material physical properties. Micromechanics studies at Case Institute will attempt to improve existing methods for predicting stiffness and strength properties of fiber composites. Work, mainly at Case but partly at Union Carbide and Bell Aerosystems, will be directed toward improving test methods for measuring design data. Union Carbide has the principal responsibility for routinely measuring design data on carbon fiber composite materials.

4. Materials Research on Carbon-Fiber, Metal-Matrix Composites (See Section VIII for results of the first year.)

Unlike the situation for resin matrix composites, fabrication processes for metal matrix composites, applicable to carbon fibers, do not exist. Thus, the initial objective of the metal matrix composite research is to develop a fabrication process for a light weight composite for general airframe use. Emphasis has been on aluminum; but, because of the low density of the carbon fiber, a high fiber content, nickel-matrix composite is of interest. Wettability, carbon diffusion, and brittle intermetallic phase formation are problems under investigation. Future work is to include studies of other metal matrices and process scale-up. This work is being done at Union Carbide.

5. Advanced Analysis and Synthesis Studies (See Section IX for results of the first year.)

The particulate composites are moderately anisotropic and highly nonlinear and nonconservative; the carbon fiber composites are highly anisotropic and moderately nonlinear and nonconservative. For both materials, rational structural design will require improvements in existing analysis and synthesis capabilities. At Case Institute, analysis methods for dealing with buckling and geometric nonlinearity in anisotropic structures will be studied. Synthesis studies at Case seek to establish the more efficient synthesis algorithms which will be required in order to include the material variables within the synthesis process. Later, work at Bell Aerosystems will incorporate these procedures into a large-scale synthesis capability. Studies at both Case and Bell deal with stress analysis procedures for anisotropic nonlinear materials. A large effort at Bell is to generalize their heat transfer and discrete element structural analysis programs to include orthotropic material properties. Later, stress-strain nonlinearity will be introduced into the discrete element structural analysis.

6. Fiber Composite Airframe Component (See Section X for results of the first year.)

The end objective of much of the work of the program is the synthesis, final design, construction, and testing of a subscale component, representative of a fuselage section and fabricated from a carbon-fiber, resin-matrix composite. The synthesis and design is to be done by Bell Aerosystems but will draw upon the experience at Case Institute on the synthesis of particulate composite components and on the advanced analysis and synthesis studies at Case and Bell. Union Carbide is to fabricate the component; the testing is to be done by Bell.

SECTION III

SUMMARY

A. Application Selection

A variety of aerospace application areas for high performance composite materials has been reviewed in order to focus the program efforts on DOD requirements. Atmospheric, space, and support systems and propulsion devices were considered. Application requirements were first related to the type of matrix which would be required and then to the expected degree of utilization of composite material in each area. Fiber reinforced resin matrix composites are of most immediate interest because of greater present availability. Applications include subsonic and supersonic aircraft, missiles, and alunch vehicles. The greatest potential of particulate composites appears to be in propulsion systems.

For the high-modulus carbon-fiber reinforced composites to be used in this program, a fuselage application has been selected as a representative airframe component. For particulate composites, a rocket throat insert has been chosen as a representative propulsion system component. Typical ranges of environmental load conditions were then determined for both applications.

B. Particulate Composite Studies

The effects of processing temperatures and pressures on physical properties have been investigated for the JT-series materials. Three-inch diameter billets have been fabricated for six different materials; and significant and well-behaved variations of the physical properties as functions of composition and density have been found to exist. Possible approaches have been reviewed for developing a multiaxial stress failure criteria for brittle, anisotropic materials which take into account the fact that these materials behave differently under tensile and compressive stresses. A statistical concept has been formulated which predicts the strength variability of an anisotropic material subjected to triaxial stresses. The concept includes consideration of the effects of compressive and shear stresses, as well as tensile stresses, on the probability of failure of the component. A multiaxial stress testing machine for thin-walled, hollow cylinders has been constructed, and preliminary data are reported for biaxial tests in the tension-tension quadrant.

Two structural synthesis problems for simple components (a three-layered cylinder and a flat plate) have been defined, and the necessary transient temperature, stress, and displacement analyses have been formulated, programmed, and subjected to numerical verification studies. The transient temperature analyses take into account temperature dependent thermal properties. The stress and displacement analyses consider the orthotropic character of the material and the temperature dependence of the mechanical properties.

Design studies for a rocket nozzle insert have been made. The high stress levels calculated on the basis of the elastic analysis emphasize the need for considering nonlinear stress-strain effects. A test program plan to provide experimental verification of the various theoretical analyses is presented.

C. Materials Research on Carbon-Fiber, Resin-Matrix Composites

Preliminary experimental evaluation of epoxy resin composites made with carbon and graphite yarn indicated a need for improved fiber-to-resin bonding for the graphite yarn. Studies of surface treatments of graphite fibers have been initiated to assess the influence of surface treatment on adhesion. Chemical etching to roughen the surface was accomplished by immersing the fibers in aqueous solutions of various oxidants. Procedures have been developed for measuring the contact angle of a liquid on a single graphite filament and for measuring wicking rates of liquids along graphite yarn. Contact angle and wicking rate measurements have shown that surface treatments have a large effect upon the wetting of graphite fibers with a high viscosity epoxy resin. Rough, oxygen-free surfaces appear to favor the best wetting and, therefore, the best adhesion. The compressive strength of epoxy resin rings reinforced with etched graphite yarn has been found to be approximately double that of rings made from unetched yarn. This increase in strength is believed to be caused by better fiber-resin bonding. However, the flexural strength of rings made from etched graphite yarn was reduced, probably as a result of yarn degradation. Less severe etching should reduce the magnitude of the decrease in flexural strength.

D. Micromechanics and Design Data Studies for Fiber Composites

A literature study of the theories for the prediction of stiffness properties of unidirectional composites has been completed. It was found that the various analytical models for the modulus in the direction of the fiber gave essentially the same result. However, the modulus transverse to the fibers and the in-plane shear modulus are heavily dependent upon the assumed fiber packing arrangement. A computer capability to simulate random packing arrangements has been developed; future work on models with random packing should yield more realistic predictions of mechanical properties. A study of test methods for the experimental determination of mechanical properties has been initiated. The magnitude of bending and frictional stresses in the split-D test of unidirectional composite rings is being investigated in order to obtain more reliable design data from this test, and a new ring test is being developed.

The first investigations of a photoelastic study of the internal stress behavior within fiber reinforced composites have been on stresses due to curing and uniaxial loading and on stress concentrations at the ends of a fiber. Curing stresses along the fiber have been found to be small, but stresses at the ends are an order of magnitude larger.

To provide preliminary data for design studies, theoretical physical properties have been calculated for several types of unidirectional composites. A new approach for determining mechanical properties of bidirectional composites has been formulated. Theoretical moduli of bidirectional high modulus carbon fiber composites have been calculated as a function of winding angle.

E. Materials Research on Carbon-Fiber, Metal-Matrix Composites

Studies on carbon-fiber, metal-matrix composites have been concerned principally with aluminum infiltration around oriented carbon fibers and hot compaction of fibers electroclad with nickel. Also, brief consideration was given to two matrices (tin and cupro-nickel), where a more favorable relationship exists between the fiber and matrix moduli. Since aluminum does not ordinarily wet pure graphite, the infiltration of aluminum into an oriented graphite fiber network can be facilitated by cladding the fibers with a coupling agent to enhance the wetting of the fibers by aluminum. Reaction and infiltration studies encompassing twelve candidate coupling materials indicated that tantalum is the only metal that is both readily wetted by aluminum and chemically compatible with the fiber and the metal matrix under infiltration conditions. Successfully infiltrated specimens were achieved with other coupling agents (Ni, Cu, and Ag), but the composite properties were adversely influenced by intermetallic phases. Carbon fibers can be electroclad reasonably uniformly with nickel by several techniques; and the nickel matrix composites, prepared by hot pressing the coated fibers, resulted in good fiber distribution and near theoretical densities. Young's moduli $(\sim 29 \times 10^6 \text{ lb/in.}^2)$ for these composites are consistent with the rule of mixtures value, but the tensile strengths $(\sim 50,000 \text{ lb/in.}^2)$ are approximately fifty percent of the anticipated value. The cupro-nickel matrix composite containing aligned carbon fibers provided the highest tensile strength achieved to date $(56,000 \text{ lb/in.}^2)$ and the greatest reinforcement efficiency (75 percent of theoretical).

F. Advanced Analysis and Synthesis Studies

The development of methods for nonlinear multiaxial stress analysis has been initiated with a study based on the concept of the incremental complementary energy search method. Initially, an isotropic Prandtl-Reuss type of material has been considered because of the existence of independent results that will provide test cases for numerical verification. Extension of this study to include orthotropic material characteristics is thought to be possible. The selection and generation of synthesis procedures are well advanced. Three modern algorithms for seeking the unconstrained minimum of a function of many variables have been programmed in modular form and checked out on test functions. The transformations of inequality constrained minimization problems into unconstrained minimization problems using penalty function concepts are reviewed. The methods of feasible directions have been selected for dealing with inequality constrained minimization problems directly, and the generation of modular computer

procedures based on these algorithms is being pursued. The powerful discrete element methods of structural analysis have been extended to accommodate anisotropic materials. A linear analysis capability for thick-walled axisymmetric structures has been generated by introducing a set of orthotropic ring discrete elements. Three orthotropic thin-shell discrete elements have been formulated and are being developed to extend the discrete element analysis capability to fiber-reinforced composite structural components. A general three-dimensional transient temperature analysis capability has been extended to include anisotropic thermal characteristics.

G. Fiber Composite Airframe Component

Preliminary minimum weight estimates have been made of the fuselage structure for several materials and several types of shell construction. The ring- and stringer-stiffened skin was found to be the lightest construction, and a carbon-fiber, resin-matrix composite was estimated to be about 30 percent lighter than a titanium structure. Plans have been prepared for studies of attachments and for component testing.

SECTION IV

APPLICATION SELECTIONS

During this program, attempts are being made to expedite the development of materials to meet DOD needs by directing the material research efforts toward application oriented goals. In the broad sense, there are many needs for materials of lower density, higher strength, higher stiffness, and greater resistance to chemical or radiation damage and of lower cost. Carbon composite materials offer great potential for meeting these objectives, but the numerous possibilities for constituent materials and proportions require specifically defined goals. Within the scope of the project, however, only a few components can be examined. Therefore, it has been decided to:

    (1) Consider only one broad application category, namely, aerospace
    (2) Emphasize common requirements
    (3) Consider representative rather than specific applications
    (4) Emphasize structural aspects

The aerospace category was chosen because the performance benefits to be obtained from composites are greatest. The use of representative components having requirements common to many applications will allow program results to have broad applicability. The emphasis on structural aspects is warranted since the primary function of the exterior of most aerospace applications is to support mechanical and/or thermal loadings.

Although major emphasis during the program is to be devoted to fiber reinforced composites, it was deemed advisable to demonstrate the advantages of the cooperative efforts of the university, the material producer and the potential user at the earliest possible date, hence, the inclusion of a particulate composite material family, the JT series, which was in an advanced state of development.

As an aid in defining representative aerospace structures for which composite materials would show a high potential, a literature review was conducted. Its purpose was to define types of airframe and propulsion system components along with mission applications, geometric configurations, environmental conditions and loadings. The results were generally disappointing with one notable exception, a series of Material Advisory Board reports, which reviewed aerospace requirements for the 1970-1985 time period. Although these reports were directed toward a definition of manufacturing technology requirements rather than toward applications for composite materials, the information on missions and system requirements formed an excellent basis for assessing the future usage of composites.

The MAB reports analyzed numerous systems which were grouped with respect to atmospheric, space, and support operations and propulsion devices, as shown in Tables I and II. While information on specific geometries and loading indices were not provided in detail, overall environmental conditions were sufficient to relate mission application areas to composite material matrix requirements and to assess the relative usage of the various fiber-matrix systems; Table III summarizes this

TABLE I

SYSTEMS CONSIDERED FOR COMPOSITE MATERIAL APPLICATIONS

ATMOSPHERIC OPERATIONS	SPACE OPERATIONS	SUPPORT OPERATIONS
SUBSONIC AIRCRAFT LONG ENDURANCE CHEMICAL LONG ENDURANCE NUCLEAR **SUPERSONIC AIRCRAFT** HIGH ALTITUDE LONG RANGE CHEMICAL HIGH ALTITUDE LONG ENDURANCE-NUCLEAR TACTICAL V/STOL FIGHTER-CHEMICAL **HYPERSONIC AIRCRAFT** ● CRUISE VEHICLES HIGH ALTITUDE LOW ALTITUDE ● BOOST GLIDE VEHICLES STRATEGIC TACTICAL ● HTOL-ORBITAL VEHICLES **MISSILES** ● TACTICAL MISSILES GROUND LAUNCH ANTI-MISSILE SPACE LAUNCH ANTI-MISSILE SRBM UNDERWATER MISSILE ● STRATEGIC MISSILES MOBILE ICBM STORABLE ICBM SPACE LAUNCHED ICBM RE-ENTRY SYSTEMS	**LAUNCH SYSTEMS** ● EARTH LAUNCH RECOVERABLE BOOSTER RECOVERABLE BOOSTER - SINGLE STAGE TO ORBIT ● SPACE LAUNCH EARTH ORBIT LAUNCH LUNAR LAUNCH PLANETARY - MARS PLANETARY - VENUS **SPACECRAFT** ● NEAR SPACE OPERATIONS EARTH SATELLITES SPACE STATION LUNAR VEHICLE ● INTERPLANETARY VEHICLES MARS MERCURY VENUS JUPITER ● SHUTTLE (MANEUVERABLE) **ENTRY SYSTEMS** ● LIFT REENTRY EARTH ORBITAL LUNAR RETURN ● DRAG ENTRY MILITARY WEAPONS & DECOYS MILITARY, MANNED RESEARCH **LANDING SYSTEMS** ● EARTH LANDING TANGENTIAL VERTICAL ● SPACE LANDING EARTH RENDEZVOUS LUNAR RENDEZVOUS LUNAR VERTICAL LANDING PLANETARY VERTICAL LANDING	**BASE EQUIPMENT** HUMAN PROTECTIVE ENCLOSURE LAUNCH FACILITIES DOCKING DEVICES FURNISHINGS AND ATTACHMENTS OTHER **TRANSPORT VEHICLES &** **LOGISTICS** SPACE SITE VEHICLES SURFACE VEHICLES OTHER **LIFE SUPPORT AND** **ENVIRONMENTAL CONTROL** INDIVIDUAL BASE OTHER **POWER GENERATION** SOLAR NUCLEAR FUEL CELLS **MISSION DEVICES** EXPERIMENTAL TEST EQUIPMENT INSPECTION EQUIPMENT SURVEILLANCE EQUIPMENT RECONNAISSANCE & ASTRONOMICAL EQUIPMENT WEAPONRY WAR MANAGEMENT CON- TRIBUTION EQUIPMENT **WORK DEVICES** OPERATION SUPPORT MATERIAL HANDLING SPECIAL FACILITIES & TOOLS VEHICLE ASSEMBLY EQUIPMENT

TABLE II
PROPULSION DEVICES

Turbojet

    Subsonic
    Supersonic
    Earth Launch
    Lift Entry

Turborocket

    Supersonic
    Hypersonic
    Tactical Missile
    Lift Entry

Ramjet & Turboramjet

    Subsonic
    Supersonic
    Hypersonic
    Earth Launch

Liquid Rocket

    Strategic Missile
    Earth Launch
    Near Space
    Interplanetary
    Shuttle (Maneuverable)
    Lift Entry

Solid Rocket

    Tactical Missile
    Strategic Missile
    Earth Launch
    Space Launch
    Near Space
    Interplanetary
    Shuttle (Maneuverable)

TABLE III

EXPECTED UTILIZATION OF COMPOSITE MATERIALS

Application Area	Matrix Material		
	Resin	Metal	Ceramic
Atmospheric Operations			
Subsonic Aircraft	x	x	-
Supersonic Aircraft	x	x	-
Hypersonic Aircraft	x	x	x
Missiles			
Tactical	x	x	x
Strategic	x	x	-
Space Operations			
Launch Systems			
Earth	x	x	x
Space	x	x	-
Spacecraft	x	x	-
Entry Systems			
Lift	-	x	x
Drag	x	x	-
Propulsion Devices			
Turbojet	x	x	-
Turborocket	-	x	x
Ramjet and Turboramjet	-	x	-
Liquid Rocket	x	x	x
Solid Rocket	x	x	x

assessment. With respect to quantity usage aircraft, missile, and launch vehicle structures operating at subsonic and supersonic speeds represent the most significant applications for composite materials in the immediate future. Resin matrices are expected to be adequate in many applications. Note, however, that as metal matrix systems become available the number of applications for composite materials should increase.

Environmental conditions corresponding to each application area were reviewed in detail but are not included here because of security requirements. Initial airframe applications for fiber reinforced composites will involve nominal load factors, relatively modest heating, but rather severe acoustic excitation. Some missile and launch vehicle applications will involve very high load factors and significant heating, but operational lives will be very short. In contrast, the lives of aircraft components should range from hundreds to thousands of hours. Initial applications for particulate composites of the JT type will undoubtedly be in the rocket propulsion area.

Based upon the review of potential uses for composite materials, it is considered appropriate to select an aircraft or missile application for initial study of the fiber reinforced composite (Section IV A), and a rocket engine application for the particulate composite (Section IV B). Notwithstanding the complex environmental conditions involved, major emphasis is to be placed upon design under quasistatic conditions of loading. When design methods are validated for such conditions, attempts to design for dynamic conditions may be initiated.

A.   Fiber Composite Application
(F.M. Anthony, D.P. Hanley, and J. Witmer, Bell Aerosystems)

The first fiber reinforced component to be studied during this program will employ a resin binder since such composite material systems will be used most extensively in the near future. Components of subsonic and supersonic aircraft and missiles and of launch vehicle systems would constitute the major usage for many of these structural applications where ablation is not important. Both fuselage and wing type configurations are of interest so that a representative selection becomes desirable. A conical thin-walled shell may be considered a common idealization of both configurations. With this common feature in mind a "fuselage" application has, therefore, been chosen for the initial fiber reinforced component. Additional factors in the fuselage selection include:

(1)   Existing filament winding techniques can be used
(2)   The configuration is generally applicable to aircraft, missile, and launch vehicle interstage structures
(3)   Complexities such as penetrations and attachments can be introduced at a later date, if desired.

The geometric configuration tentatively established is a slightly tapered, ring and stringer stiffened shell as shown conceptually in Figure 2. Preliminary analyses indicate minimum weight will be achieved with this type of construction as discussed under Section X A.

-21-
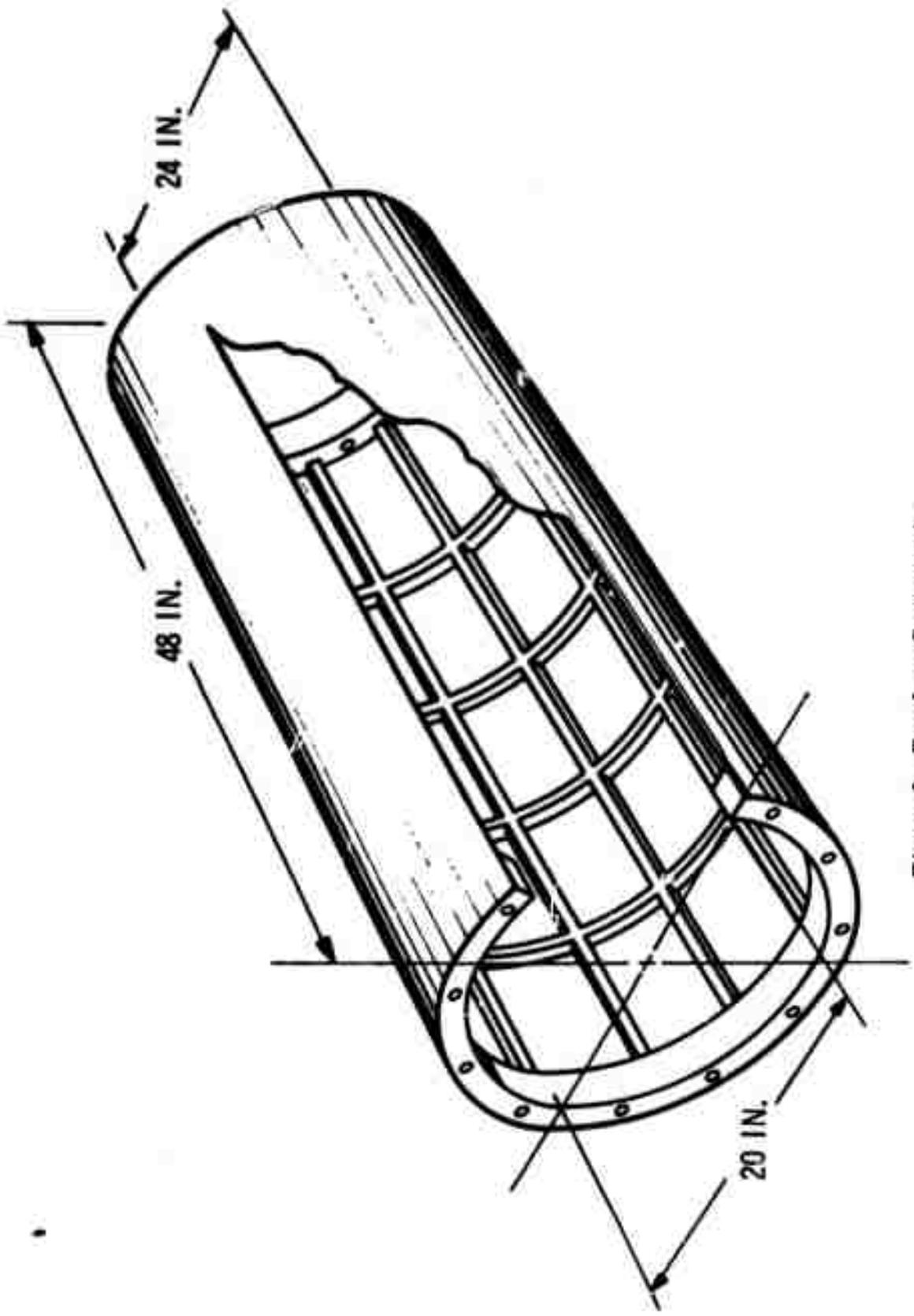
Figure 2. Fuselage Component.

24 IN.

48 IN.

20 IN.

Typical ranges of loading intensities for various aircraft and launch vehicles are shown in Figure 3. These data have been assembled from a review of the literature and many of Bell's structural systems. Included are V/STOL aircraft, supersonic fighters, cruise vehicles, hypersonic boost-glide vehicles, large transport applications, and solid and liquid propelled boost vehicles. The load intensity plot serves to define the ranges of multiaxial loading encountered in practice.

For thin-walled shells of generally cylindrical cross section, a bending moment/diameter index $(M/d^3)^{1/3}$ is used in conjunction with the load intensities. Figure 3 identifies typical values of this parameter for the various fuselage and launch vehicle data. Selecting then the central area of greatest overlap from Figure 3 as being the most representative loading conditions, axial and shear loading intensities of 2000 and 200 lb/in. respectively were chosen with an $(M/d^3)^{1/3} = 4.0$ for initial design studies of the fuselage section.

B. Particulate Composite Application
(F.M. Anthony, D.P. Hanley, and J. Witmer, Bell Aerosystems)

The JT particulate composite material family possesses characteristics which include high thermal conductivity, low thermal expansion, moderate modulus of elasticity values, good strength retention at elevated temperatures, and good oxidation resistance up to temperatures of 3500°F. When such characteristics are considered in the light of potential application areas for composite materials, the most logical area for immediate application is for rocket propulsion devices. To minimize the amount of effort to be devoted to particulate composite materials within the framework of this program, a logical component for study is a rocket throat insert. While relatively simple in geometric configuration, rocket throat inserts are subjected to severe heating environments which generate steep transient temperature gradients and high thermal stresses, the magnitude of which depend upon the particular geometry and environmental conditions involved.

The severity of the environmental conditions will vary with the propellant composition, chamber pressure, and engine size. In order to establish the relationships among environmental conditions and system operating parameters, heating intensity was calculated as a function of throat diameter and chamber pressure for a single propellant combination. The propellant combination was assumed to be $N_2O_4/50$ UDMH + 50 N_2H_4 which has a combustion temperature of about 5400°F at a mixture ratio of 2:1. Nozzle throat diameters were varied from 0.5 inch to 24.0 inches while chamber pressures were varied from 100 to 1000 psia. Although liquid propellant engines rarely operate above 500 psia, higher chamber pressures were assumed to make the results somewhat representative of solid propellant engines. The resulting heating conditions are presented in Figure 4, in the form of a carpet plot of the throat heat flux as a function of chamber pressure and throat diameter. It is apparent that the chamber pressure has a dominant influence on the cold wall heat flux. The effect of throat diameter becomes relatively insignificant when diameters are above approximately 5 inches.

While it is not considered to be economically desirable to test large inserts during the present program, insert proportions were chosen so that the selected environmental
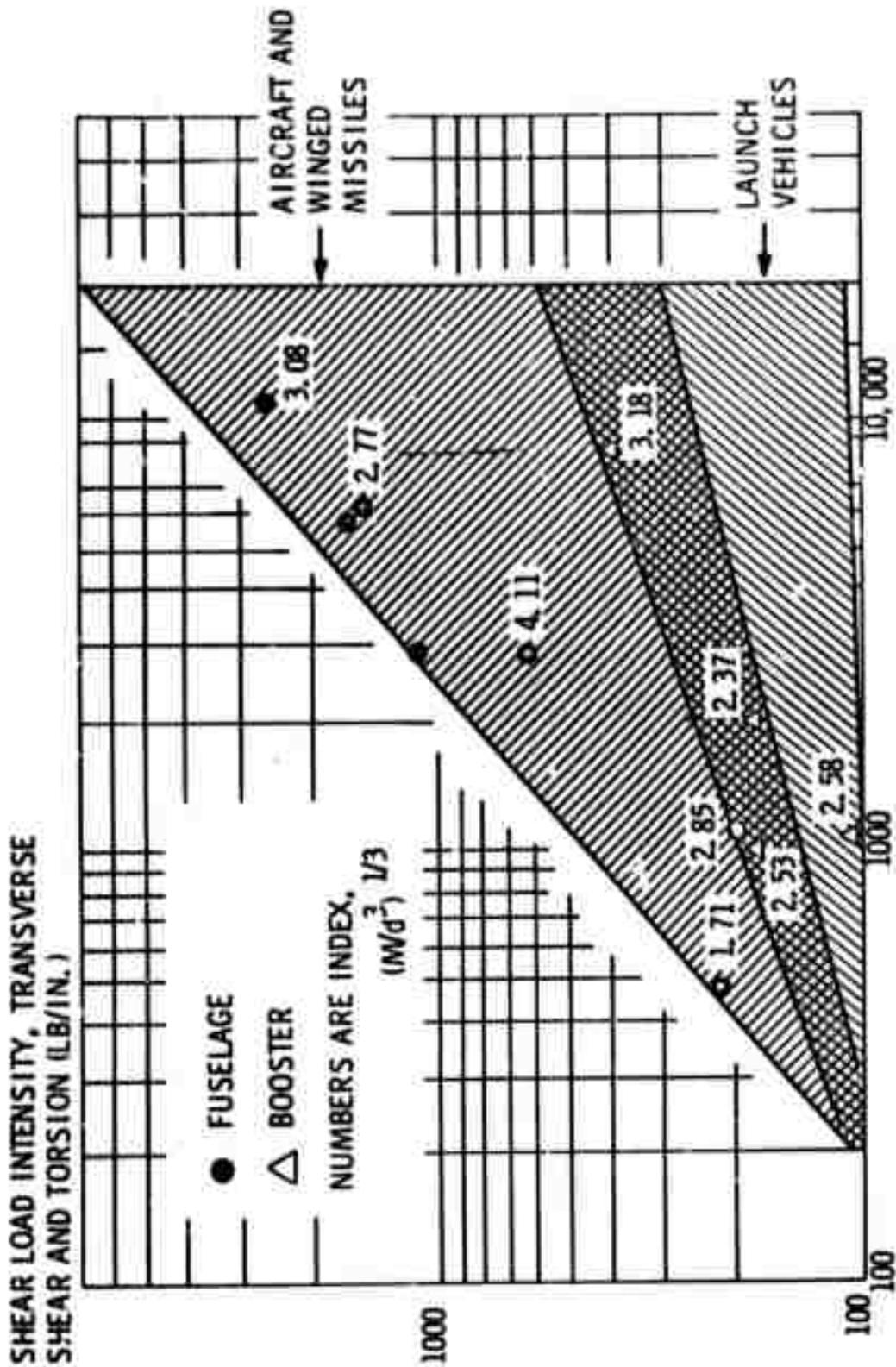
Figure 3. Shear Loading Versus Axial Loading For Various Vehicle Constructions.

THROAT HEAT FLUX - BTU/ IN.^{2} SEC.

FUEL: N$_2$O$_4$ / 50 UDMH + 50 N$_2$H$_4$

THROAT DIA — IN.

CHAMBER PRESSURE - PSIA
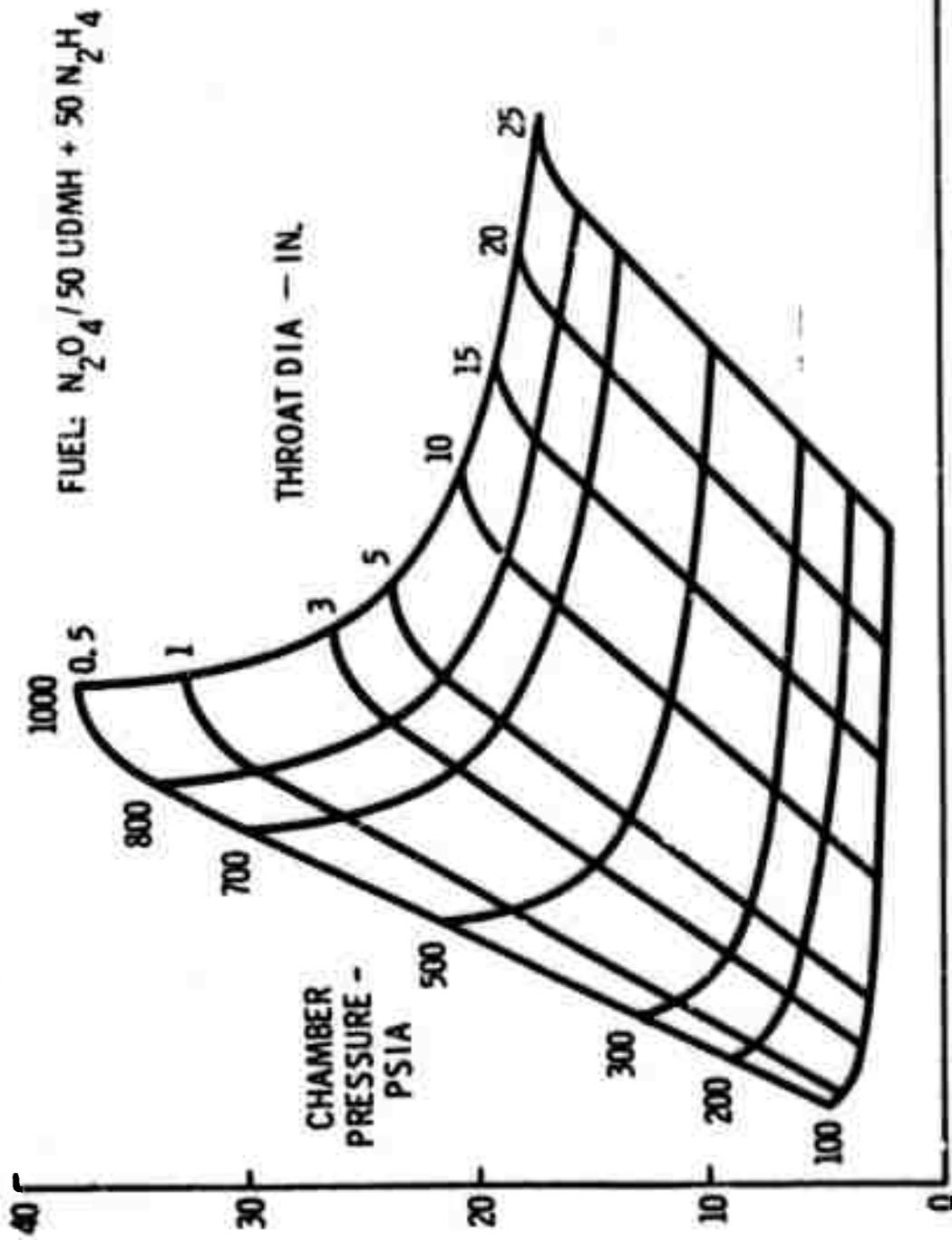
Figure 4 . Cold Wall Heat Flux at Throat.

conditions will give temperature and stress levels which are representative of a range of sizes. Results of design studies which define representative temperature and stress levels are precented in Sections IX C and D. Two geometric configurations were considered, as shown in Figure 5, along with variations in diameter, wall thickness, length, external restraints, and chamber pressure. Temperature distributions were determined using a computer program which was available prior to the initiation of the present effort, and which included temperature dependence of material properties but permitted consideration only of transversely isotropic materials; this program under the present effort has been extended to account for generalized thermal anisotropy. Discrete element matrix methods described in Section IX C were used for the calculation of thermal stresses. Structural idealization was accomplished by means of a triangular ring element whose behavior characteristics were based on temperature dependent, linearly elastic, transversely isotropic behavior.
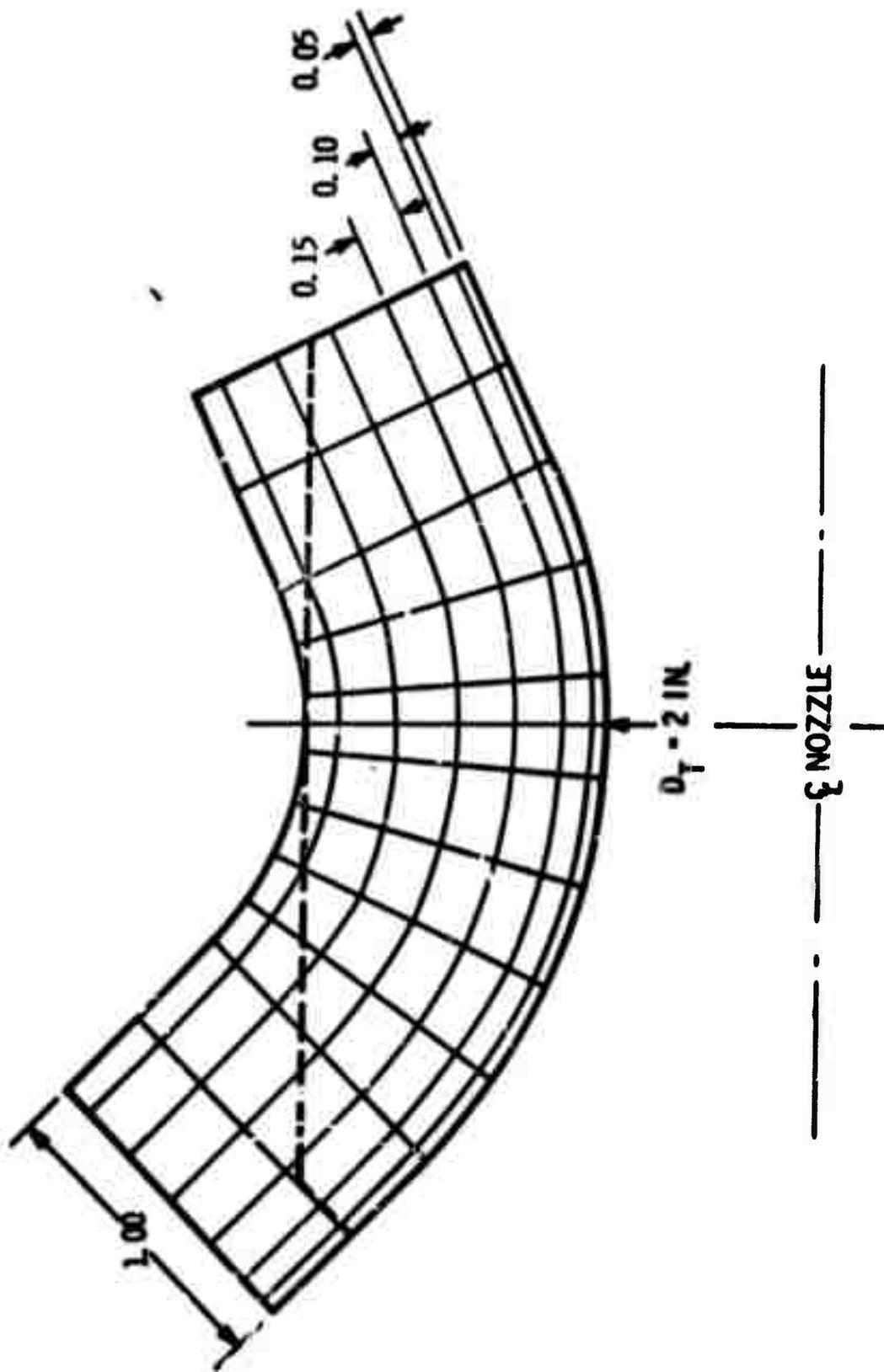
Figure 5. Nozzle Insert – Uniform Wall Nonuniform Grid.

SECTION V

PARTICULATE COMPOSITE STUDIES

The JT-series composite materials represent a specific class of
particulate composite materials which were selected for initial implementa-
tion of the integrated approach to applied materials research.   The main
goal of this effort is to demonstrate a quantified approach to the
simultaneous design of structural geometry and material.   In this instance
(JT-series composites), the material properties are varied by changing the
composition (i. e. , percent metallic additives) and the porosity of the
particulate composite material.   The porosity is thought of as a processing
variable since it can be controlled by means of processing temperatures and
pressures.   The thermal and mechanical properties of materials in this
JT series can be thought of as functions of composition, porosity, and
operating temperature.

Consider now the design of a simple component to perform a specified
set of functional purposes.   The design task is to determine the geometric
proportions, material composition, and porosity such that the component
performs the functional purposes adequately, while at the same time progress
toward an optimum design is achieved with respect to some stated function
(for example, minimum weight).   This task may be attacked by considering
several discrete materials, each one of which is within the JT series, and
then obtaining an optimum design of the geometric proportions for each
discrete material.   These optimum design weights-versus-composition and
porosity can be used to construct a function which estimates the optimum
design weight as a function of composition and porosity.   Functions of this
sort will be referred to as materials evaluation functions. Seeking the
minimum of the materials evaluation function, subject to constraints which
limit the range of values of the arguments, leads to a quantitatively based
recommendation for an improved material. With the recommended
composition and porosity information, a new material within the JT series
can be fabricated.   The properties of the improved candidate material can
then be obtained; and, as before, the optimum design of the geometric
proportions determined.   It is to be expected that the weight associated with
this optimum design will not agree exactly with that predicted by the
materials evaluation function; but the improved material is likely to be
superior to any previous material in the family, provided that the dependence
of the material properties on the composition and porosity is continuous and
well behaved. Subsequently, it should be possible to treat the geometric
proportions, composition, and porosity simultaneously within the structural
synthesis procedure. When this goal is accomplished, the quantified
approach to the simultaneous design of structural geometry and material
will have been clearly demonstrated.

In Section V A, the fabrication of JT-series materials with various
compositions and porosities is described, and in Section V B the
experimental determination of thermal and mechanical material properties

is discussed. A review of stress-strain relations and multiaxial stress
failure theories for anisotropic materials is reported in Section V C. An
examination of statistical aspects of failure in anisotropic brittle materials
is presented in Section V D. An experimental program to establish an
operational failure criterion for JT series materials subject to multiaxial
stress conditions is reported in Section V E. In parallel with the quest for
a rational and/or semiempirical multiaxial stress failure theory (as
represented by Sections V C, D, and E), effort has been directed toward
formulating two structural synthesis problems for simple structural
components. The analyses on which these two synthesis capabilities will
rest include orthotropy and temperature dependent material properties.
The principal purpose of these two structural synthesis studies is to
demonstrate the integrated approach. Various idealizations and
simplifications have been made in the analysis and failure criteria in order
to expedite completion of these initial demonstrations. In Section V F,
progress to date on the structural analysis and synthesis of a three-layer
thick-walled cylinder is described. In Section V G, the analysis and
synthesis formulations for a flat-plate system which exhibit several
important structural behavior characteristics are reported. Both of these
simple components are geometrically regular and highly idealized. The
study reported in Section V H deals with the application of axisymmetric
finite elements to the analysis of rocket throat inserts. This analysis study
deals with the actual insert geometry. Finally, in Section V I, test plans
of JT-series simple components are given. The results of these tests will
provide an experimental base which can be used to assess the accuracy of
the thermal and stress analysis techniques described in Sections V F, G,
and H.

A. Fabrication of JT-Series Materials
(R. G. Fenish, Union Carbide)

1. Description of JT-Series Materials

The JT-series materials are graphite-base refractory composites
similar to the commercial material with the grade designation JTA produced
by the Carbon Products Division (JTA is one member of the series). On a
weight basis, grade JTA is composed of 48.1 percent C, 42.4 percent
ZrB_2, and 9.5 percent Si. There is a minimum density limit for grade JTA
of 3.0 g/cm^3. During manufacture, the silicon combines with part of the
carbon to form silicon carbide.

In this work, the elements Zr, B, and Si will be called the metallic
additives; and these elements will always be present in the same proportions
as in JTA: 42.4 parts of ZrB_2 to 9.5 parts of Si. Let

c = mass fraction of metallic additive
in the fabricated product and

ρ = density;

grade JTA may, then, be specified by composition $c = 51.9$ percent and density $\rho > 3.0$ g/cm^3.

The JT-series materials are a class of materials produced by varying the amount of metallic additives and the density. In order to vary the density at a fixed composition, variations must be made in processing temperatures or pressures; otherwise, the manufacturing conditions are kept as close as possible to those for grade JTA.[1] Therefore, to a good approximation, each member of the JT series can be identified by values of the compositional variable, c, and by that which is equivalent to a processing variable, the density, ρ. To the same approximation, the physical properties of the JT-series materials may be considered to be functions of only two material variables, c and ρ.

2. Material Symmetry, Coordinate Orientation, and Billet Notation

All of the JT-series materials are molded in cylindrical billets. This process yields material with the symmetry characteristic of transverse isotropy, i.e., all physical properties are invariant with respect to arbitrary rotations about the symmetry axis, which is parallel to the direction of molding and perpendicular to the molding ram face.

Throughout this study, physical properties of the JT-series materials will be specified with respect to a Cartesian coordinate system oriented with the x_1 and x_2 axes in the plane of transverse isotropy and the x_3 axis parallel to the axis of rotational symmetry. These symmetry oriented coordinates should not be confused with other types and orientations of coordinate systems used in the stress analysis problems. In JT material, as in other molded material, the elongated graphite particles or grains tend to be aligned with their two larger dimensions parallel to the plane of transverse isotropy, a situation which has led to properties (Young's modulus, coefficient of thermal expansion, etc.) in directions parallel to the plane of isotropy being called "with-grain" properties and properties in the direction parallel to the symmetry axis being called "against-grain" or "across-grain" properties.

The billets of JT material fabricated especially for this program will be identified by the letters JT, followed by the nominal composition, and, finally, the sequential fabrication number. Thus, JT30-4 designates that the billet is the fourth to be fabricated and that the composition is approximately 30 percent metallic additive.

Commercial JTA billets from the standard production material which are used for this program will be identified by the letters JTA followed by the sequential order number. Thus, JTA-9 designates the ninth piece of commercial JTA used for this program.

3. Calculation of Theoretical Maximum Density and Porosity

Because the density varies with the composition as well as with porosity in the material, it is better for some purposes to choose composition c and porosity p as the material variables, rather than composition and density. Part of the porosity is in closed pores, the volume of which is not easily measured. Therefore, the porosity must be calculated from the measured bulk density ρ and the calculated theoretical maximum density ρ_m:

$$p = 1 - \rho/\rho_m \qquad\qquad\text{(V A-1)}$$

The theoretical maximum density can be calculated from the mass fraction and X-ray density of each phase in the composite material. Based on the following assumptions

mass ratio of ZrB_2 to Si is 42.4/9.5,

all Si is in the form of α- and β-SiC, and

X-ray density of pure C is 2.267 g/cm^3, of ZrB_2 is 6.10 g/cm^3, and of SiC is 3.216 g/cm^3,

the calculated theoretical maximum density is given by

$$\rho_m = \frac{2.267}{1 - 0.5905\,c} \qquad\qquad\text{(V A-2)}$$

where c $(0 < c < 1)$ is, as above, the mass fraction of Zr, B, and Si in the fabricated composite. In practice, there are uncertainties of perhaps one percent in the mass fraction c and ZrB_2/Si ratio and in the density of ZrB_2. At low porosity levels of less than 5 percent, the corresponding uncertainty in the calculated porosity is several tens of percent. The possible error in the calculated porosity will not affect the stress analysis and structural synthesis work provided that Formulas V A-1 and V A-2 are used consistently in calculating the porosity.

4. Fabrication of Initial Billets in September, 1965

The initial series of billets to be fabricated was selected to provide the initial trend of property data with composition at a fixed porosity and the trend with porosity at a fixed composition. Billets 3 inches in diameter by 3-1/2 inches in length were pressed on production-size equipment at a maximum observed outside-surface mold temperature of 2130°C and at pressures ranging between 3,300 and 5,500 lb/in.^{2} Two attempts to fabricate composites with 10 percent additive were unsuccessful due to mold failures. Two other billets were of smaller size. Table IV gives the composition and average density and porosity of the good billets and of a commercial JTA billet. All of these billets have been cut into specimens for physical properties testing. The test results are given in Section V B.

TABLE IV

COMPOSITION, DENSITY, AND POROSITY OF INITIAL JT-SERIES BILLETS

Billet Number	Composition Percent Metallic Additive	Average Density g/cm³	Average Porosity Percent
JT30-5	31.5	2.31	17.2
JT30-6	31.5	2.38	14.7
JT30-4	31.5	2.58	7.4
JT40-9	41.7	2.81	6.7
JTA-9	51.9	3.05	6.7
JT70-3	71.4	3.66	6.7
JT70-8	71.4	3.66	6.7

5. Process Studies on 1- and 1.5-Inch Diameter Billets

A basic premise of the entire JT-series program is that the physical properties of the materials depend on only two material variables, composition and density, and not on, say, the individual values of processing temperature and pressure used to attain a certain density. When it was found that the physical properties of commercial JTA did not fit smoothly with those of the initial experimental billets, a limited study of processing conditions was initiated to determine conditions for the development laboratory equipment which would yield material more compatible with commercial JTA.

a. **Method of Fabrication.** Experimental billets 1.0 and 1.5 inches in diameter with the same composition as JTA were hot-pressed by a floating mold technique. The mold was heated in a 4-inch diameter tube furnace. Resistance heating, rather than the induction heating normally employed for manufacturing JTA, was used to obtain closer temperature uniformity than that which can be achieved by induction heating. During hot pressing, an initial pressure of 2500 lb/in.² was applied and maintained until the mold temperature reached 1800°C; at that time, the selected maximum pressure was applied. All samples were held for 1 hour at the selected hot-pressing temperature. They were then cooled under maximum pressure to a temperature of 1700°C, at which time the pressure was released. These experimental billets are designated by the letter E followed by a sequential fabrication number.

b. **Temperature Series.** Effects of pressing temperature on the density and microstructure were examined on samples hot pressed at temperatures ranging from 2210° to 2280°C at a pressure of 2900 lb/in.² The solidus temperature for JT composites was determined to be

2260±10°C by incipient melting experiments. Examination of the run-out material by metallography and X-ray diffraction disclosed a eutectic between ZrB_2 and SiC. Processing and density data are given in Table V.

TABLE V

PROCESSING CONDITIONS AND DENSITY OF EXPERIMENTAL JT-SERIES BILLETS

Specimen Number	Processing Temperature $T \pm 10°C$	Processing Pressure lb/in.^{2}	Density g/cm^3	Diameter in.
E-2*	2210	2900	2.84	1.5
E-3*	2230	2900	2.98	1.5
E-4*	2250	2900	3.11	1.5
E-5*	2270	2900	3.11	1.5
E-6*	2280	2900	3.06	1.5
E-17	2240	2900	2.86	1.5
E-18	2260	2900	3.00	1.5
E-20	2265	2900	3.03	1.5
E-16	2290	2900	2.97	1.5
E-13	2150	3500	2.78	1.0
E-14	2150	4500	2.89	1.0
E-12	2150	5500	2.97	1.0
E-10	2210	5500	3.11	1.0
E-11	2230	3500	2.96	1.0
E-9	2230	4500	3.09	1.0
E-6	2230	5000	3.11	1.0
E-7	2230	5500	3.13	1.0
E-19	2260	5500	3.15	1.0

* Specimens E-2 through E-6 were inadvertently made with 53.7 instead of 51.9 percent metallic additive.

Figure 6 illustrates the effect of pressing temperature on density and microstructure. Density increases with increasing pressing temperature to an extrapolated temperature of 2258°C and then decreases at higher temperatures. This decrease in density is caused by some run-out of the ZrB_2, SiC liquid eutectic. The 250 X magnification photomicrographs adjacent to the data points on Figure 6 show the representative structure of the material at different pressing temperatures. As the temperature is raised from 2210° to 2250°C, the porosity of the material decreases; the general physical structure and distribution of the ZrB_2-SiC-C phases remain essentially unchanged. As the temperature is raised above 2260°C (the solidus temperature), some of the dense metallic phases are pressed

out, causing a change in composition of the billet. Both the porosity and the density of the billet decrease, and the structure shows the presence of an increased amount of a well-dispersed metallic phase.
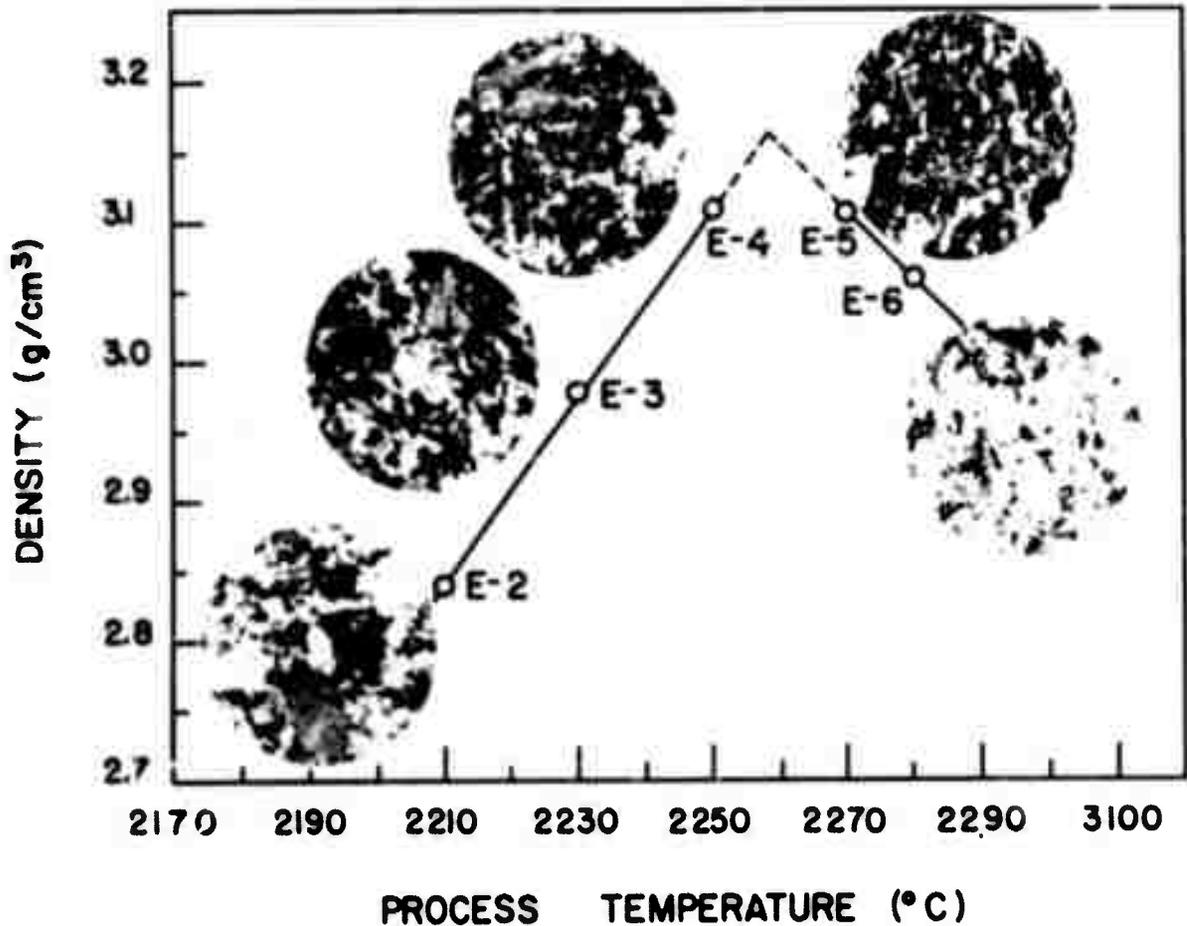
Figure 6. Effect of Processing Temperature on Density and Microstructure of JT Material of 53.7 Percent Composition. White Phase Is ZrB_2, Light Gray Phase Is SiC, and Dark Gray and Black Phases Are Graphite and Porosity.

An X-ray analysis was made on the liquid run-out from a specimen taken to 2400° C, well above the solidus temperature; the analysis showed only the presence of ZrB_2, SiC, and graphite.

    c. Pressure Series. The effect of molding pressure on density was examined on samples molded at pressures ranging from 3500 to 5500 lb/in.[2] at temperatures of 2150±10 and 2230±10° C. Figure 7 shows the dependence of density on molding pressure; the figure also shows the density change with temperature for four samples pressed at 5500 lb/in.[2]

These data indicate that, to achieve densities of 95 or higher percent of theoretical maximum density (.95 x 3.27 = 3.11 g/cm³), temperatures in excess of 2200°C and pressures in excess of 5000 lb/in.² are necessary.
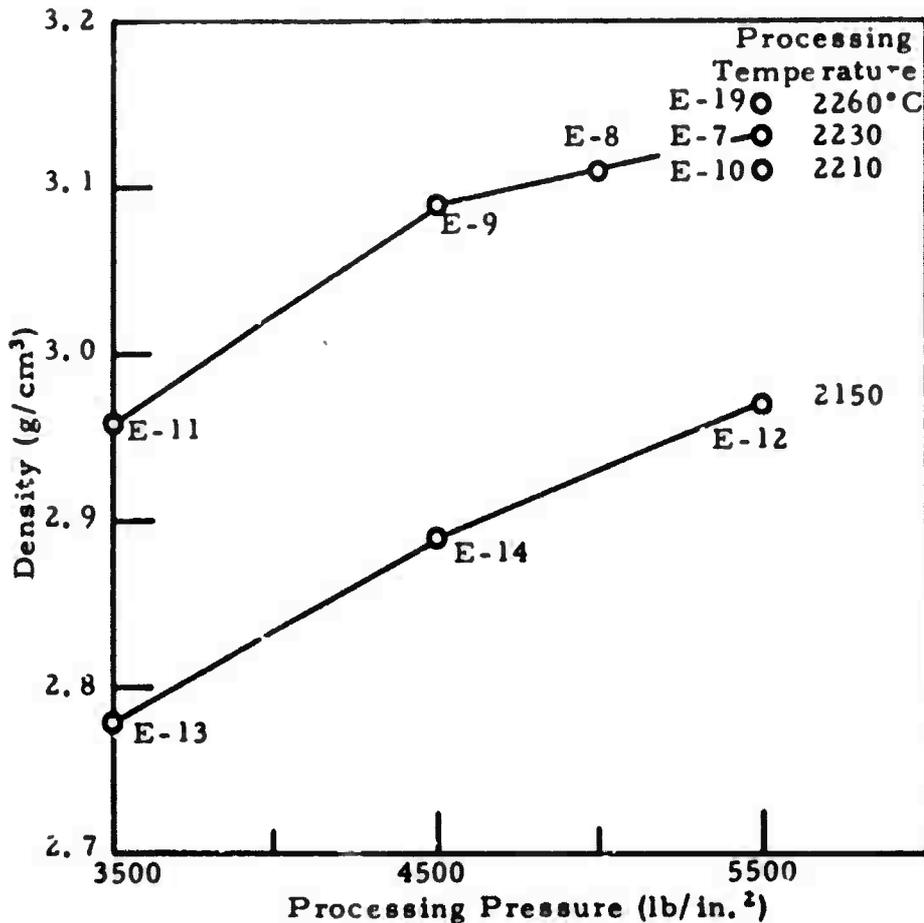
N-9481

Figure 7.   Effect of Processing Pressure and Temperature on
Density of JT Material of 51.9 Percent Composition.

    d.   Ultrasonic Elastic Stiffness Constants.   The elastic stiffness constants c_{ij} have been determined for the experimental billets from measurements of the velocity of ultrasonic pulses at 1 megacycle per second frequency.   Figure 9 shows the stiffness constants c_{11}, c_{33}, and c_{44} and the density for a series of billets processed at successively higher temperatures.   At a given density, the value of each constant is 15 to 20 percent higher if the processing temperature is above rather than below the solidus temperature.   It is thought that the consistently high values of the elastic constants of the 3-inch diameter billets fabricated in September 1965 are due to the maximum billet temperatures having been higher than the solidus temperature, even though the outside mold temperature was only 2130°C.   (See Section V B for data on elastic constants of 3-inch diameter billets.)
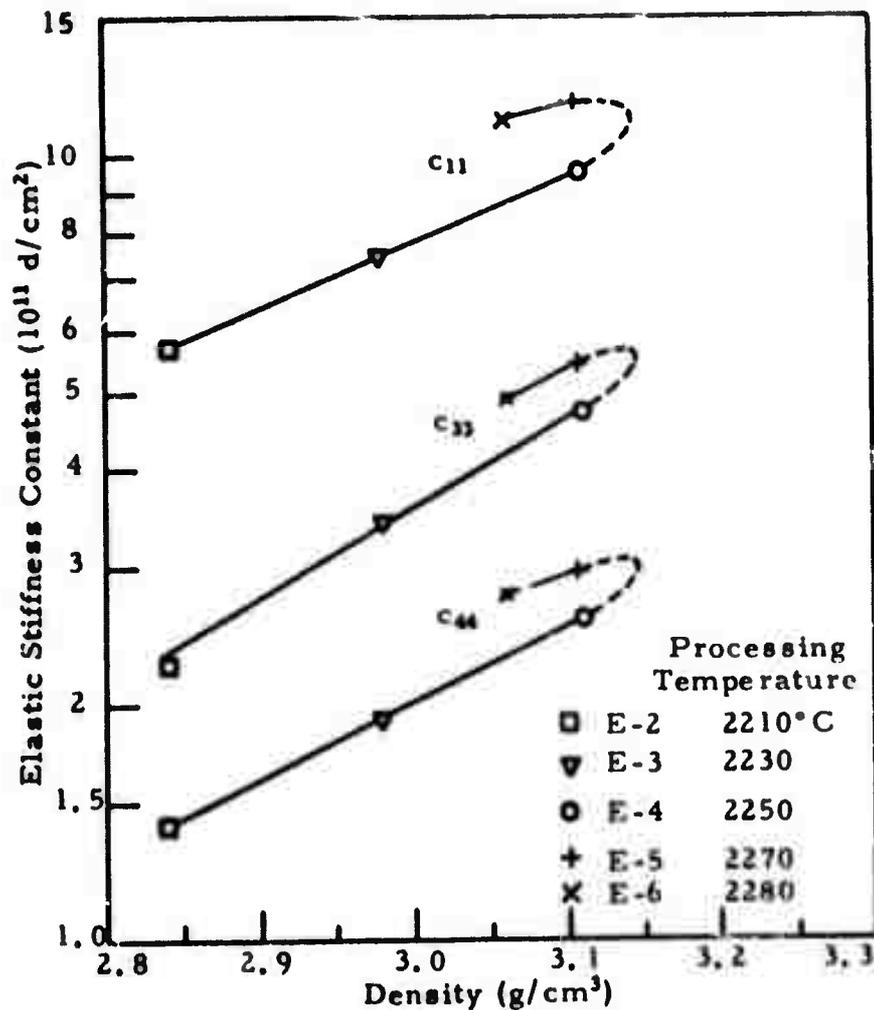
Figure 8.   Effect of Processing Temperature on Density and
Ultrasonic Elastic Stiffness Constants of JT Material
of 53.7 Percent Composition.

Figure 9 shows the stiffness constants c_{33} and c_{44} versus density for
all the 51.9 percent composition billets fabricated at various pressures and
various temperatures less than the solidus temperature (see Table V for the
processing conditions).   It appears that, within the reproducibility of the
experiments, the elastic constants at fixed composition depend only on the
density and not on the individual processing temperatures and pressures
used to achieve that density, provided that the temperature is less than the
solidus temperature.   This result strengthens the original premise that
the JT-materials program can be based entirely on composition and density
as material variables.
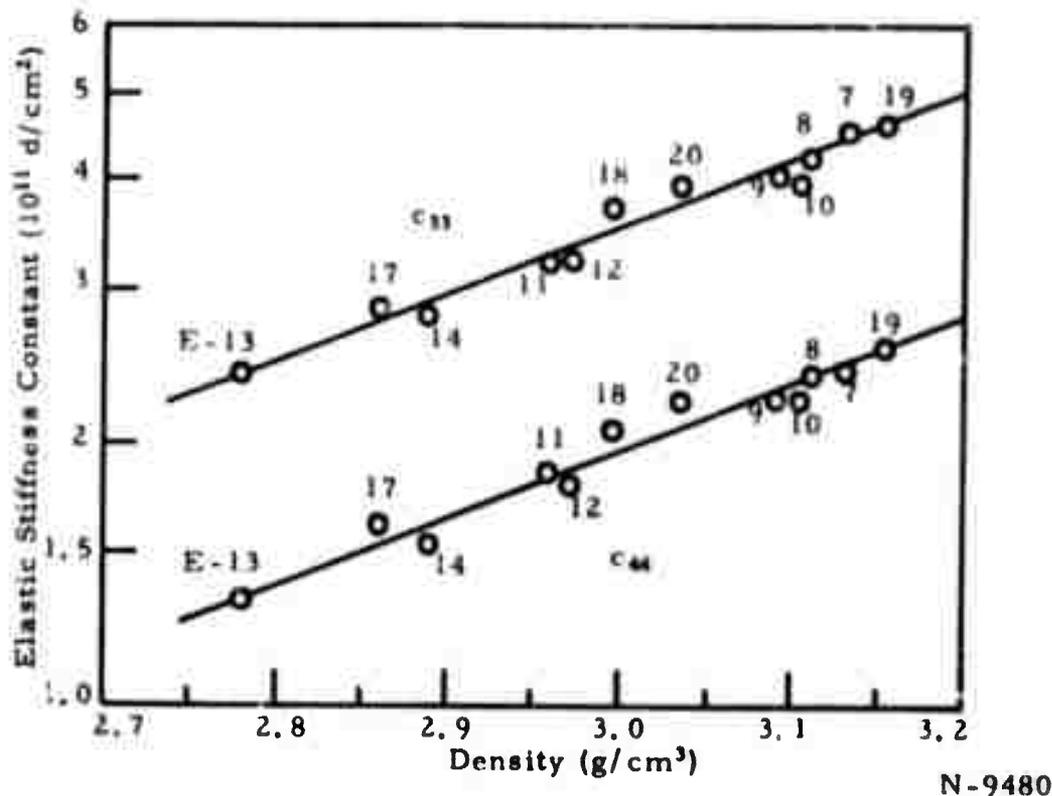
Figure 9. Ultrasonic Elastic Stiffness Constants Versus Density for JT Materials of 51.9 Percent Composition.

6. Process Studies on 3-Inch Diameter Billets

A 40-ton press with an induction furnace capable of attaining temperatures higher than 3000°C has been put into operation at this laboratory. Figure 10 shows an overall view of the press, including the induction coil and furnace assembly.

In induction heating at high heating rates, there is a difference between the temperature of the outside surface of the mold (which acts as the susceptor) and the temperature of the billet. During normal fabrication, only the outside mold temperature is measured. Therefore, it was necessary to correlate the surface temperature of the mold to the interior temperature of the billet. This correlation was established by simultaneous temperature measurements on the mold surface and at the center of a specially prepared, prepressed billet of 51.9 percent composition. The maximum temperature difference is 140°C.

A three-inch diameter billet of JT material of 51.9 percent composition was hot pressed to 92.5 percent of theoretical density by single ram pressing. The billet was sectioned, and a density profile consisting of 15 specimens (1/2 x 1/2 x 1/2 inch) was obtained. The density variation
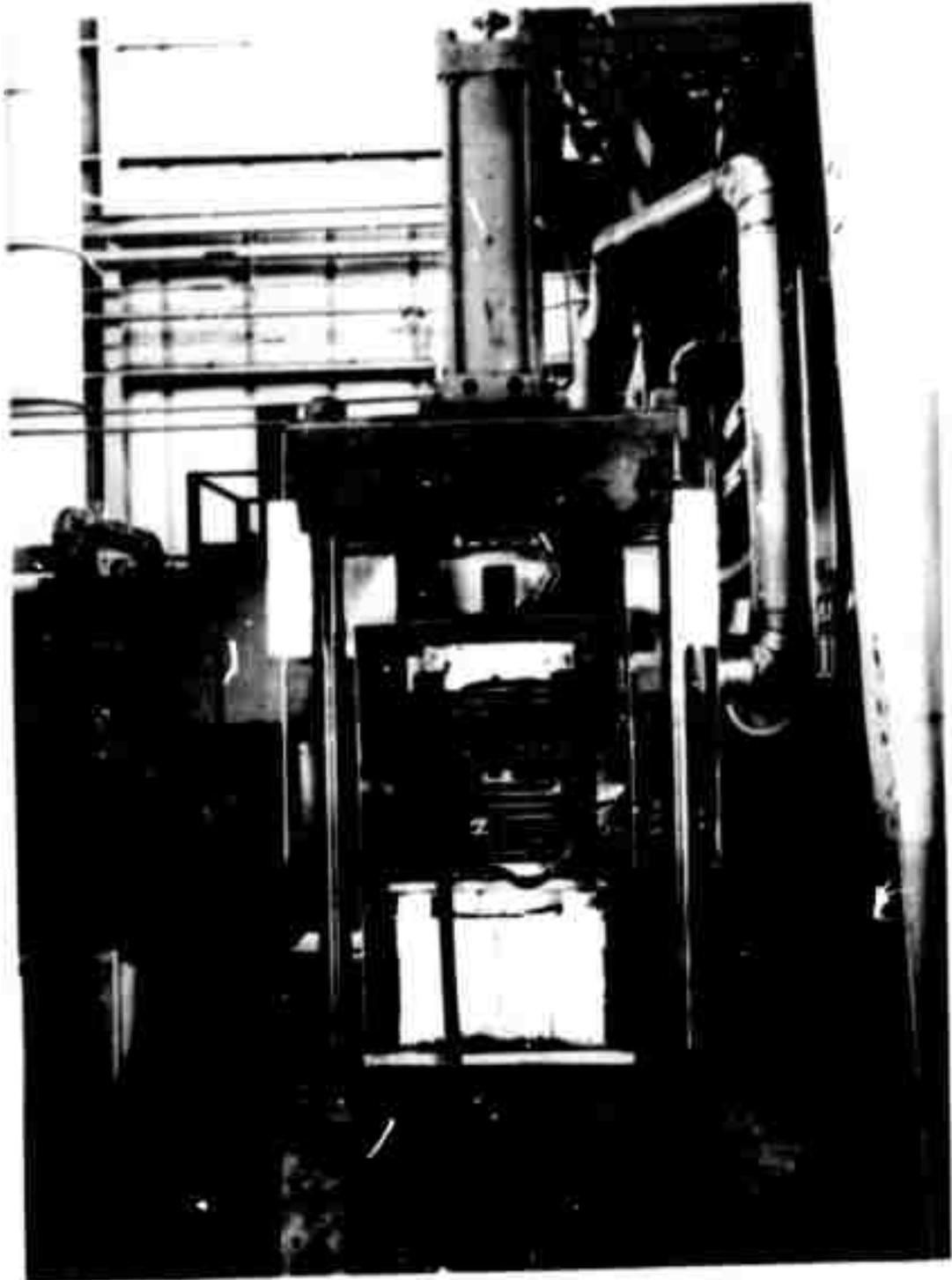
N-9557

Figure 10.   Forty-Ton Press and Induction Furnace Used for
the Fabrication of the JT-Series Materials.

within the billet was determined to be 3.0 percent; densities ranged from 3.01 to 3.10 g/cm^3. A three-inch diameter billet of 31.5 percent composition was hot pressed by float molding. The density profile of the sectioned billet resulted in a 1.2 percent density variation; densities varied from 2.47 to 2.50 g/cm^3. Thus, float molding reduced the density variation in a three-inch diameter billet from three percent to one percent. Based on these results, additional billets of JT material will be fabricated employing the float molding technique.

B. Physical Properties Evaluation of JT-Series Materials
(O. L. Blakslee and T. Weng, Union Carbide)

The objective of this work is to obtain physical property data to be used as input information to the stress analysis and structural synthesis calculations performed at Case Institute and Bell Aerosystems. Testing to date has been at room temperature; future work will include determining or estimating high-temperature trends. The physical properties of interest are the elastic moduli, stress-strain relations, fracture strengths, thermal diffusivities, specific heats, and coefficients of thermal expansion.

At the start of this work, very little was known of the variation of the physical properties with composition and porosity. Therefore, the first objective was to obtain quickly approximate trends to aid the stress analysis and synthesis programs. For this purpose, six billets of varying composition and porosity were prepared in September of 1965 and one billet of commercial JTA was obtained, as discussed in Section V A4; measurements were made of their physical properties. These measurements revealed that physical properties values predicted for JTA by interpolation of data for the experimental billets did not agree with values measured on commercial JTA. In order to remove or lessen this discrepancy, the study of processing conditions discussed in Section V A5 was initiated. As a result of this study, billets prepared in the future will have properties which are more compatible with those of commercial JTA. It must be kept in mind that the physical properties values given in this report on the billets made in September, 1965, will differ by perhaps 10 to 30 percent from the final values for JT-series materials. In addition, it appears that the moduli and strengths for billet JTA-9 are on the lower edge of the range of values for commercial JTA and are not typical of average values.

Even though the present data will ultimately be revised somewhat, it is felt that the data should be reported at this time to give a general picture of how the physical properties of JT-series materials depend on composition and porosity. It has been found that a 10 percent change in composition or a 5 percent change in porosity causes most physical properties to change by amounts that are large compared with the scatter and possible error in the measurements. A significant variation of physical properties with changes in material variables (composition and porosity) is, of course, a necessary prerequisite for any materials optimization study.

1. Methods of Measurement

   a. Ultrasonic. Elastic constants were determined from the velocities of propagation of longitudinal and transverse ultrasonic pulses at one megacycle per second frequency. Due to the high attenuation of the JT-series material, a through-transmission method was used with a path length of about 1.25 inches and with directions of propagation parallel, perpendicular, and at 45 degrees to the symmetry axis of the material.

   b. Resonant Bar. Elastic constants were determined from the frequencies of longitudinal, flexural, and torsional vibrations of bars of dimensions 1/4 x 1/4 x 3 inches. In addition, measurements were made on the static tension and flexural specimens to detect defects and unusual characteristics of the specimens prior to static testing and to provide a check of the moduli determined from the initial slope of the stress-strain curves.

   c. Tension and Compression Tests. Both longitudinal and transverse strains were measured using pairs of strain gages mounted on dog bones in tension and on rectangular prisms in compression. The dog-bone blank dimensions were 1/4 x 5/8 x 2-3/4 inches, and the gage-section dimensions were 1/4 x 1/4 x 1-1/2 inches. The size of the compression sample was 1/4 x 1/4 x 1 inch.

   d. Flexural Test. Flexural tests were run using four-point loading on bars of dimensions 1/4 x 1/4 x 3 inches. Transverse and longitudinal tensile and compressive strains were measured at the top and bottom surfaces with strain gages. Because the load-versus-strain relations are nonlinear and slightly different in tension and compression, the data obtained from flexural tests were converted to uniaxial stress-strain relations by means of Naidai's graphical method. [2] In addition, the effect of frictional forces at the loading and supporting edges was also taken into account in the calculation of the true stresses.

   e. Thermal Diffusivity. Thermal diffusivities were measured from ambient to approximately 600°C by a flash method. [3] The sample size was 5/8 x 5/8 x 0.04 inch.

   f. Specific Heat. Specific heats were calculated by multiplying the weight percent of each constituent phase by the specific heat per unit mass of that phase (carbon, [4] zirconium diboride, [5] and silicon carbide, [6] assuming complete conversion of Si into SiC). The calculations were made at 100 degree intervals from room temperature to 700°C.

   g. Coefficient of Thermal Expansion. The coefficients of thermal expansion were measured by the Newton's rings method on cubes of nominal edge length of 1/2 inch.

2. Ultrasonic Elastic Constants

A complete set of five elastic stiffness constants, c_{ij}, has been determined from ultrasonic measurements on one sample from each billet. All of the Young's and shear moduli and Poisson's ratios have been calculated from these c_{ij} by standard transformation formulas, although there is a loss of accuracy due to the accumulation of errors in the calculation. The ultrasonic data shown in Table VI illustrate the trends of the elastic constants with composition for approximately six percent porosity and the trend with porosity for 30 percent additive composites.

TABLE VI

ELASTIC CONSTANTS OF JT BILLETS FROM ULTRASONIC MEASUREMENTS

| | JT 30 | | | JT 40 | JTA | JT 70 |
	-4	-5	-6	-9	-9	-3
Young's Modulus						
$1/s_{11}$	8.1	3.7	4.4	10.4	10.8	23.5
$1/s_{33}$	2.9	1.5	1.6	4.0	3.8	13.7
Shear Modulus						
$1/s_{44}$	1.9	0.9	1.0	2.5	2.6	7.4
Poisson Ratios						
$-s_{12}/s_{11}$	0.08	---	0.10	0.07	0.06	0.12
$-s_{13}/s_{33}$	0.13	0.13	0.14	0.15	0.15	0.15
$-s_{13}/s_{11}$	0.38	0.32	0.38	0.39	0.42	0.26
Density	2.616	2.313	2.414	2.833	3.042	3.682
Porosity	6.1	17.0	13.3	5.8	7.0	6.1

Units: moduli - 10^6 lb/in.^{2}
density - g/cm^3
porosity - percent

Two indications of the degree of material anisotropy can be calculated from the c_{ij}: the ratio c_{11}/c_{33}, determined from the longitudinal wave velocities along the x_1 and x_3 axes, and c_{66}/c_{44}, determined from the two shear wave velocities. These two ratios are plotted against the percent metallic additive in Figure 11. Extrapolation of these ratios to 100 percent metallic additive indicates that the metallic additive phase is isotropic, as expected. The difference is evident between the data obtained from the commercial JTA-9 billet and the data obtained by interpolation for the experimental billets.
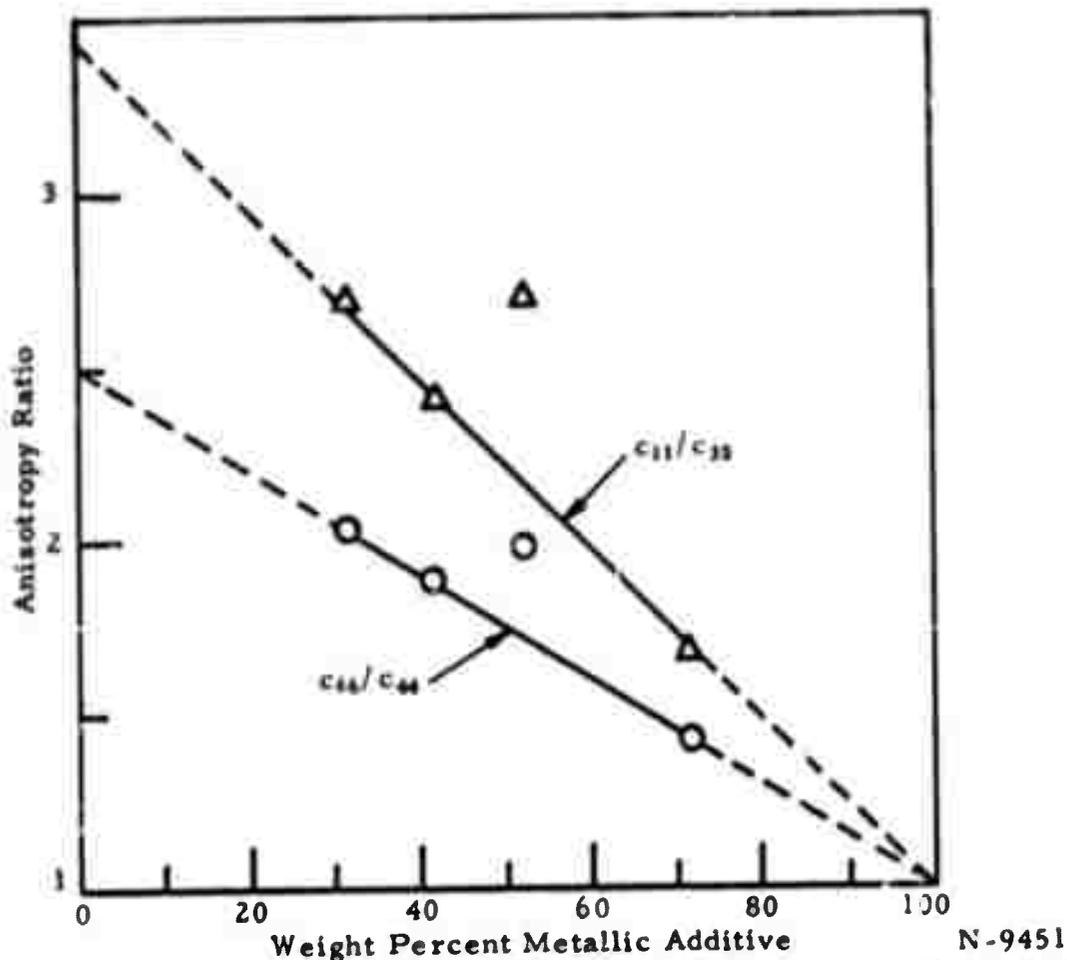
Figure 11. Anisotropy Ratio of Ultrasonic Elastic Constants Versus Composition for about Six Percent Porosity JT Composites.

3. Elastic Moduli

The elastic moduli in the limit of zero stress have been determined from ultrasonic and sonic resonant bar tests, and from the initial slope of static tension and compression stress-strain curves. The trend of the Young's moduli $1/s_{11}$ and $1/s_{33}$ and the shear modulus $1/s_{44}$ with density and porosity is shown in Figure 12 for the nominal 30 percent additive JT composites (JT30-4, JT30-5, and JT30-6). The good agreement between values obtained by ultrasonic, sonic resonant bar, and static tests has also been found for all other billets tested. The trend of moduli with composition is shown in Figure 13 for JT composites with five percent porosity (the data reduction to five percent porosity for JTA and 40 and 70 percent compositions involves some uncertainty until more porosity trends are established). The extrapolation of $1/s_{11}$ and $1/s_{33}$ to 100 percent additive shows, as did
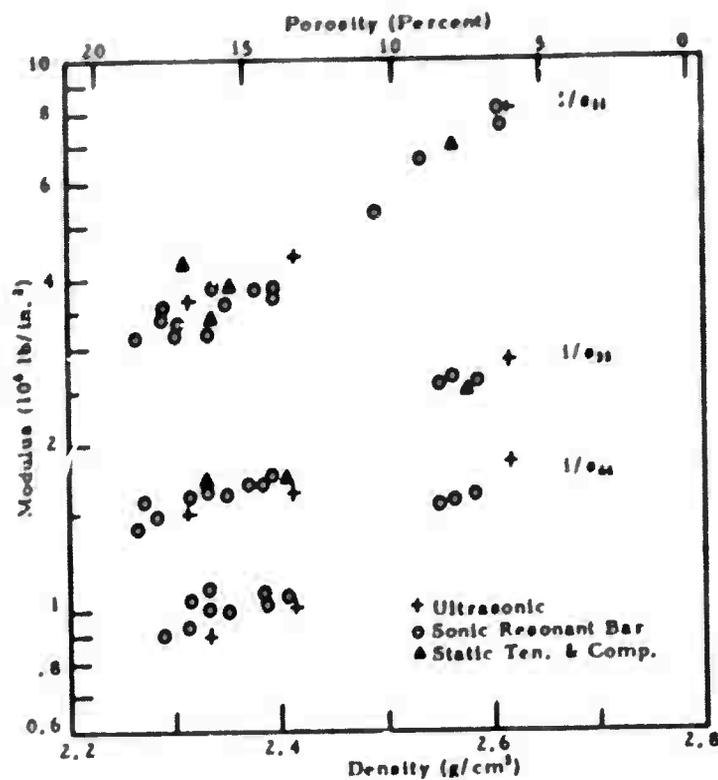
N-9452

Figure 12. Young's and Shear Moduli in the Zero-Stress Limit
Versus Density and Porosity for 31.5 Percent Additive
JT Composites.
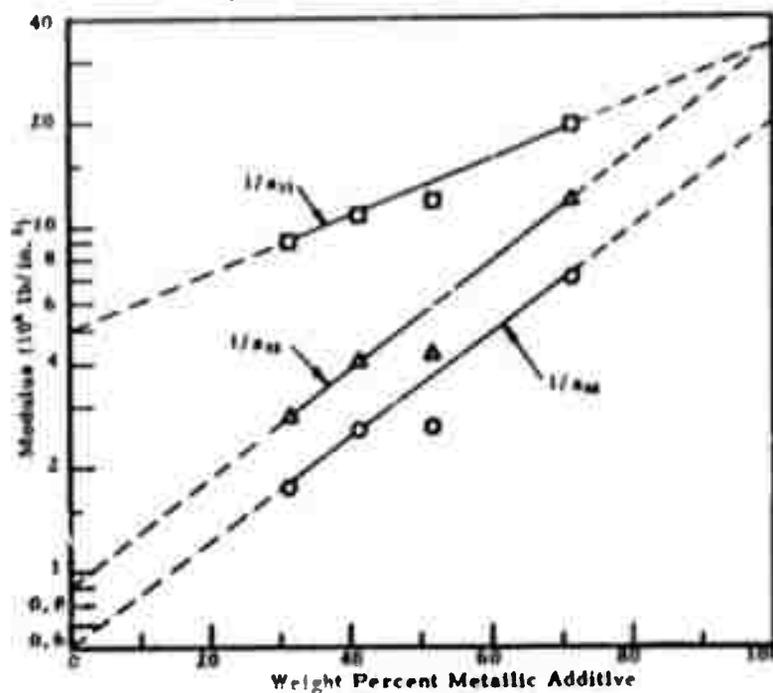
N-9453

Figure 13. Young's and Shear Moduli in the Zero-Stress Limit
Versus Composition for Five Percent Porosity JT
Composites.

the ultrasonic anisotropy ratios. that the metallic phase is isotropic. The data for commercial JTA is again not compatible with that of the nominal 30, 40, and 70 percent experimental billets.

Figure 14 shows the dependence of the three Poisson's ratios on composition. The data are averages from ultrasonic and static measurements. As in the case of the moduli, no significant differences were found between the Poisson's ratios measured by the two methods. At this time, no clear dependence of the Poisson's ratios on porosity has been detected.
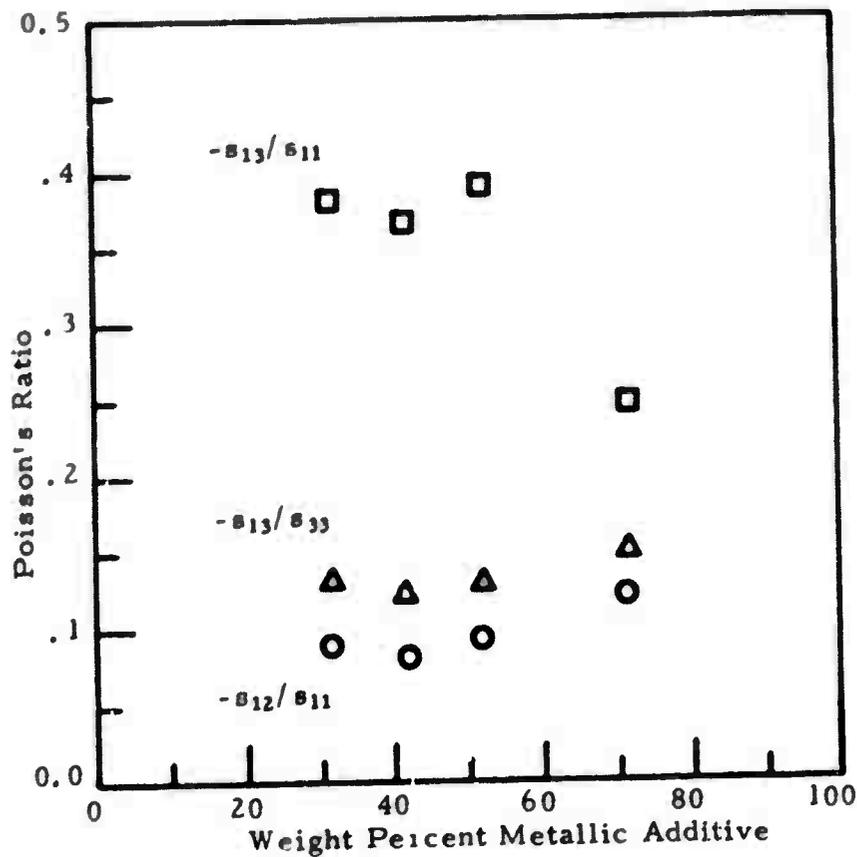
N-9454

Figure 14.   Poisson's Ratios in the Zero-Stress Limit Versus Composition for Five Percent Porosity JT Composites.

4.   Stress-Strain Relations

Typical stress-versus-longitudinal and transverse strain curves, showing the nonconservative and nonlinear elastic behavior, are given in Figure 15. Figures 16, 17, 18, and 19 show typical tensile and compressive stress-strain curves to fracture for all four compositions at approximately five percent porosity. Most of the tensile stress-versus-transverse strain curves exhibit a decreasing slope, i.e., greater strain than predicted by a
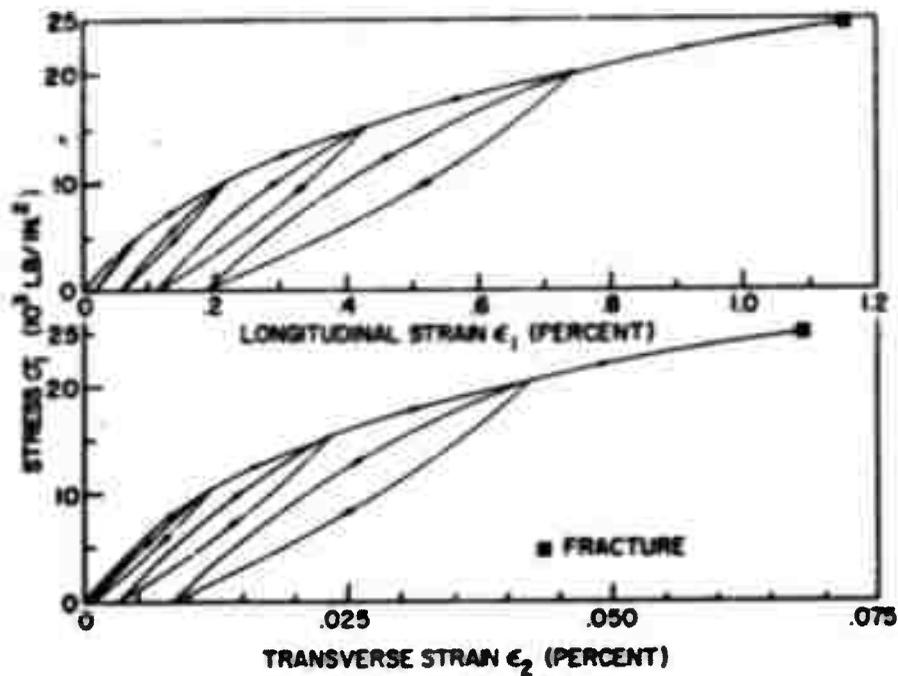
N-8627

Figure 15. Compression Stress-Strain Curves for Billet JT40-9. Specimens Oriented Perpendicular to Symmetry Axis of Billet.
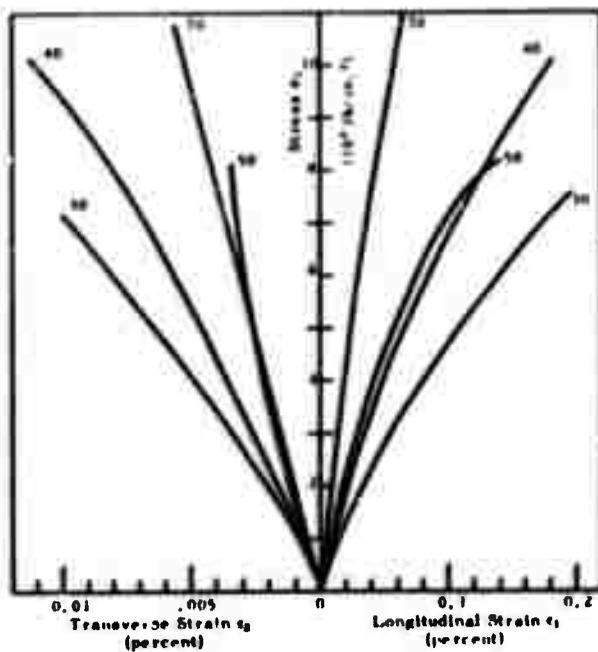
N-9466

Figure 16. Tensile Stress-Strain Curves (σ_1 vs. ϵ_1 and σ_1 vs. ϵ_2) for Nominal 30, 40, 50, and 70 Percent Additive JT Composites at about Five Percent Porosity.
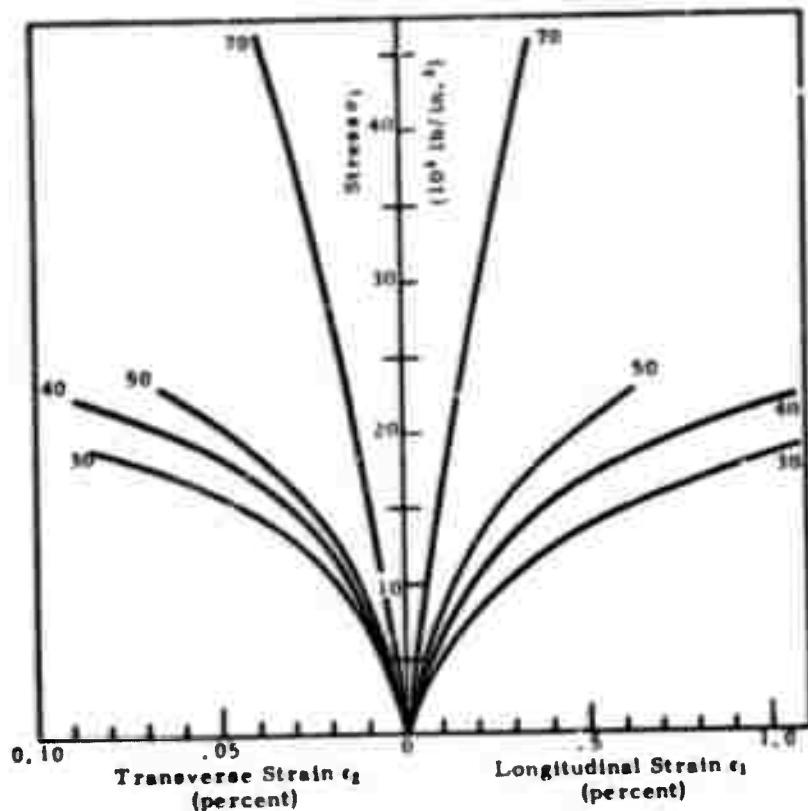
Figure 17. Compressive Stress-Strain Curves (σ_1 vs. ϵ_1 and σ_1 vs. ϵ_2) for Nominal 30, 40, 50, and 70 Percent Additive JT Composites at about Five Percent Porosity.

N-9472
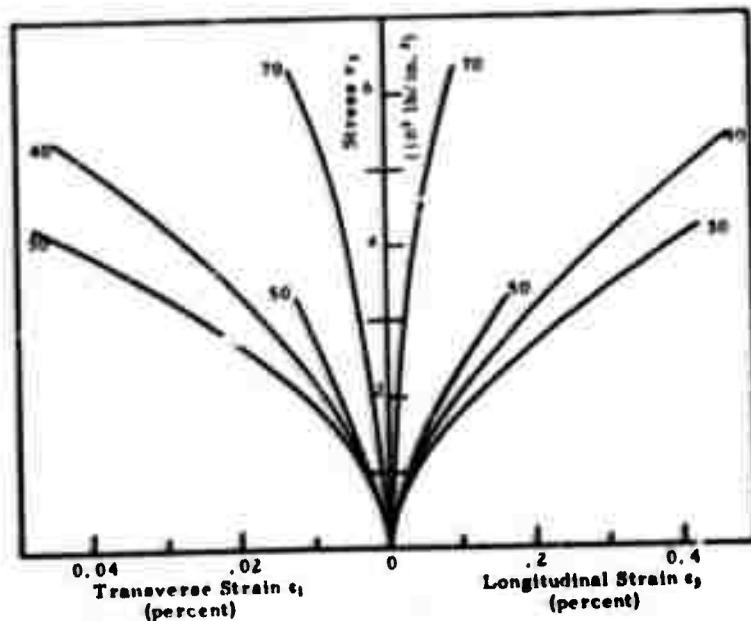
Figure 18. Tensile Stress-Strain Curves (σ_3 vs. ϵ_3 and σ_3 vs. ϵ_1) for Nominal 30, 40, 50, and 70 Percent Additive JT Composites at about Five Percent Porosity.

N-9456
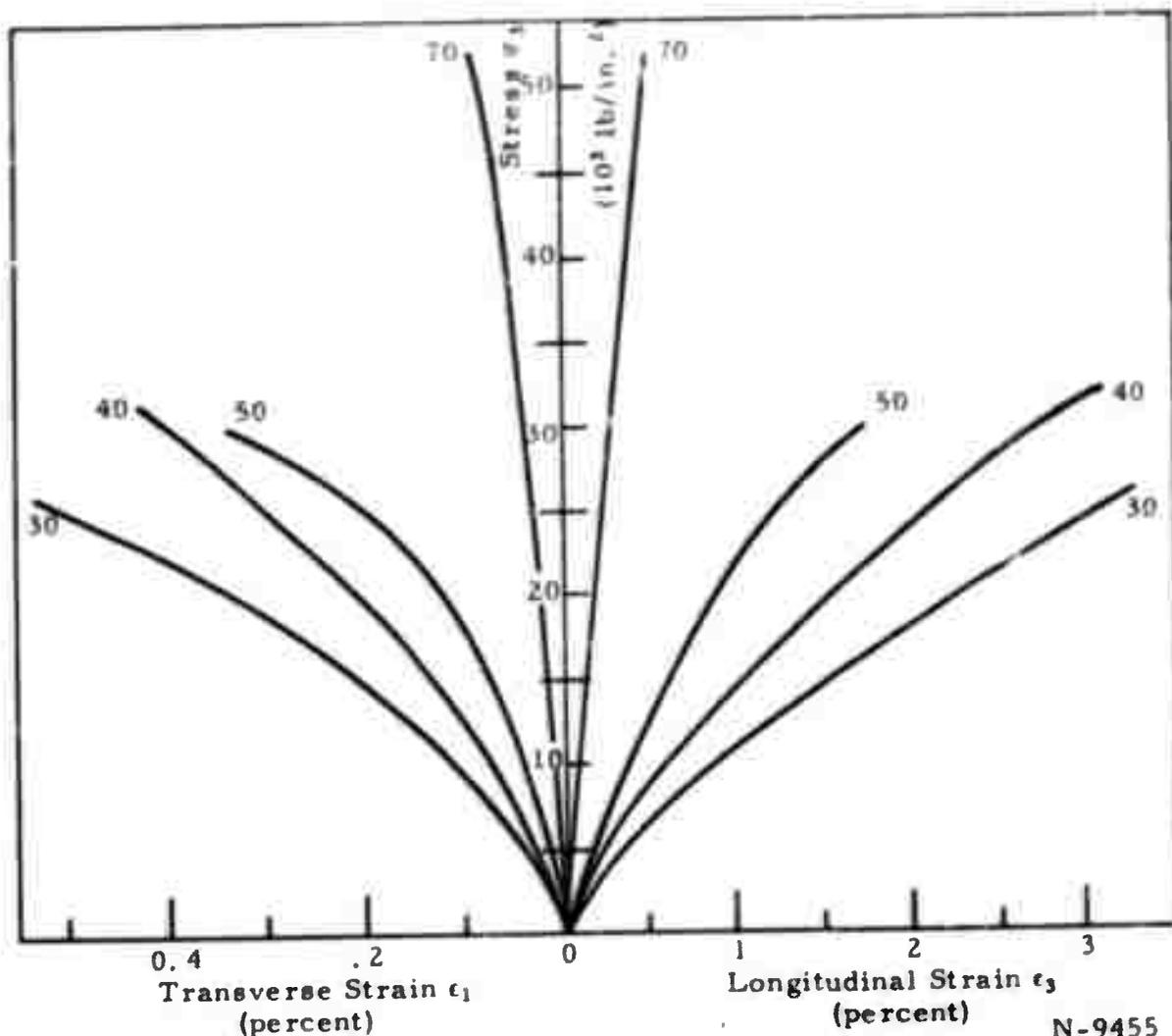
Figure 19. Compressive Stress-Strain Curves (σ_3 vs. ϵ_3 and σ_3 vs. ϵ_1) for Nominal 30, 40, 50, and 70 Percent Additive JT Composites at about Five Percent Porosity.

linear relation. This shape is of opposite curvature to that of the corresponding transverse strain curves for polycrystalline graphite. Surprisingly, the only tensile stress-versus-transverse strain curves which are similar to those of polycrystalline graphite are some of the curves for the 50 and 70 percent additive composites.

5. Fracture Strengths

The flexural strength was found to be consistently higher than the tensile strength (see Figure 20). The strengths of all samples have been adjusted to five percent porosity. Part of the difference between flexure and tension may be due to a statistical dependence of strength on test volume. (This

-47-
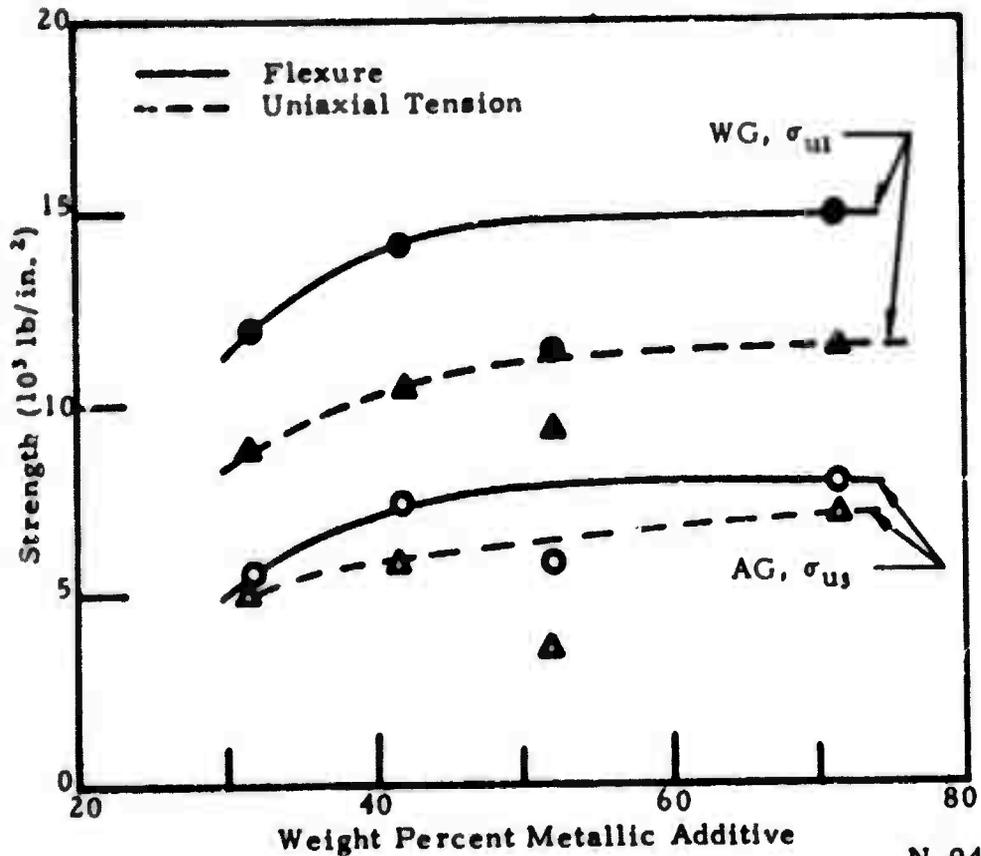
Figure 20. Flexural and Tensile Strengths Versus Composition for Five Percent Porosity JT Composites.

point is being investigated for JTA by IIT Research Institute.[7]) In addition, some of this difference may be due to bending moments in the tensile specimens. The magnitude of bending moments was investigated by measuring the strain with single gages on opposite sides of the tensile specimen. The measured tensile strengths were corrected for bending by assuming that the strain due to bending is one-half of the difference between the strains on opposite surfaces. The average correction for 13 specimens was a four percent increase in the measured tensile strength; the tensile strengths for other specimens were also increased by this amount. This procedure gives a lower limit to the correction; the true correction might be a few percent larger. The remaining difference between the flexural and tensile strengths is probably due to stress concentrations at the shoulders of the tensile dog bone. The effect of a larger fillet will be investigated.

The strengths for the commercial billet JTA-9 at 51.9 percent additive are lower than values reported for other commercial JTA material. Preliminary results on JTA reported by IITRI[7] appear to be slightly higher

-48-

than the value interpolated from the results for the 30, 40, and 70 percent additive levels.

The trend of tensile strength with grain σ_{u1} and against grain σ_{u3} with porosity is shown in Figure 21 for 30 percent additive. The linearity on a semilogarithmic plot indicates an exponential dependence of strength on porosity, a result similar to that found for the moduli.
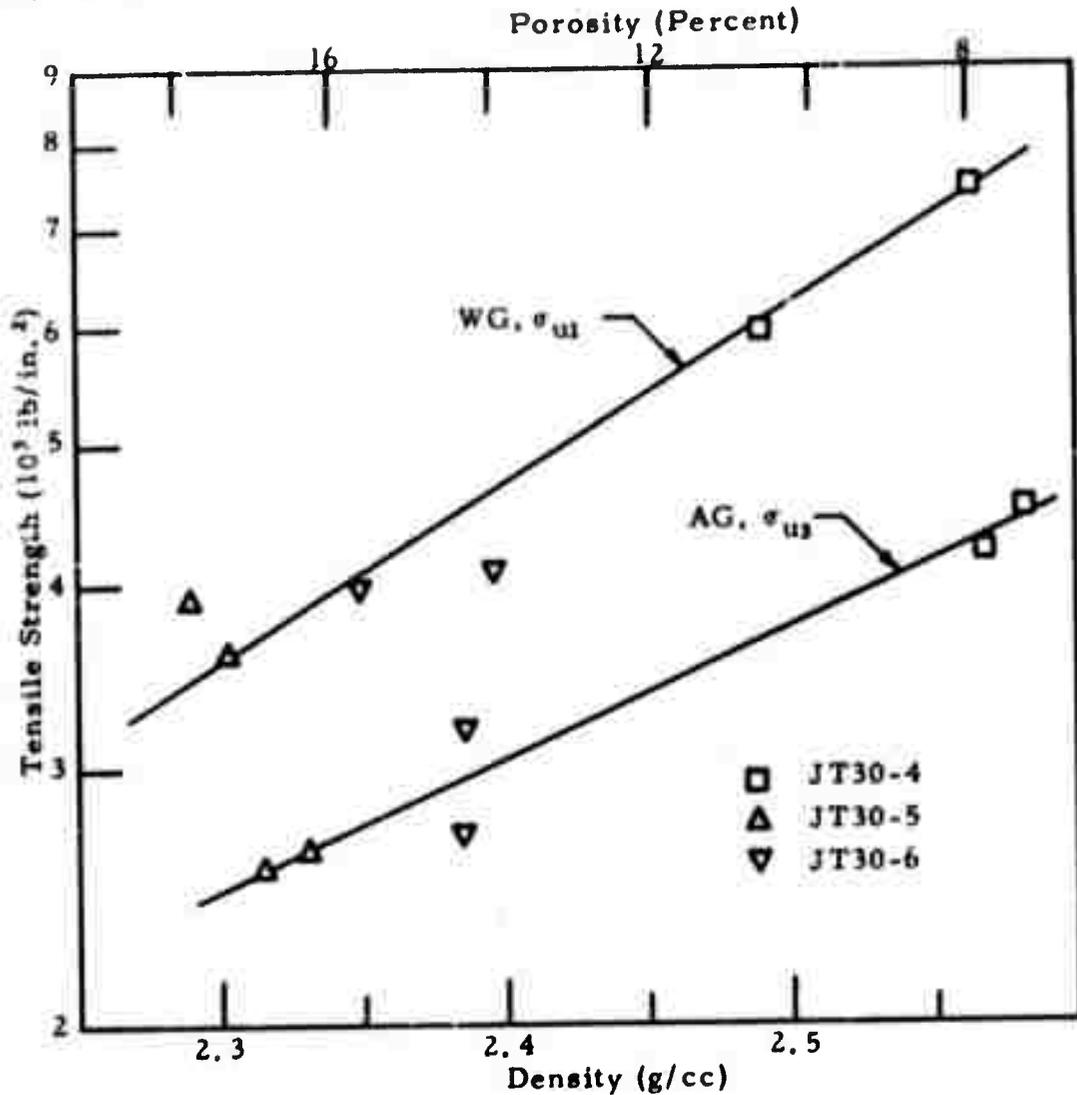
N-9458

Figure 21. Tensile Strength Versus Density and Porosity for 31.5 Percent Additive JT Composites.

-49-

Figure 22 shows the dependence of the compressive strengths on composition for five percent porosity JT composites. Investigation shows that $\sigma_{u3} > \sigma_{u1}$ in compression, whereas $\sigma_{u1} > \sigma_{u3}$ in tension; the same relationship exists in polycrystalline graphite.
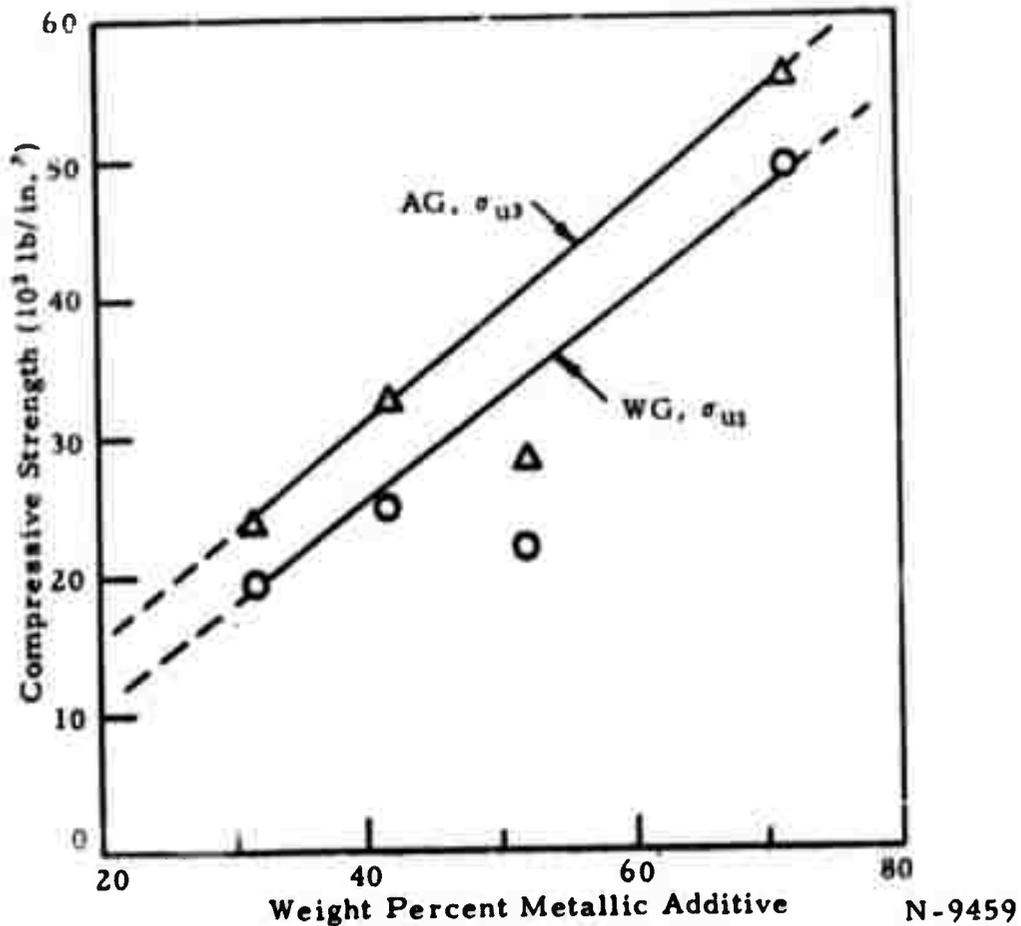
Figure 22. Compressive Strength Versus Composition for Five Percent Porosity JT Composites.

6. Thermal Diffusivities

The dependence of the thermal diffusivities K_1 and K_3 on temperature for four compositions at about five percent porosity is shown in Figures 23 and 24. The dependence of K_1 and K_3 on temperature for three porosities for 31.5 percent additive JT composites is given in Figures 25 and 26. The thermal diffusivity K_3 appears to show little variation with either composition or porosity. It is not known whether or not the observed dependences of K_1 on composition and porosity are real.
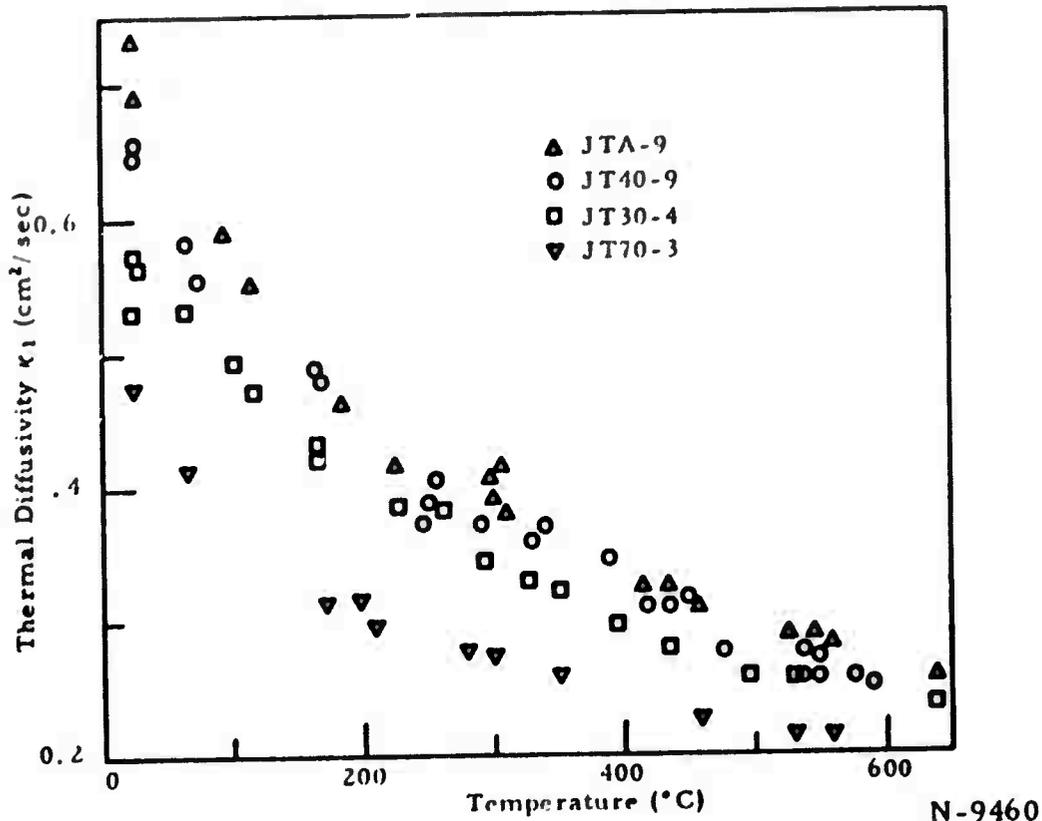
Figure 23. Thermal Diffusivity κ_1 Versus Temperature for Nominal 30, 40, 50, and 70 Percent Additive JT Composites at about Five Percent Porosity.
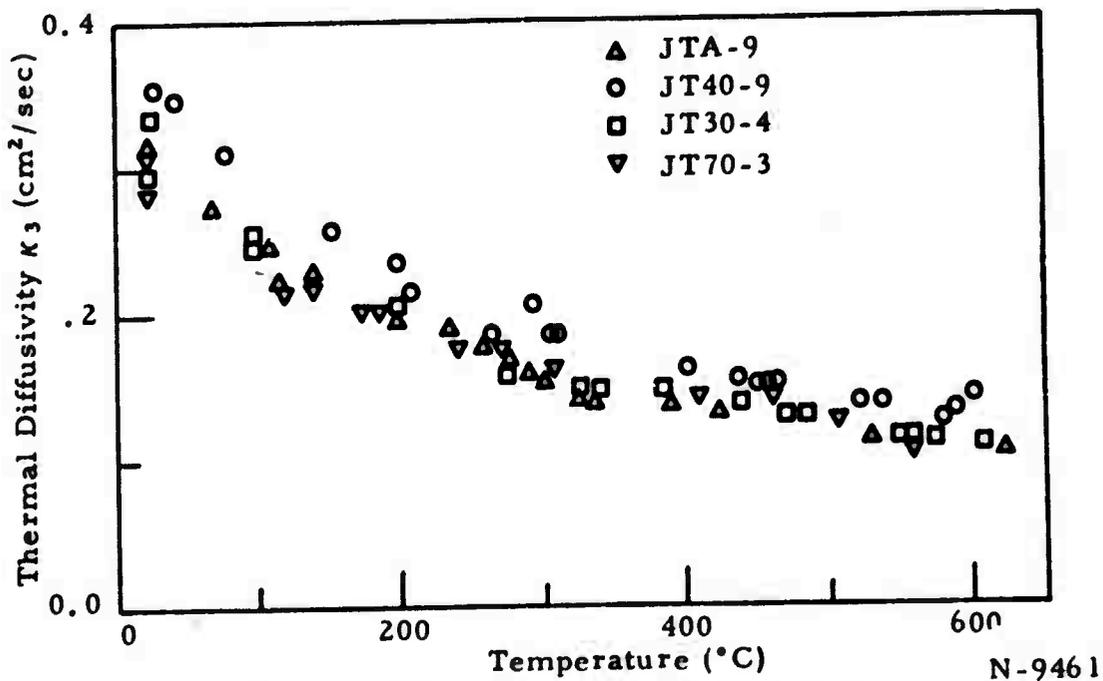
Figure 24. Thermal Diffusivity κ_3 Versus Temperature for Nominal 30, 40, 50, and 70 Percent Additive JT Composites of about Five Percent Porosity.
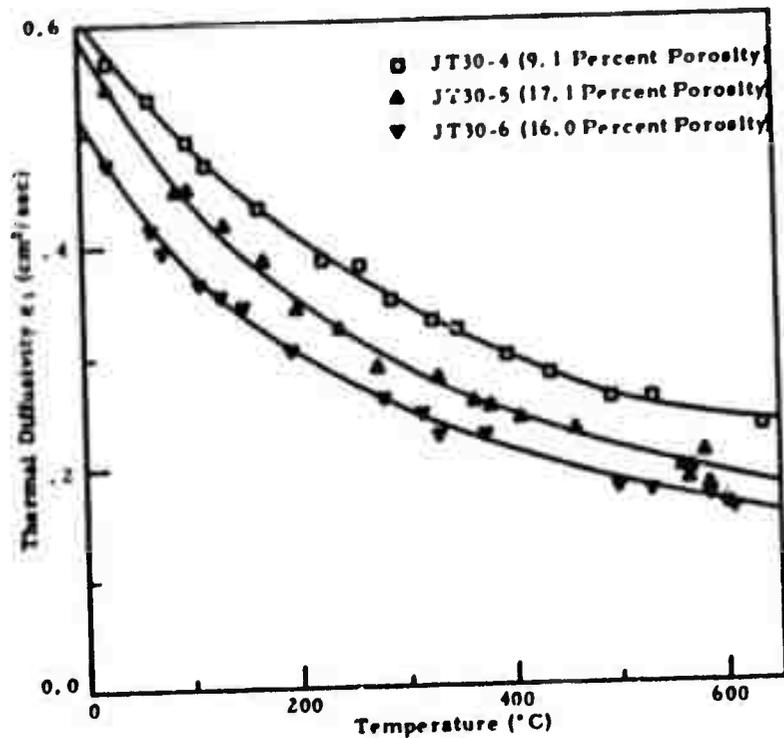
N-9462

Figure 25. Thermal Diffusivity κ_1 Versus Temperature at 9.1, 16.0, and 17.1 Percent Porosity for 31.5 Percent Additive JT Composites.
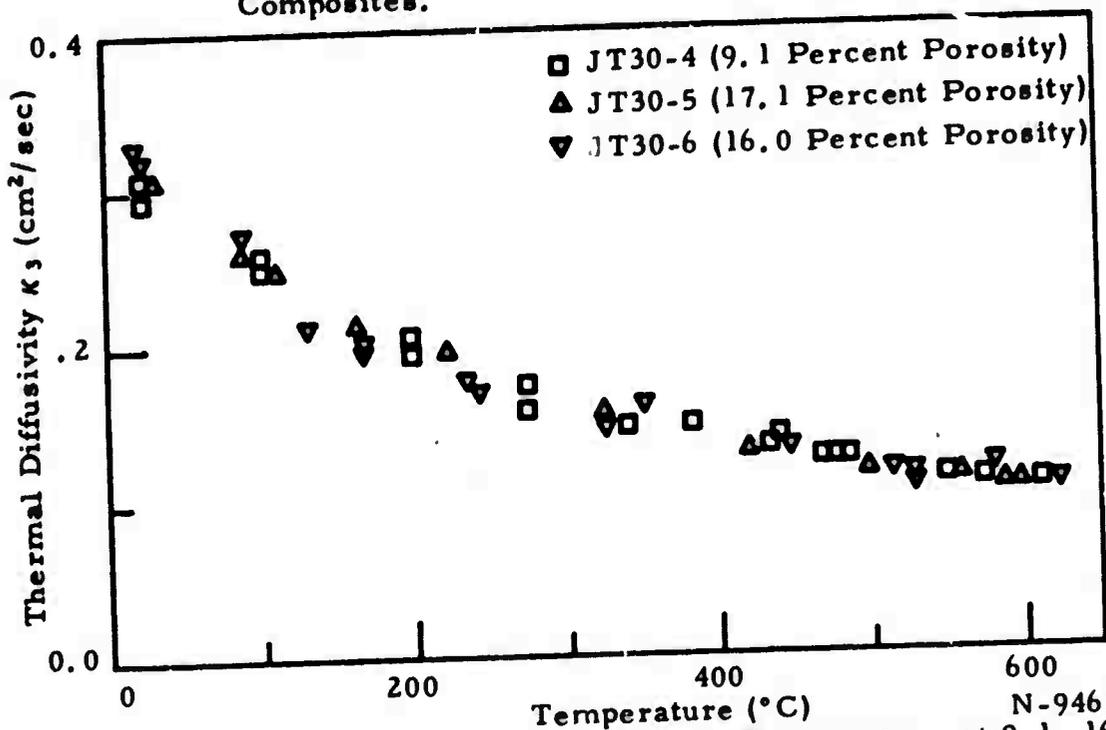
N-9463

Figure 26. Thermal Diffusivity κ_3 Versus Temperature at 9.1, 16.0, and 17.1 Percent Porosity for 31.5 Percent Additive JT Composites.

7. Specific Heat

Calculated values of the specific heat c_p as a function of temperature are shown in Figure 27 for four compositions of JT composites. The figure also shows experimental values measured on commercial JTA by the IIT Research Institute;[8] the agreement between calculated and experimental values is satisfactory.
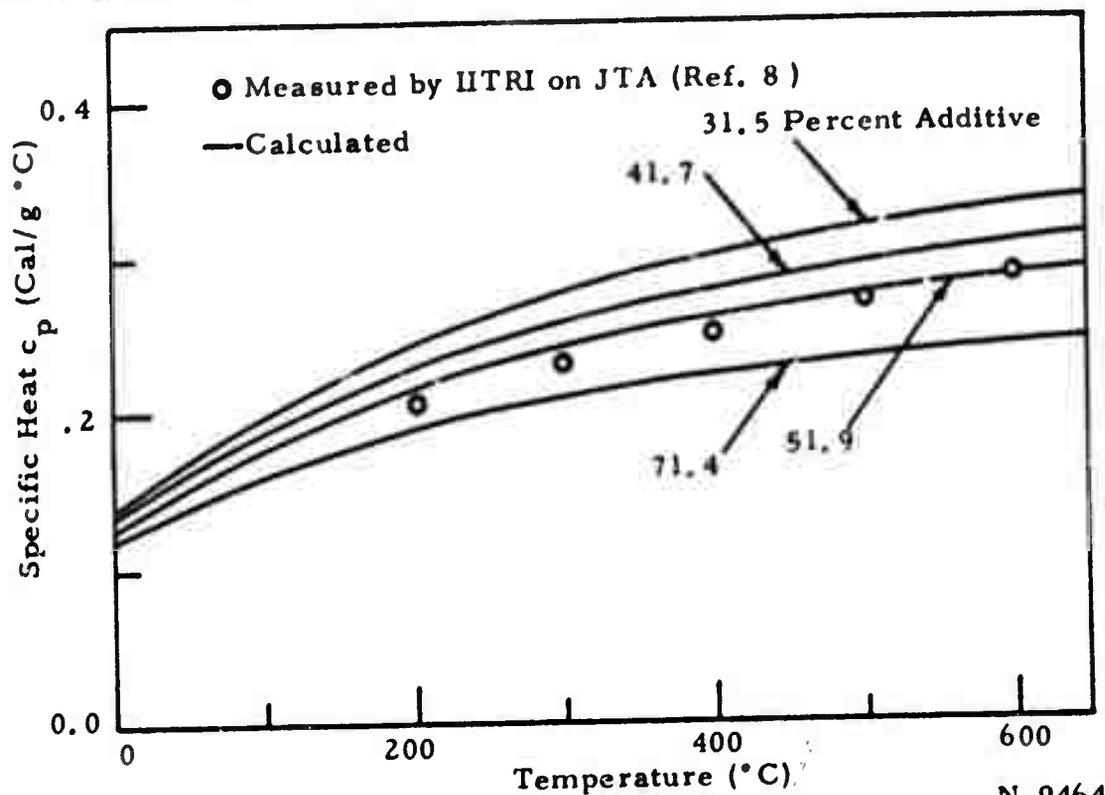
Figure 27. Specific Heat c_p Versus Temperature for Nominal 30, 40, 50, and 70 Percent Additive JT Composites.

The thermal conductivity k can be calculated from the relation

$$k_i = c_p \rho \kappa_i \qquad \text{(V B-1)}$$

where ρ is the bulk density.

8. Coefficients of Thermal Expansion

The temperature dependence of the coefficients of thermal expansion a_1 and a_3 is shown in Figure 28 for the 31.5 percent additive JT composite.

-53-
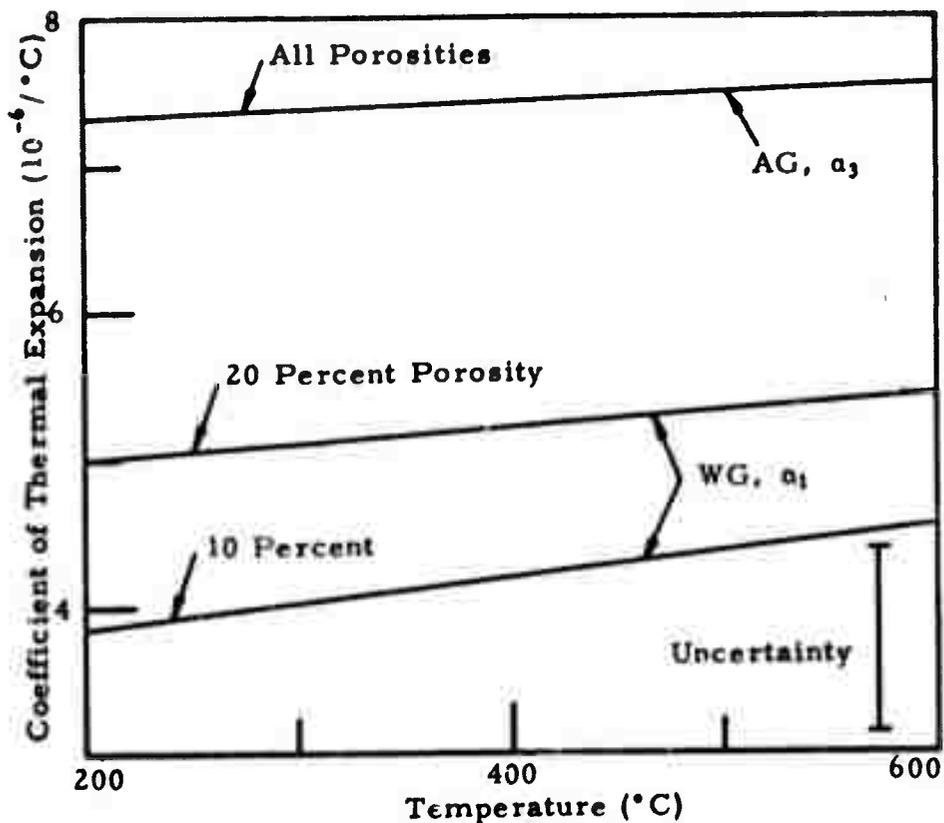
Figure 28. Coefficients of Thermal Expansion a_1 and a_3 Versus
Temperature at Various Porosities for 31.5 Percent
Additive JT Composites.

The experimental uncertainty is excessively large, and the experimental
procedure is being improved to reduce the scatter and extend the
temperature range. At present, there is no significant dependence of a_3
on porosity; the apparent dependence of a_1 on porosity may not be real.

C. Stress-Strain Relations and Multiaxial Stress Failure Theories for
    Anisotropic Materials - A Survey
        (Professor Saada, Case Institute)

Most, if not all, of the stress-strain relations suggested for anisotropic materials have been patterned on the well known relations developed for isotropic materials. In the elastic range, the strains are linearly related to the stresses, and in the plastic range the strain rates are linear functions of the stresses. Yield or fracture conditions are extensions of conditions established for isotropic materials, in particular the energy of distortion criterion.

In the following a brief survey of what is available in the field of stress-strain relations and yield or fracture conditions for anisotropic material is given. A slightly more detailed presentation is given to the Generalized Tresca failure condition which is relatively new and quite promising.

1. Stress Strain Relations

    a. Elastic Stress-Strain Relations.   Let us consider an elastic medium maintained at a fixed temperature and assume that there exists a one to one analytic relation between the stress tensor and the strain tensor:

$$\sigma_{ij} = F_{ij} (\epsilon_{ij}) \qquad\qquad\qquad \text{(V C-1)}$$

where $$\epsilon_{ij} = \frac{1}{2}(\frac{\partial u_i}{\partial x_j} + \frac{\partial u_j}{\partial x_i})$$

If the function F_{ij} are expanded in power series in ϵ_{ij} and only the linear terms retained, we get

$$\sigma_{ij} = C_{ijk\ell} \epsilon_{k\ell} \qquad (i,j,k,\ell = 1,2,3) \qquad \text{(V C-2)}$$

In Equation V C-2 the assumption is also made that in the initial unstrained state the body is unstressed. If the $C_{ijk\ell}$ are independent of the position of the points, the medium is called elastically homogeneous. Equation V C-2 is the generalization of Hooke's Law. The $C_{ijk\ell}$ are symmetric with respect to the two first and the last indices, so that the maximum number of elastic constants is 36. This number is however reduced to 21 because of the existence of a strain energy density function

$$W = \frac{1}{2} C_{ijk\ell} \epsilon_{ij} \epsilon_{k\ell} \qquad\qquad\qquad \text{(V C-3)}$$

with the property,

$$\frac{\partial W}{\partial \epsilon_{ij}} = \sigma_{ij} \qquad \text{(V C-4)}$$

If the medium is elastically symmetric with respect to certain directions, the number of elastic constants is further reduced. The degree of symmetry is expressed by the statements that C_{ijkl} are invariant in a change of coordinates. The expression of C_{ijkl} when passing from a system of x_i coordinates to x_i' coordinates is obtained as follows:

$$\sigma_{ij}' = C_{ijkl}' \epsilon_{kl}' \qquad \text{(V C-5)}$$

since

$$\sigma_{ij}' = \ell_{im} \ell_{jn} \sigma_{mn} \qquad \text{(V C-6)}$$

then

$$\sigma_{ij}' = \ell_{im} \ell_{jn} C_{mncd} \epsilon_{cd} \qquad \text{(V C-7)}$$

and

$$C_{ijkl}' \epsilon_{kl}' = \ell_{im} \ell_{jn} C_{mncd} \epsilon_{cd} \qquad \text{(V C-8)}$$

we have

$$\epsilon_{kl}' = \ell_{kr} \ell_{ls} \epsilon_{rs} \qquad \text{(V C-9)}$$

then

$$\epsilon_{kl} = \ell_{rk} \ell_{sl} \epsilon_{rs}' \qquad \text{(V C-10)}$$

and

$$C_{ijkl}' \epsilon_{kl}' = \ell_{im} \ell_{jn} C_{mncd} \ell_{rc} \ell_{sd} \epsilon_{rs}' \qquad \text{(V C-11)}$$

then

$$C_{ijkl}' = \ell_{im} \ell_{jn} \ell_{kc} \ell_{ld} C_{mncd} \qquad \text{(V C-12)}$$

The coefficients of elasticity are therefore components of a tensor of the 4th order.

For an orthotropic material the C_{ijkl} do not change in a transformation of coordinates

$$x_i = - x_i' \qquad \text{(V C-13)}$$

Only nine independent elastic constants remain. They are given by

$$\begin{vmatrix} C_{1111} & C_{1122} & C_{1133} & 0 & 0 & 0 \\ C_{1122} & C_{2222} & C_{2233} & 0 & 0 & 0 \\ C_{1133} & C_{2233} & C_{3333} & 0 & 0 & 0 \\ & & & C_{2323} & 0 & 0 \\ & & & & C_{1313} & 0 \\ & & & & & C_{1212} \end{vmatrix} \qquad \text{(V C-14)}$$

For a transverse isotropic material, the $C_{ijk\ell}$ do not change in the transformation

$$X_1' = x_1 \cos\theta + X_2 \sin\theta \qquad \text{(V C-15)}$$

$$X_2' = -x_1 \sin\theta + X_2 \cos\theta \qquad \text{(V C-16)}$$

$$X_3' = X_3 \qquad \text{(V C-17)}$$

Only five independent elastic constants remain. They are given by

$$\begin{vmatrix} C_{1111} & C_{1122} & C_{1133} & 0 & 0 & 0 \\ C_{1122} & C_{1111} & C_{1133} & 0 & 0 & 0 \\ C_{1133} & C_{1133} & C_{3333} & 0 & 0 & 0 \\ & & & C_{1313} & 0 & 0 \\ & & & & C_{1313} & 0 \\ & & & & & \frac{1}{2}(C_{1111} - C_{1122}) \end{vmatrix} \qquad \text{(V C-18)}$$

References 9 and 10 give detailed computations regarding the transformation of axes and the equations leading to the reduction in number of the elastic constants.

b. <u>Plastic Stress-Strain Relations</u>. The approach here is similar to the one used for isotropic materials, namely, that the strain rates are proportional to the stresses and that they are linear functions of the stresses. Using the same notation, the stress-strain relations are written[11]:

$$\dot{\epsilon}_{ij} = \dot{A}_{ijkl} \, \sigma_{kl} \tag{V C-19}$$

where

$$\dot{\epsilon}_{ij} = \frac{\partial \epsilon_{ij}}{\partial t} \tag{V C-20}$$

and $\dot{A}_{ijkl}$ has the dimension of a strain rate divided by a stress and is called the coefficient of plasticity. The quantities $\dot{A}_{ijkl}$ are a function of the previous history of plastic flow, and consequently the symmetry of the matrix of coefficients found in the elastic case is not present here. In other words:

$$\dot{A}_{ijkl} \neq \dot{A}_{klij} \tag{V C-21}$$

Here too the number of coefficients $\dot{A}_{ijkl}$ is reduced depending on the degree of symmetry in the material. This degree of symmetry is expressed by the statement that the $\dot{A}_{ijkl}$ are invariant in a transformation of coordinates. For planar plastic flow, Dorn[11] gives the various forms Equation (V C-19) takes for different types of symmetries.

The coefficients of plasticity $\dot{A}_{ijkl}$ are not constant but change with large strains. Dorn[11] makes the assumption that the ratios of the coefficients of plasticity remain constant and writes in Equation (V C-19)

$$A_{ijkl} = \alpha_{ijkl} \, \frac{\dot{\phi}}{\sigma} \tag{V C-21}$$

where α_{ijkl} is a coefficient of anisotropy and $\dot{\phi}$ is a generalized strain rate and σ a generalized stress. The definition of σ and $\dot{\phi}$ is completed by assuming:

$$\sigma = \frac{dW}{d\phi} \tag{V C-22}$$

-58-

where

$$dW = \sigma d\phi = \sigma_{ij} d\epsilon_{ij}$$ (V C-23)

$$\sigma d\phi = a_{ijk\ell} \sigma_{ij} \sigma_{k\ell} \frac{d\phi}{\sigma}$$

$$\sigma = [a_{ijk\ell} \sigma_{ij} \sigma_{k\ell}]^{1/2}$$ (V C-24)

The expression of $d\phi$ is obtained in a similar fashion

Starting from the expression of a plastic potential written

$$2f = F(\sigma_{22} - \sigma_{33})^2 + G(\sigma_{33} - \sigma_{11})^2 + H(\sigma_{11} - \sigma_{22})^2 + 2L \sigma_{23}^2$$

$$+ 2M \sigma_{13}^2 + 2N \sigma_{12}^2 = 1$$ (V C-25)

Where F, G, H, L, M, N are constants characterizing the current state of anisotropy, Hill[12,13] obtains the stress-strain increment relations for an orthotropic material from:

$$d\epsilon_{ij} = \frac{\partial f}{\partial \sigma_{ij}} d\lambda$$ (V C-26)

$$d\epsilon_{11} = [(H + G) \sigma_{11} - H \sigma_{22} - G \sigma_{33}] d\lambda$$ (V C-27)

$$d\epsilon_{22} = [- H \sigma_{11} + (F + H) \sigma_{22} - F \sigma_{33}] d\lambda$$ (V C-28)

$$d\epsilon_{33} = [- G \sigma_{11} - F \sigma_{22} + (F + G) \sigma_{33}] d\lambda$$ (V C-29)

$$d\epsilon_{23} = L \sigma_{23} d\lambda$$ (V C-30)

$$d\epsilon_{13} = M \epsilon_{13} d\lambda$$ (V C-31)

$$d\epsilon_{12} = N \sigma_{12} d\lambda$$ (V C-32)

The assumptions in the previous equations are that the yield stress in tension and compression are the same, the stress and strain increments are along the axes of orthotropy, and there occurs no volume change during the application of stresses. The zero volume change is directly connected with the assumption that the yielding is independent of hydrostatic pressure.

2. Yield and Failure Conditions

Conditions in use for isotropic materials have been extended to aniso-
tropic ones. Hill[12,13] extended the Huber-Mises criterion for isotropic
material to orthotropic ones in which the principal axes of stress and
orthotropy are coincident. The condition is written

$$F(\sigma_{22}- \sigma_{33})^2 + G(\sigma_{33}- \sigma_{11})^2 + H(\sigma_{11}- \sigma_{22})^2 + 2L \sigma_{23}^2 + 2M \sigma_{13}^2 + 2N \sigma_{12}^2 = 1$$

$$(V \ C-33)$$

F, G, H, L, M, N are coefficients of anisotropy to be determined by experi-
ments. If X, Y, Z are the tensile yield stress in the principal anisotropic
directions, it is seen that

$$2F = \frac{1}{Y^2} + \frac{1}{Z^2} - \frac{1}{X^2} \qquad (V \ C-34)$$

$$2G = \frac{1}{Z^2} + \frac{1}{X^2} - \frac{1}{Y^2} \qquad (V \ G-35)$$

$$2H = \frac{1}{X^2} + \frac{1}{Y^2} - \frac{1}{Z^2} \qquad (V \ C-36)$$

Also if R, S, T are the yield stresses in shear with respect to the principal
axes of anisotropy then:

$$2L = \frac{1}{R^2} , \qquad 2M = \frac{1}{S^2} , \qquad 2N = \frac{1}{T^2} \qquad (V \ C-37)$$

For transverse isotropy the number of coefficients is reduced to three since

$$N = F + 2H = G + 2H , \qquad L = M$$

It is clear that Equation V C-33 predicts the same yield in simple tension
and in simple compression.

For the case of plane strain $d\epsilon_{33}$ is set equal to zero in equation V C-29
and the resulting value of σ_{33} is inserted in Equation V C-33 to give

$$\frac{(\sigma_{11} - \sigma_{22})^2}{4(1 - C)} + \sigma_{12}^2 = T^2 \qquad (V \ C-38)$$

where

$$C = 1 - \frac{N (F + G)}{2 (FG + GH + HF)}$$
(V C-39)

Equation V C-38 can be written in the standard notations of strength of materials as:

$$\frac{(\sigma_x - \sigma_y)^2}{4 (1 - C)} + \tau_{xy}^2 = T^2$$
(V C-40)

and, if we set $\sigma_x - \sigma_y = S_x$ and $\tau_{xy} = \tau_x$, then Equation V C-40 can be written:

$$W (S_x, \tau_x) = 0$$
(V C-41)

Thus the condition expressed by Equation V C-41 can be represented by a curve in a plane S_x, τ_x. More details on this representation will be given in the following paragraphs.

Griffith and Baldwin[14] extended the distortion-energy theory of failure to include generally orthotropic materials. The material has to remain perfectly elastic up to yield or failure. The generalized Hooke's Law is written as in Equation V C-13

$$\left.\begin{array}{c} \sigma_{ij} = C'_{ijk\ell} \, \epsilon_{k\ell} \\[2ex] \text{or} \\[2ex] \epsilon_{ij} = S_{ijk\ell} \, \epsilon_{k\ell} \end{array}\right\}$$
(V C-42)

$$U_D = \sigma_{11}^2 (\frac{S_{1111}}{3} - \frac{S_{1122}}{6} - \frac{S_{1133}}{6}) + \sigma_{22}^2 (\frac{S_{2222}}{3} - \frac{S_{1122}}{6} - \frac{S_{2233}}{6})$$

$$+ \sigma_{33}^2 (\frac{S_{3333}}{3} - \frac{S_{1133}}{6} - \frac{S_{2233}}{6})$$

$$+ \sigma_{11}\sigma_{22} (\frac{2S_{1122}}{3} - \frac{S_{1111}}{6} - \frac{S_{2222}}{6} - \frac{S_{1133}}{6} - \frac{S_{2233}}{6})$$
(V C-43)

$$+ \sigma_{22}\sigma_{33} \left(\frac{2S_{2233}}{3} - \frac{S_{1122}}{6} - \frac{S_{2222}}{6} - \frac{S_{1133}}{6} - \frac{S_{3333}}{6} \right)$$

$$+ \sigma_{11}\sigma_{33} \left(\frac{2S_{1133}}{3} - \frac{S_{1111}}{6} - \frac{S_{1122}}{6} - \frac{S_{2233}}{6} - \frac{S_{3333}}{6} \right)$$

$$+ 4 \sigma_{23}^2 S_{2323} + 4 \sigma_{13}^2 S_{1313} + 4 \sigma_{12}^2 S_{1212}$$

For transverse isotropic materials

$$S_{1212} = \frac{1}{2} (S_{1111} - S_{1122}), \quad S_{1111} = S_{2222}, \quad S_{1133} = S_{2233}, \quad S_{1313} = S_{2323}$$

$$(V \ C\text{-}44)$$

Radenkovic and Boschat[15] extended the Tresca condition of failure in plane strain to the case of a material in which the shear strength of any plane is a function of the position of this plane. As shown on Figure 29 failure will not occur along a plane whose normal makes α with the x axis when

$$K_2 (\alpha) < \tau_n < K_1 (\alpha) \qquad (V \ C\text{-}45)$$

Since the resistance to shear is the same for two opposite planes, then:

$$K_1 (\alpha) = K_1 (\alpha + \pi) \qquad (V \ C\text{-}46)$$

$$K_2 (\alpha) = K_2 (\alpha + \pi) \qquad (V \ C\text{-}47)$$

So that in the x,y plane the curve representing $K_1 (\alpha)$ and $K_2 (\alpha)$ is symmetric with respect to the origin (Figure 30).

If we assume that $K_1 (\alpha) = - K_2 (\alpha)$ then the two curves coincide and the condition for incipience of yield or fracture becomes:

$$[|\tau_n| - K (\alpha)] = 0 \qquad (V \ C\text{-}48)$$

If the material is orthotropic (Figure 31) then

$$K (-\alpha) = K (+\alpha) \qquad (V \ C\text{-}49)$$

$$K (\pi-\alpha) = K (\alpha) \qquad (V \ C\text{-}50)$$
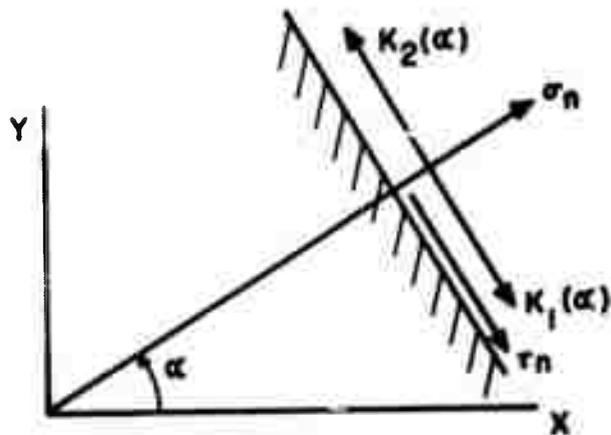
Figure 29. Failure Plane in the Extended Tresca Criterion.
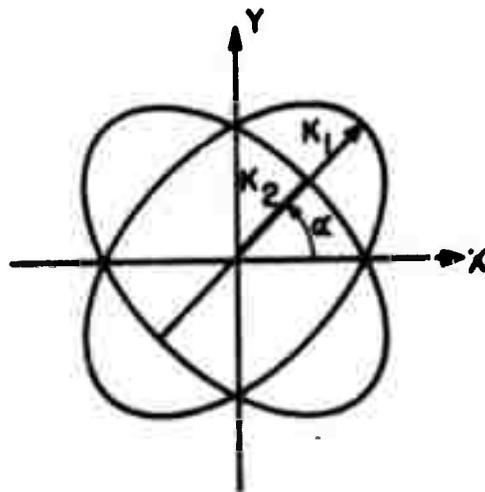
Figure 30. Limiting Values of the Shear Stress on a Plane α.
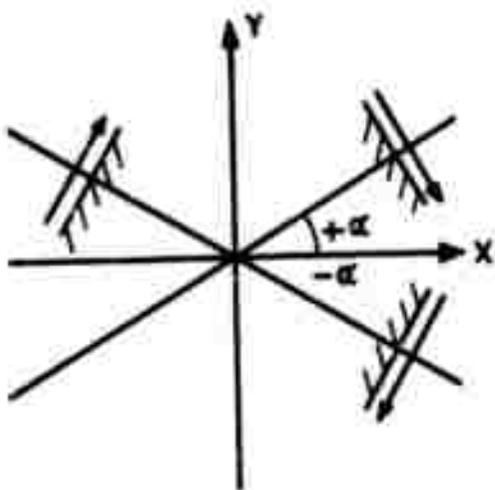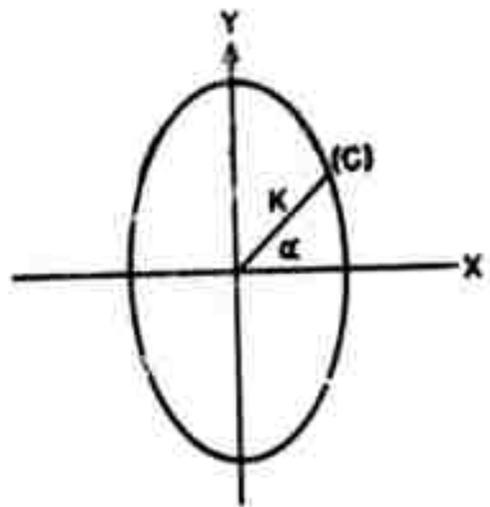
Figure 31.

Figure 32.

Extended Failure Criterion for an Orthotropic Material.
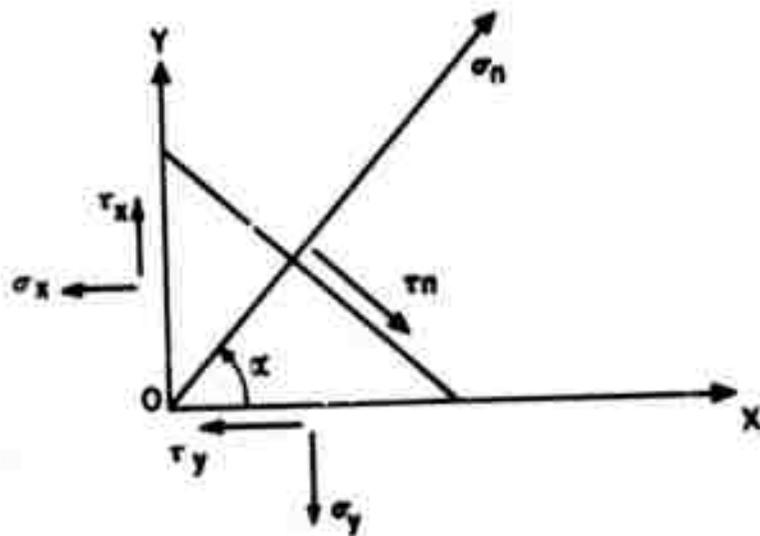
Figure 33. Stresses on an α Plane through a Point O.

then the curve of $K(\alpha)$ is symmetric with respect to OX and OY (Figure 32). If $K(\alpha + \frac{\pi}{2}) = K(\alpha)$ then one quadrant is enough to define the curve.

a. <u>Space Representation</u>. The generalized Tresca condition can be represented in a space $\sigma_x/\sqrt{2}$, $\sigma_y/\sqrt{2}$, τ_x and this representation is a cylinder parallel to the bisector OP of $\sigma_x/\sqrt{2}$ and $\sigma_y/\sqrt{2}$. This can be shown as follows:

If we set (Figure 33)
$$\tau_{xy} = \tau_y \qquad \text{(V C-51)}$$

and
$$\tau_{xy} = -\tau_x \qquad \text{(V C-52)}$$

we have
$$\sigma_n = \frac{\sigma_x + \sigma_y}{2} + \frac{\sigma_x - \sigma_y}{2} \cos 2\alpha + \tau_{xy} \sin 2\alpha \qquad \text{(V C-53)}$$

$$\tau_n = \frac{\sigma_x - \sigma_y}{2} \sin 2\alpha - \tau_{xy} \cos 2\alpha \qquad \text{(V C-54)}$$

In terms of principal stresses (Figure 34)
$$\sigma_x = \frac{\sigma_1 + \sigma_2}{2} + \frac{\sigma_1 - \sigma_2}{2} \cos 2\theta \qquad \text{(V C-55)}$$

$$\sigma_y = \frac{\sigma_1 + \sigma_2}{2} - \frac{\sigma_1 - \sigma_2}{2} \cos 2\theta \qquad \text{(V C-56)}$$

$$\tau_{xy} = \frac{\sigma_1 - \sigma_2}{2} \sin 2\theta = -\tau_x \qquad \text{(V C-57)}$$

If in Figure 35, M represents the state of stress at the considered point in the material, and OO' is the projection of OM on the bisector of $\sigma_x/\sqrt{2}$ and $\sigma_y/\sqrt{2}$ then (Figures 35 and 36)

$$\overline{OO'} = \frac{\sigma_x + \sigma_y}{2} = \frac{\sigma_1 + \sigma_2}{2} = P \qquad \text{(V C-58)}$$

$$\overline{O'H} = \frac{\sigma_x - \sigma_y}{2} = S_x = -S_y \qquad \text{(V C-59)}$$

$$\overline{O'M} = \frac{\sigma_1 - \sigma_2}{2} \qquad \text{(V C-60)}$$

-65-
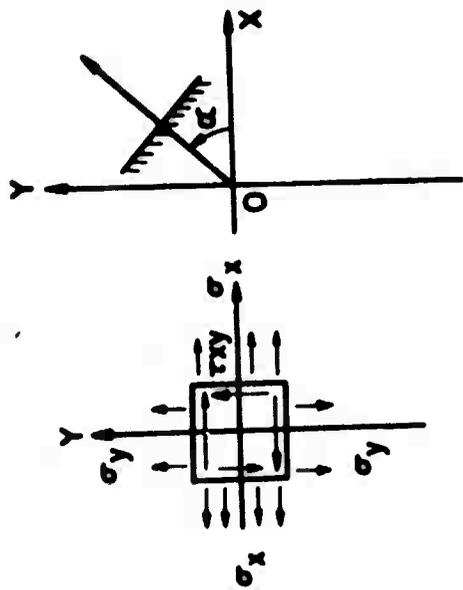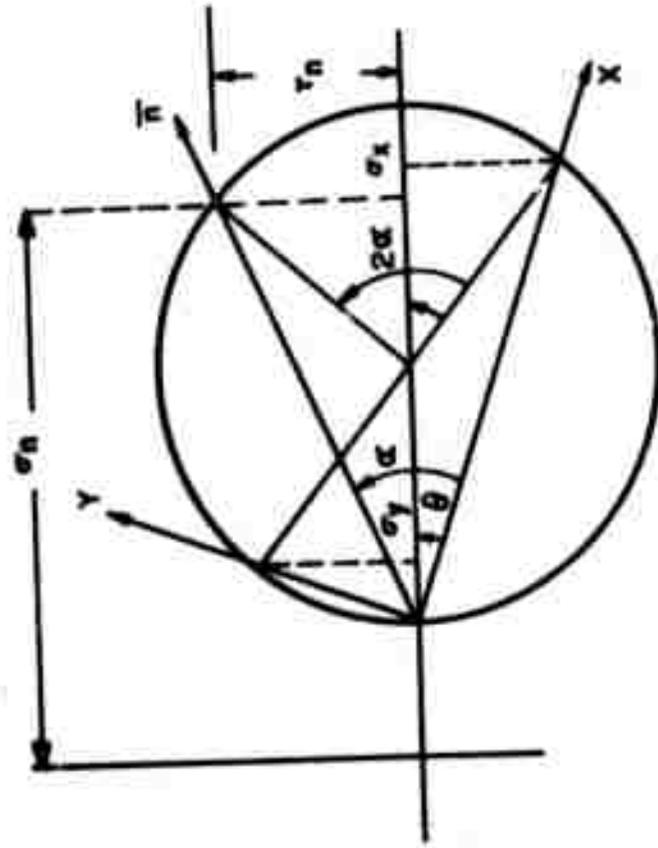
Figure 34. Mohr's Representation of the State of Stress at Point O.
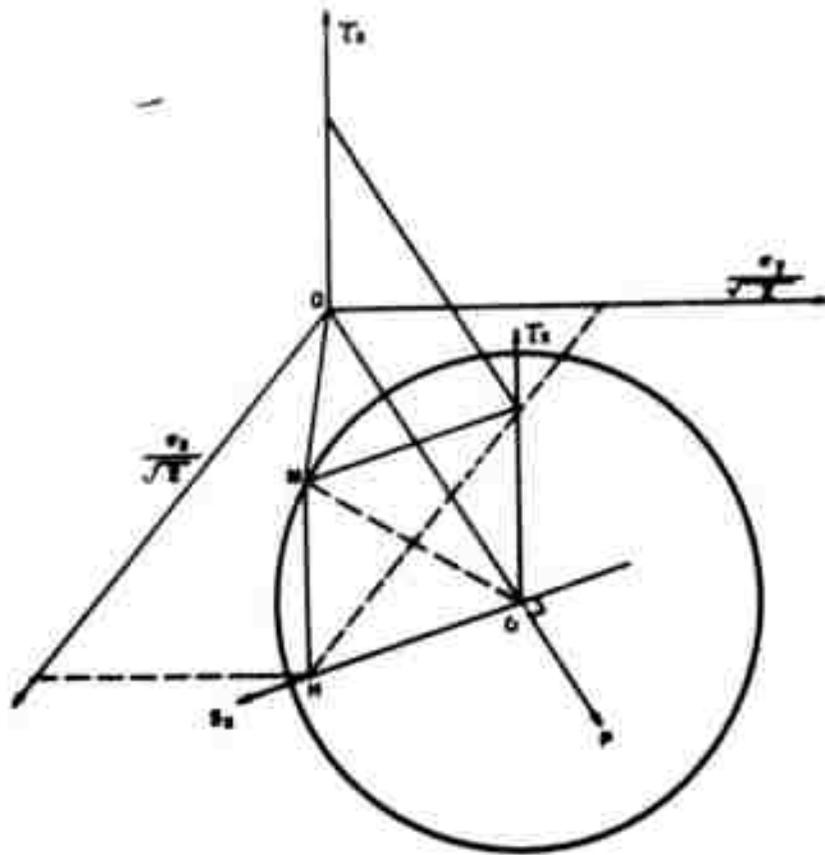
Figure 35. Space Representation of the State of Stress.
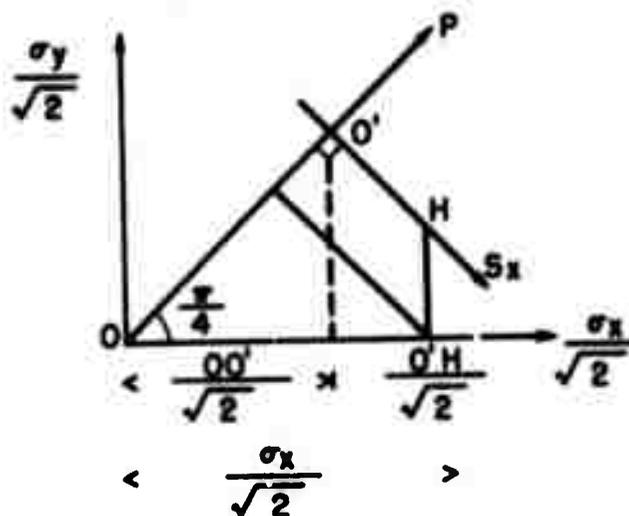
Figure 36. Projection of the Space Representation of the $\sigma_x/\sqrt{2}$, $\sigma_y/\sqrt{2}$ Plane.

Therefore in Figure 35, the circle at O' is the Mohr Circle for the state of stress

$$\left| \begin{array}{cc} \dfrac{\sigma_x - \sigma_y}{2} & \tau_{xy} \\[3mm] \tau_{xy} & \dfrac{\sigma_y - \sigma_x}{2} \end{array} \right| \qquad (\text{V C-61})$$

The plane O'M H is called the deviator plane. The shear stress on a plane α is then written (Figure 37):

$$\tau_n = S_x \sin 2\alpha + \tau_x \cos 2\alpha \qquad (\text{V C-62})$$

and if the failure condition is written

$$|\tau_n| = K(\alpha) \qquad (\text{V C-63})$$

we get a relation between S_x and τ_x independent of P. This shows that the criterion is a cylinder parallel to OP (Figure 35).

    b. <u>Representation in a Deviator Plane.</u>   From Equations V C-62 and V C-63 failure occurs when

$$S_x \sin 2\alpha + \tau_x \cos 2\alpha = K(\alpha) \qquad (\text{V C-64})$$

or

$$S_x \sin 2\alpha + \tau_x \sin 2 = -K(\alpha) \qquad (\text{V C-65})$$

Any combination of S_x and τ_x satisfying these equations gives on a certain plane α a failure or yield condition. For each value of α, Equations V C-64 and V C-65 represents 2 straight lines D_1 and D_2 (Figure 38).

The properties of D_1 and D_2 are shown on Figure 38. When α varies from 0 to π, D_1 and D_2 envelope two curves C_1 and C_2 symmetric to one another with respect to O'. The curves C_1 and C_2 can take different shapes depending on the failure criterion. Figures 39(a,b) show the form of these curves for the criterion $K(\alpha) = A + B \cos^2 3\alpha$. It is to be noticed that only the points on C_1 and C_2 between their intersection are possible (active) limiting points $\tau = K(\alpha)$.
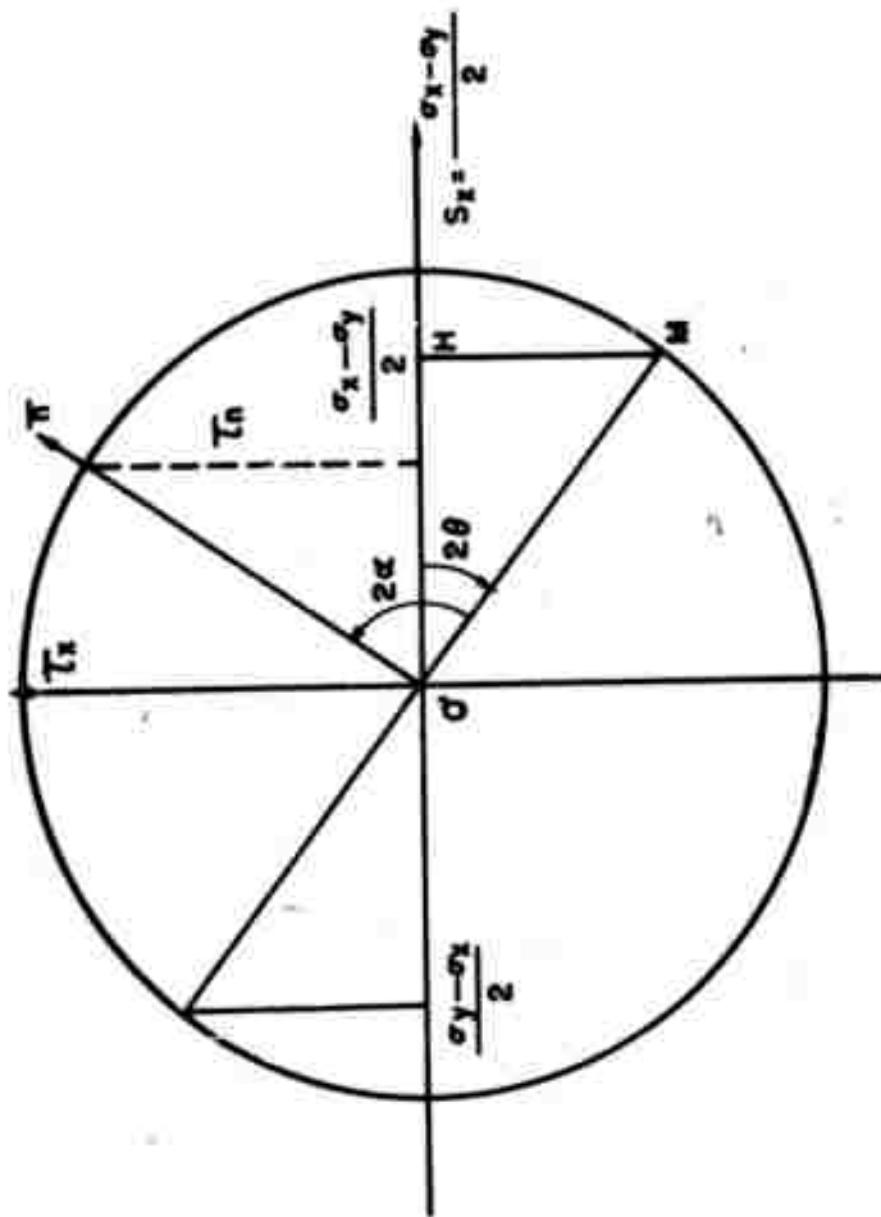
Figure 37. Representation of the State of Stress on the Deviator Plane.

Figure 38. Properties of Lines D_1 and D_2.
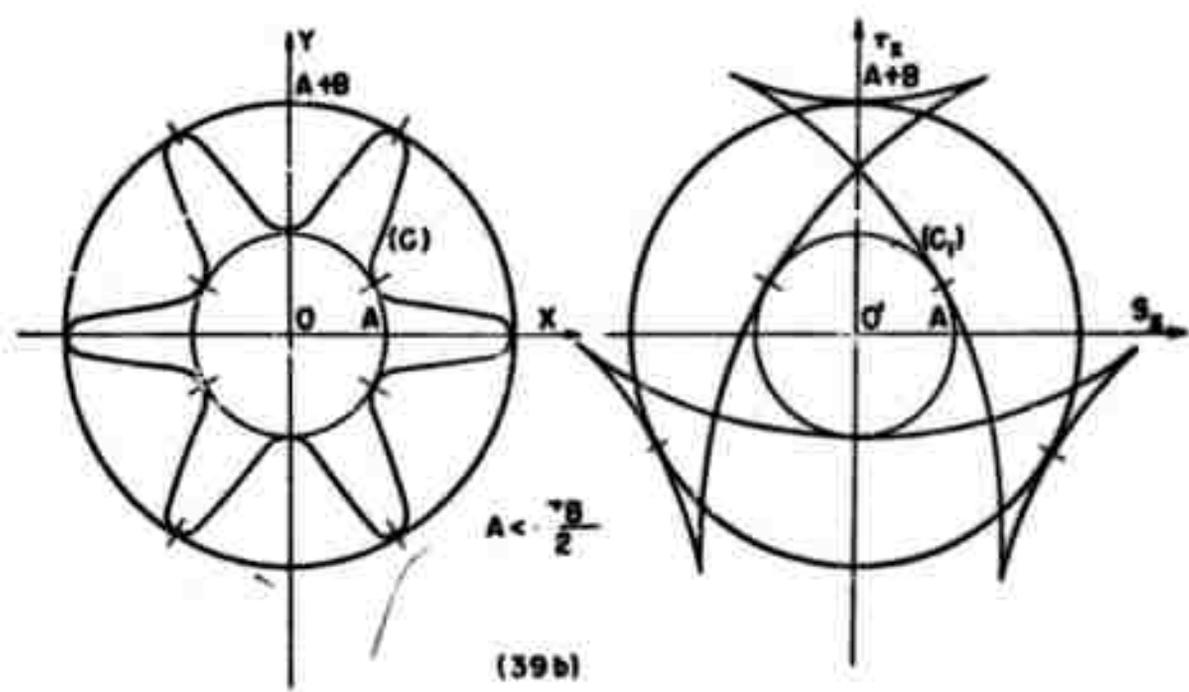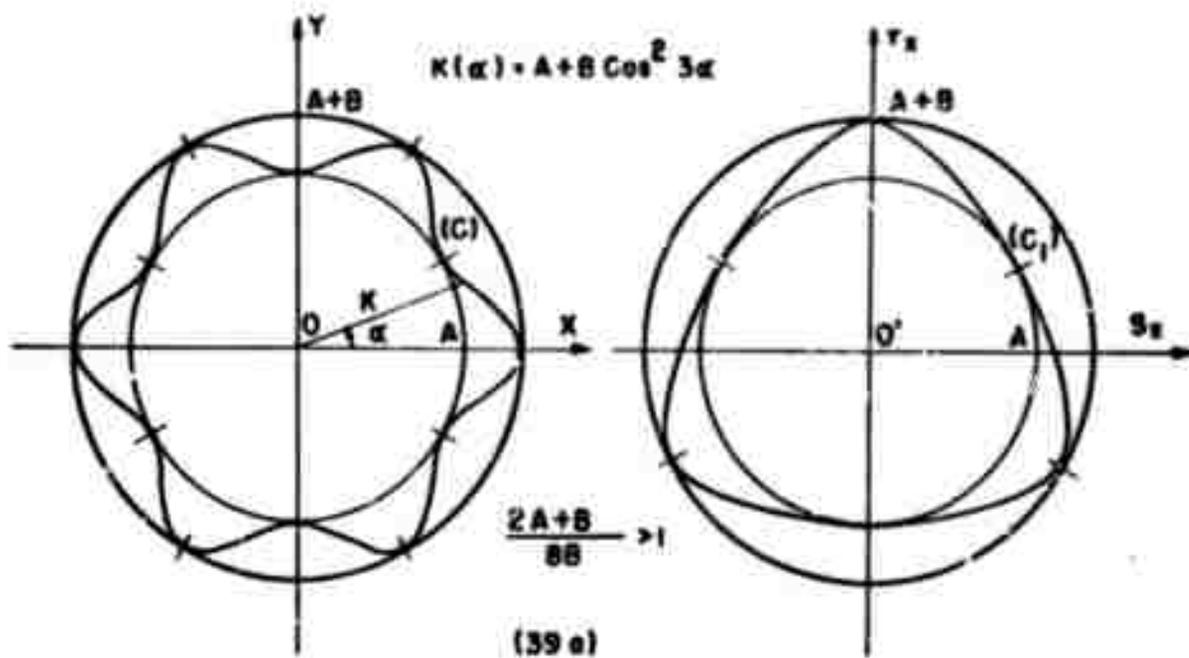
Figure 39. Representation in the X,Y Plane and in the τ_x, S_x Plane of the Criterion $K(\alpha) = A+B \cos^2 3\alpha$.
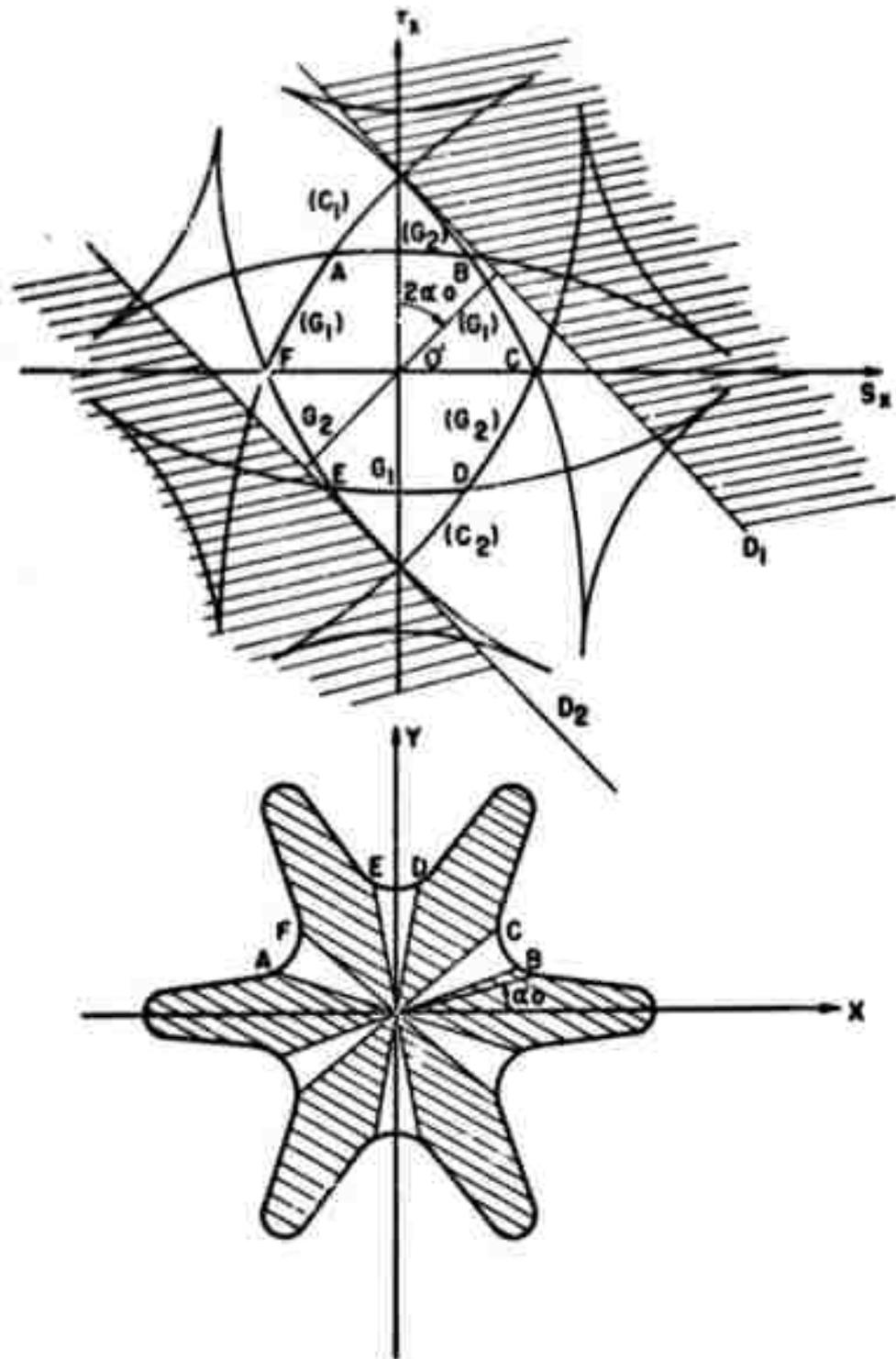
Figure 40. Active and Passive (Hatched) Zones for the Criterion $K(\alpha) = A + B \cos^2 3\alpha$ when $A < 7B/2$.

Figure 40 shows active points for the criterion $K(\alpha) = A + B \cos^2 3\alpha$ when $A < \frac{7B}{2}$. Points following in the hatched zones (passive zones) are not possible limiting points. It is worth mentioning that for a curve $G(S_x, \tau_x) = 0$ to represent a failure condition of the type

$$\max |\tau| = K(\alpha) \qquad \text{(V C-66)}$$

the curve must be regular, concave towards the origin and symmetrical with respect to 0'. This would correspond to

$$K(\alpha + \frac{\pi}{2}) = K(\alpha) \qquad \text{(V C-67)}$$

which is Hill's case previously mentioned.

c. <u>Conclusion</u>. The case of interest in this program is that of brittle materials in which the behavior in tension is different from that in compression. For isotropic materials, the Mohr-Coulomb failure criterion accounts for such a behavior but nothing equivalent to it has been introduced in the study of anisotropic ones. A formula of the form

$$\text{Max} |\tau| = K(\alpha) + f(\alpha) \sigma_n \qquad \text{(V C-68)}$$

could be of value in such cases. Extensive experimentation is necessary before attempting any stress-strain formulation.

D. **Statistical Aspects of Failure**
   (J. Y. L. Ho and F. M. Anthony, Bell Aerosystems)

   1. **Background**

   It is generally recognized that the strength behavior of brittle materials is statistical in nature. If, for example, 100 seemingly identical samples were loaded to failure in an essentially identical manner, the ratio of strengths between the strongest and weakest samples would range from about 1.5 to about 5.0. With such materials, the design allowable strength level must be related to a probability of failure. Hence, the assessment of structural integrity becomes a problem of determining the probability of failure under given loading conditions rather than whether or not the part will fail.

   Ideally, the variability of strength behavior of a particular component configuration made from a specific material can be determined by subjecting a large number of parts to simulated service loadings. Such an approach is prohibitively expensive in most instances. Consequently, less expensive approaches have been under investigation in recent years.[16-21] While universal agreement has not been reached as to the specifics involved, trends in the manner of dealing with isotropic materials have been defined.

   Three types of failure behavior have been postulated: series, parallel, and series-parallel. Series or "weakest-link" behavior implies that local fracture is synonymous with complete failure. The parallel model allows for load redistribution in the event of local failure as in the case of a wire rope where the failure of one strand does not cause complete failure. The series-parallel model may be constituted in a number of ways to define combined behavior. Analytical development is most advanced for the series model. In addition, the assumption of series behavior provides conservative predictions of failure probability. Therefore, series behavior is generally assumed.

   The approach followed for isotropic materials is to fit strength data from uniaxial tests of small samples with a statistical distribution function and to predict the behavior of samples of larger sizes. The distribution function by W. Weibull[16] is generally employed although its choice is rather arbitrary and other functions may be more appropriate for specific materials. Inasmuch as the Weibull function employs three parameters which are evaluated from an analysis of test data, rather than two parameters as required for most other distribution functions, better fits of experimental data can usually be obtained with the Weibull function.

   Relationships have been derived for employing data obtained under one type of uniaxial stress state to predict the probability of failure under a different uniaxial or a specific biaxial stress state;[17] i.e., relationships among tension, bending and torsion loadings. The influence of multiaxial stress states can be included by means of experimental data or by the assumption of a multiaxial failure criterion. While there is still insufficient data to positively verify the statistical design approach for brittle materials, recent results [18-20] provide sufficient encouragement to warrant the extension of the statistical approach to brittle anisotropic materials.

-74-

When an anisotropic material is considered, the statistical problem becomes more complex because (1) different statistical distribution function parameters may be necessary to define strength behavior in each major material direction, (2) different distribution function forms may be applicable in each major material direction, or (3) different failure mechanisms may operate in each major material direction. Furthermore, it is necessary to define strength as a function of orientation since the applied stresses may not coincide with the major material axes. When the anisotropic material is a fiber reinforced composite, definition of statistical strength behavior is even more complex because of the different constituents and their possible interactions, but the series model should still provide conservative predictions.

The cost of experimentally defining the statistical strength behavior of an anisotropic material subjected to multiaxial stress states is obviously too expensive to be practical. Analytical approaches are essential. Once established, selected experiments can be conducted to assess their validity.

2. Anisotropic Material Subjected to a Multiaxial Stress State

As initially planned, the extension of statistical theory from the relatively well established procedures for isotropic materials subjected to a uniaxial stress state to the more general case of anisotropic materials subjected to multiaxial stress states was to proceed in three steps. The first step was to consider the anisotropic material subjected to a uniaxial stress state. The second step was to extend the analytical development for the isotropic material from the uniaxial to the multiaxial stress state. The third step was to consider the anisotropic material subjected to the multiaxial stress state. During the anlytical developments for the first two steps which attempted to follow the approaches suggested by Weibull[16-22] difficulties were encountered. At various points, assumptions were necessary but there was no way of ascertaining the proper assumptions to make. Different assumptions led to different results. The initial approach was abandoned, therefore, and an independent formulation of the problem was pursued as described herein.

The well-known statistical theory of Weibull for the strength of a material defines the probability of failure for isotropic materials in the uniaxial stress state as

$$F = 1 - e^{-B} \qquad \qquad \text{(V D-1)}$$

and

$$B = B_x = \int_v K \left[\frac{\sigma_x - \sigma_u}{\sigma_0} \right]^m dV \left[\sigma_x \geq \sigma_u \geq 0 \right] \qquad \text{(V D-2)}$$

$$B = B_x = 0 \quad \left[\sigma_x \leq \sigma_u \geq 0 \right]$$

where

F = Probability of failure

B = Total risk of rupture

B_x = Risk of rupture due to uniaxial stress

-75-

σ_x = Uniaxial stress in X – direction
σ_u = Threshold stress
σ_0 = Characteristic stress
m = Material flaw intensity
K = Coefficient
V = Volume

The above equations are based on the assumption that the compressive stress will not contribute to the risk of rupture. The value of the threshold stress σ_u is always greater than or equal to zero. As long as σ_x is smaller than σ_u, whether it is tensile (positive) or compressive (negative with a large magnitude), it is postulated that rupture will never occur.

When this concept is extended to the multiaxial stress state, the total risk of rupture B may be assumed to have the following form

$$B = B_x + B_y + B_z = \int_v K \left[\frac{\sigma_x - \sigma_u}{\sigma_0} \right]^m dV + \int_v K \left[\frac{\sigma_y - \sigma_u}{\sigma_0} \right]^m dV + \int_v K \left[\frac{\sigma_z - \sigma_u}{\sigma_0} \right]^m dV$$

$$\left[\sigma_x \geq \sigma_u \geq 0 \right] \qquad \left[\sigma_y \geq \sigma_u \geq 0 \right] \qquad \left[\sigma_z \geq \sigma_u \geq 0 \right]$$

$$B_x = 0 \qquad \left[\sigma_x < \sigma_u \geq 0 \right]$$

$$B_y = 0 \qquad \left[\sigma_y < \sigma_u \geq 0 \right] \qquad\qquad (V \ D-3)$$

$$B_z = 0 \qquad \left[\sigma_z < \sigma_u \geq 0 \right]$$

For anisotropic materials, considering that the shear stresses also contribute portions of the total risk of rupture, the most general form of B will be

$$B = \sum_{i=1}^{3} \sum_{j=1}^{3} B_{ij} \qquad\qquad (V \ D-4)$$

$$B_{ii} = \int_v K_{ii} \left[\frac{\tau_{ii} - (\tau_u)_{ii}}{(\tau_0)_{ii}} \right]^{m_{ii}} dV \qquad \left[\tau_{ii} \geq (\tau_u)_{ii} \geq 0 \right] \qquad (V \ D-5)$$

$$B_{ii} = 0 \qquad \left[\tau_{ii} < (\tau_u)_{ii} \geq 0 \right] \left[i = 1, 2, 3 \right]$$

$$B_{ij} = \int_v K_{ij} \left[\frac{|\tau_{ij}| - |(\tau_u)_{ij}|}{|(\tau_0)_{ij}|} \right]^{m_{ij}} dV \qquad \left[|\tau_{ij}| \geq |(\tau_u)_{ij}| \geq 0 \right] \qquad (V \ D-6)$$

$$B_{ij} = 0 \qquad \left[|\tau_{ij}| < |(\tau_u)_{ij}| \geq 0 \right] \left[i \neq j \right] \left[i, j = 1, 2, 3 \right]$$

-76-

where B_{ij} = Risk of rupture tensors
T_{ij} = Stress tensors
$(\tau_u)_{ij}$ = Threshold stress tensors
$(\tau_o)_{ij}$ = Characteristic stress tensors
m_{ij} = Material variability tensors
K_{ij} = Coefficient tensors

It is still assumed that the normal compressive stresses τ_{11}, τ_{22} and τ_{33} will not cause rupture. As far as shear stresses τ_{ij} $(i \neq j)$ are concerned, they may cause rupture when their absolute values are greater than the absolute values of the shear threshold stresses $(\tau_u)_{ij}$ $(i \neq j)$.

The development of the failure criterion is incomplete at this stage, simply because when the uniaxial compressive stress is applied, failure does occur. Brittle materials may be infinitely strong under triaxial compressive stresses, (hydrostatic pressure), yet they have finite strength under uniaxial (or biaxial) compressive stress.

Hence analogous to the uniaxial tensile stress case, the risk of rupture due to uniaxial compressive stress will take the following form

$$B = B_x' = \int_v K' \left[\frac{|\sigma_x'| - |\sigma_u'|}{|\sigma_o'|} \right]^{m'} dV = \int_v K' \left[\frac{\sigma_x' - \sigma_u'}{\sigma_o'} \right]^{m'} dV$$

$$\left[|\sigma_x'| \geq |\sigma_u'| \geq 0 \right] \quad \text{or} \quad \left[\sigma_x' \leq \sigma_u' \leq 0 \right] \tag{V D-7}$$

$$B = B_x' = 0 \quad \left[|\sigma_x'| < |\sigma_u'| \geq 0 \right] \quad \text{or} \quad \left[\sigma_x' > \sigma_u' \leq 0 \right]$$

where σ_x, σ_u and σ_o are all negative values.

The distribution functions of probability of failure for both uniaxial tensile and compressive stresses are presented in Figure 41. This figure indicates two important facts:

(a) The brittle materials are not infinitely strong under uniaxial compressive stress. It does have a bound in the compressive region.
(b) The ultimate strength of brittle materials in either tension or compression, should be stated as a function of probability of failure.

Concept (b) is not very apparent for ductile materials because their distribution functions are almost like step functions. The range of variability of the yield or ultimate stress is very narrow. For brittle materials, the ultimate stresses (tensile and compressives) are increasing according to their distribution function as the probability of failure increases from 0% and up.

When the biaxial stress state is considered, the Mohr's stress circles are shown in Figure 42, and the maximum principle stress failure criterion assumed at zero probability of failure is shown in Figure 43. Isotropic behavior is assumed
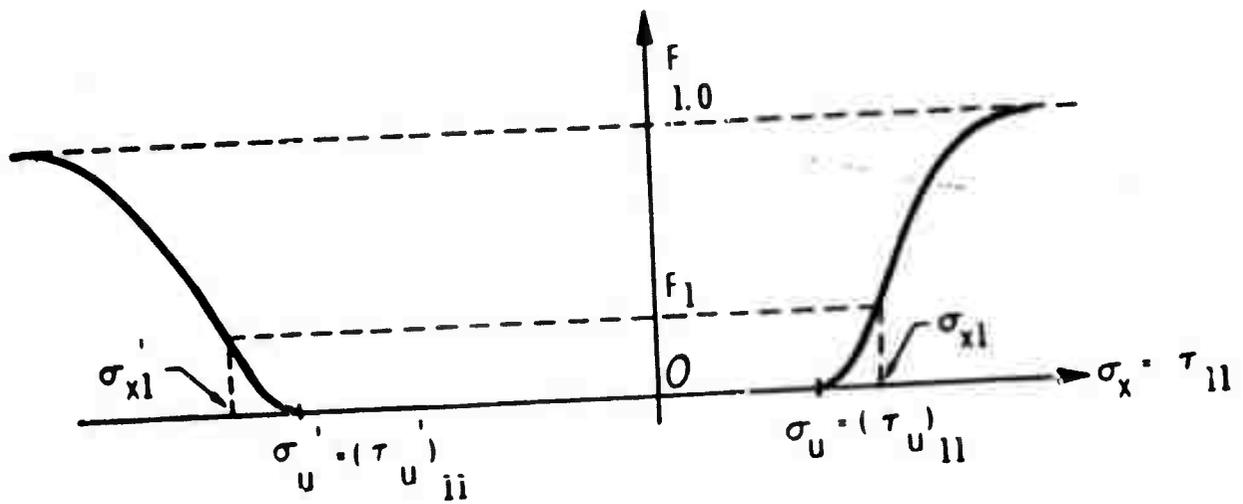
Figure 41. Distribution Function of Probability of Failure.
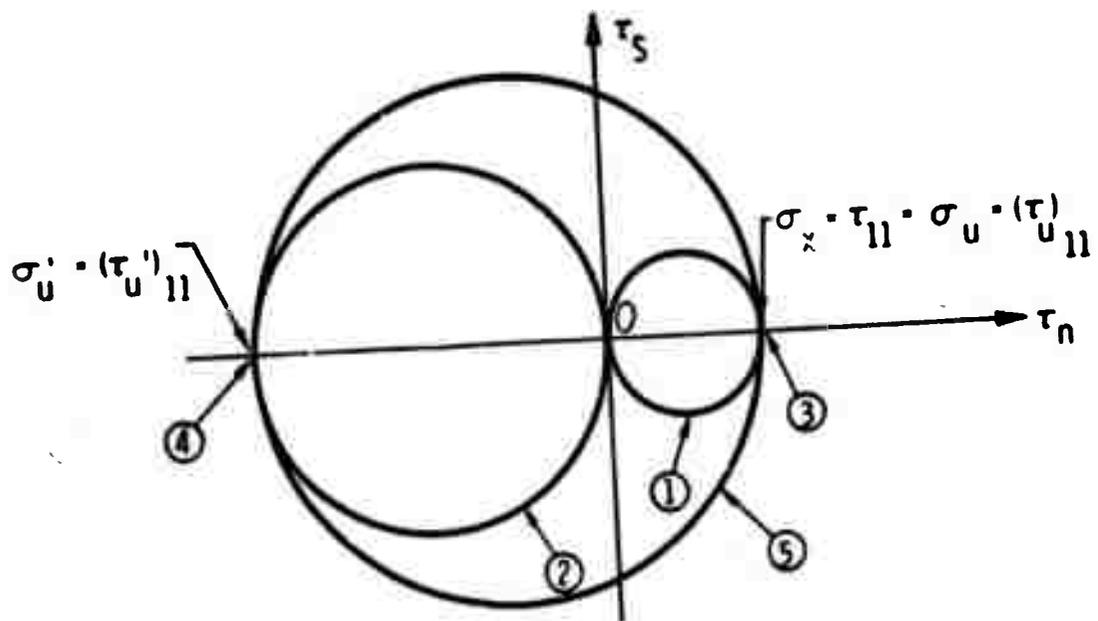
Figure 42. Mohr's Stress Circles for Biaxial Stress State.
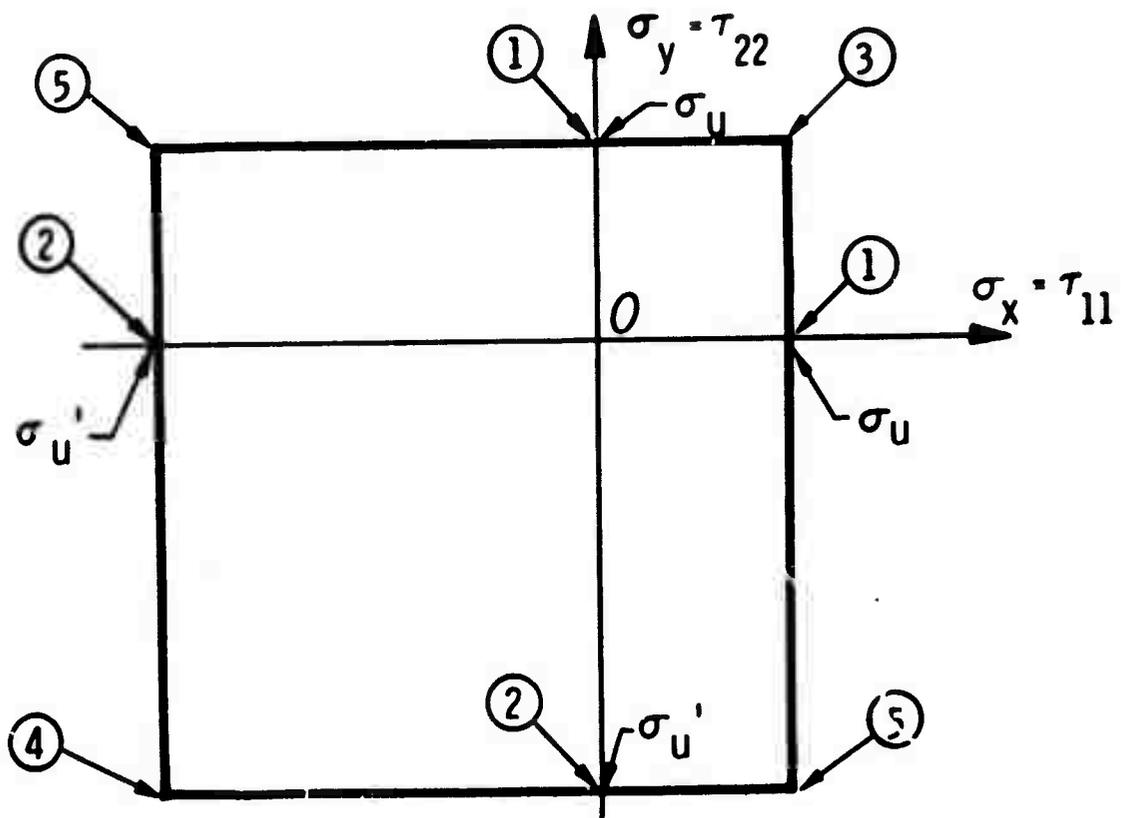
Figure 43. Failure Criteria for Biaxial Stress at Zero
Probability of Failure.

for simplicity of illustration. It is considered temporarily that the shear threshold stresses of the material are so high that they may not be reached. The following table explains the various cases in Figures 42 and 43.

Figure 42	Figure 43	Description
Circle-(1)	Point-(1)	Uniaxial tensile stress
Circle-(2)	Point-(2)	Uniaxial compressive stress
Point-(3)	Point-(3)	Equal Biaxial tensile stresses
Point-(4)	Point-(4)	Equal biaxial compressive stresses
Circle-(5)	Point-(5)	Biaxial tensile and compressive stress s

The safe region and the rupture region are inside and outside the square boundary of Figure 43 respectively.

When the probability of failure is greater than zero, $F = F_1$, the failure criterion for biaxial stress states, as shown in Figure 44 indicates deviations from the originally assumed failure criterion at $F = 0$. Note that for uniaxial loadings Points 1 and 2 move to Points 1' and 2' as would be expected from Figure 41. Reasons for the deviations under biaxial stress conditions are discussed in subsequent paragraphs.

Consider first the biaxial tension region and the specific case of equal tensile stresses, $\sigma_x = \sigma_y > \sigma_u$. The total risk of rupture is

$$B = B_x + B_y = \int_v K \left[\frac{\sigma_x - \sigma_u}{\sigma_o} \right]^m dV + \int_v K \left[\frac{\sigma_y - \sigma_u}{\sigma_o} \right]^m dV = 2 \int_v K \left[\frac{\sigma_x - \sigma_u}{\sigma_o} \right]^m dV \qquad \text{(V D-8)}$$

In order to reach the same probability of failure, $F = F_1$, the equal biaxial tensile stresses are smaller than for the uniaxial tensile stress because the risk of rupture in the x- and y-directions are added together. Hence Point 3 will move to 3" instead of 3'.

Under biaxial tension-compression conditions Point 5 will move to 5" or 5''' rather than 5' because of the reasons to be discussed. First, the total risk of rupture is

$$B = B_x + B_y' = \int_v K \left[\frac{\sigma_x - \sigma_u}{\sigma_o} \right]^m dV + \int_v K' \left[\frac{\sigma_y' - \sigma_u'}{\sigma_o'} \right]^{m'} dV$$

$$\qquad \text{(V D-9)}$$

$$\left[\sigma_x \geq \sigma_u \geq 0 \right] \qquad \left[\sigma_y' \leq \sigma_u' \leq 0 \right]$$

Since the compressive stress σ_y' may contribute a portion of the total risk of rupture, the tensile stress σ_x in the biaxial stress state does not have to be as large as the tensile stress in the uniaxial stress state in order to reach the same probability of failure F_1. Second, in brittle fracture, although compressive stress is applied, the
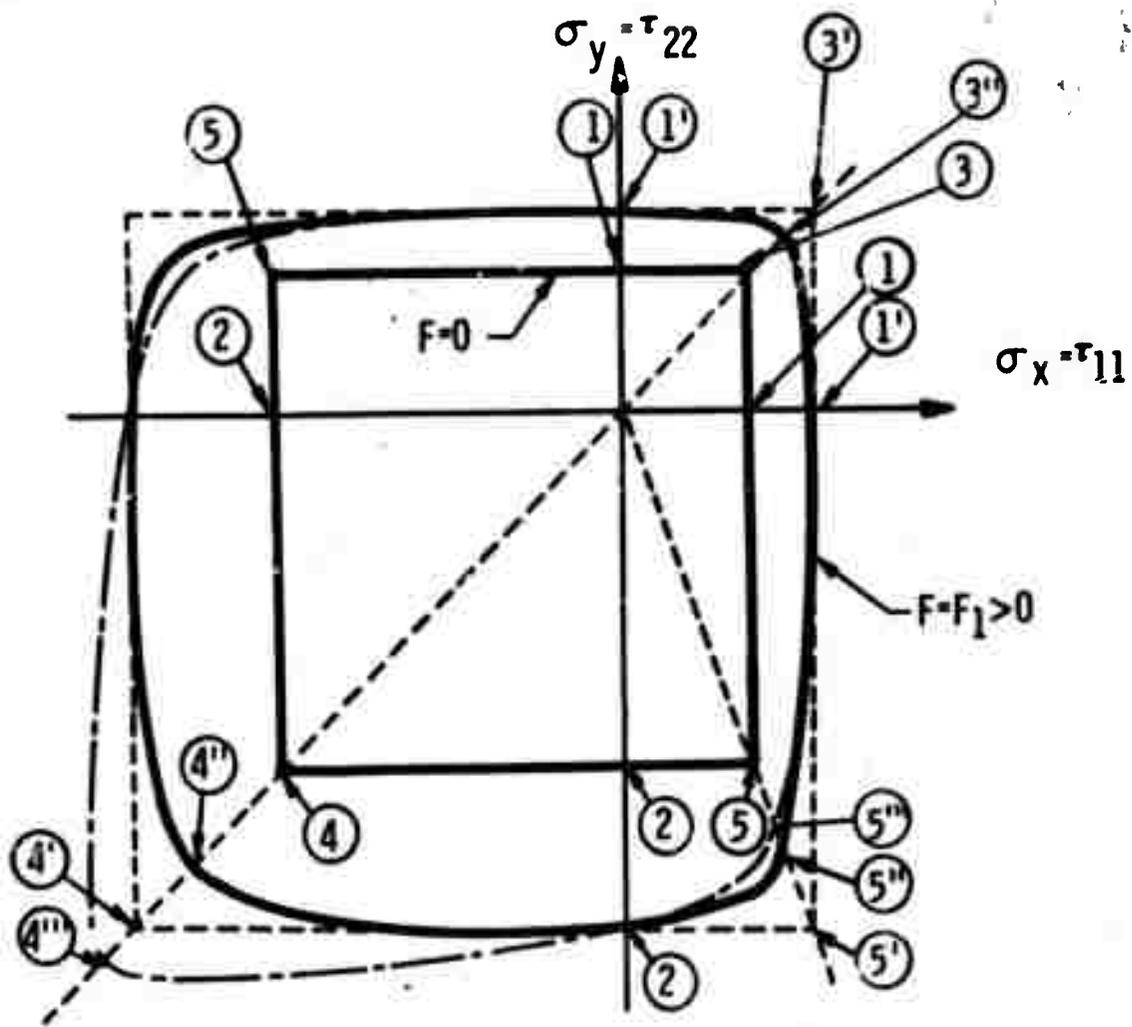
Figure 44. Failure Criteria for Biaxial Stress at
Various Probabilities of Failure.

material may still be broken by tension in the perpendicular direction from the normal compressive stress. In other words, the compressive stress σ_y' in y-direction may contribute some effect of the risk of rupture in x-direction and z-direction. Also, the tensile stress σ_x in x-direction may contribute some (negative) effect of the risk of rupture in y-direction and z-direction. Third, for some types of bittle materials, the threshold shear stress $(\tau_u)_{ij}$ (or σ_u'') is relatively low, the shear stress τ_{ij} $(i \neq j)$ (or σ_{xy}, etc.) will have some effect on the risk of rupture. All of these effects are additive to the contribution of total risk of rupture. Combined stresses at point 5'' or 5''' will be sufficient to achieve the same level of probability of failure F_1 as that in the uniaxial stress state.

$$B = B_x + B_y' + B_{xy} = \int_V K \left[\frac{\sigma_x - \sigma_u}{\sigma_0} \right]^m dV + \int_V K' \left[\frac{\sigma_y' - \sigma_u'}{\sigma_0'} \right]^m dV + \int_V K'' \left[\frac{\sigma_{xy} - \sigma_u''}{\sigma_0''} \right]^{m''} dV \tag{V D-10}$$

$$\left[\sigma_x \geq \sigma_u \geq 0 \right] \quad \left[\sigma_y \leq \sigma_u \leq 0 \right] \quad \left[|\sigma_{xy}| \geq |\sigma_u''| \geq 0 \right]$$

$$B_{xy} = 0 \quad \left[|\sigma_{xy}| < |\sigma_u''| \geq 0 \right]$$

For any ratio $\gamma = \dfrac{\sigma_x}{-\sigma_y'}$ the shear stress will be

$$\sigma_{xy} = \frac{1}{2} \left[\sigma_x - \sigma_y' \right] = \frac{1}{2} \left[1 + \gamma \right] \sigma_x \tag{V D-11}$$

As shown in Figure 45, circle-(5) represents a biaxial tensile and compressive stress state. When σ_x and σ_y' are small (yet $\sigma_x > \sigma_u > 0$, $\sigma_y' < \sigma_u' < 0$), $B_x \neq 0$, $B_y' \neq 0$, $B_{xy} = 0$ because the value of σ_{xy} is still smaller than σ_u''. As the values of σ_x and σ_y' increase, the shear stress σ_{xy} will increase correspondingly until

$$\sigma_{xy} = \frac{1}{2} \left[\sigma_x - \sigma_y' \right] > \sigma_u'' \tag{V D-12}$$

then,

$$B_{xy} \neq 0 \tag{V D-13}$$

Circle-(5') in Figure 45 explains how the shear stress σ_{xy} contributes its effect to the total risk of rupture.

The interaction effects on risk of rupture between tensile, compressive and shear stresses are not clear at this stage. More work is required in the future.
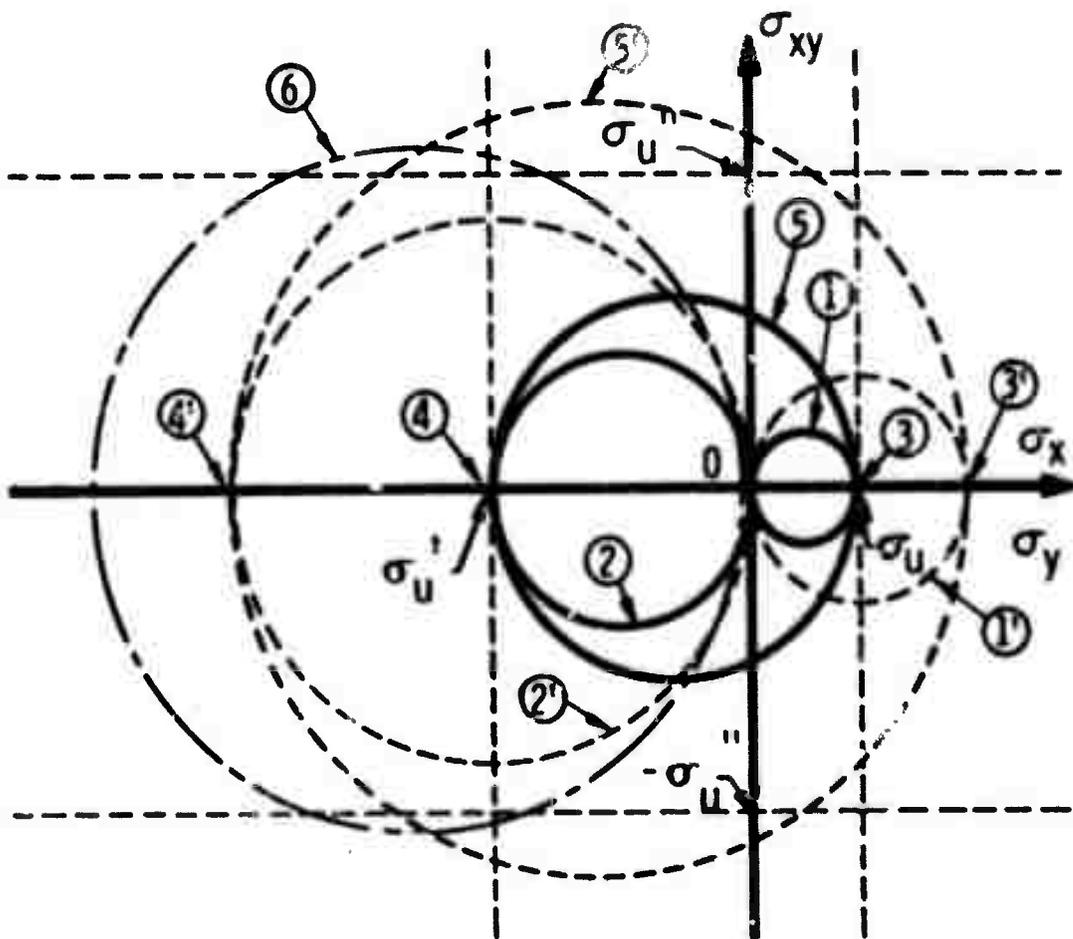
Figure 45. The Effect of Threshold Shear Stress to the Risk of Rupture and the Probability of Failure.

Finally, consider the compression-compression region with $\sigma_x' = \sigma_y' < \sigma_u' \leq 0$. If there is no interaction on the risk of rupture between the two compressive stresses σ_x' and σ_y', then

$$B = B_x' + B_y' = \int_V K' \left[\frac{\sigma_x' - \sigma_u'}{\sigma_0} \right]^{m'} dV + \int_V K' \left[\frac{\sigma_y' - \sigma_u'}{\sigma_0'} \right]^{m'} dV \qquad (V\ D\text{-}14)$$

$$\left[\sigma_x' \leq \sigma_u' \leq 0 \right] \qquad \left[\sigma_y' \leq \sigma_u' \leq 0 \right]$$

Analogous to the equal biaxial tension case, Point 4 in Figure 44 will move to 4''. In the special case when $\sigma_x' << \sigma_y' < 0$ and $\sigma_{xy} = \frac{1}{2} |\sigma_x' - \sigma_y'| > \sigma_u''$, then

$$B = B_x' + B_{xy} = \int_V K' \left[\frac{\sigma_x' - \sigma_u'}{\sigma_0'} \right]^{m'} dV + \int_V K'' \left[\frac{\sigma_{xy} - \sigma_u''}{\sigma_0''} \right]^{m''} dV \qquad (V\ D\text{-}15)$$

$$B_x' \neq 0 \left[\sigma_x' < \sigma_u' \leq 0 \right], \; B_y' = 0 \left[\sigma_y > \sigma_u' \leq 0 \right], \; B_{xy} \neq 0 \left[\sigma_{xy} > \sigma_u'' \geq 0 \right]$$

This special case is represented by Circle-(6) in Figure 45 which will also make Point-(4) in Figure 44 move to 4'' rather than to 4'. If there is interaction between the two compressive stresses σ_x' and σ_y', the total risk of rupture will take the following form

$$B = B_x' \; (\sigma_x', \; \sigma_y') + B_y' \; (\sigma_x', \; \sigma_y') + B_{xy} \; (\sigma_x', \; \sigma_y')$$

Point 4 in Figure 44 will then move to 4''''.

When this concept is extended to a triaxial stress state, a boundary surface of safe region can be drawn in the three-dimensional space. For $\sigma_x' = \sigma_y' = \sigma_z' < \sigma_u' < 0$ (triaxial compression) the boundary surface of safe region will be extended to infinity because rupture will not be possible.

Figure 46 shows the probability of failure surface for the biaxial stress state assuming the maximum principle stress failure criterion.

Thus, a basic approach has been established with respect to the statistical aspects of failure for materials which exhibit series behavior. Effects of anisotropy and multiaxial stress state are included. For purposes of illustration the maximum principle stress criterion was assumed but the approach is equally valid for any other failure criterion and can deal with shear and compressive stresses as well as tensile stresses. The relative influences of shear and compressive stresses are currently being examined.
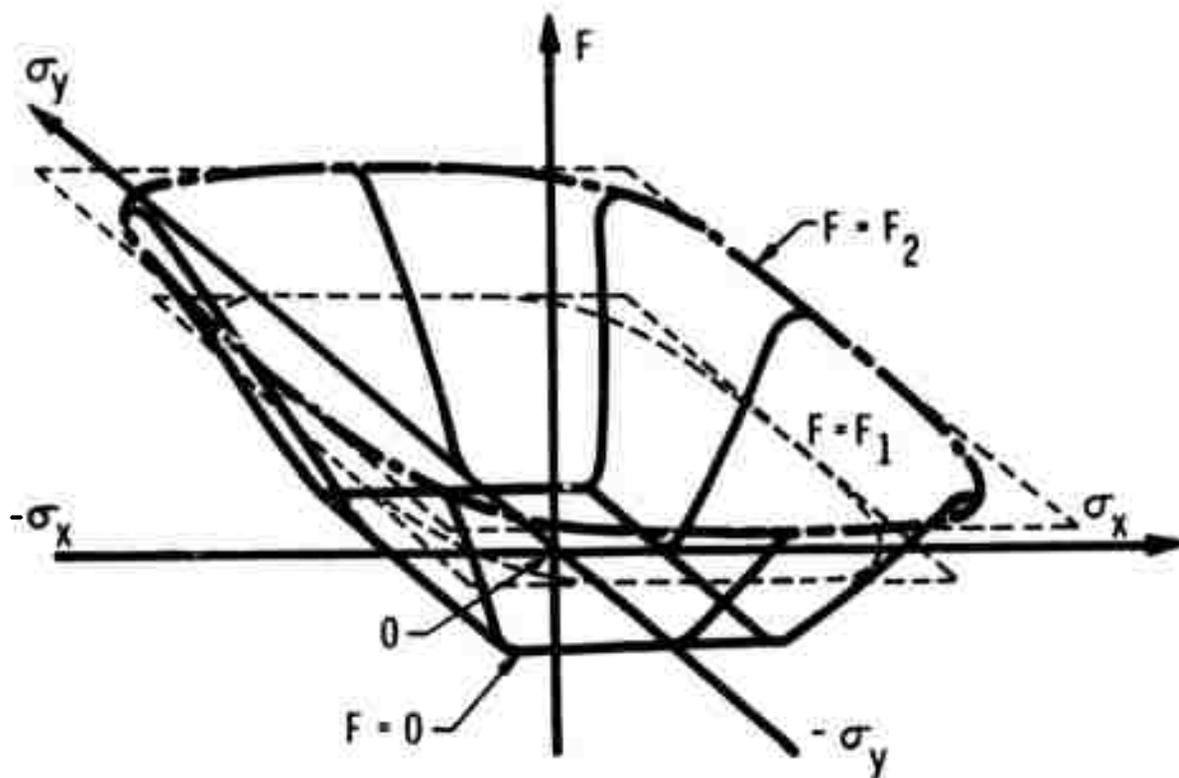
Figure 46. Probability of Failure Surface for the Biaxial
Stress State Assuming the Maximum Principle
Stress Failure Criterion.

E. Failure Criteria and Multiaxial Stress Test Apparatus
(T. Weng, Union Carbide)

1. Introduction

The objectives of this research program are to build a multiaxial stress testing machine, to obtain, experimentally, failure criteria for brittle and composite materials, and to represent the failure criteria in forms which can be used by designers.

In order to establish the shape of the yield surface, to verify theories of plasticity, and to study the processes of plastic deformation, biaxial stress tests on ductile materials have been conducted by several investigators. For brittle and composite materials, however, very little work has been reported on biaxial stress tests and failure criteria. The usual method employed in these investigations is to test a thin-walled, hollow cylinder under a combination of internal pressure and an axial tensile or compressive load; for a more sophisticated test, a torque is also applied. This type of biaxial stress test is relatively versatile and easy to conduct, and the stresses in the test cylinder under various loading conditions can be calculated easily. A multiaxial stress testing machine for thin-walled, hollow cylinders is being constructed for this program. To date, three tests of JTA cylinders have been made with a preliminary version of the test apparatus.

2. Multiaxial Stress Testing Machine

In order to obtain some failure strengths under biaxial stresses for JT-series materials early in the research program, a simplified version of the multiaxial stress testing machine has been assembled. Provisions for applying external pressure, axial tension, and torques will be added later.

a. Hydraulic System. A simple hydraulic system, shown schematically in Figure 47, has been constructed for applying an internal pressure and an axial compressive load. The hydraulic power unit, A, can supply internal pressure up to 5000 lb/in.^{2} and the capacity of the hydraulic press, B, is 12,000 lb in compression. The internal pressure can be increased, decreased, or maintained at a given pressure by adjusting a screw in a pressure relief valve, C, mounted at the outlet port of the hydraulic power unit. Continuously variable and accurately controlled rates of pressure increase can be obtained by replacing the adjusting screw in the pressure relief valve with a threaded plunger, which rotates and moves axially, in a linear actuator, D. The rate and direction of the axial motion of the plunger in the linear actuator are remotely controlled by a control box, E. The installation of the linear actuator into the pressure relief valve is not yet completed. A strain-gage type pressure transducer, F, which has a capacity of 5000 lb/in.^{2}, is connected to the hydraulic line. The pressure recording system can be modulated to measure 0.5 lb/in.^{2} per inch recorder chart to 500 lb/in.^{2} per inch recorder chart. Since at higher pressures, considerable heat may be generated in the oil, a water

cooling bath, H, is installed in the hydraulic system. The hydraulic press, B, is used for applying a compressive load to a specimen as well as to a fixture used in the hoop tensile stress test. An arrangement for internal pressure and axial loading in the hydraulic press (shown in Figure 47) will be described later.
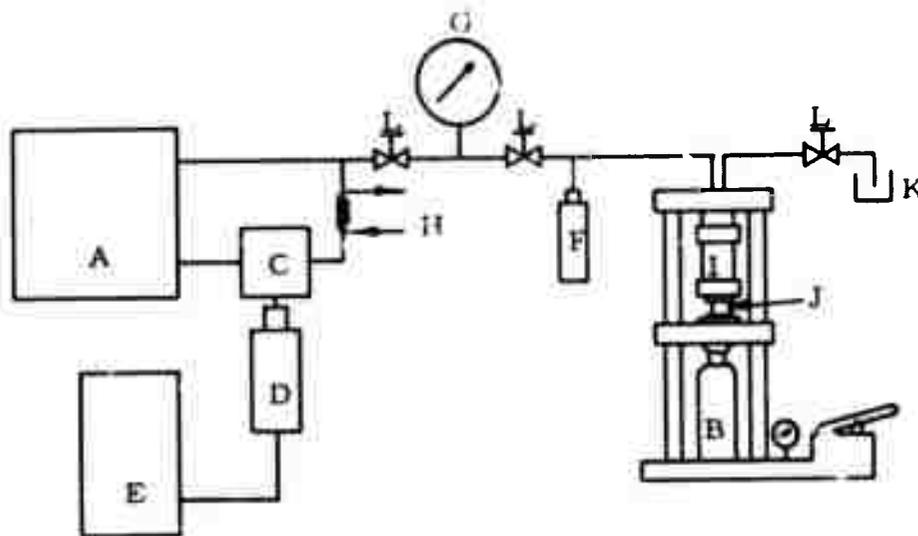
A. Hydraulic Power Unit
B. Hydraulic Press
C. Pressure Relief Valve
D. Linear Actuator
E. Control Box
F. Pressure Transducer

G. Pressure Gage, 0-5000 lb/in.^{2}
H. Cooling Coil
I. Specimen
J. Axial Load Cell
K. Drain
L. Hand Speed Valves

N-9608

Figure 47. Schematic Diagram of Hydraulic System for Biaxial Testing Machine.

b. Hoop Tensile Stress Test Fixture. A fixture, similar to one originally designed by the Stanford Research Institute,[23] has been constructed for hoop tensile stress testing by pressurizing a short, open-end, thin-walled, hollow cylinder. The test fixture containing a test specimen and a Neoprene bag for pressurization is shown in Figure 48. By means of the hydraulic press, the upper and lower plates of the test fixture are pressed against the spacers, which slide freely over the guiding pins. Because the length of the specimen is slightly shorter than the length of the spacers, there is a small clearance between the upper plate and the specimen; thus, the specimen is free from end loads. When the Neoprene bag is pressurized, the specimen is under pure hoop tensile stress. Talc is applied between the specimen and the Neoprene bag to minimize friction. The inside and outside diameters of the test cylinders are, respectively, 0.885 and 0.985 inch; the length can be 0.5, 1.0, or 2.0 inches.

Conical Plug
Upper Plate
Spacer
Pin
Specimen
Neoprene Bag
Bottom Plate
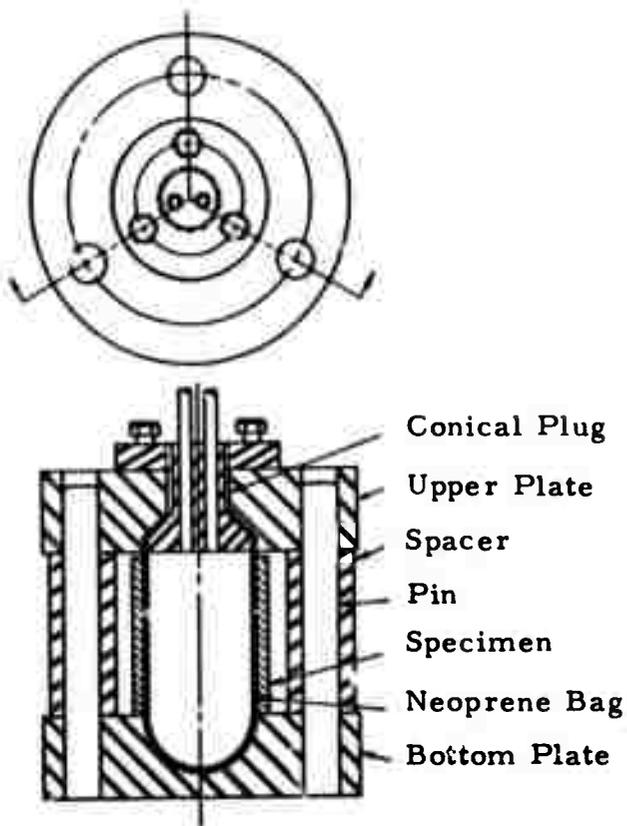
Figure 48. Specimen and Test Fixture for Hoop Tensile
Stress Testing.

c. Internal Pressure and Axial Compressive Stress Test Fixture.
A fixture for testing a cylindrical specimen under internal pressure and an
axial compressive stress, either separately or together, is shown in
Figure 49. For an internal pressure test alone, the axial compression load
cell and the steel plate are not required. The bore of the steel end cap
tapers off slightly to allow epoxy glue to fill in between the cap and the
specimen. An "O" ring groove is made on the steel end cap so that the
specimen may later be placed inside a pressure chamber for internal and
external pressure tests. On the end of the bottom steel end cap, a 7/16
inch radius and 1/16 inch deep crater is machined so that the assembly can
roll freely on a 7/16 inch radius and 1/8 inch high mound on the top of the
load cell for alignment when a compressive load is applied. The bottom
surface of the load cell and the top surface of the steel plate are highly
polished. A thin layer of light oil between the load cell and steel plate
makes the load cell slide very freely on the steel plate. At an early stage
of the application of the compressive load, the load cell slides into position

to give an excellent match between the mound of the load cell and the crater
of the steel end cap. Under a few pounds of axial compressive load, the
lubricating oil is squeezed out, and the load cell is securely locked in place.
Bending moments due to misalignment under axial compression are
practically eliminated by this arrangement.
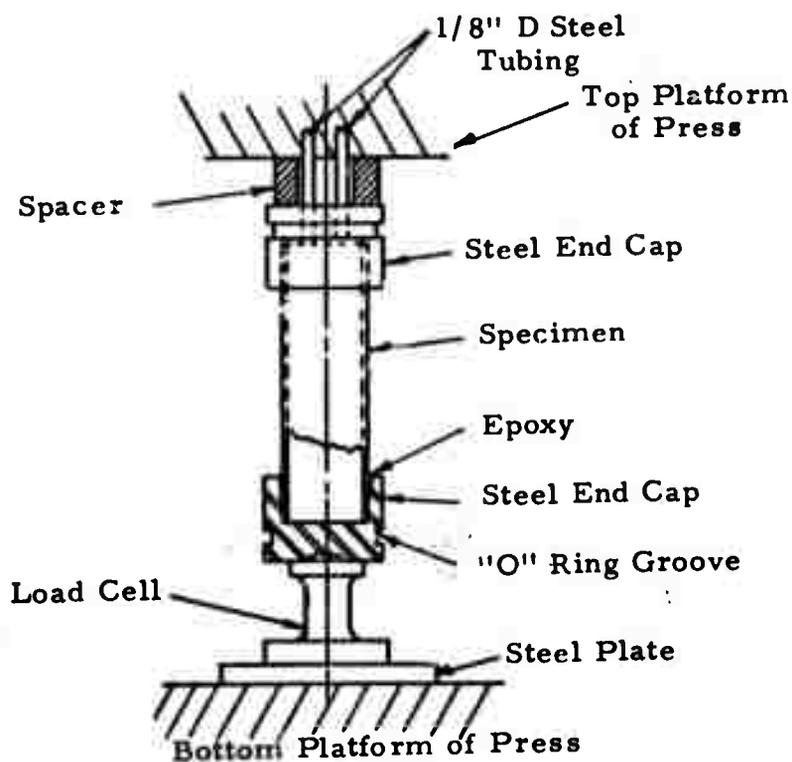
N-9606

Figure 49. Specimen and Test Fixture for Internal Pressure
and Axial Compressive Stress Testing.

3. Test Results

a. Hoop Tensile Stress Test. In order to check the test fixture,
an epoxy cylinder 2 inches long and aluminum cylinders of lengths 1 and 2
inches have been tested to examine the effect of the specimen length and
pressure loading on uniformity of strain distribution.

The strain distribution in the epoxy cylinder was investigated with a
reflection polariscope, and the variation of fringe pattern was estimated to
be less than 0.1 fringe. This small variation is believed to be due to
variations in the properties of the epoxy cylinder itself, rather than to
variations in loading stresses. Strain distributions in the 1.0 and 2.0 inch
aluminum cylinders were investigated with strain gages. It was also found

-89-

that strain distributions in the cylinders were uniform; the experimental and theoretical values of the strains are in good agreement.

Grade ATJ graphite cylinders with lengths of 1 and 2 inches were also tested. The variation of the hoop strains measured with strain gages at 4 locations on the 2 inch long ATJ graphite cylinder was ± 2 percent. Tensile strengths and strains obtained from these ATJ graphite cylinders are in good agreement with those obtained by the uniaxial tensile test. A JTA-9 composite cylinder 1 inch long has been tested. The tensile fracture stress and strain for this cylinder are 7500 lb/in.^{2} and 1180 μin./in., respectively.

b. Internal Pressure Test. An aluminum cylinder having an inside diameter of 0.885 inch, an outside diameter of 0.985 inch, and a length of 3.5 inches was tested under internal pressure to check the performance of the test apparatus. The gage length of the test cylinder was approximately 2 inches. The axial and hoop strains at several locations on the outside surface of the aluminum cylinder were measured with strain gages. The variation of strain with location was approximately 5 percent. The difference between the measured values of the strains and theoretical values calculated by using the manufacturer's values for the moduli was approximately 9 percent. Most of this discrepancy is probably due to material anisotropy in the extruded aluminum cylinder.

A cylinder from the billet JTA-10 and 2 cylinders from the billet JTA-9 have been tested under internal pressure. The cylinder axis is parallel to the axis of material symmetry. For the JTA-9 cylinders, the variation of strain with location was approximately 28 percent. The greater variation of strain compared to that in the aluminum cylinder is probably due to greater material nonhomogeneity in the JTA billets.

Stresses in the hoop and longitudinal directions on the inside surface are given by Lame's formulas: for the hoop stress,

$$\sigma_1 = \sigma_\theta = \frac{(b/a)^2 + 1}{(b/a)^2 - 1} P_i \tag{V E-1}$$

and for the longitudinal stress,

$$\sigma_3 = \sigma_z = \frac{1}{(b/a)^2 - 1} P_i \tag{V E-2}$$

where P_i is the internal pressure, b is the outside diameter, and a is the inside diameter. The hoop strain $\varepsilon_{\theta a}$ on the inside surface can be calculated from the hoop strain $\varepsilon_{\theta b}$ measured on the outside surface by the formula:

$$\varepsilon_{\theta a} = \left[\frac{(1 + s_{12}/s_{11} + s_{13}/s_{11}) + (1 - s_{12}/s_{11})(b/a)^2}{2 + s_{13}/s_{11}} \right] \varepsilon_{\theta b} \tag{V E-3}$$

These formulas are derived for the case of linearly elastic material. For a cylinder subjected to internal pressure, the longitudinal stress and strain are uniform through the thickness; and the longitudinal stress is always one-half of the sum of the hoop stress and the radial stress. Therefore, the ratio of the longitudinal stress to the hoop stress can be assumed to be 0.5 in a thin-walled, hollow cylinder subjected to internal pressure, for the magnitude of the radial stress is very small and can be neglected.

Stress-strain relations in the hoop (outside surface) and longitudinal directions of a JTA-10 composite cylinder are shown in Figure 50. It should be noted that (at the same pressure) the longitudinal strain is about the same as the hoop strain for JTA composites, because of the highly anisotropic properties of this material. For an aluminum cylinder, which is much more isotropic than JTA composite, the longitudinal strain is about 0.2 of the hoop strain (at the same pressure) in the elastic range and considerably smaller in the plastic range.
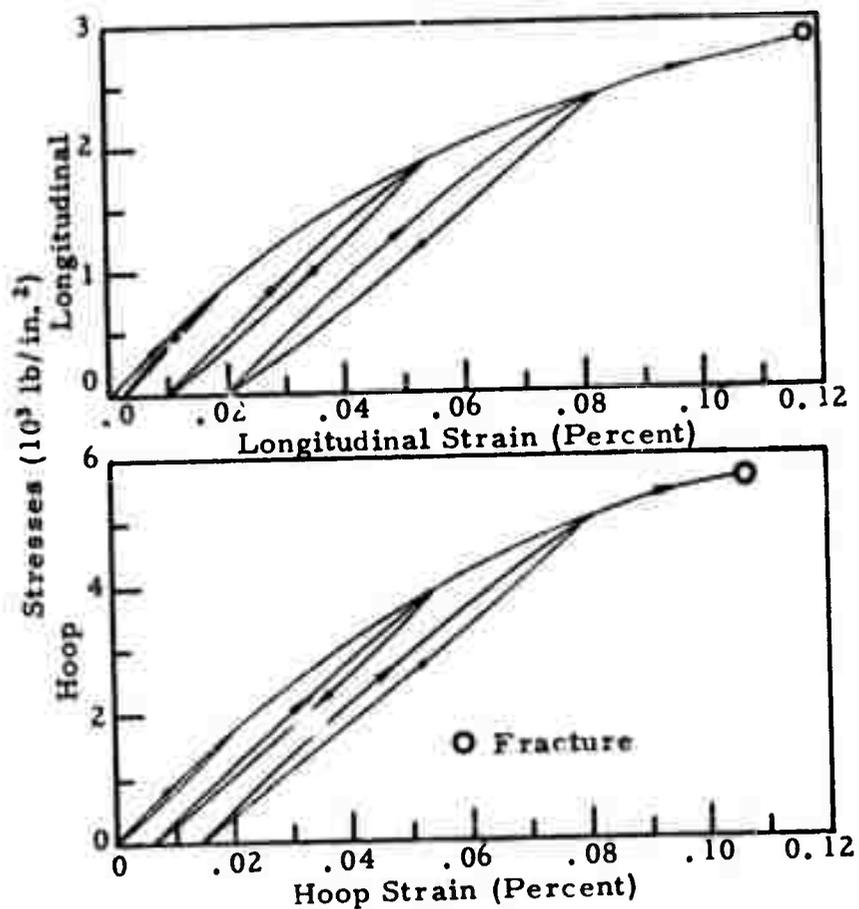
N-9607

Figure 50. Longitudinal and Outside Hoop Stress-Strain Curves for JTA-10 Composite Cylinder under Internal Pressure.

The fracture stresses and strains for JTA-composite cylinders tested under internal pressure were calculated with Equations V E-1 to V E-3 by using the internal pressure at fracture and the measured outside fracture strain. The results are given in Table VII. These fracture properties are

TABLE VII

FRACTURE STRESS AND STRAIN OF JTA COMPOSITE
CYLINDERS UNDER INTERNAL PRESSURE

| Specimen | Stress (lb/in.^{2}) | | Strain (μ in./in.) | |
	Inside Hoop σ_{u1}	Longitudinal σ_{u3}	Inside Hoop ϵ_{u1}	Longitudinal ϵ_{u3}
JTA-9-1	8030	3600	2020	1850
JTA-9-2	7530	3440	1900	1200
JTA-10-1	6260	2830	1250	1170

plotted on the two-dimensional fracture surfaces for JTA composites shown in Figures 51 and 52. The uniaxial properties in tension and compression

Unit: 10^3 lb/in.^{2}
O = JTA-9 Billet
● = JTA-9 Billet Tested in Hoop Tensile Stress
Δ = JTA-10 Billet
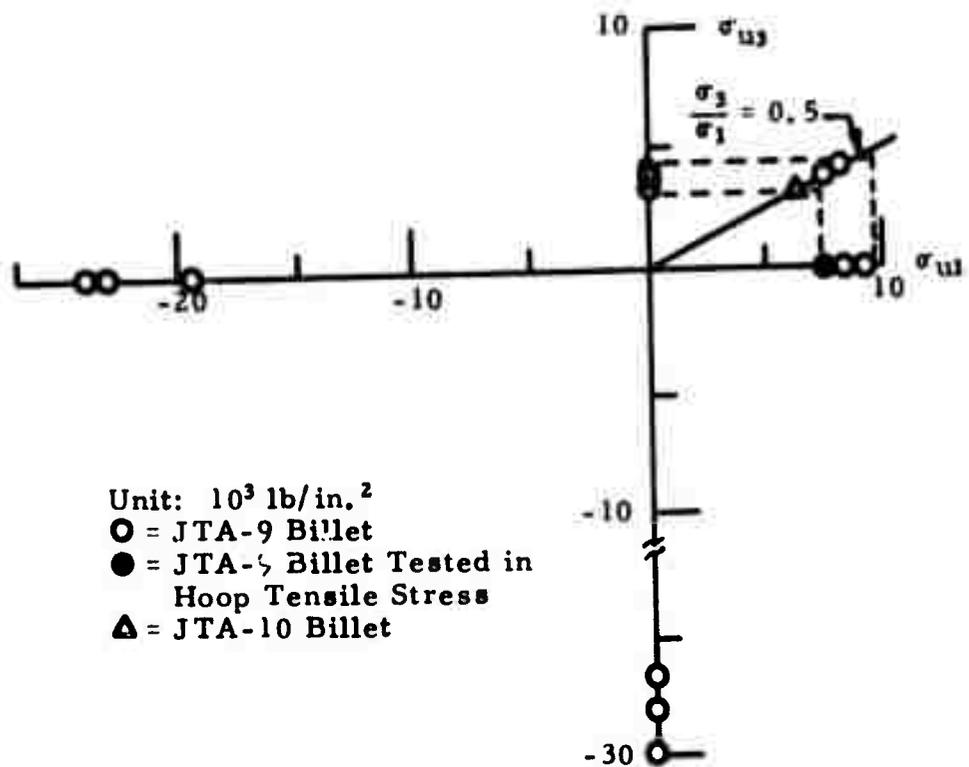
N-9604

Figure 51. Fracture-Stress Surface for JTA Composites.
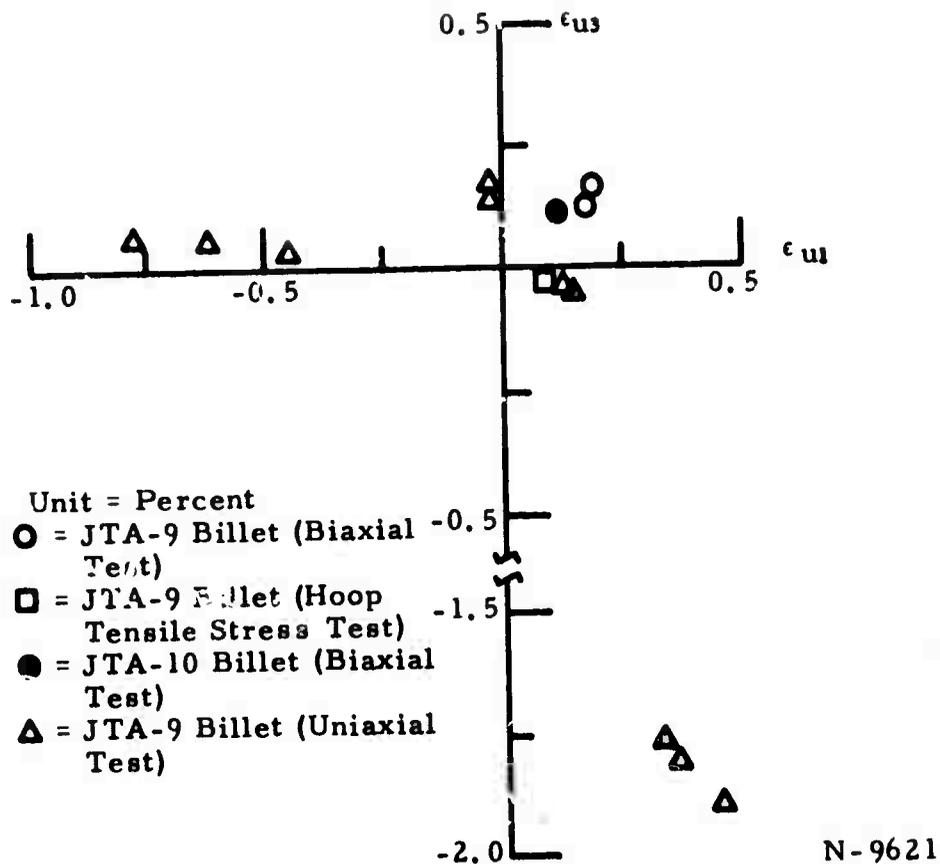
Figure 52. Fracture-Strain Surface for JTA Composites.

in Figures 51 and 52 were measured on samples from the JTA-9 billet, and the shaded circles are the results obtained by the hoop tensile stress test on a JTA-9 cylinder. These preliminary results indicate that the fracture criterion of JTA composites in the tension-tension stress state may be the maximum stress theory of failure.

Figure 53 shows one of the JTA-9 cylinders after fracture resulting from internal pressure. Inspection of the fractured specimens failed to reveal whether the initial fracture was due to the hoop or the axial stress. The irregular fracture surface may be due to the fact that the stresses in the cylinder, just prior to fracture, were approaching simultaneously the uniaxial tensile strengths in both the hoop and axial directions, since the stress ratio σ_z/σ_θ in the cylinder is 0.5 and the uniaxial tensile strength ratio σ_{u3}/σ_{u1} of JTA composites is approximately 0.4. Examination of the fracture stress surface in Figure 51 indicates that fracture of the cylinder was more likely initiated by the axial stress.

c. Internal Pressure with an Axial Compressive Load Test. The aluminum cylinder which was used for examination of strain distribution under internal pressure has been tested under internal pressure plus axial

-93-

Figure 53. JTA-9 Composite Cylinder Fractured under
Internal Pressure.

compressive loading. The bending moment produced by misalignment under
a compression load has been practically eliminated by means of the special
load cell with a sliding bearing which was described earlier. In order to
examine the performance of the test machine and to gain some experiences
for later tests with JTA and fiber composites, the aluminum cylinder was
loaded to the desired stress states using various loading sequences. The
satisfactory performance of the test machine has been demonstrated by
the excellent agreement between the experimental and theoretical strains at
all the stress states, regardless of the loading path. Several ATJ graphite
cylinders have been prepared for testing in order to examine the effect of
the loading sequence on fracture stresses in a nonconservative material.

F. Analysis and Synthesis of Three Layer Cylinder
(Professor Schmit and Mr. V. Genberg, Case Institute)

1. Introduction

An axially infinite three layered thick walled cylinder (see Figure 54) was chosen as a representative component which will exhibit many behavior characteristics found in certain high temperature nozzle inserts. The cylinder is subjected to high thermal and pressure loading on its inner surface. Each of the three layers is treated as cylindrically orthotropic material whose thermal and mechanical properties are assumed to have a known temperature dependence. The preassigned parameters are the internal radius (r_a) and the temperature dependent material properties. The individual layer thicknesses (D_1, D_2, D_3) are the design variables (see Figure 54). Each of several distinct load conditions is specified by giving the internal ($p_a(t)$) and external pressure ($p_d(t)$) as well as the internal ($T_{-1}(t)$) and external temperature ($T_{-3}(t)$) or, alternatively, the heating rate at the inner surface ($q(t)$). Failure modes to be guarded against in each load condition include temperature and radial displacement limits as well as failure under combined stress. The objective function for the synthesis is minimization of the weight per unit length of the cylinder.

2. Thermal Analysis

For any particular trial design (D_1, D_2, D_3) the thermoelastic analysis is carried out in two steps. First the transient heat conduction problem neglecting mechanical coupling is solved. Then using the temperature distribution, the thermal stress analysis is carried out neglecting inertia effects.

It is assumed that the thermal and pressure loading are axisymmetric and uniform along the axis (z), thereby reducing the transient heat conduction analysis to a one-dimensional problem governed by the following partial differential equation

$$\rho c \frac{\partial T}{\partial t} = \frac{1}{r} \frac{\partial}{\partial r} \left(k r \frac{\partial T}{\partial r} \right) \qquad \text{(V F-1)}$$

in which the temperature $T(r,t)$ is the dependent variable, the time t and the radial position r are independent variables, and the density ρ, the heat capacity c, and the thermal conductivity k are the pertinent material properties. This one-dimensional equation is non-linear due to the temperature dependence of the heat capacity and the thermal conductivity.
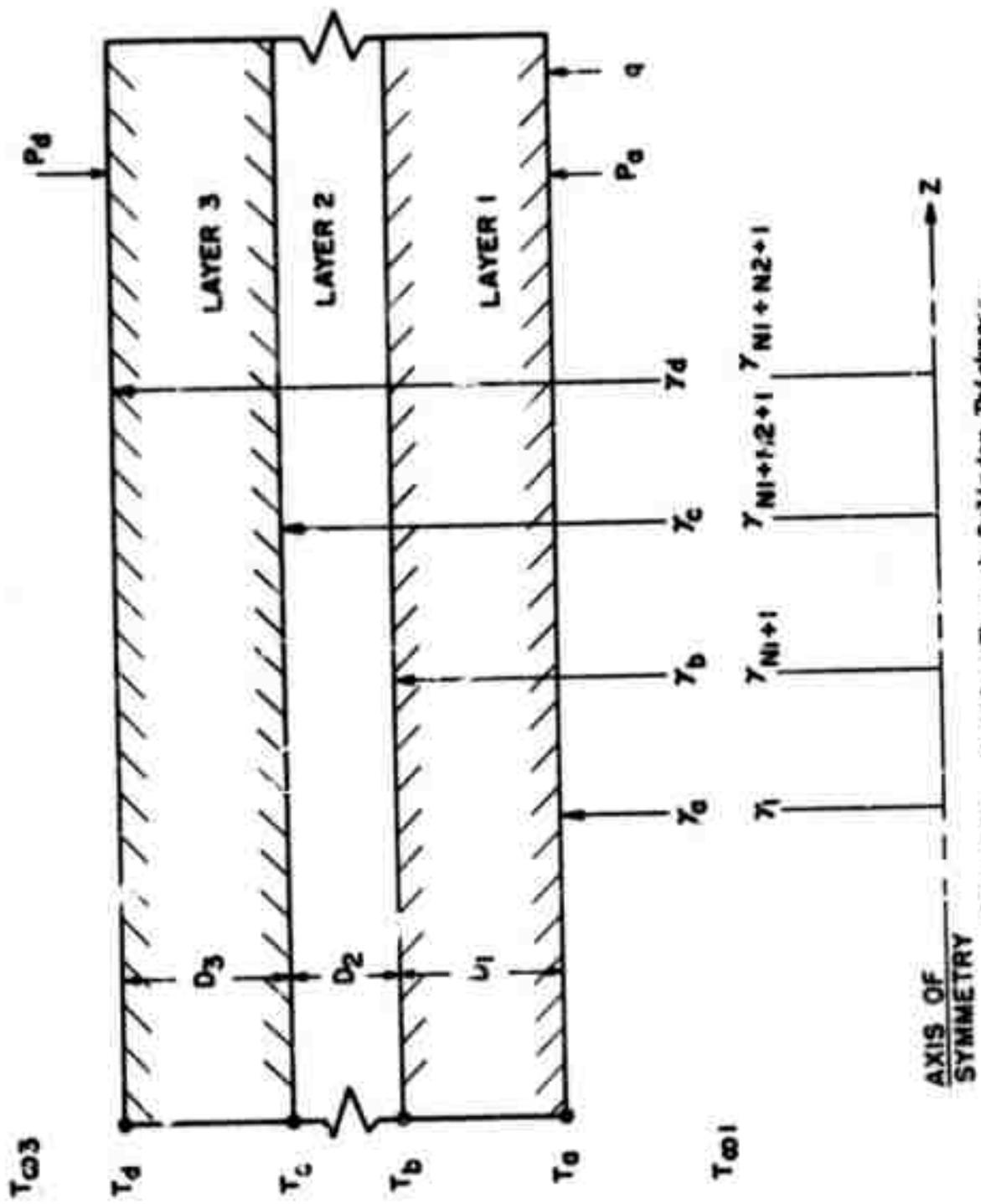
Figure 54. Section Thru 4 Cylinder Thickness.

The initial condition is assumed to be a uniform temperature distribution (T_0). The thermal boundary conditions are general enough to permit a prescribed time varying heat flux input, a convection heating input on the inner surface (r_a), as well as convection cooling and reradiation cooling on the outer surface $(r_d = r_a + D_1 + D_2 + D_3)$

$$- k \left. \frac{\partial T}{\partial r} \right|_{r=r_a} = q(t) + h_{c1} (T_{\infty 1} - T_a) \qquad (V F-2)$$

$$- k \left. \frac{\partial T}{\partial r} \right|_{r=r_d} = \sigma Fe (T_d^4 - T_{\infty 3}^4) + h_{c3} (T_d - T_{\infty 3}) \qquad (V F-3)$$

Perfect thermal contact is assumed at the interface between layers, thereby requiring both the temperature and the heat flux to be continuous across the interfaces at $r_b = r_a + D_1$ and $r_c = r_a + D_1 + D_2$.

$$T_b^{(1)} = T_b^{(2)} \qquad\qquad k_b^{(1)} \left. \frac{\partial T^{(1)}}{\partial r} \right|_b = k_b^{(2)} \left. \frac{\partial T^{(2)}}{\partial r} \right|_b \qquad (V F-4)$$

$$T_c^{(2)} = T_c^{(3)} \qquad\qquad k_c^{(2)} \left. \frac{\partial T^{(2)}}{\partial r} \right|_c = k_c^{(3)} \left. \frac{\partial T^{(3)}}{\partial r} \right|_c \qquad (V F-5)$$

The nonlinear transient heat conduction problem can be cast in finite difference form for numerical solution on a high speed digital computer. The implicit finite difference formulation was chosen over the explicit form since the implicit form is not limited to small time increments by the stability criterion. According to Forsythe and Wasow (Reference 24) the implicit form is faster than the explicit if the implicit time interval is at least four times as large as the explicit interval.

If the number of subdivisions in layers 1, 2, and 3 are N1, N2, and N3 respectively (see Figure 55), then the total number of nodes is NT+1 where

$$NT = N1 + N2 + N3 \qquad (V F-6)$$
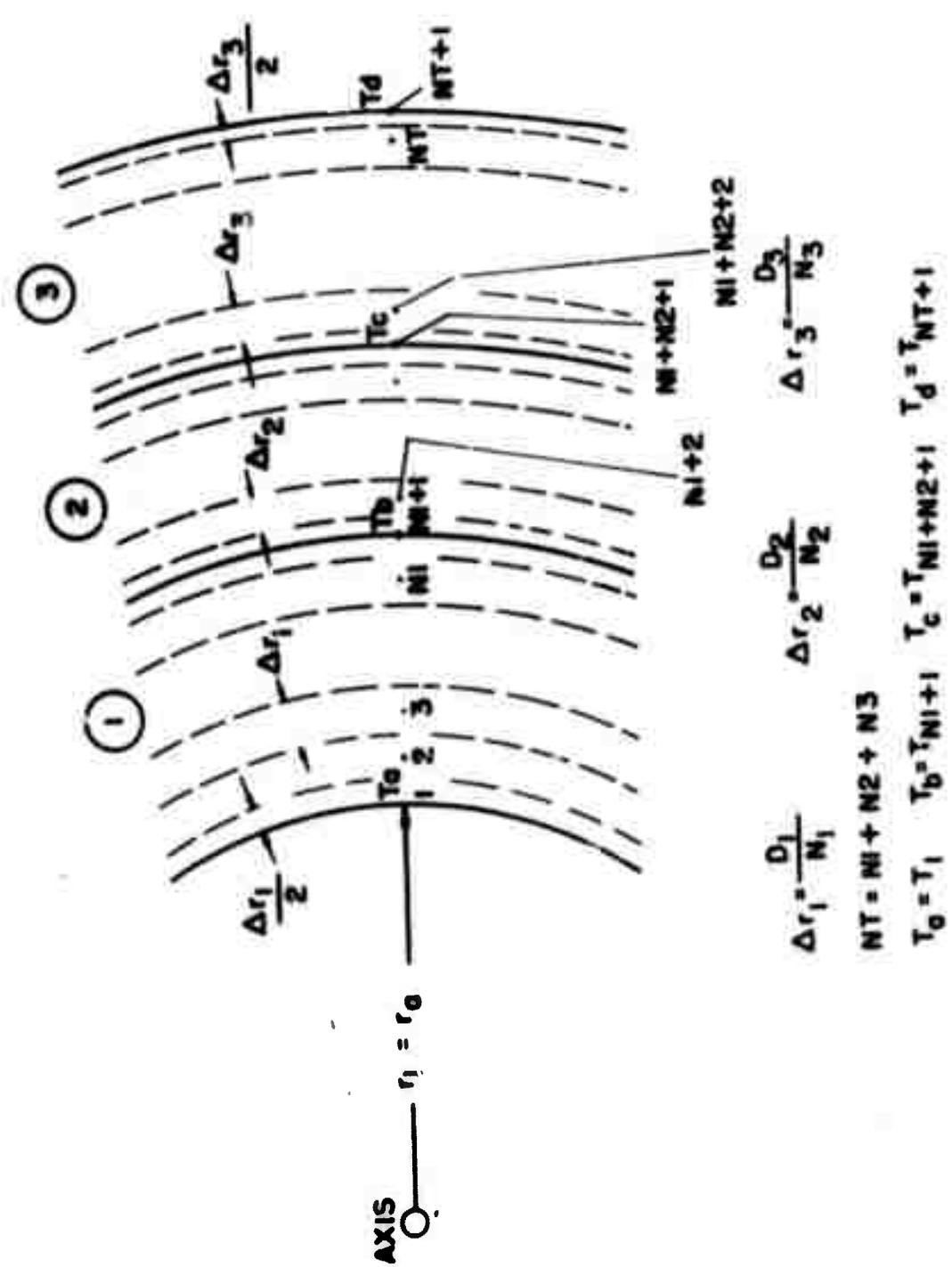
Figure 55. Finite Difference Stations.

For each node there is an equation of the form

$$A_j \, X_{j-1} + B_j \, X_j + C_j \, X_{j+1} = D_j \qquad \text{(V F-7)}$$

This tridiagonal system of equations can be solved efficiently by a modified Gauss elimination procedure (Reference 24).

3. Stress Analysis

At any particular time increment the temperature is known at a discrete set of mesh points radially through the thickness of the cylinder. The stress analysis then determines the stress state for a given temperature distribution over the same set of mesh points. The stress function technique (see Reference 25) can be extended to accomplish this purpose. Based on the assumption of axisymmetric, axially uniform behavior and the additional assumption that cross sections of the cylinder remain plane, it can be reasoned that $\tau_{r\theta} = \tau_{\theta z} = \tau_{zr} = 0$, $\gamma_{r\theta} = \gamma_{\theta z} = \gamma_{zr} = 0$, and $\varepsilon_z = $ constant. The remaining quantities of interest are σ_r, σ_θ, σ_z, ε_r, ε_θ and u which are all functions of the radial position, r.

The radial equilibrium equation reduces to

$$\frac{d\,\sigma_r}{dr} + \frac{\sigma_r - \sigma_\theta}{r} = 0 \qquad \text{(V F-8)}$$

which is identically satisfied by defining the stresses in terms of a stress function ϕ as follows

$$\sigma_r = \frac{\phi}{r} , \qquad \qquad \sigma_\theta = \frac{d\phi}{dr} \qquad \text{(V F-9)}$$

The pertinent compatability equation is

$$\varepsilon_r = \varepsilon_\theta + r \frac{d\,\varepsilon_\theta}{dr} \qquad \text{(V F-10)}$$

and the stress-strain-temperature relation for the cylindrically orthotropic elastic material is given by

$$
\left\{
\begin{array}{c}
\epsilon_r \\
\epsilon_\theta \\
\epsilon_z
\end{array}
\right\}
=
\left[
\begin{array}{ccc}
1/E_r & -\nu_{r\theta}/E_\theta & -\nu_{rz}/E_z \\
-\nu_{\theta r}/E_r & 1/E_\theta & -\nu_{\theta z}/E_z \\
-\nu_{zr}/E_r & -\nu_{z\theta}/E_\theta & 1/E_z
\end{array}
\right]
\left\{
\begin{array}{c}
\sigma_r \\
\sigma_\theta \\
\sigma_z
\end{array}
\right\}
+ \Delta T
\left\{
\begin{array}{c}
\alpha_r \\
\alpha_\theta \\
\alpha_z
\end{array}
\right\}
$$

<div align="right">(V F-11)</div>

where it is understood that

$$
\frac{\nu_{r\theta}}{E_\theta} = \frac{\nu_{\theta r}}{E_r}, \qquad
\frac{\nu_{\theta z}}{E_z} = \frac{\nu_{z\theta}}{E_\theta}, \qquad
\frac{\nu_{zr}}{E_r} = \frac{\nu_{rz}}{E_z}
$$

Using Equations (V F-9) through (V F-11) the compatability equation in terms of the stress function ϕ and the undetermined constant strain ϵ_z is found to be

$$
\frac{1}{E_r} [1 + \nu_{\theta r} + (\nu_{\theta z} - \nu_{rz}) \nu_{zr}] \frac{\phi}{r}
$$

$$
- \frac{1}{E_\theta} [1 + \nu_{r\theta} - (\nu_{\theta z} - \nu_{rz}) \nu_{z\theta}] \frac{d\phi}{dr}
$$

<div align="right">(V F-12)</div>

$$
+ (\nu_{\theta z} - \nu_{rz}) \epsilon_z + [\alpha_r - \alpha_\theta - (\nu_{\theta z} - \nu_{rz}) \alpha_z] \Delta T =
$$

$$
r \frac{d}{dr} \left[\frac{(1 - \nu_{\theta z} \nu_{z\theta})}{E_\theta} \frac{d\phi}{dr} - \frac{(\nu_{\theta r} + \nu_{\theta z} \nu_{zr})}{E_r} \frac{\phi}{r} - \nu_{\theta z} \epsilon_z + (\nu_{\theta z} \alpha_z + \alpha_\theta) \Delta T \right]
$$

The above equation can be cast in implicit finite difference form to obtain equations of the following form which can be solved efficiently by a modified Gauss elimination.

$$A_j \, \phi_{j-1} + B_j \, \phi_j + C_j \, \phi_{j+1} = D_j \, \epsilon_z + E_j \qquad (V \ F-13)$$

If the value of ϵ_z is known, the system of equations reduces to a tridiagonal system. An initial guess is made for ϵ_z. The solution is then obtained by iteration on ϵ_z, since the estimated value of ϵ_z can be improved after each solution of the tridiagonal system by using the requirement that the resultant axial force on a cross section must vanish

$$2\pi \left[\sum_{j=2}^{NT} \sigma_{z,j} \, r_j \, \Delta r + \sigma_{z,1} \, r_1 \, \frac{\Delta r}{2} + \sigma_{z,NT+1} \, r_{NT+1} \, \frac{\Delta r}{2} \right] = 0$$

$$(V \ F-14)$$

The boundary conditions require that the radial stress equal the negative of the applied pressure at the inner and outer surface.

$$\sigma_{ra} = - \, P_a \, , \qquad \qquad \sigma_{rd} = - \, P_d \qquad (V \ F-15)$$

At each interface the radial stress and displacement in the adjacent layers must be equal.

$$\sigma_{rb}^{(1)} = \sigma_{rb}^{(2)} \qquad \qquad \sigma_{rc}^{(2)} = \sigma_{rc}^{(3)} \qquad (V \ F-16)$$

$$u_b^{(1)} = u_b^{(2)} \qquad \qquad u_c^{(2)} = u_c^{(3)} \qquad (V \ F-17)$$

4. Numerical Evaluation of Analysis

To date both the thermal and stress analyses have been programmed in Algol 60 for use on a Univac 1107 computer. The results for one layered isotropic and orthotropic cylinders agree with results in the literature.

For a cylinder with 40 nodes, the temperature distribution for a single time interval can be determined in 0.4 seconds. Thus, for a 100 second (real time) load condition, an accurate temperature distribution with 10 second intervals requires 4 seconds (machine time). For a given temperature distribution, the stress state over the 40 nodes can be determined in 1 second of machine time. Based on past experience it is estimated that by translating the analysis programs into FORTRAN IV compiler language running times will be reduced by a factor of five. Clearly the repeated cycles of analysis, design modification and reanalysis will be feasible for this problem because the analysis run times are not excessive.

-101-

5. Constraints

The side constraints place upper and lower limits on each layer thickness as determined by fabrication processes and other requirements. Behavior constraints include temperature upper limits for each layer, a radial displacement upper limit, and failure under combined stress. The combined stress state at any point at any time in this problem (σ_r, σ_θ, σ_z) is known as a result of the thermal and stress analyses. An interaction formula of the following form will be employed to guard against failure.

$$\frac{\sigma_r^2}{S_r^2} + \frac{\sigma_\theta^2}{S_\theta^2} + \frac{\sigma_z^2}{S_z^2} - K_{r\theta}\frac{\sigma_r \sigma_\theta}{S_r S_\theta} - K_{\theta z}\frac{\sigma_\theta \sigma_z}{S_\theta S_z} - K_{zr}\frac{\sigma_z \sigma_r}{S_z S_r} \leq 1 \qquad \text{(V F-18)}$$

The form of this expression is consistent with the generalized distortion energy failure criterion (see Reference 14) but permits the use of different uniaxial strength values (S_r, S_θ, S_z) depending upon whether the corresponding stress component (σ_r, σ_θ, σ_z) is tension or compression. The coefficients ($K_{r\theta}$, $K_{\theta z}$, K_{zr}) can be determined experimentally from biaxial tests or they can be estimated on a theoretical basis (see Reference 14) using the elastic constants of the material. For the special case of an isotropic material with uniaxial strength values identical in tension and in compression, these coefficients ($K_{r\theta}$, $K_{\theta z}$, K_{zr}) reduce to unity.

6. Synthesis

With the analysis completed and the constraints identified the structural synthesis problem for the three layer cylinder can be undertaken. The objective will be to find a design that minimizes the weight per unit length of the system while satisfying the constraints placed on the system. The weight per unit length can be expressed as follows:

$$W = \pi (r_b^2 - r_a^2) \rho_1 + (r_c^2 - r_b^2) \rho_2 + \pi(r_d^2 - r_c^2) \rho_3 \qquad \text{(V F-19)}$$

where

$$r_b = r_a + D_1; \quad r_c = r_a + D_1 + D_2; \quad r_d = r_a + D_1 + D_2 + D_3$$

Initially only the layer thicknesses D_1, D_2, and D_3 will be treated as design variables. The synthesis technique to be employed will be a sequential process in design space of the type

-102-

$$\vec{D}^{q+1} = \vec{D}^q + \alpha_q \vec{S}^q \qquad\qquad (V\ F\text{-}20)$$

where the superscript q designates the current design, the superscript $q+1$ denotes the next trial design in the sequence, $\vec{D}$ represents a design vector, α the step length, and $\vec{S}$ the direction of travel for the design modification. In putting together a synthesis technique for the three layer cylinder problem some of the preprogrammed procedures discussed in Section IX B will be drawn upon.

G. Analysis and Synthesis of Flat Plate
(Professor Schmit and Mr. C. Chamis, Case Institute)

1. Introduction

A flat simply supported orthotropic rectangular panel (See Figure 56) was chosen as a second simple representative component. This system exhibits several important structural behavior characteristics such as bending, buckling, multiaxial stress states, and thermal stress response. The loadings on this panel include thermal inputs on the exposed surface [for example q(t)], transverse pressure loading (p) and in plane membrane forces (N_x, N_y, and N_{xy}). The planform dimensions of the plate (a,b) are preassigned parameters and initially the material of the plate will also be preassigned. When the material is preassigned, the temperature dependent thermal and mechanical properties of the plate are assumed to be known. Initially then the design variables are the plate thickness h and the angle θ orienting the material axes (1,2) with respect to the planform axes of the plate (x,y). Failure modes to be guarded against in each load condition include temperature and transverse displacement limits as well as failure under combined stress. The objective of the structural synthesis is taken to be minimization of the total weight of the plate.

The analysis of the panel consists of three parts; the transient temperature distribution solution, the displacement response and the stress analysis. The thermal analysis is carried out using the one dimensional heat conduction equation including temperature dependent thermal properties. The transient temperature response through the thickness of the plate is obtained using an implicit finite difference solution technique. The displacement analysis is based on small deflection elastic thin plate theory. The basic field equation is a vertical equilibrium equation in terms of the unknown transverse displacement w(x,y). The series expansion selected to represent the transverse displacement w(x,y) approximately, satisfies the imposed boundary conditions (namely, that w(x,y) = 0 on all four simply supported edges). The field equation subject to the natural boundary conditions (namely, M = 0 on all four simply supported edges) is solved approximately by applying the generalized Galerkin method which yields a system of linear simultaneous equations. Solution of this system of simultaneous equations gives the values of the coefficients in the series expansion for w(x,y) and hence an approximate functional expression for the transverse displacement pattern of the plate. The stress analysis is based on the stress displacement relations and the end result essentially expresses the stresses in terms of the applied temperature distribution, the applied in-plane forces, and the applied transverse load distribution.

2. Thermal Analysis

The flat plate is assumed to be exposed to heating conditions that are uniform over the planform (that is, with respect to x and y). The transient temperature response of the plate is therefore essentially one dimensional (through the thickness of the plate). The partial differential equation
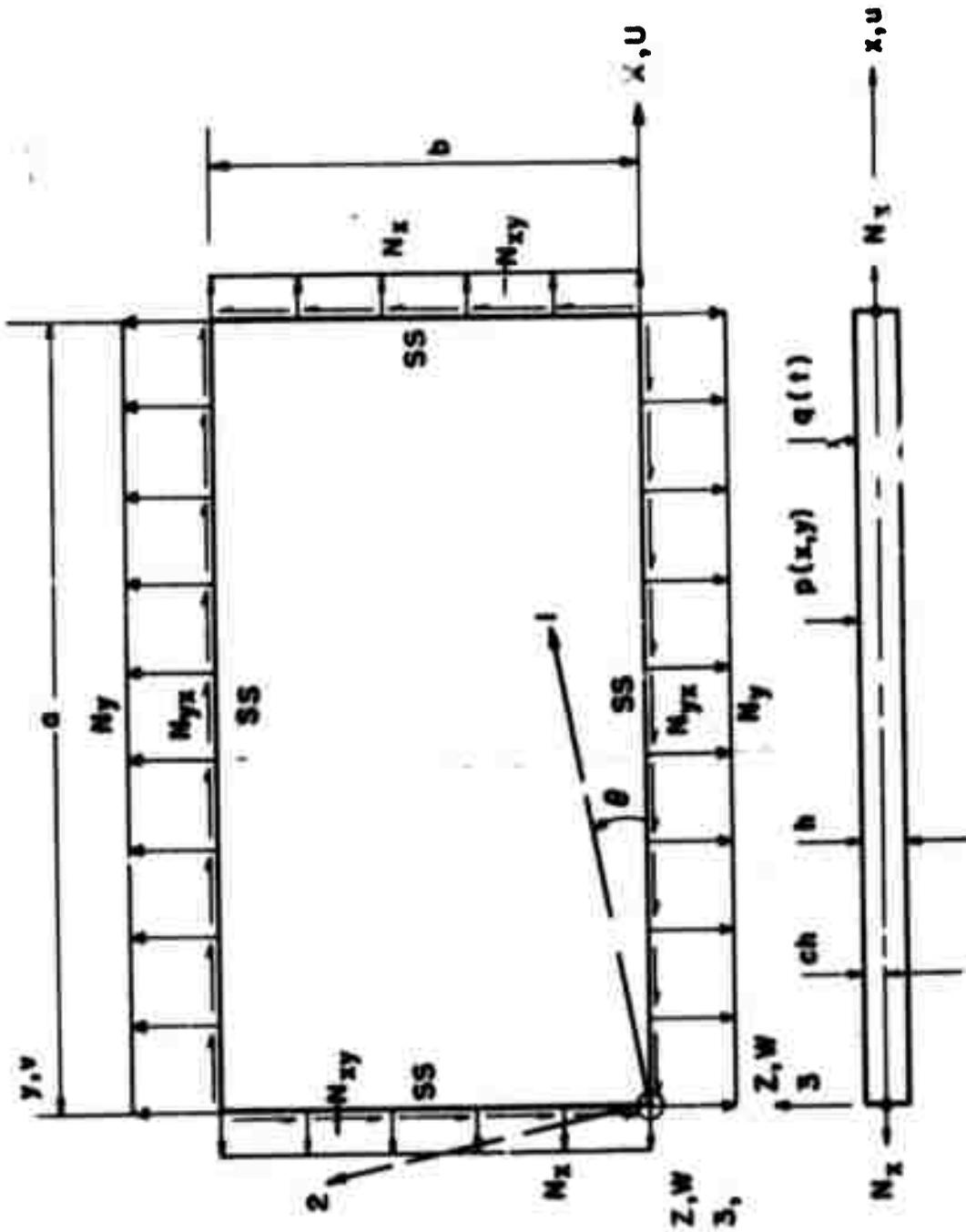
Figure 56. Schematic of Flat Plate.

governing this temperature response is

$$\frac{\partial}{\partial \bar{z}} \left(k \frac{\partial T}{\partial \bar{z}} \right) = \rho c \frac{\partial T}{\partial t} \qquad (V\ G-1)$$

in which $T(\bar{z}, t)$ is the dependent temperature variable; the time t and the position $\bar{z}$ (see Figure 57) are independent variables; and the density ρ, the heat capacity c and the thermal conductivity k are the pertinent material properties. The boundary condition at the exposed surface of the plate $\bar{z} = 0$ is quite general and permits a variety of options with respect to the kind of thermal loading that can be dealt with. This boundary condition is

$$T(0, t) = T_p(t) \qquad (V\ G-2)$$

where $T_p(t)$ designates the prescribed temperature at the surface as a function of time or

$$- k \frac{\partial T}{\partial \bar{z}} (0, t) = q(t) + \bar{h}_c [T_{aw} - T(0, t)] - \sigma\epsilon[T^4(0, t) - T_\infty^{\ 4}] + \alpha_s\ G_s\ A_p$$
$$(V\ G-3)$$

where q(t) designates a prescribed heat flux input as a function of time; the second term permits consideration of convective heating or cooling, the third term permits consideration of reradiation cooling, and the fourth term provides for solar heating. The boundary condition on the unexposed surface is assumed to be

$$\frac{\partial T}{\partial \bar{z}} (h, t) = 0 \qquad (V\ G-4)$$

which imposes a condition of zero heat loss from the unexposed surface at $\bar{z} = h$.

This nonlinear transient heat conduction problem has been cast in finite difference form for numerical solution on a high speed digital computer. The implicit finite difference formulation was chosen over the explicit because it is not limited to small time increments by a stability criterion. As previously noted (Section V F2), the implicit method will be more efficient provided the time intervals employed are at least four times larger than the time intervals required to satisfy the stability criterion when using the explicit formulation.

If the thickness of the plate is subdivided into n-1 layers of equal thickness $(\Delta \bar{z} = \frac{h}{n-1})$ then the total number of nodes at which the temperature is evaluated will be n. For each node there is an equation of the form shown in Equation V F-7. As note previously a tridiagonal system of equations can be solved efficiently using a modified Gauss elimination procedure.
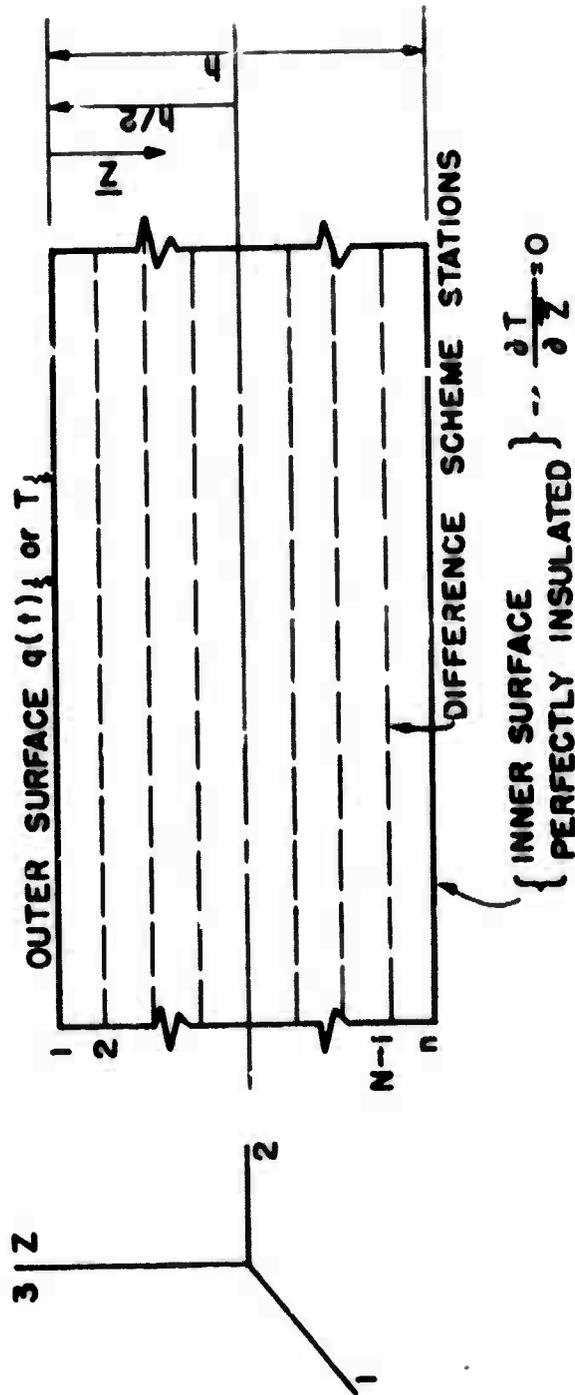
Figure 57. Section Through Flat Plate's Thickness.

3. Displacement Analysis

The vertical equilibrium equation for an arbitrary element of the plate shown in Figure 56 can be written as follows:

$$\frac{\partial^2 M_x}{\partial x^2} - 2\frac{\partial M_{xy}}{\partial x \partial y} + \frac{\partial^2 M_y}{\partial y^2} + N_x \frac{\partial^2 w}{\partial x^2} + 2N_{xy}\frac{\partial^2 w}{\partial x \partial y} + N_y \frac{\partial^2 w}{\partial y^2} + p = 0 \quad (V\ G\text{-}5)$$

where the transverse load p is taken positive in the positive z direction (i.e. upward) and the sign convention and force resultant definitions are given in Figures 58 and 59. This expression takes into account the influence of the inplane force system on the behavior of the plate and it is independent of the orthotropic character of the plate material. The stress-strain temperature relations for the plate in the orthotropic material axis system (1,2,3) is written as follows:

$$\left\{\begin{array}{c} \varepsilon_{11} \\ \varepsilon_{22} \\ \gamma_{12} \end{array}\right\} = \begin{bmatrix} \dfrac{1}{E_{11}} & -\dfrac{\nu_{12}}{E_{22}} & 0 \\ -\dfrac{\nu_{21}}{E_{11}} & \dfrac{1}{E_{22}} & 0 \\ 0 & 0 & \dfrac{1}{E_{12}} \end{bmatrix} \left\{\begin{array}{c} \sigma_{11} \\ \sigma_{22} \\ \tau_{12} \end{array}\right\} + \Delta T \left\{\begin{array}{c} \alpha_{11} \\ \alpha_{22} \\ 0 \end{array}\right\}$$

$$(V\ G\text{-}6)$$

or more briefly

$$\{\varepsilon\}_m = [E]_m^{-1} \{\sigma\}_m + \Delta T \{\alpha\}_m \quad (V\ G\text{-}7)$$

where the definitions of the matrices are implied by comparing Equation V G-6 with Equation V G-7. The stresses in terms of the strains and the temperature increment are expressed as follows:

$$\{\sigma\}_m = [E]_m \left\{ \{\varepsilon\}_m - \Delta T \{\alpha\}_m \right\} \quad (V\ G\text{-}8)$$

where
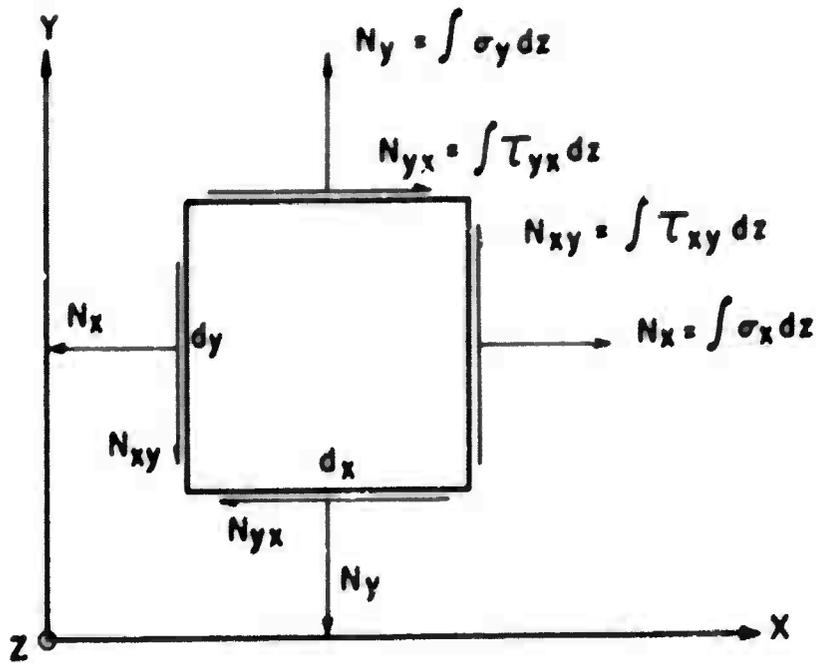
Figure 58. Membrane Force Resultants.
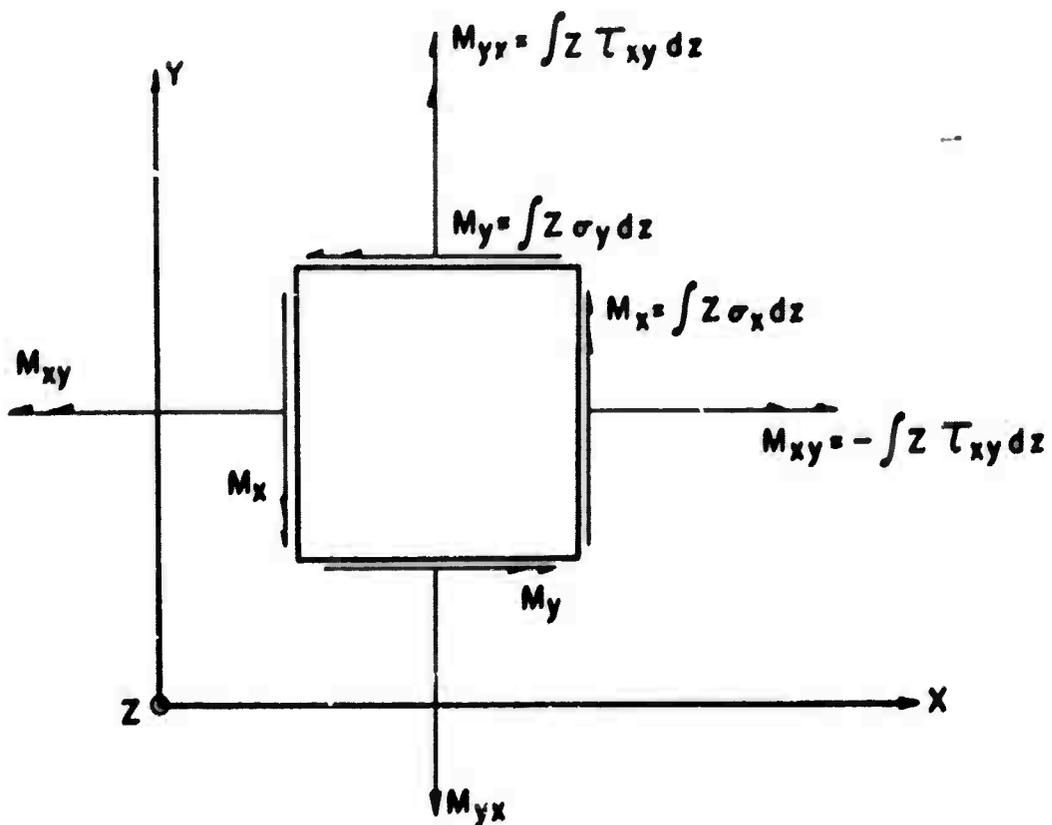
Figure 59. Bending Force Resultants.

$$[E]_m = \begin{bmatrix} \dfrac{E_{11}}{(1-\nu_{12}\nu_{21})} & \dfrac{\nu_{12} E_{11}}{(1-\nu_{12}\nu_{21})} & 0 \\[4mm] \dfrac{\nu_{21} E_{22}}{(1-\nu_{12}\nu_{21})} & \dfrac{E_{22}}{(1-\nu_{12}\nu_{21})} & 0 \\[4mm] 0 & 0 & E_{12} \end{bmatrix} \qquad (V\ G\text{-}9)$$

The strains in the orthotropic material axis system (1,2,3) can be expressed in terms of the strains in the planform coordinate system of the structure (x,y,z) as follows:

$$\begin{Bmatrix} \epsilon_{11} \\[3mm] \epsilon_{22} \\[3mm] \gamma_{12} \end{Bmatrix} = \begin{bmatrix} \cos^2\theta & \sin^2\theta & \tfrac{1}{2}\sin 2\theta \\[3mm] \sin^2\theta & \cos^2\theta & -\tfrac{1}{2}\sin 2\theta \\[3mm] -\sin 2\theta & \sin 2\theta & \cos 2\theta \end{bmatrix} \begin{Bmatrix} \epsilon_{xx} \\[3mm] \epsilon_{yy} \\[3mm] \gamma_{xy} \end{Bmatrix} \qquad (V\ G\text{-}10)$$

or more briefly

$$\{\epsilon\}_m = [R]\,\{\epsilon\}_s \qquad (V\ G\text{-}11)$$

where the definitions of the matrices are implied by comparing Equation V G-10 with Equation V G-11. The stresses in the planform coordinate system of the structure (x,y,z) may be expressed in terms of the stresses in the orthotropic material axis system (1,2,3) as follows:

$$
\left\{ \begin{array}{c} \sigma_{xx} \\ \sigma_{yy} \\ \tau_{xy} \end{array} \right\} = \left[\begin{array}{ccc} \cos^2\theta & \sin^2\theta & -\sin 2\theta \\ \sin^2\theta & \cos^2\theta & +\sin 2\theta \\ \frac{1}{2}\sin 2\theta & -\frac{1}{2}\sin 2\theta & +\cos 2\theta \end{array} \right] \left\{ \begin{array}{c} \sigma_{11} \\ \sigma_{22} \\ \tau_{12} \end{array} \right\}
\qquad \text{(V G-12)}
$$

or more briefly

$$
\{\sigma\}_s = [R]^T \{\sigma\}_m
\qquad \text{(V G-13)}
$$

The small deflection strain-displacement relations expressed in the planform coordinate system of the structure (x,y,z) are

$$
\left\{ \begin{array}{c} \epsilon_{xx} \\ \epsilon_{yy} \\ \tau_{xy} \end{array} \right\} = \left\{ \begin{array}{c} \dfrac{\partial u}{\partial x} \\[2mm] \dfrac{\partial v}{\partial y} \\[2mm] \dfrac{\partial u}{\partial y} + \dfrac{\partial v}{\partial x} \end{array} \right\} - z \left\{ \begin{array}{c} \dfrac{\partial^2 w}{\partial x^2} \\[2mm] \dfrac{\partial^2 w}{\partial y^2} \\[2mm] 2\dfrac{\partial^2 w}{\partial x\, \partial y} \end{array} \right\}
\qquad \text{(V G-14)}
$$

or more briefly

$$
\{\epsilon\}_s = \{\epsilon\}_s - z \{\kappa\}_s
\qquad \text{(V G-15)}
$$

where the definitions of the column matrices are implied by comparing Equation V G-14 with Equation V G-15. The bending force resultants M_x, M_{xy} and M_y can be shown to depend upon the displacements in the following manner

$$
\{M\}_s = - [R]^T [D] [R] \{\kappa\}_s - [R]^T \{M_T\}_m
\qquad \text{(V G-16)}
$$

-111-

where

$$\{M\}_s = \left\{ \begin{array}{c} M_x \\ \\ M_y \\ \\ -M_{xy} \end{array} \right\} \; ; \qquad \{M_T\}_m = \left\{ \begin{array}{c} \displaystyle\int z \; \frac{\Delta T \; E_{11}}{(1-\nu_{12}\nu_{21})} \; (a_{11} + \nu_{12}a_{22}) \; dz \\ \\ \displaystyle\int z \; \frac{\Delta T \; E_{22}}{(1-\nu_{12}\nu_{21})} \; (a_{22} + \nu_{21}a_{11}) \; dz \\ \\ 0 \end{array} \right\}$$

(V G-17)

and

$$[D] = \left[\begin{array}{ccc} \displaystyle\int z^2 \; \frac{E_{11}}{(1-\nu_{12}\nu_{21})} \; dz & \displaystyle\int z^2 \; \frac{\nu_{12} \; E_{11}}{(1-\nu_{12}\nu_{21})} \; dz & 0 \\ \\ \displaystyle\int z^2 \; \frac{\nu_{21} \; E_{22}}{(1-\nu_{12}\nu_{21})} & \displaystyle\int z^2 \; \frac{E_{22}}{(1-\nu_{12}\nu_{21})} \; dz & 0 \\ \\ 0 & 0 & \displaystyle\int z^2 \; E_{12} \; dz \end{array} \right]$$

(V G-18)

and the other terms have been defined previously. Substituting the expressions for M_x, M_y, and M_{xy} contained in Equation V G-16 into Equation V G-5 gives the vertical equilibrium equation for an arbitrary element of the plate in terms of transverse displacement $w(x,y)$.

$$- \lfloor \cos^2\theta, \ \sin^2\theta, \ -\sin 2\theta \rfloor \ [D] \ [R] \ \begin{Bmatrix} \dfrac{\partial^4 w}{\partial x^4} \\[2em] \dfrac{\partial^4 w}{\partial x^2 \partial y^2} \\[2em] 2\dfrac{\partial^4 w}{\partial x^3 \partial y} \end{Bmatrix}$$

$$(\text{V G-19})$$

$$- 2 \lfloor \tfrac{1}{2}\sin 2\theta, \ -\tfrac{1}{2}\sin 2\theta, \ \cos 2\theta \rfloor \ [D] \ [R] \ \begin{Bmatrix} \dfrac{\partial^4 w}{\partial x^3 \partial y} \\[2em] \dfrac{\partial^4 w}{\partial x \partial y^3} \\[2em] 2\dfrac{\partial^4 w}{\partial x^2 \partial y^2} \end{Bmatrix}$$

$$- \lfloor \sin^2\theta, \ \cos^2\theta, \ \sin 2\theta \rfloor \ [D] \ [R] \ \begin{Bmatrix} \dfrac{\partial^4 w}{\partial x^2 \partial y^2} \\[2em] \dfrac{\partial^4 w}{\partial y^4} \\[2em] 2\dfrac{\partial^4 w}{\partial x \partial y^3} \end{Bmatrix}$$

$$+ N_x \frac{\partial^2 w}{\partial x^2} + 2 N_{xv} \frac{\partial^2 w}{\partial x^2} + N_y \frac{\partial^2 w}{\partial y^2} + p = 0$$

The transverse displacement $w(x,y)$ can be approximated by a series expansion of the following form

$$w(x,y) = \tilde{w}(x,y) = \sum_{n=1}^{N} \sum_{m=1}^{M} A_{mn} \sin \frac{m\pi x}{a} \sin \frac{n\pi v}{b} \qquad \text{(V G-20)}$$

Note that each of the terms in this series expansion satisfies the displacement boundary conditions exactly. Substituting the approximate representation for $w(x,y)$ [namely $\tilde{w}(x,y)$] into the left hand side of Equation V G-19 will yield a function $R(x,v)$ which is not strictly zero over the region $0 \le x \le a$, $0 \le y \le b$. The function $R(x,v)$, frequently called the residual, represents the distribution of transverse static unbalance due to the fact that $w(x,y)$ is approximate. The series expansion representing the approximate solution $w(x,v)$ does not satisfy the moment boundary conditions exactly. The moments corresponding to the approximate displacement representation $w(x,y)$ are given by the following expressions which follows from Equation V G-16 with $w(x,y)$ replaced by $\tilde{w}(x,v)$.

$$\bar{M}_x = - \lfloor \cos^2\theta \; \sin^2\theta - \sin 2\theta \rfloor \; [D] \; [R] \left\{ \begin{array}{c} \dfrac{\partial^2 \tilde{w}}{\partial x^2} \\[2ex] \dfrac{\partial^2 \tilde{w}}{\partial v^2} \\[2ex] 2\dfrac{\partial^2 \tilde{w}}{\partial x \partial y} \end{array} \right\}$$

$$- \lfloor \cos^2\theta, \; \sin^2\theta, \; - \sin 2\theta \rfloor \; \{M_T\}_m \qquad \text{(V G-21)}$$

$$\tilde{M}_y = - \lfloor \sin^2\theta \ \cos^2\epsilon \ \sin 2\theta \rfloor \ [D] \ [R] \left\{ \begin{array}{c} \dfrac{\partial^2 w}{\partial x^2} \\[12pt] \dfrac{\partial^2 w}{\partial v^2} \\[12pt] 2\dfrac{\partial^2 w}{\partial x \partial y} \end{array} \right\}$$

$$- \lfloor \cos^2\theta \ \sin^2\theta \ \sin 2\theta \rfloor \ \{M_T\}_m \qquad \text{(V G-22)}$$

Let $\bar{M}_x$ and $\bar{M}_y$ denote the prescribed edge moments on the plate (zero in this particular case). The virtual work associated with the static unbalance due to the fact that $\tilde{w}(x,y)$ is approximate can be written as follows:

$$\delta W = \int_0^b \int_0^a R(x,y) \ \delta\tilde{w} \ dxdy \ - \ \int_0^b (\bar{M}_x - \tilde{M}_x) \ \delta(\frac{\partial \tilde{w}}{\partial x}) \ dy \Bigg|_{x=a}$$

$$+ \ \int_0^b (\bar{M}_x - \tilde{M}_x) \ \delta(\frac{\partial \tilde{w}}{\partial x}) \ dy \Bigg|_{x=0}$$

$$- \ \int_0^a (M_y - \tilde{M}_y) \ \delta(\frac{\partial \tilde{w}}{\partial y}) \ dx \Bigg|_{v=b}$$

$$+ \ \int_0^a (M_y - \tilde{M}_y) \ \delta(\frac{\partial \tilde{w}}{\partial y}) \ dx \Bigg|_{y=0} \qquad \text{(V G-23)}$$

Imposing the requirement that the virtual work done by the static unbalance be zero for each independent assumed mode yields a system of (NM) simultaneous equations of the form

$$[C] \{A_{mn}\} = \{B\} \tag{V G-24}$$

which when solved for the coefficients A_{mn} yield the approximate solution for the displacement distribution (see Equation V G-20).

4. Stress Analysis

The membrane force resultants can be related to the displacements in the following manner

$$\{N\}_s = [R]^T [A] [R] \{\epsilon\}_s - [R]^T \{F_T\}_m \tag{V G-25}$$

where

$$\{N\}_s = \left\{ \begin{array}{c} N_x \\ N_y \\ N_{xy} \end{array} \right\} \quad ; \quad \{F_T\}_m = \left\{ \begin{array}{c} \int \dfrac{\Delta T \, E_{11}}{(1-\nu_{12}\nu_{21})} \, (\alpha_{11} + \nu_{12}\alpha_{22}) \, dz \\ \\ \int \dfrac{\Delta T \, E_{22}}{(1-\nu_{12}\nu_{21})} \, (\alpha_{22} + \nu_{21}\alpha_{11}) \, dz \\ \\ 0 \end{array} \right\}$$

$$\tag{V G-26}$$

and

$$[A] = \begin{bmatrix} \int \dfrac{1}{E_{11}} \, dz & - \int \dfrac{\nu_{12}}{E_{22}} \, dz & 0 \\[4mm] - \int \dfrac{\nu_{21}}{E_{11}} \, dz & \int \dfrac{1}{E_{22}} & 0 \\[4mm] 0 & 0 & \int \dfrac{1}{E_{12}} \, dz \end{bmatrix} \qquad (V\ G\text{-}27)$$

Solving for the neutral surface strains $\{\varepsilon\}_s$ from Equation V G-25 gives

$$\{\varepsilon\}_s = [R]^{-1} [A] \left\{ [R^T]^{-1} \{N\}_s + \{F_T\}_m \right\} \qquad (V\ G\text{-}28)$$

The stress at any location (x,y,z) expressed in the orthotropic material axis system can now be obtained. Rewriting Equation V G-8

$$\{\sigma\}_m = [E]_m \left\{ \{\varepsilon\}_m - \Delta T \{\alpha\}_m \right\} \qquad (V\ G\text{-}29)$$

substituting for $\{\varepsilon\}_m$ from Equation V G-11

$$\{\sigma\}_m = [E]_m \left\{ [R] \{\varepsilon\}_s - \Delta T \{\alpha\}_m \right\} \qquad (V\ G\text{-}30)$$

substituting for $\{\varepsilon\}_s$ from Equation V G-15

$$\{\sigma\}_m = [E]_m \left\{ [R] \{\varepsilon\}_s - z[R] \{\kappa\}_s - \Delta T \{\alpha\}_m \right\} \qquad (V\ G\text{-}31)$$

and replacing $\{\varepsilon\}_s$ using Equation V G-28 yields

$$\{\sigma\}_m = [E]_m \left\{ [A][R^T]^{-1} \ \{N\}_s + [A] \ \{F_T\}_m - z[R] \ \{\kappa\}_s - \Delta T \ \{\alpha\}_m \right\} \quad (V \ G-32)$$

Examining Equation V G-32 it can be observed that the first term represents the influence of the applied membrane loads on the stresses, the second term represents the influence of the thermal forces $\{F_T\}_m$, the third term

represents the influence of the displacement solution, and the last term represents the influence of the temperature distribution through the depth.

5. Numerical Evaluation of Analysis

The thermal analysis; the displacement analysis and the stress analysis previously described have all been programmed in Algol 60 for use on a Univac 1107 computer. A variety of test cases have been run and compared with independent results in the literature. The results of these test cases support the validity of the analyses. It should be noted that these test cases are for isotropic plates with temperature independent properties. Further effort will be required to check out the temperature dependent features of the thermal analysis as well as the orthotropic features of the displacement and stress analyses.

For a plate with five mesh points through the thickness, the total analysis of twelve minutes real time takes on the average fifty-six seconds, or approximately a ratio of real time to computer time of 12:1. Based on past experience it is estimated that by translating the analyses programs into Fortran IV compiler language computer times will be reduced by a factor of five. Stated differently, real time to computer time ratios of 60:1 should be attainable.

Clearly the repeated cycles of analysis, design modification and reanalysis, required for the synthesis activity, will be feasible for this problem since the analysis run times are reasonable.

6. Constraints

The side constraints place upper and lower limits on the panel thickness and on the orientation of the material axes relative to the panel axes. Behavior constraints include temperature upper limits, displacement (w) upper limits and failure under combined stress.

The combined stress state $(\sigma_{11}, \sigma_{22}, \sigma_{12})$ at any point at any time is known as a result of the thermal, displacement and stress analysis. An inter-action formula of the following form will be employed to guard against failure

$$\frac{\sigma_{11}^2}{S_{11}^2} + \frac{\sigma_{22}^2}{S_{22}^2} + \frac{\sigma_{12}^2}{S_{12}^2} - k_{12} \frac{\sigma_{11} \sigma_{22}}{S_{11} S_{22}} \leq 1 \qquad \text{(V G-33)}$$

An analogous expression was employed in Section V F-5.

7. Synthesis

With the analysis completed and the constraints identified the structural synthesis for the flat rectangular panel can be undertaken. The objective will be to find a design that minimizes the total weight of the panel while satisfying the constraints placed on the panel behavior and design.

Initially only the thickness (h) and the angle (θ) will be treated as design variables. The synthesis technique to be employed will be a sequential process in design space. Procedures discussed in Section IX B will be drawn upon to construct a synthesis technique appropriate to this particular problem.

H. Design Studies of Rocket Throat Insert
    (A.L. Mistretta and F.M. Anthony, Bell Aerosystems)

The rocket throat insert was selected for the particulate composite application based on the considerations given in Section IV B. Initial design studies were conducted to define the relationships among environmental conditions, geometric variables, and external restraint conditions.

Two different external geometric configurations, as shown in Figure 60 were examined. One was of uniform wall thickness while the other employed a constant external diameter. For initial analyses, the throat diameter was taken as 2.0 inches with a maximum wall thickness of 1.0 inch. A convergent angle of 45° and a divergent angle of 25° were assumed with a blend radius of 2.0 inches as shown. The effects of external restraint, axial length, wall thickness, and chamber pressure were investigated for this size. Subsequent analyses examined the influence of throat diameter.

Heating conditions at the throat were obtained from Figure 4 while the Bartz equation (26) was used to determine heating conditions along the inner surface. A forward finite difference procedure was used to determine temperature distributions in the throat inserts. Temperature dependence of material properties was included as was orientation dependence of thermal conductivity. The influence of the number of discrete elements used for representing the insert was examined in Reference 27. In the first case, the throat inserts were divided into lamina having thicknesses of 0.15 and 0.20 inches and in the second case, the inner most lamina which had been 0.15 inches thick for both configurations was divided into yet thinner lamina, the inner most of which was 0.05 inch and the other 0.10 inch thick. For the assumed lamina thicknesses, it was found there was essentially no difference in radial temperature distribution at the throat for the two insert configurations, but the finer lamina thicknesses, however, did indicate a somewhat steeper gradient and was used for subsequent analyses. The radial temperature distribution at the minimum throat diameter 2 seconds after engine ignition is shown in Figure 61.

The transient analyses conducted in Reference 27, assuming two types of external boundary conditions (perfect insulation and complete freedom to radiate from the outer surface), show during the first few seconds of engine operation, that temperature distributions are essentially independent of the thermal boundary conditions along the external surface of the insert.

The throat temperature as a function of chamber pressure for the 2.0 inch throat diameter insert at the time of the maximum overall temperature gradient and maximum local temperature gradient is shown in Figure 62. The times at which these gradients occur are as follows:
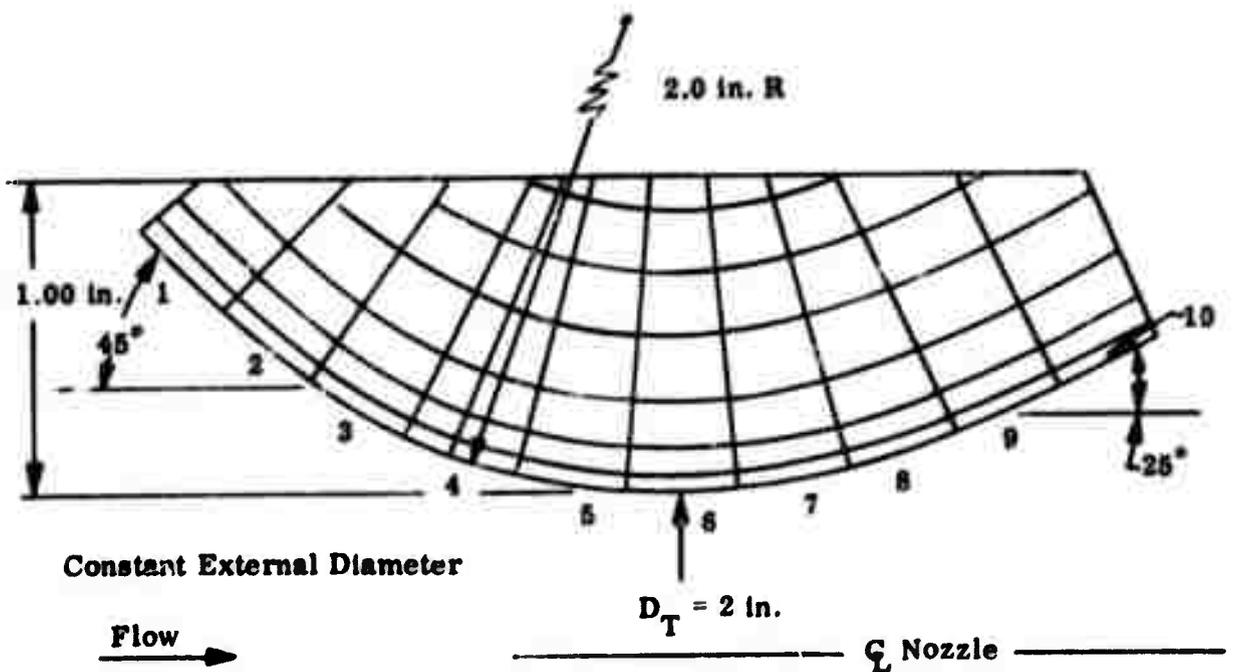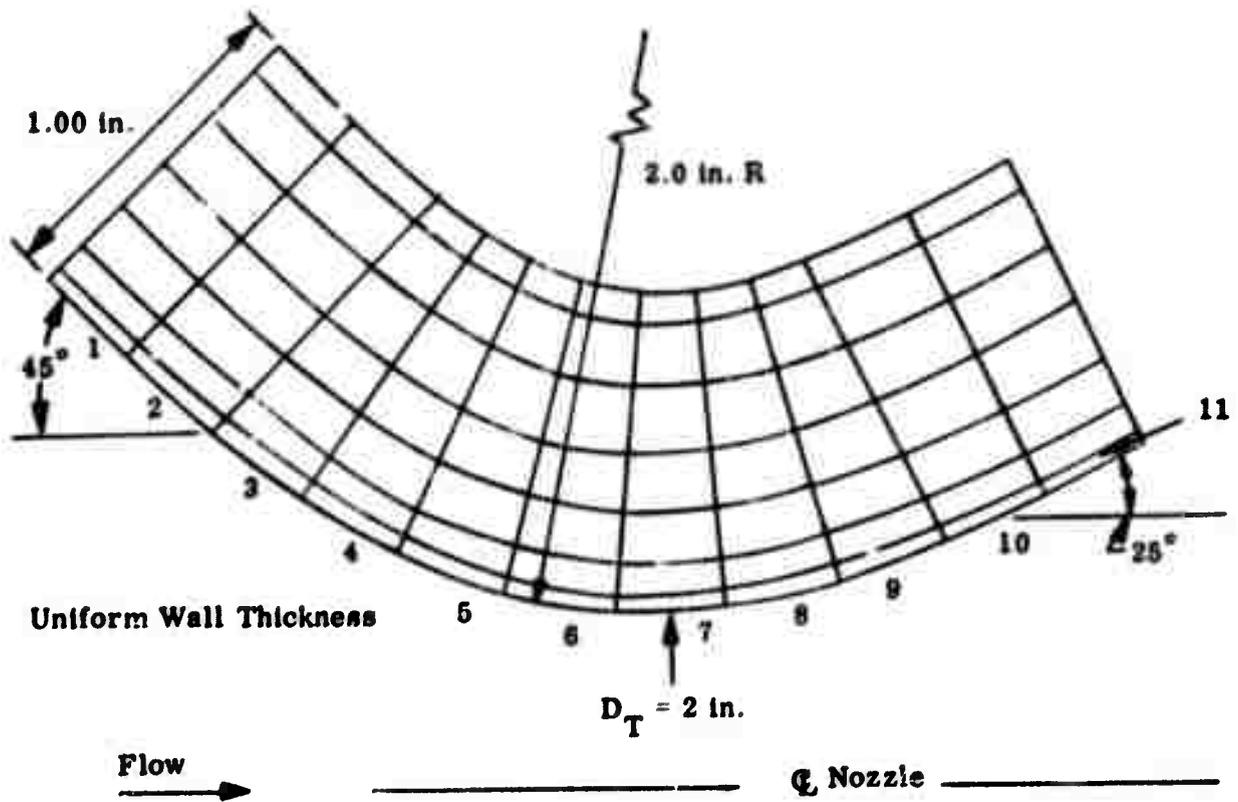
Figure 60. Insert Configurations.
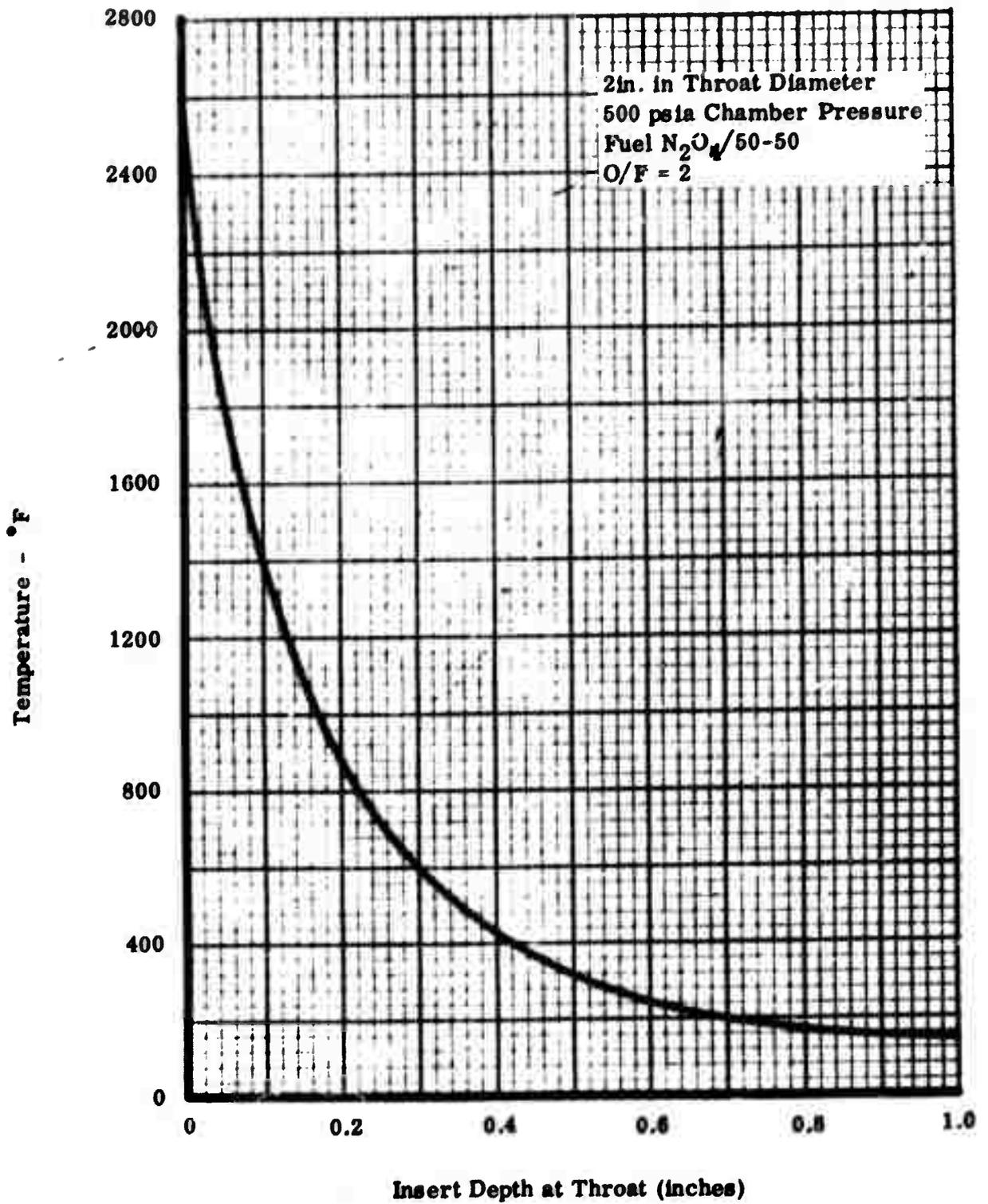
Figure 61.   Insert Temperatures at Throat 2 seconds after Ignition.
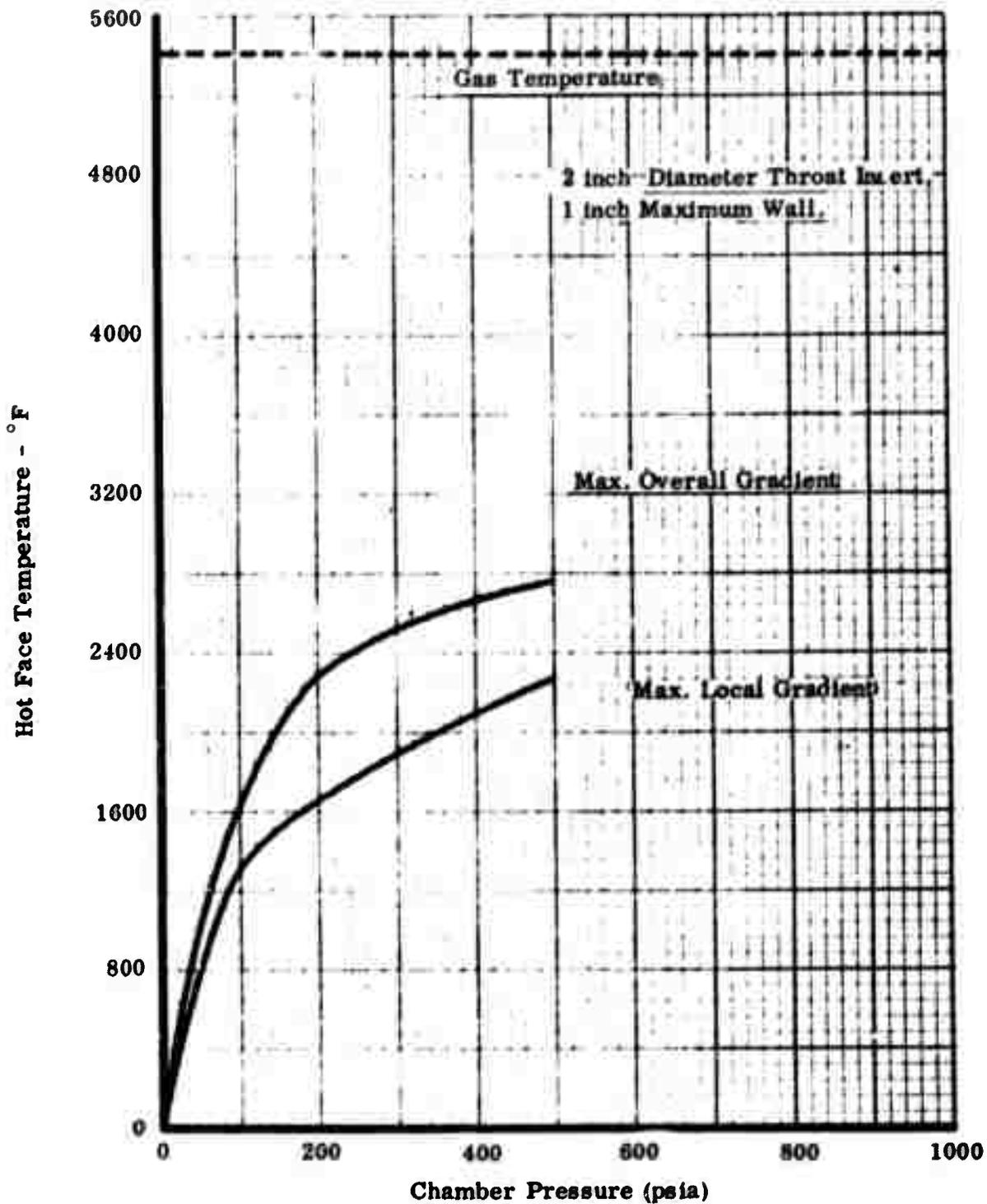
Figure 62. Hot Face Temperature as a Function of Chamber Pressure at Time of Maximum overall Temperature Gradient and Maximum Local Temperature Gradient.

Chamber Pressure (psia)	Max. Local Gradient (sec)	Max. Overall Gradient (sec)
100	3.5	6.0
200	1.8	6.0
500	0.8	2.0

The temperature distributions used for the thermal stress analyses are at the time of maximum overall temperature gradient since these gradients induced the largest thermal stresses.

The resulting temperature distributions from the heat transfer analyses served as input to a computer program which determines stresses. The concept of physically idealizing structures as assemblies of discrete elements which is discussed in Section IX C was employed. For analysis of the throat insert, the element chosen was the triangular cross section ring. Element characteristics were based on temperature dependent linearly elastic, transverse isotropic behavior. The JTA material properties were obtained from Reference 27 and the room temperature values are listed below.

	With Grain	Against Grain
Young's Modulus (10^6 psi)	17	6.1
Shear Modulus (10^6 psi)		2.9
Poisson's Ratio	0.22	0.079
Coefficient Thermal Expansion ($10^{-6}/°F$)	2.9	3.2

The number of triangular elements used for structural idealization was investigated in Reference 27. It was found that 126 ring-elements were adequate for the constant outside diameter insert. Coarser representation was adequate for predicting compressive stresses, but gave conservative results for tensile stresses.

In addition to the analyses for the 2.0 inches throat diameter inserts of constant outside diameter and constant wall thickness, analyses of the constant outside diameter insert were conducted to examine the effects of external restraint, axial length, chamber pressure and throat diameter. The results from these analyses are summarized in Table VIII. Also included in Table VII is the case of an insert which is assumed to be isotropic and to have the JTA "with grain" properties.

For the cases which consider transverse isotropic material behavior, maximum tensile stresses occur when the insert is unrestrained while maximum compressive stresses occur when the insert is restrained both axially and circumferentially. Stress levels are influenced by the type of restraint with greatest effect on the axial stress levels. The primary advantage of restraint is to reduce axial and circumferential tensile stresses.

Shortening the length of the insert has little effect on maximum stress levels but increases the minimum axial stress level by about 15% and decreases the minimum circumferential stress level about 25%. When the wall thickness is decreased for the

TABLE VIII

SUMMARY OF THROAT INSERT ANALYSIS

Conditions	Case	Axial Stress - (psi) Maximum[1]	Minimum	Circumferential (psi) Maximum	Minimum
500 psia Chamber Pressure 2.0 Inch Throat Diameter 1.0 Inch Max. Wall	1. Unrestrained[2]	7,500 (T)	-70,000 (T)	28,000 (E) 20,000 (T)	-300,000 (T)
	2. Unrestrained	7,500 (T)	-90,000 (T)	37,000 (E) 21,000 (T)	-250,000 (T)
	3. Restrained	-5,000 (T)	-120,000 (T)	-10,000 (T)	-325,000 (T)
	4. Full Hoop Restraint	-2,000 (T)	-98,000 (T)	-10,000 (T)	-320,000 (T)
	5. Hoop Restraint	1,000 (T)	-95,000 (T)	-7,000 (T)	-315,000 (T)
	6. Axial Restraint	-6,000 (T)	-140,000 (T)	20,000 (T)	-235,000 (T)
	7. Isotropic, Unrestr.	20,000 (T)	-195,000 (T)	38,000 (E) 20,000 (T)	-325,000 (T)
	8. Reduced Length, Unrestrained	6,000 (T)	-82,000 (T)	23,000 (T)	-220,000 (T)
0.6 Inch Max. Wall Thickness	9. Reduced Length Wall, Unrestrained	9,000 (T)	-62,000 (T)	40,000 (E) 34,000 (T)	-165,000 (T)
200 psia Chamber Pressure 2.0 Inch Throat Diameter 1.0 Inch Max. Wall	10. Unrestrained	5,200 (T)	-31,000 (T)	22,000 (E) 18,000 (T)	-110,000 (T)
	11. Restrained	-11,000 (T)	-58,000 (T)	-28,000 (T)	-210,000 (T)
100 psia Chamber Pressure 2.0 Inch Throat Diameter 1.0 Inch Max. Wall	12. Unrestrained	3,100 (T)	-19,000 (T)	12,000 (E) 11,000 (T)	-67,000 (T)
	13. Restrained	-9,000 (T)	-37,000 (T)	-22,000 (T)	-130,000 (T)
500 psia Chamber Pressure 2.0 Inch Throat Diameter 1.0 Inch Constant Wall	14. Unrestrained	6,500 (T)	-90,000 (T)	18,000 (E) 6,000 (T)	-255,000 (T)
	15. Restrained	-5,000 (T) -3,000 (E)	-110,000 (T)	-11,000 (T)	-330,000 (T)
500 psia Chamber Pressure 5.0 Inch Throat Diameter 1.5 Inch Max. Wall	16. Unrestrained	10,000 (T)	-52,000 (T)	50,000 (E) 26,000 (T)	-167,000 (T)
	17. Restrained	-6,000 (T)	-120,000 (T)	-10,000 (T)	-322,000 (T)
500 psia Chamber Pressure 24.0 Inch Throat Diameter 4.0 Inch Max. Wall	18. Unrestrained	10,000 (T)	-90,000 (T)	28,000 (E) 18,000 (T)	-205,000 (T)
	19. Unrestrained	-3,000 (T)	-120,000 (T)	-5,000 (T)	-315,000 (T)

1. The magnitude of the stresses are considered in an algebraic sense, that is -300,000 psi is considered minimum when compared to -20,000 psi.

2. This case coarse descrete element used, all other cases a finer descrete element used.

3. + is tension. - is compression.

4. (T) indicated throat section, (E) indicated upstream or downstream edges.

reduced length insert, there is an approximately 80% increase in the maximum tensile, but a substantial reduction in the maximum compression stress.

It is interesting to note the influence of anisotropy on the calculated thermal stresses. This can be done by comparison of Cases 2 and 7 in Table VIII. For the assumption of isotropy with "with grain" properties, axial stresses are almost tripled while circumferential stresses are changed to a lesser degree. Thus, there appears to be a decided advantage for the anisotropic material: not only are the stresses lower with the transversely isotropic material, but the rate of stress decrease is more rapid than the rate of strength decrease with respect to orientation.

The effect of chamber pressure on the maximum and minimum stresses for the 2.0 inch throat diameter and 1.0 inch maximum wall thickness insert is shown in Figures 63 and 64, for the unrestrained and fully restrained conditions, respectively. The increasing chamber pressure levels subjects the insert to a more severe thermal environment and, as would be expected, there is a corresponding increase in thermal stresses. Stresses are increased when the insert is fully restrained, but all of the stresses are compression rather than tension and compression.

Figures 65 and 66 depict the effect of the insert diameter on the maximum and minimum stresses for a chamber pressure of 500 psia for the unrestrained and fully restrained cases. For the fully restrained case, the minimum thermal stresses decrease for throat diameters up to 5.0 inches, with gradually increasing thermal stresses for diameters greater than 5.0 inches. The maximum thermal stresses are relatively unaffected by changes in throat diameter.

Perhaps the major result of the analyses conducted to date is the high stress levels calculated on the basis of the elastic analysis. The JTA materials, however, do not have linear stress-strain curves even at room temperature. Inclusion of non-linearity is expected to significantly reduce stress levels. The importance of non-linearity will be assessed in the immediate future.
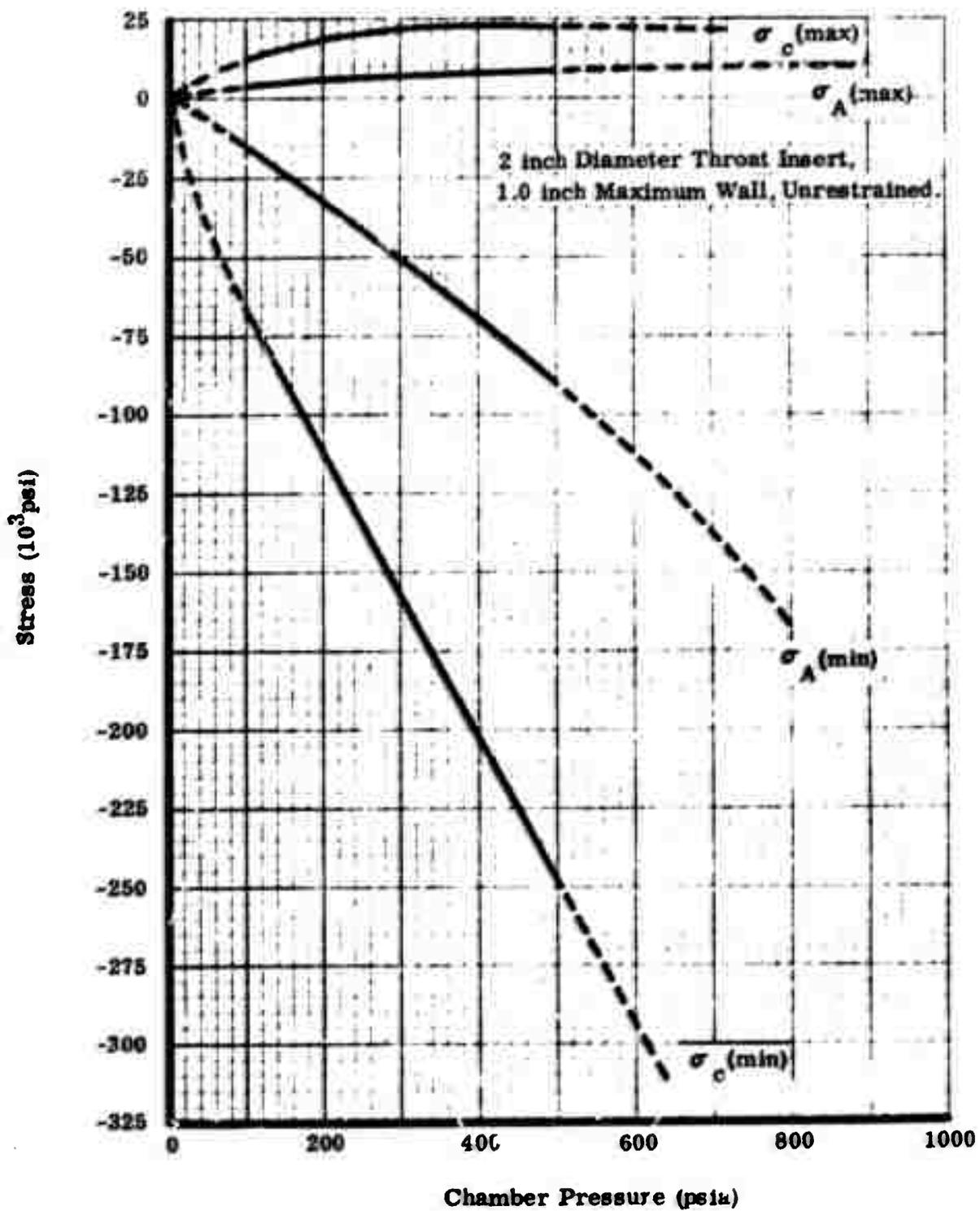
Figure 63. Maximum and Minimum Circumferential and Axial Stresses as a Function of Chamber Pressure.
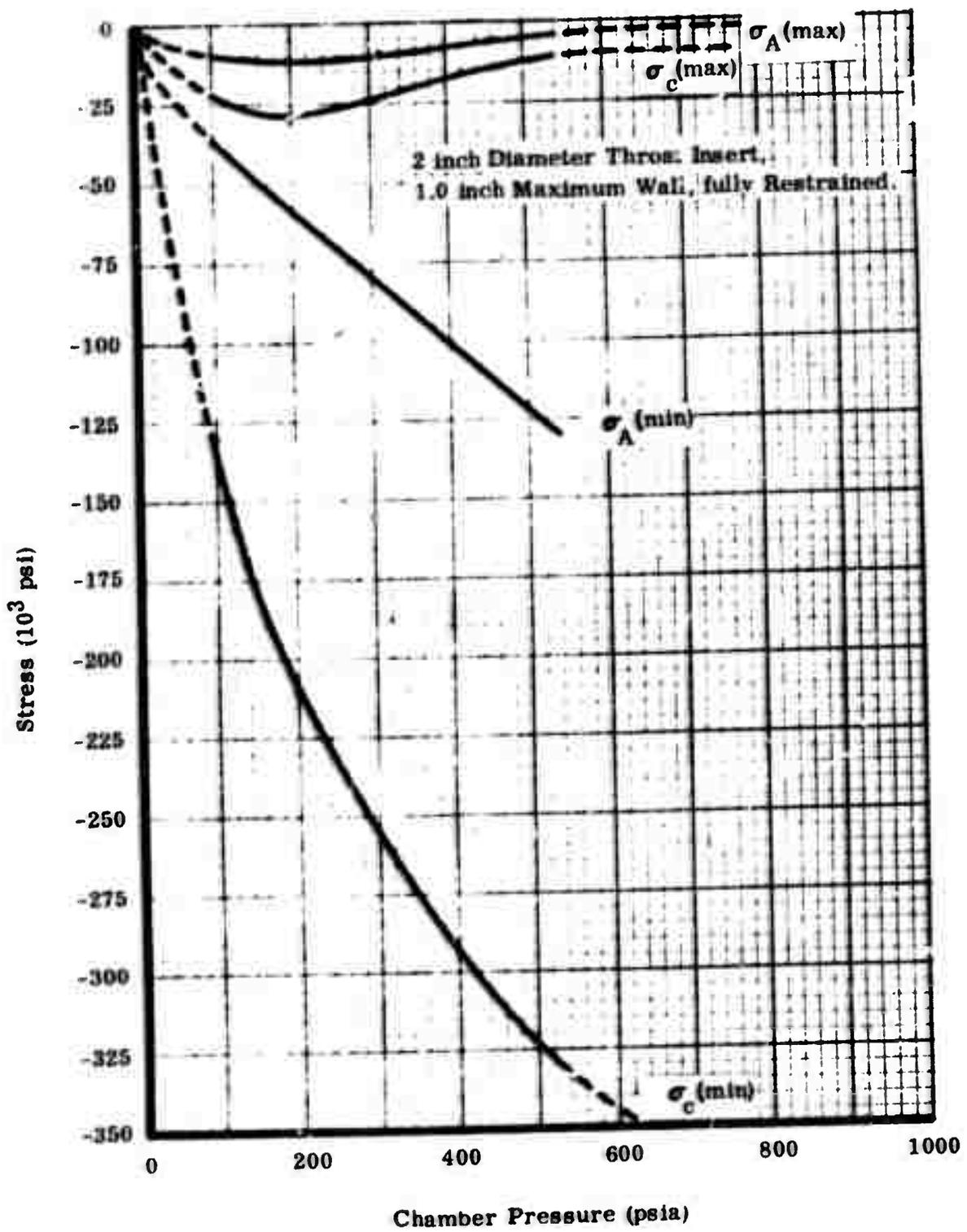
Figure 64.   Maximum and Mimimum Circumferential and Axial Stresses as a Function of Chamber Pressure.
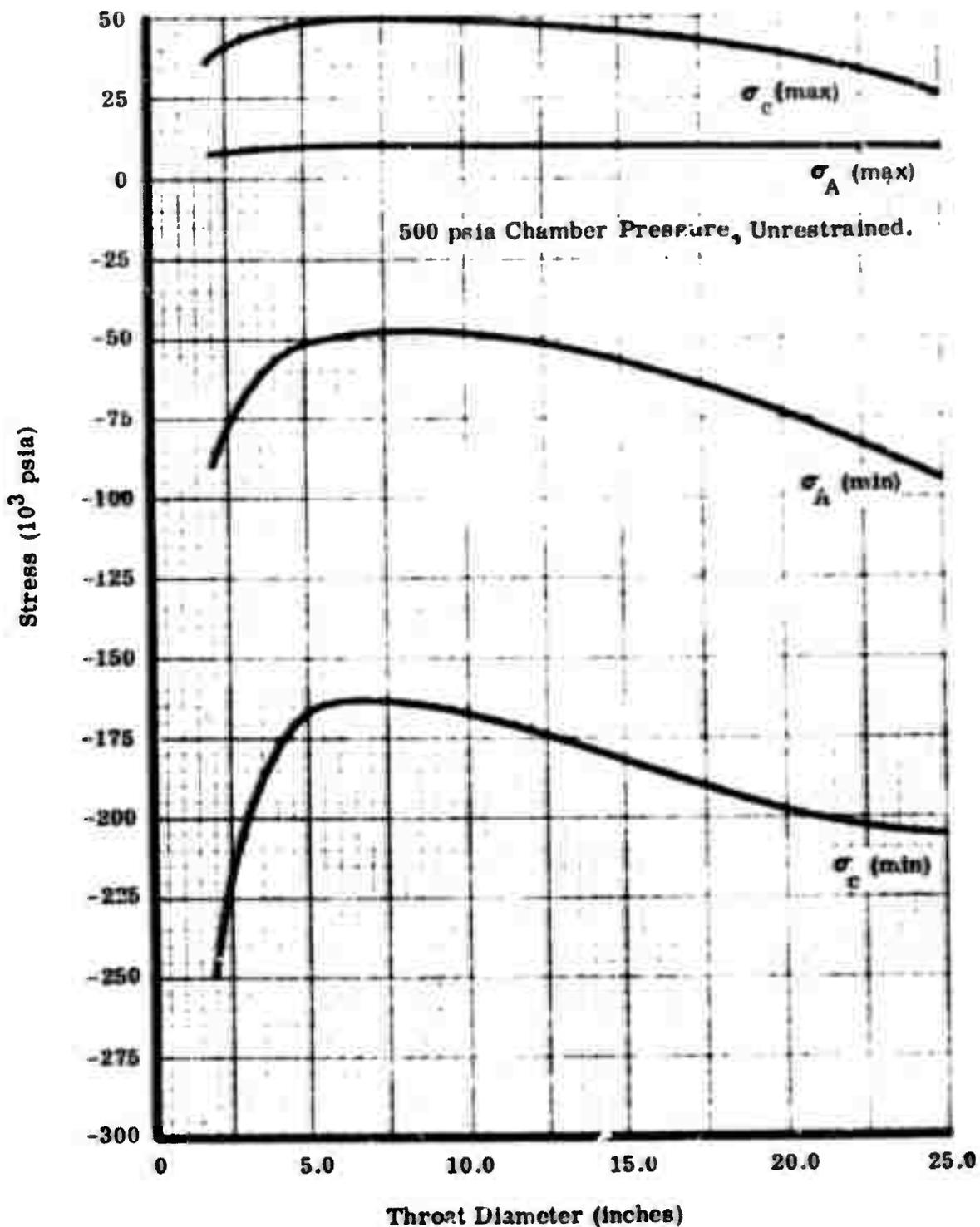
Figure 65. Maximum and Minimum Circumferential and Axial Stresses as a Function of Throat Diameter.
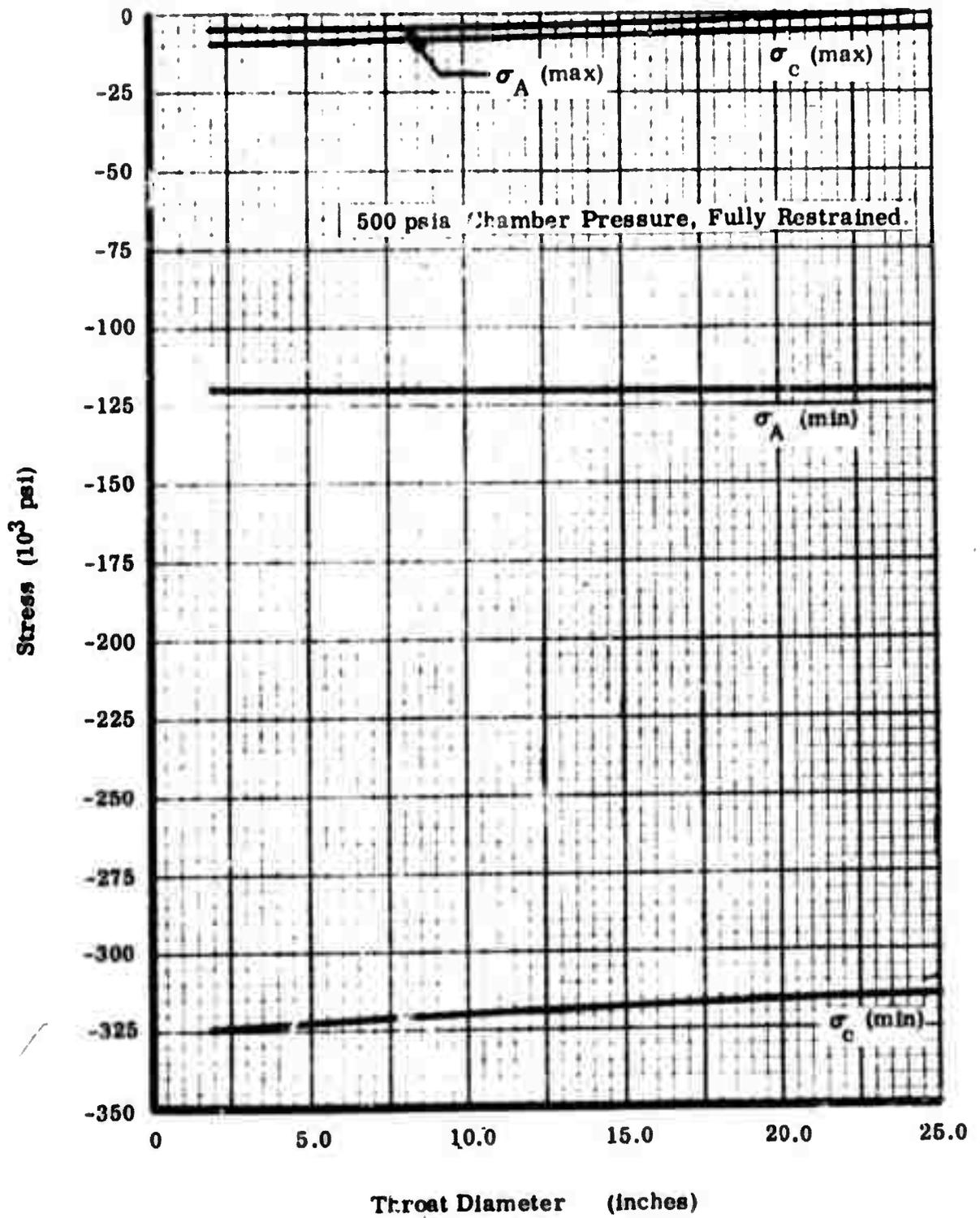
Figure 66. Maximum and Minimum Circumferential and Axial Stresses as a Function of Throat Diameter.

I.   Testing JT Series Materials
      (F. M. Anthony and D. P. Hanley, Bell Aerosystems)

Testing of particulate composites falls into three categories: (1) tests of the statistical approach, (2) tests of simple components, and (3) tests of the representative components. Program plan definitions and the status of work in each of these areas are discussed in the following sections.

1.   Statistical Approach

When attempting to correlate analytical predictions of the statistical aspects of failure with test data, a large number of data points are required. To keep costs within reason and still provide meaningful data, a simple bend bar test specimen using JTA will be studied. The purpose of this testing is to evaluate possible analytical approaches for dealing with stresses which are not parallel or perpendicular to the material axes. Statistical parameters will be determined from samples cut with and across grain. Analytical procedures will then be employed to predict the statistical distribution of strength for samples having stress applied at angles to the material axes. Samples will then be tested in this manner and the test results will be compared with the analytical predictions. Test bars are currently being machined for this study.

2.   Simple Components

The purpose of the simple component tests of the JTA material is to verify analysis procedures before they are used for the optimization of material and geometric parameters. Both the Case analysis for the infinitely long cylinder and the Bell analysis for the short cylinder are to be checked. Cylindrical specimens will be used to simulate the throat insert application. Instrumentation will consist of strain gages and thermocouples on the outside diameter. In addition, temperatures will be measured within the wall at two radial locations for the long cylinder and at three locations for the short cylinder. Specimens will be machined from 3-inch diameter by 3-inch long billets.

Testing will consist of rapidly heating the internal cylinder bores. This heating will be accomplished by radiation from a resistance heated graphite rod. The long cylinders and one of the short ones will have constant internal and external diameters while one of the short cylinders will have a constant outside diameter and a variable inside diameter. Another short cylinder configuration will have a constant inside diameter and a stepped outside diameter so as to simulate a heavy integral ring.

Temperatures and strains will be recorded continuously during the test. The linear analyses should compare quite well with the data obtained early in each test. As temperatures and strains increase, the material response should become increasingly nonlinear. The inaccuracy introduced by linear analysis will be defined quantitatively and these test results will be available for use with the nonlinear analysis capability to be developed later in the program.

The precise number of tests to be conducted on each sample has not been determined as yet. Four sample configurations will be tested and duplicate runs would be desirable. From another Bell program, it should be possible to assess the maximum stress which will not introduce significant damage. If this is high enough, one sample of each configuration may be made and two or three tests of each will be run. If this approach is not possible, tests will be run on duplicate samples.

The tests described above constitute a minimum effort on JT material. The equipment required for the tests is available and experimental studies to demonstrate its applicability are nearly complete.

3. Representative Components

Fabrication and testing of the particulate composite nozzle throat insert has been considered, but at the present time, it appears that actual testing of this component may not be necessary. If the simple component tests described above adequately verify the regimes of theoretical behavior as expected, further work should not be required. A decision on testing the representative insert component, therefore, will depend upon the results of the simple component tests.

SECTION VI

MATERIALS RESEARCH ON CARBON-FIBER, RESIN-MATRIX COMPOSITES

Realization of the superior properties of high modulus graphite fibers in resin matrix composites requires strong fiber-resin bonding. Work sponsored by the Carbon Products Division[28] has shown that epoxy resin composites made with carbon fibers have better compressive, flexural, and shear strengths than composites made with graphite fibers of either low or high (THORNEL 25) modulus. Table IX gives typical mechanical properties

TABLE IX

PROPERTIES OF FIBER RESIN RINGS

| Composite Property | Type of Yarn in Composite | | |
	Carbon VYB	Graphite WYB	THORNEL 25
Tensile strength (10^3 lb/in.^{2})	80	65	96
Tensile modulus (10^6 lb/in.^{2})	3.1	3.2	---
Compressive strength (10^3 lb/in.^{2})	130	60	57
Compressive modulus (10^6 lb/in.^{2})	3.5	3.6	15
Flexural strength (10^3 lb/in.^{2})	110	80	69
Bending modulus (10^6 lb/in.^{2})	3.3	3.3	15
Short-beam shear strength (10^3 lb/in.^{2})	11	3.6	2.3
Fiber content (percent by volume)	62	70	72

for rings wound with carbon and graphite yarns impregnated with an ERL 2256/MPDA epoxy-resin system. The lower compressive, flexural, and shear strengths for the graphite yarn composites suggest that the graphite fiber-to-resin adhesion is not so good as the carbon fiber-to-resin adhesion. This hypothesis is supported by fiber characterization studies, discussed in Section VI A, which show that the carbon fibers have a much greater surface area and open porosity than the graphite fibers.

Adhesive bond strength is affected by many factors, the more important of which are: the surface condition of the fibers, fiber-resin wetting, fiber volume fraction, and the strain at the fiber-resin interface after the resin has polymerized. The present program seeks to improve composite properties through studies of the first three of these factors. The effect on surface properties of oxidation of the fiber surface is reported in Section VI B. Theoretical relations between contact angles, wetting rates, and

adhesion are discussed briefly in Section VI C. The influence of fiber surface treatments on contact angle and wicking (as a measure of wetting) rates is investigated in Sections VI D and E. The procedure used here to fabricate NOL rings is given in Section VI F. Preliminary studies indicate the effect on composite properties of varying fiber content (Section VI G) and of surface treatments of the yarn (Section VI H).

A. Characterization of As-Received Fiber Surfaces

Electron micrographs of carbon, graphite, and high modulus graphite fiber surfaces appear in Figures 67, 68, and 69. The appearance of the

N-9713

Figure 67. Electron Micrograph of As-Received Carbon Filament Surface. 22,100X.
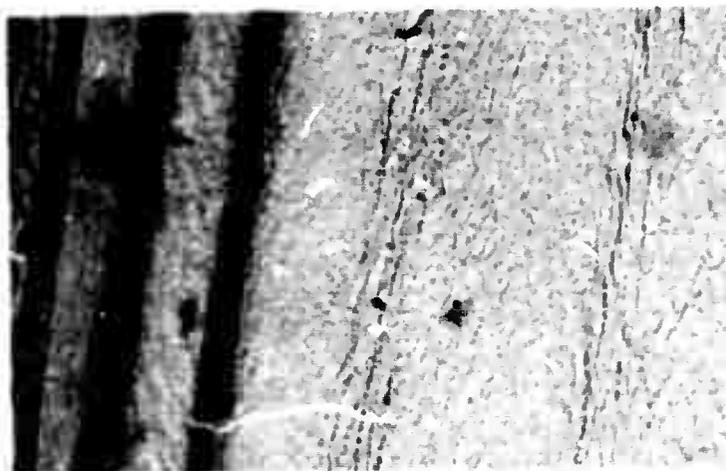
N-9714

Figure 68. Electron Micrograph of As-Received Graphite Filament Surface. 21,000X.

-134-
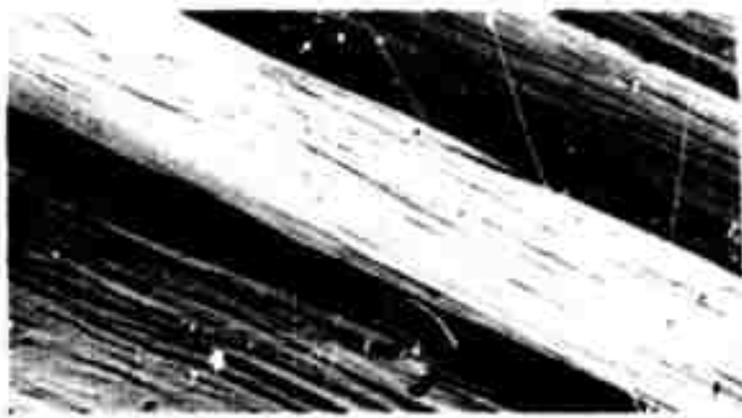
Figure 69. Electron Micrograph of As-Received High Modulus
Graphite Filament Surface. 29,000X.

fiber surfaces is in qualitative accord with the surface property data
presented in Table X. Carbon fibers are highly porous and their surfaces
are rough. The effect of graphitization is to reduce greatly the amount of
porosity open to the surface and to anneal out much of the surface rough-
ness. The high modulus graphite fibers have an even smoother surface
with striations parallel to the axis of the filament. Structural studies
indicate that the crystallites of the high modulus fibers are more highly
oriented than in ordinary graphite fibers.

TABLE X

SURFACE PROPERTIES OF CARBON AND GRAPHITE FIBERS

Property	Carbon Fiber	Graphite Fiber
Surface area (m^2/g)	260	3
Open porosity (cm^3/g)	0.22	0.017
Surface oxygen (percent)	2	0.1

B. Surface Treatments of Graphite Fibers
(R. J. Bobka, Union Carbide)

Among the possible surface treatments which will affect the wetting
properties of graphite fibers are the production of surface-oxygen com-
plexes and roughening of the surface by chemical treatment. Both types
of treatment were investigated.

1. Nature of Surface Oxygen Complexes

Surface oxygen complexes of variable stoichiometry form on all carbons exposed to air at room temperature and above. The amount and nature of the complexes depends upon the activity of the carbon surface, the concentration of oxidizing agent, and the temperature at which the complexes are formed.[29] The following sequence of reactions is generally applicable to the oxidation of all carbons:

$$\text{Complex formation: } C + O_2 \rightarrow C(O)_x + CO_2 + CO \qquad \text{(VI B-1)}$$

$$\text{Complex decomposition: } C(O)_x \rightarrow C + CO_2 + CO \qquad \text{(VI B-2)}$$

The amount of complex formation is at maximum between 300 to 400°C, depending upon the activity of the surface. Most of the gaseous product formed during the production of these "low temperature" complexes is CO_2. Above approximately 450°C, "high temperature" complexes are formed, and most of the gaseous product is CO. Thermal decomposition of the low temperature complexes produces an evolved gas rich in CO_2; thermal decomposition of high temperature complexes produces an evolved gas rich in CO. The stability of these complexes is variable, and temperatures higher than 900°C are required to decompose all but the last traces.

The presence of oxygen complexes markedly alters the surface properties of all carbons. In the absence of these complexes, carbons are hydrophobic; in their presence, carbons are hydrophilic. At any point on the surface where a carbon-oxygen complex exists, one or more molecules of water will very quickly be adsorbed from air, impeding wetting by other compounds and forming gas bubbles in the polymerized resin. At the same time, oxygen-complexes could promote adhesion by forming hydrogen bonds with suitable resins, provided the water adsorbed is first removed.

2. Gaseous Oxidation of Graphite Fibers

Graphite fibers were oxidized at 400 to 600°C in oxygen by heating graphite yarn in a $2 \text{ cm}^3/\text{min}$ stream of oxygen at a controlled rate of temperature rise. After oxidation, a stream of argon was substituted for oxygen and the temperature raised to approximately 1000°C. The apparatus permitted measurements of sample weights before and after oxidation or thermal decomposition. The results showed that both graphite and high modulus yarn require temperatures above 400°C in order for oxidation to proceed at a significant rate under these conditions. The monitoring of the effluent gases during thermal decomposition of the surface oxygen complexes showed no CO_2 or CO below 400°C and only CO above that temperature. The decomposition was completed by 900°C. The complexes initially formed were therefore of the high temperature type. Examination of the oxidized fibers in an optical microscope revealed that approximately 5 percent of the fibers were greatly degraded and that the rest seemed to have remained unoxidized.

3. Chemical Etching of Graphite Fibers

Strong oxidizing solutions of known concentration were employed to chemically etch graphite fibers. The yarn was wound in a single strand thickness on an open framework of glass and then weighed. It was then immersed in the etching solution at controlled temperature for a measured period of time. The etched yarn was thoroughly rinsed in distilled water, dried for a half hour at 105° C, and weighed once more. Portions of several of these etched yarns were used for electron micrographs (Figures 70 to 73) and wetting measurements. The results of these experiments are presented in Figure 74.

All but one of the treatments listed in Figure 74 resulted in a yarn weight loss, showing that only relatively mild treatments are necessary to accomplish some degree of roughening. The $KMnO_4$ - H_2SO_4, 60° C, 5 min treatment was of special interest because it seemed to roughen the fiber surface without removing carbon. However, examination of the surface showed many small particles (Figure 70) which added to the weight. Chemical analysis showed the presence of 0.5 percent Mn on this yarn. It is probable that the small particles are MnO_2, corresponding to a total MnO_2 content of 0.8 percent. This amount of MnO_2 is less than the observed weight gain of about 1.3 percent., leaving open the possibility that etching in this system is accomplished with low carbon loss. More work on this system is contemplated.

N-9716

Figure 70. Electron Micrograph of Graphite Filament Surface Etched in $KMnO_4$-H_2SO_4 Solution. 12,200X.

N-9717

Figure 71. Electron Micrograph of Graphite Filament Surface Etched in Sulfuric Acid. 12,200X.
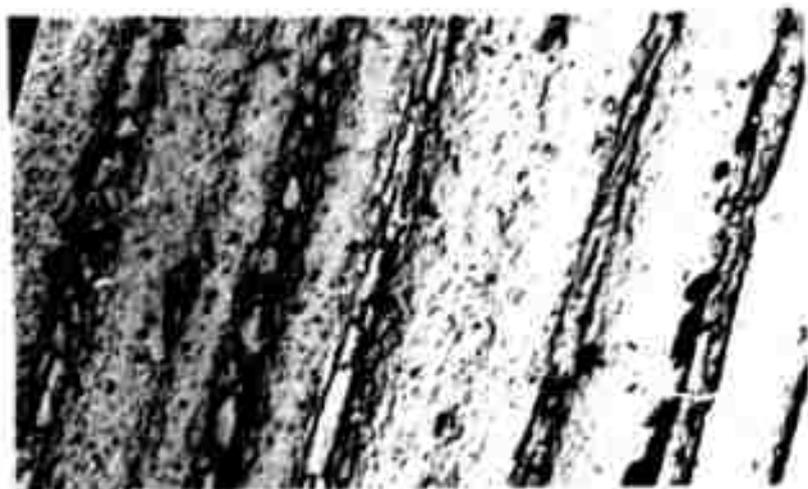
Figure 72.   Electron Micrograph of Graphite Filament
Surface Etched in Hypochlorous Acid (Bleach).
12,200X.

N-9719

Figure 73.   Electron Micrograph of Graphite Filament
Surface Etched in Chromic Acid.   12,200X.
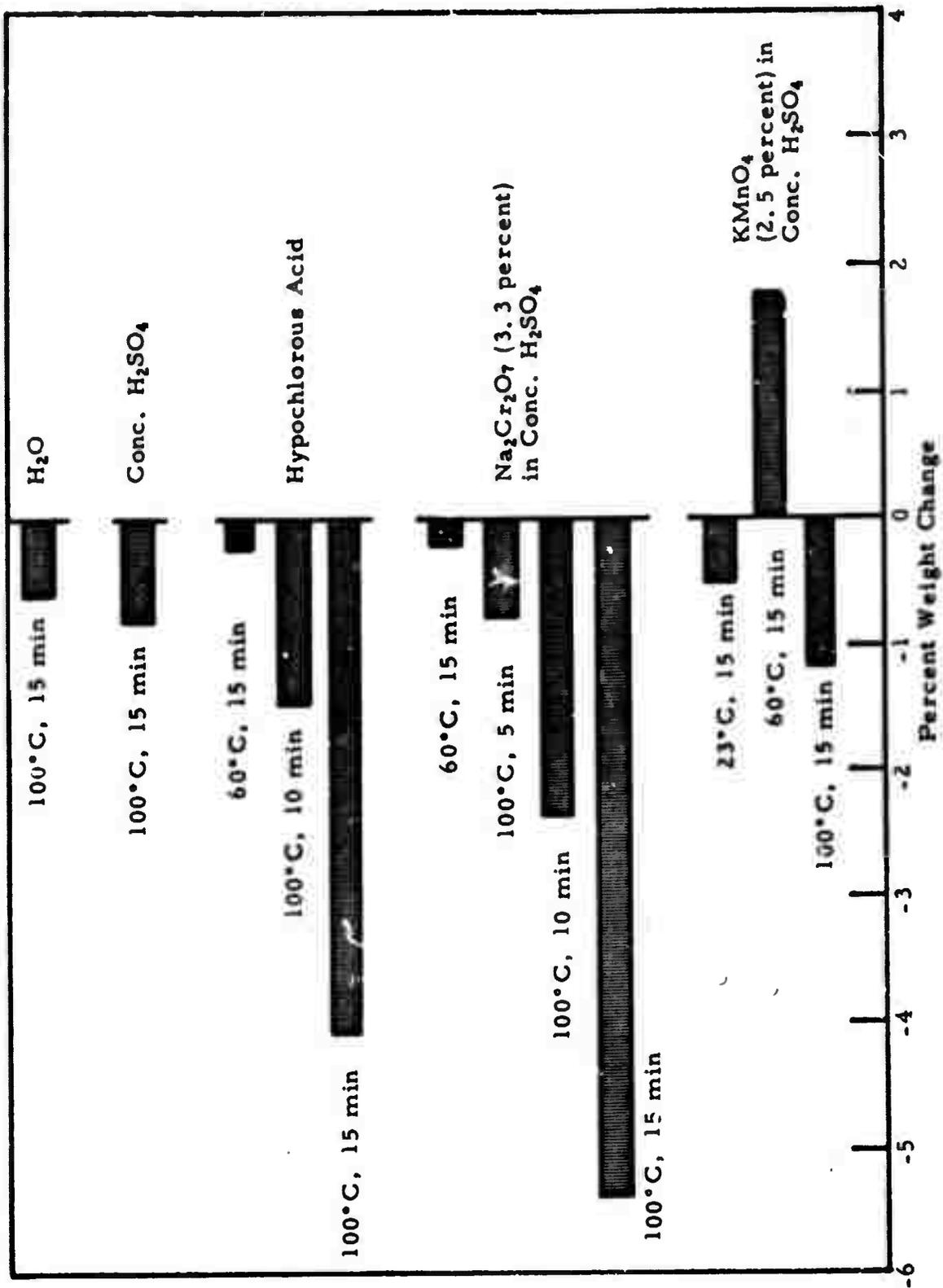
Figure 74. Weight Loss of Graphite Yarn Due to Etching.

N-9467

-139-

C. Interrelation of Contact Angle, Wetting Rate, and Adhesion
(R. J. Bobka, Union Carbide)

The surface forces which operate at a planar solid-liquid interface come to an equilibrium which produces a liquid drop with the shape of a spheroidal segment, as in Figure 75. The contact angle θ (see Figure 75) is related to the solid, liquid, and vapor surface tensions by

$$\nu_{sv^\circ} = \nu_{lv^\circ} \cos \theta + \nu_{sl} \qquad \text{(VI C-1)}$$

in which ν_{sv° and ν_{lv° are the surface tensions of the solid and liquid, respectively, in equilibrium with the vapor and ν_{sl} is the solid-liquid inter-facial tension.
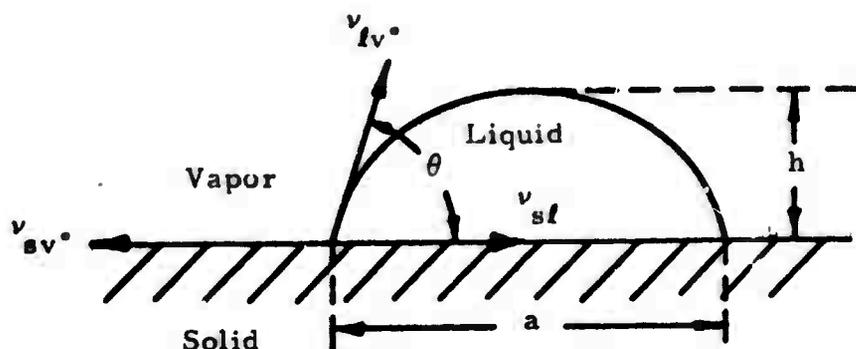
N-9470

Figure 75. Profile of a Liquid Drop on a Solid.

Rigorous thermodynamic derivations of Equation VI C-1 require precise definitions of the various surface tensions. There is controversy as to the applicability of the term ν_{sv° in real situations. If one assumes true equilibrium, the work of adhesion W°_{adh}, the work necessary to remove the liquid from the solid, is given by

$$W^\circ_{adh} = \nu_{lv^\circ} (1 + \cos \theta) \qquad \text{(VI C-2)}$$

which shows very simply how liquid-solid adhesion is improved by decreased contact angles. Harkins[90] first pointed out that, when θ is nearly zero, there may be a further contribution to W°_{adh}:

$$W^\circ_{adh} = \nu_{lv^\circ} (1 + \cos \theta) + \pi^\circ \qquad \text{(VI C-3)}$$

The term π° is the difference between the energy ν_s of the base solid and energy ν_{sv° of the solid in equilibrium with the vapor of the liquid, i.e.,

$$\pi^\circ = \nu_s - \nu_{sv}\circ \qquad\qquad\text{(VI C-4)}$$

Conservative theoretical calculations of work of adhesion based on Equation VI C-2 predict far greater adhesive strengths than those actually realized in practical systems. The greatest importance of a zero contact angle is that the liquid can, under its own spreading pressure, penetrate pores, crevices, and roughness and minimize the formation of gas bubbles or voids which become areas of stress concentration when the adhesive is polymerized.

Real surfaces are invariably rough to some degree. A measure of this roughness has been derived by Wenzel:[91]

$$\frac{\cos \theta'}{\cos \theta} = R \ (R \geq 1) \qquad\qquad\text{(VI C-5)}$$

where θ is the contact angle on a perfectly smooth surface, θ' is the contact angle on the real surface, and R is the "roughness factor." In most situations encountered in this study, the true contact angle θ is greater than the observed contact angle θ'.

D. Contact Angle Studies
(R. J. Bobka and L. P. Lowell, Union Carbide)

1. Measurements on Bulk Graphite

The sessile drop method for contact angle measurement was applied to two bulk graphites in an exploratory experiment designed to orient work on graphite and high modulus fibers. When a very small drop of liquid (a ≤ 0.5 mm, Figure 75) is placed on a solid surface, the contact angle is given by the simple relation

$$\tan \theta/2 = 2 h/a \qquad\qquad\text{(VI D-1)}$$

where h and a are quantities identified in Figure 75.

Pyrolytic and grade SA-25 graphites were used to determine the effect of oxidation on the contact angles of epoxy resins and water. Pyrolytic graphite is highly anisotropic and nonporous. Grade SA-25 is isotropic and moderately porous. The crystallites in both pyrolytic and SA-25 graphite are only 200 to 500 A across and have poor three-dimensional order. The two epoxy resins which were used vary principally in their viscosities. Contact angle measurements by the sessile drop method were made on the as-prepared material, after oxidation at 600°C for one hour, and after thermal desorption in argon at 1000°C; the results are given in Table XI. The effects of surface treatments on contact angles with water are very pronounced, especially in the case of SA-25. Although the 20° contact angle for ERL 2774 may be partly a consequence of its high viscosity, spontaneous spreading does not occur under the conditions of the experiment;

TABLE XI

EFFECT OF SURFACE TREATMENTS OF BULK GRAPHITES ON CONTACT ANGLES

Liquid	Solid	Treatment	Contact Angle (Degrees)
Water	PG-Face	Polished	73
Water	PG-Face	Polished, Oxidized	64
Water	PG-Face	Polished, Oxidized, Thermally Desorbed	83
Water	PG-Edge	Polished	77
Water	PG-Edge	Polished, Oxidized	35
Water	PG-Edge	Polished, Oxidized, Thermally Desorbed	95
Water	SA-25	None	112
Water	SA-25	Oxidized	0
Water	SA-25	Oxidized, Thermally Desorbed	121
ERLA 0400	SA-25	None	0
ERLA 0400	SA-25	Oxidized	0
ERLA 0400	SA-25	Oxidized, Thermally Desorbed	0
ERL 2774	SA-25	None	28
ERL 2774	SA-25	Oxidized	27
ERL 2774	SA-25	Oxidized, Thermally Desorbed	20

PG - Pyrolytic graphite
SA-25 - An electrographitic, polymorphic graphite
ERLA 0400 - A Union Carbide Corporation epoxy resin, viscosity ~ 40 cps
ERL 2774 - A Union Carbide Corporation epoxy resin, viscosity ~ 12,000 cps

and the wetting is much poorer than with ERLA 0400. It is expected that the response of graphite fibers to oxidation will be intermediate between those of SA-25 and pyrolytic graphite.

2. Method for Small Filaments

The direct goniometric measurement of the contact angle between a filament and a liquid is unreliable when both the filament and the contact angle are small. An alternative method, based on a solution of the mathematical function which fits the observed profile of the liquid in the vicinity of a filament (see Figure 76) has been developed and applied to untreated and treated filaments.

The theory is based on the Young-Laplace equation

$$\Delta p = \nu(1/R_1 + 1/R_2) \qquad \text{(VI D-2)}$$

which relates the pressure drop Δp across a curved liquid-vapor interface with surface tension ν to the principal radii of curvature R_1 and R_2. For surfaces of revolution, as in Figure 76, this equation can be put in the form[32]

$$\frac{d^2z/dr^2}{\left[1 + (dz/dr)^2\right]^{3/2}} + \frac{dz/dr}{r\left[1 + (dz/dr)^2\right]^{1/2}} - \frac{z}{a^2} = 0 \qquad \text{(VI D-3)}$$

in which z is the rise of the liquid at a distance r from the axis of the filament. The parameter a is defined by

$$a^2 = \nu/g \, \Delta \rho \qquad \text{(VI D-4)}$$

where g is the acceleration of gravity and $\Delta \rho$ is the difference in density of the liquid and vapor.
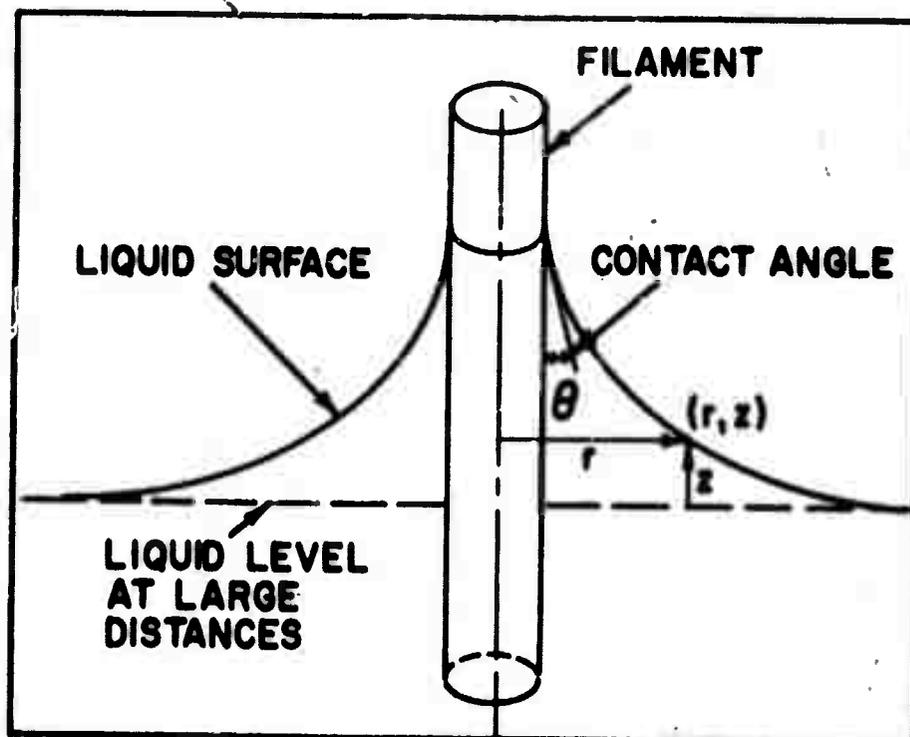
N-9323

Figure 76. Profile of a Liquid Surface Near a Filament.

Since a closed-form solution of Equation VI D-3 is not known, various approximations for its solution have been employed.[33] Recently,

-143-

A. T. Lauria and B. L. Kopfstein of this laboratory developed a program for solving the equation on a digital computer. The program first finds the solution to the differential equation by a 4th-order Runga-Kutta[34] method to give the best fit to the observed values (r, z) of the liquid profile and then computes the contact angle θ by finding the slope of the solution at the filament surface.

The experimental problem is to take a photomicrograph of the region of intersection of a 10 μ diameter filament with a liquid. The arrangement of cell, microscope, and camera is pictured in Figure 77. The photo-
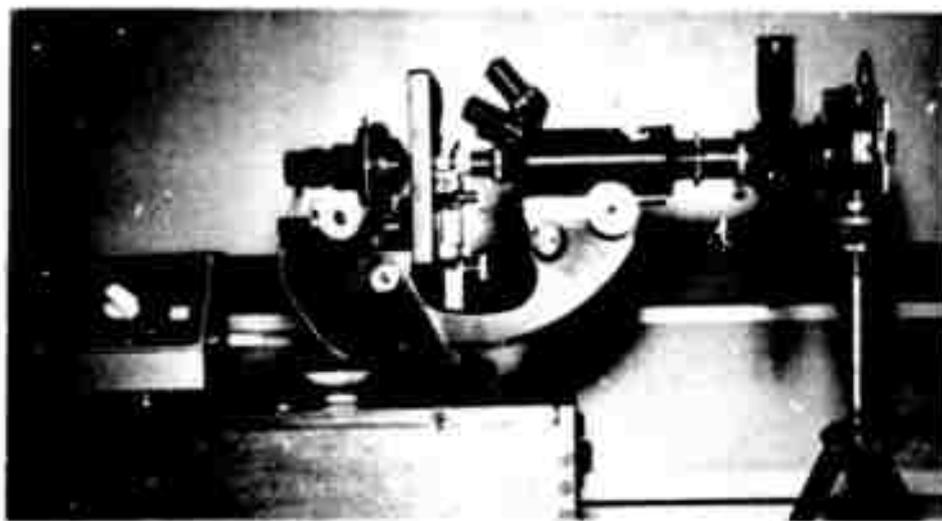
N-9324

Figure 77. Cell, Microscope, and Camera for Measurement of Contact Angle on Single Filaments.

micrograph must be taken with the optical axis normal to the filament and in the plane of the liquid surface. Moreover, the filament must be immersed in a perfectly horizontal portion of the liquid surface, i. e., several millimeters from the cell wall. Once the pnotomicrograph is taken and suitably enlarged, the liquid rise is characterized by (r, z) values taken along the profile. These values are then used to obtain computer-calculated values of the contact angle. Figure 78 shows the rise of epoxy ERLA 0400 on a 98.3 μ diameter glass filament, and Figure 79 shows the rise of the same resin on a 10.7 μ diameter graphite filament.

The large filament (98.3 μ) shown in Figure 78 allowed both a goniometric measurement of contact angle and a computer-calculated contact angle; good agreement was obtained. There was equally good agreement between the calculated contact angles on large and small diameter glass filaments. Care had to be taken to keep the surfaces clean.

N-9325
Figure 78. Surface of Epoxy ERLA
0400 Near a 98.3 μ Diameter Glass
Filament. 102X.
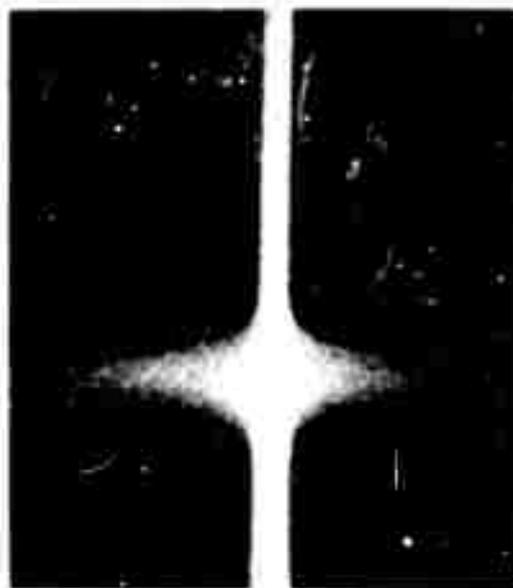
N-9326
Figure 79. Surface of Epoxy
ERLA 0400 Near a 10.7 μ
Diameter Graphite Filament.
370X.

Once the method was developed, the procedure was applied to the measurement of contact angles on graphite filaments.

3. Measurements on Graphite Filaments

Contact angle measurements in water and in epoxies ERLA 0400 and ERL 2774 were made on graphite filaments taken from surface treated yarn. The results are presented in Table XII, in which the surface treatments are abbreviated as follows:

As Rec'd.: No treatment,

T. D.: As-received yarn heated to 1000°C at a pressure of 10^{-5} mm Hg,

Ox.: As-received yarn heated in a 2 cm³/min stream of oxygen at 500°C for 15 min, and

Ox. + T. D.: Oxidation followed by thermal desorption.

The interpretation of the contact angle values in Table XII should take into account the observation that the surfaces of yarns subjected to the indicated treatments are quite nonuniform. In particular, the oxidized fibers varied

TABLE XII

CONTACT ANGLE OF SURFACE-TREATED GRAPHITE FILAMENTS

Wetting Liquid	Yarn Treatment[*]			
	As Rec'd.	T. D.	Ox.	Ox. + T. D.
Water	~36	8±6 (12)	18±13 (17)	38±8 (4)
ERLA 0400	12±7 (16)	4.8±0.2 (5)	4.8±0.8 (3)	4.3±0.6 (7)
ERL 2774	32±8 (4)	7.4±2.6 (4)	11±5 (4)	5.4±0.7 (4)

[*] See text for description of treatment. Values of contact angles are measured in degrees. Numbers in parentheses are numbers of observations. Values less than 5° are inaccurate due to current limitations in the method.

widely in appearance from one filament to another. It is to be expected that liquids which poorly wet nonuniform surfaces will exhibit wide variations in contact angles.

In all cases, the as-received filaments wet more poorly than treated filaments. Thermal desorption without prior oxidation causes ERLA 0400 to wet the yarns very well. With ERL 2774, thermal desorption of oxidized yarn produced results in the best wetting. Oxidation had either a slightly deleterious or negligible effect on wetting by either resin. The results with water are largely as expected, except that the thermal desorption of the as-received yarn apparently did not produce an oxygen-free surface. The results in Table XII suggest the possibility that the wettabilities of yarns by water and resins may be inversely related, i.e., the higher the contact angle with water the lower the contact angle with epoxy resins.

E. Wicking Rates
(R. J. Bobka and L. P. Lowell, Union Carbide)

Thermodynamically, wetting is characterized by a finite contact angle or spreading. Most wetting operations, in practice, are dynamic; and the rate of approach to equilibrium is often the limiting factor in determining the extent of solid-liquid interaction. It is necessary, therefore, to understand the factors which govern the rate of penetration of yarns by resins. A comprehensive theoretical model for resin impregnation into graphite yarn would be very complex, since it would have to include mechanical, geometrical, and chemical contributions. We have chosen to study relationships between fiber surface properties and resin penetration into graphite fibers by the measurement of wicking rates. Two experimental techniques were developed for this purpose.

1. Mass Pickup Technique

In this technique, the mass pickup by a yarn bundle immersed for a definite time is measured. The yarn sample was suspended from one arm of an analytical balance from which the pan had been removed. Weights were adjusted to give a null reading. A Petri dish filled with liquid and supported by a jack was placed directly beneath the yarn. The Petri dish was raised until the liquid just touched the yarn sample and was kept there for a standard time interval, after which the Petri dish was lowered to break the liquid-fiber contact. Fifteen seconds after the break of contact, a weight measurement was made and recorded. Fifteen seconds more were permitted to elapse before the liquid level was again brought to the fiber end and a new cycle of measurements begun. The procedure was repeated for 10 immersions or until no further weight gain was observed.

The yarn samples used in these experiments were three-inch lengths of graphite yarns bundled together and tied about 1/4 inch from the ends; these samples presented 28,800 filament ends to the liquid. Five-second immersion intervals were used. All measurements were made at room temperature.

The following simple liquids are ranked in order of decreasing wicking rates, as given by the mass pickup technique:

1.	chloroform	7.	Octoil - S
2.	methylethylketone (MEK)	8.	50% epoxy - MEK solution
3.	acetone	9.	epoxy
4.	ethyl bromide	10.	glycerol
5.	N-butyl alcohol	11.	water
6.	2-propanol		

Examination of the physical properties of these liquids indicates that the property which controls wicking rates under these circumstances is viscosity.

2. Surface Velocity Technique

a. Experimental Procedure. A second method for measuring wicking rates, called the surface velocity technique, has been developed. The technique is more complex than the mass pickup technique, but it is more flexible and provides true wicking rates.

A yarn strand is placed between the metal prongs in the cell shown in Figure 80. A single thickness of "Kimwipe" tissue is inserted between the yarn and one of the prongs. As long as the Kimwipe remains dry, the electrical resistance across the prongs is of the order of megohms. When the pad is wetted by liquids the resistivity of which is much lower than that of the pad, the resistance across the prongs drops markedly, and the change may be detected by suitably sensitive electronic instruments. A diagram of the circuit used in the surface velocity technique is given in Figure 80.
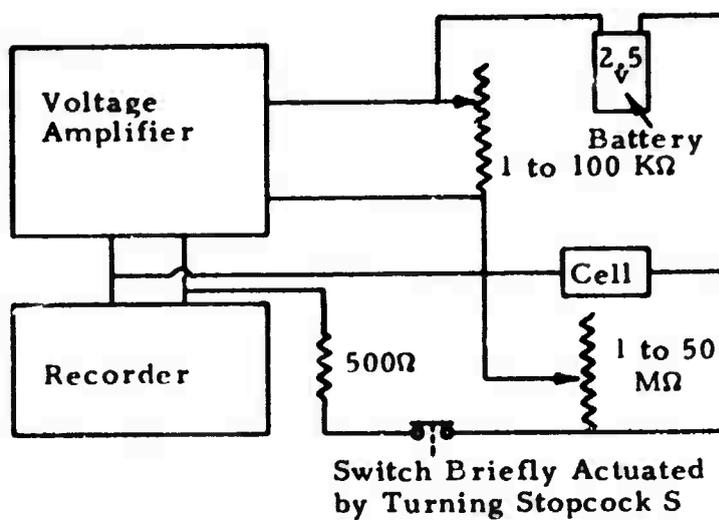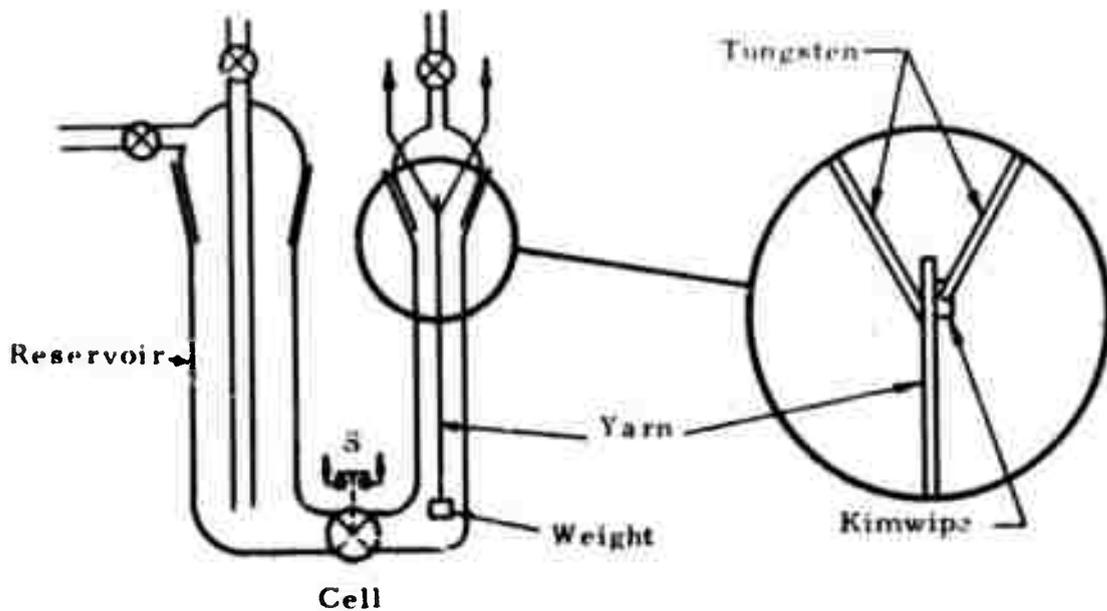
N-9468

Figure 80. Cell and Circuit for Wicking Rate Measurements
by Surface Velocity Technique.

Each run is started by adding liquid to the reservoir arm of the cell and immersing the cell in a constant temperature bath. The yarn and Kimwipe pad are placed between the prongs, and the cell is assembled. The liquid is brought to the desired level by introducing gas under pressure through one of the reservoir inlets. A pair of electrical leads at S, which lead to the recording potentiometer, are positioned in such a way as to momentarily complete a low resistance input circuit into the recorder exactly at the time when the stopcock is turned to stop the rise of the liquid level. A brief excursion of the recorder trace is obtained, marking the start of the wicking time interval. When enough liquid has reached the absorbent pad to wet it, a deflection of the recorder trace occurs marking the end of the run. The distance between the yarn-pad juncture and the liquid level is read with a cathetometer. If the vapor pressure of the liquid is sufficiently high, the cell can be completely dried under vacuum between runs and the same system used repeatedly. With other liquids, a new yarn sample must be used for each run.

b. Experimental Results. The application of the surface velocity technique to graphite yarn and relatively simple liquid systems produced results in complete accord with the relative wetting rates obtained by the mass pickup technique. In addition, the surface velocity technique was used to measure wicking rates of ERLA 0400 at 50°C on surface-treated graphite yarns. The yarns which were used in these measurements were selected from the group which had been etched in strong oxidizing solutions (Figure 74). As a control, one sample was immersed in hot water to determine any effects which may be induced mechanically by handling, thereby establishing a basis for evaluating the effects of surface treatments on wicking rates. These results, which are shown in Figure 81, demonstrate that the surface velocity technique distinguishes between the effects of different surface treatments.

c. Analysis of Wicking Rate Measurements. Equations describing the flow in capillaries account for the observed wicking rates quite well. Washburn's equation[35] for the rate of flow dh/dt at a height h in a capillary of radius r is

$$\frac{dh}{dt} = \frac{r \nu \cos \theta}{4 \eta h} - \frac{r^2 g \rho}{8 \eta} \qquad \text{(VI E-1)}$$

where ρ, ν, and η are the liquid density, surface tension, and viscosity, respectively, θ is the contact angle, and g is the acceleration of gravity.

Equation VI E-1 arises from the application of Poiseuille's law to flow in capillaries with uniform, circular cross section. Peek and McLean[36] used assumptions which are closer to the actual situation in a yarn bundle to derive the equation
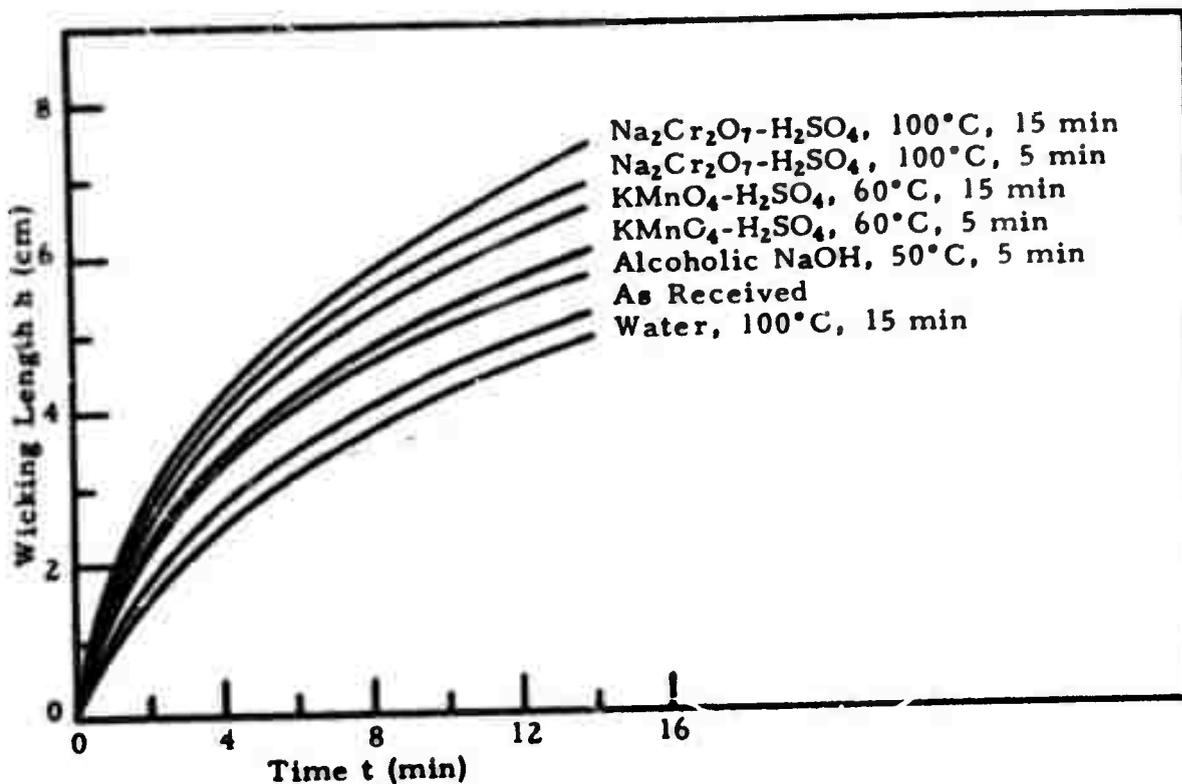
Figure 81. Effect of Surface Treatments of Graphite Yarn on Wicking Rates Determined by Surface Velocity Technique.

$$\frac{dh}{dt} = \frac{2\xi \int_{-\infty}^{\infty} r^{-1} \phi(r)\,dr - h\rho g}{8\eta h \int_{-\infty}^{\infty} r^2 \phi(r)\,dr \int_{-\infty}^{\infty} r^{-4} \phi(r)\,dr} \qquad \text{(VI E-2)}$$

in which

$\phi(r)dr$ = fraction of the total number of channels having a radius between r and $r + dr$

and ξ is a parameter called the penetration tension which is equal to $v\cos\theta$ when the only driving pressure is that due to capillary force. This equation may be written in the form

$$\frac{dh}{dt} = \frac{A\xi}{4\eta h} - \frac{B\rho g}{8\eta} \qquad \text{(VI E-3)}$$

-150-

where A and B are constants with values which depend on the distribution function $\wedge(r)$. If all channels have radius r and $\xi = \nu \cos \theta$, the equation of Peek and McLean reduces to Washburn's equation.

An attempt to extract a quantitative measure of the effect of surface treatment on wicking rates has been made by fitting the observed data with the equation

$$\frac{dh}{dt} = \frac{K}{h} \qquad \text{(VI E-4)}$$

which is obtained from either Equation VI E-1 or Equation VI E-2 by neglecting the influence of gravity in retarding the wicking rate. The integration of Equation VI E-4 yields

$$h^2 = 2Kt \qquad \text{(VI E-5)}$$

for the initial condition that h = 0 at t = 0. The observed wicking rate data can be fit reasonably well by this equation, particularly at small heights for which the gravity term is negligible.

A least squares fit of the data of Figure 81 was applied to Equation VI E-5 to determine values, K_s, of K for each treatment, s. A dimensionless figure of merit T_s for the treatment s was then defined by

$$T_s = K_s / K_{H_2O} \qquad \text{(VI E-6)}$$

which compares the wicking rate of yarn after receiving treatment s with the wicking rate of yarn which has only been heated in water. Table XIII lists T_s factors for the wicking rates of epoxy ERLA 0400 at 50°C on graphite yarns with various treatments; the data used is taken from Figure 81.

TABLE XIII

WICKING RATE T FACTORS FOR
SURFACE TREATMENTS OF GRAPHITE YARN

Treatment s	T_s
Washed in 100°C H_2O, 15 min	1.00
As Received	1.22
Alcoholic NaOH, 50°C, 5 min	1.54
$KMnO_4$ - H_2SO_4, 60°C, 5 min	1.72
$KMnO_4$ - H_2SO_4, 60°C, 15 min	1.97
$Na_2Cr_2O_7$ - H_2SO_4, 100°C, 5 min	2.36
$Na_2Cr_2O_7$ - H_2SO_4, 100°C, 15 min	2.53

The T factors increase with increasing severity of surface treatment and provide a convenient numerical comparison of the effects of different surface treatments.

Wicking rate measurements show that the bundle of yarn can be treated fairly accurately as a system of capillaries. The rate of penetration of resins into these capillaries is governed by the equation of Peek and McLean (Equation VI E-2), which defines the relative contributions of capillary diameter distribution, resin viscosity, surface tension, and contact angle to wicking rate. The surface velocity method for determining wicking rates has provided a simple quantitative measure for determining the effect of surface treatment on yarn wicking rates.

Contact angle and wicking rate measurements are complementary. When both are applied to the same fiber-resin system, the fiber and resin parameters which lead to best overall wetting are well defined. These parameters can then be balanced against processing constraints such as resin pot life and fiber strength and the results used to aid in the definition of the optimum conditions for resin loading.

F. Fabrication of NOL Rings
(A. A. Pallozzi, Union Carbide)

The filament-wound ring constitutes an accepted and standardized method for evaluating unidirectional fiber composites. Advantages of this type of specimen are simplicity and low cost of sample preparation and fabrication, reproducibility of test results, and relative ease of interpreting test results.

The method devised by the Naval Ordnance Laboratory[37] is being used to prepare rings and measure their properties. A schematic drawing of the apparatus used to wet-wind rings from carbon and graphite yarn with epoxy resins is shown in Figure 82. Prior to fabricating ring specimens, the apparatus was modified to meet ASTM standards.[38]

The method of preparing ring specimens consists of passing the carbon or graphite yarn through an electric furnace maintained at $900 \pm 10°C$ in a nitrogen atmosphere. This treatment removes any volatile constituents present on the yarn surface. From the furnace, the yarn passes through a thermostat-controlled resin bath, over and between two grooved rollers designed to control tension, and onto a rotating split mold. When the yarn passes through the resin bath, it is under low tension to facilitate resin infiltration between the filaments. Tension on the resin-coated yarn is controlled by a magnetic clutch, used as a brake, which varies the drag on the tension rollers.

Tension on the yarn affects the amount of resin which is squeezed out on the mandrel during the wet-winding operation; consequently, a limited degree of control over fiber-resin ratio in the composite is achieved.
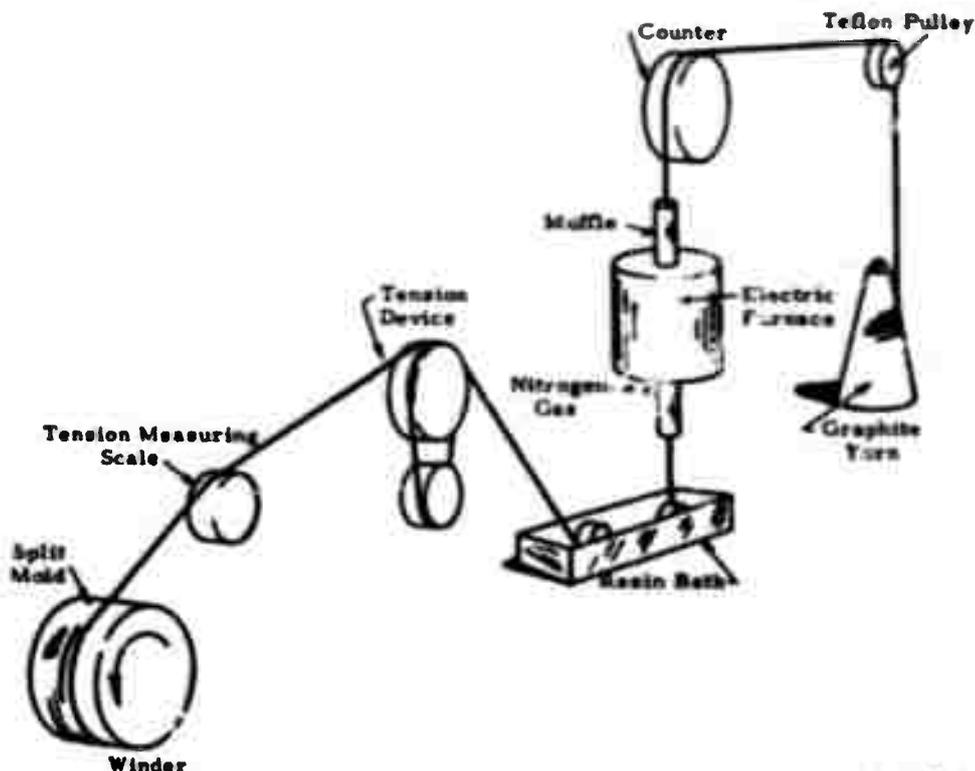
Figure 82. Schematic Diagram of Ring Winding Apparatus.

N-8612

Immediately after the ring is wound, the ring and mold are removed from the winding machine and placed on a rotating shaft in an oven to cure the resin. After the resin is cured, the split mold is disassembled to remove the ring. Prior to physical testing of the cured ring, peripheral resin-rich areas are ground away, and the ring is machined to close dimensional tolerances.

G. Effect of Fiber Content Upon Composite Properties
     (A. A. Pallozzi, Union Carbide)

1. Fabrication of Rings

A series of filament wound rings were fabricated at three levels of winding tension in order to determine the effect of winding tension on the fiber-resin ratio and the effect of the fiber-resin ratio on composite properties. Two different lots of low modulus five-ply graphite yarn were used in fabricating these rings; from each lot, eight rings were made at 375 g yarn winding tension, eight at 600 g, and eight at 1100 g. The matrix was epoxy resin ERL-2256 with 19.2 parts of metaphenylenediamine hardener per one hundred parts resin.
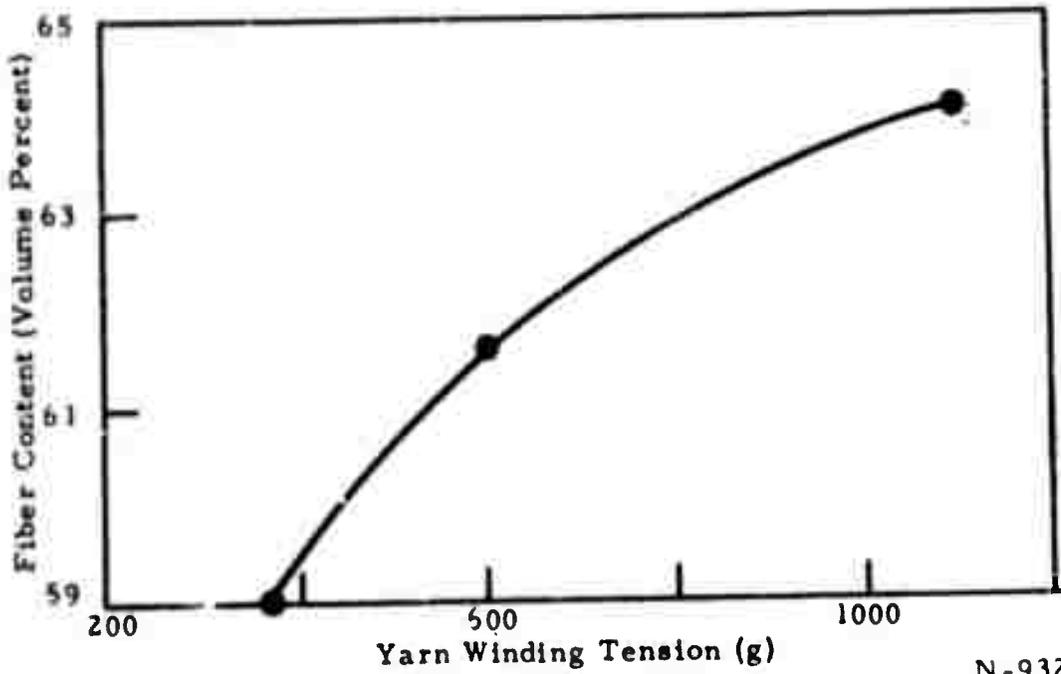
Figure 83. Fiber Content in Resin Rings Versus Winding Tension for 5-Ply Graphite Yarn.

N-9327
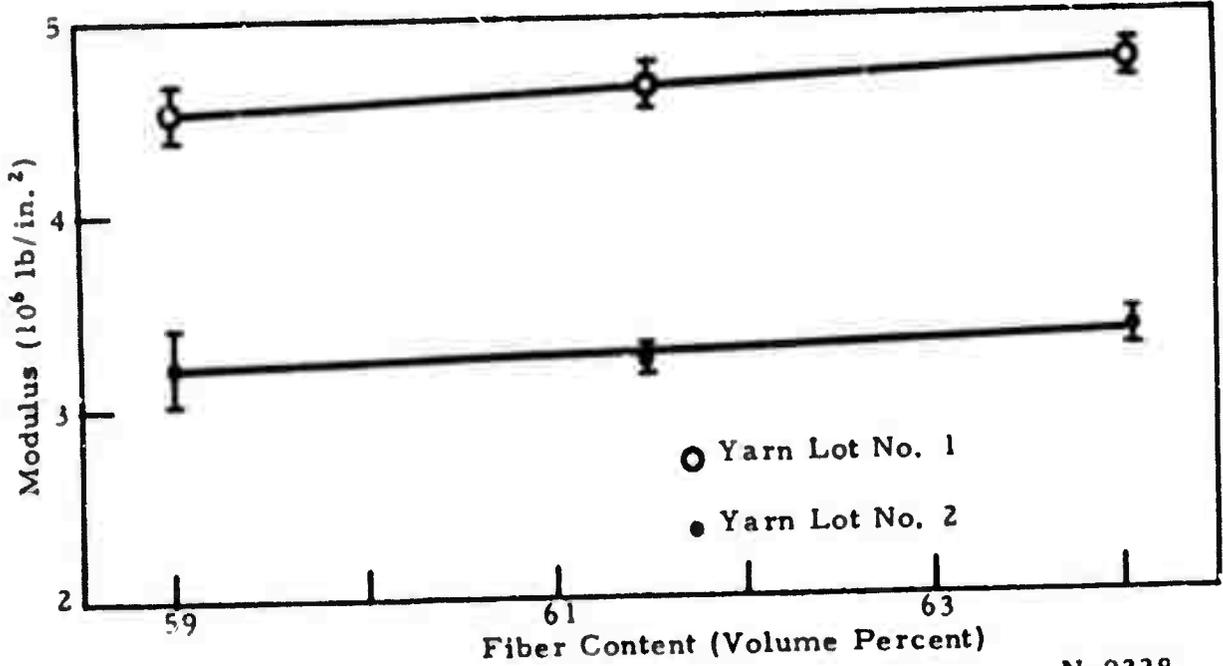
Figure 84. Young's Modulus of Resin Rings Versus Fiber Content.

N-9328

As shown in Figure 83, the fiber content of the cured rings ranged from 59 percent by volume for 375 g tension to 64 percent for 1100 g tension, which is a smaller range than was expected. The Kjeldahl method of analysis for amides and amines was used to determine the resin fraction.

2. Composite Properties

The dependence of the Young's modulus of the composite rings on fiber content is shown in Figure 84. There is a large and significant difference in composite moduli which is dependent upon the lot of graphite yarn from which the composites were made. There was no significant variation of tensile, flexural, and compressive strength of the composite rings with fiber content, nor was there any significant difference in strength of rings from the two lots of yarn.

In Table XIV, the properties are given of monofilaments from the two lots of graphite yarn used in these experiments; the two lots of yarn are

TABLE XIV

GRAPHITE MONOFILAMENT PROPERTIES

Yarn Lot Number	Elastic Modulus (10^6 lb/in.^{2})	Tensile Strength (10^3 lb/in.^{2})
1	7.1	98.6
2	4.6	95.2

similar in tensile strength but substantially different in modulus. In Table XV, the elastic modulus and tensile strength measured on rings made from these lots of yarn are compared with predicted values, calculated

TABLE XV

CALCULATED AND MEASURED RESIN COMPOSITE PROPERTIES

Fiber Content Volume Percent	Elastic Modulus (10^6 lb/in.^{2})				Tensile Strength (10^3 lb/in.^{2})			
	Yarn Lot No. 1		Yarn Lot No. 2		Yarn Lot No. 1		Yarn Lot No. 2	
	Calc.	Meas.	Calc.	Meas.	Calc.	Meas.	Calc.	Meas.
59	4.4	4.5	3.0	3.2	63	60	61	63
61	4.6	4.6	3.1	3.3	65	60	63	60
64	4.8	4.8	3.2	3.4	67	62	65	63

from the law of mixtures on the basis of monofilament properties. There is good agreement between the measured and calculated values of the composite properties. These results lead to the following conclusions: (1) the sampling and testing procedures used for obtaining both monofilament and composite properties are providing data representative of the materials being sampled, and (2) monofilament properties of graphite yarn vary significantly from lot-to-lot; this variation must be taken into account in studies of composite properties.

H. Effect of Yarn Surface Treatment Upon Composite Properties
(A. A. Pallozzi, Union Carbide)

One approach to increasing the shear and compressive strengths of graphite-fiber, resin-matrix composites involves an attempt to improve the graphite fiber-to-resin adhesion. There are many examples where adhesive bond strength has improved with increasing surface roughness. Therefore, an exploratory experiment was performed to see if etching the graphite yarn would improve composite properties. Etching of the yarn was accomplished with a solution of sodium dichromate in sulfuric acid, and the amount of etching was controlled by varying both solution temperature and the time of immersion of the yarn in the solution. Surface area measurements were made on the etched yarn to determine the magnitude of the etching. Measurements of monofilament strengths indicated that etching for 25 minutes at 100°C (the most severe etching conditions used) did not decrease the monofilament strength.

Data for the initial set of etching experiments are given in Table XVI.

TABLE XVI
PROPERTIES OF ETCHED GRAPHITE YARN AND RESIN RINGS

Etching Conditions*		Surface Area of Yarn m^2/g	Flexural Strength of Composite 10^3 lb/in.^{2}	Compressive Strength of Composite 10^3 lb/in.^{2}
Solution Temp. °C	Immersion Time min			
Unetched Yarn	---	4	71	63
50-55	5	4	57	124
	10	5	47	134
95-105	5	8	35	105
	10	20	37	136
	20	12	28	---
	24	23	28	---

*Yarn Lot No. 4

As the severity of the etching was increased by increasing the solution temperature or immersion time, the surface area of the yarn tended to increase continually and the composite flexural strength tended to decrease continually. The decrease in flexural strength appears to be in conflict with the fact that the monofilament strength did not change; this point will be investigated further. All etching conditions caused the compressive strength to increase by about a factor of two; it appears that, within this range, the increase in strength is independent of the severity of the etching conditions. Short beam shear specimens made with etched yarn broke in tension at the outside surface instead of in shear. This fact together with the increase in compressive strength indicates that etching the yarn probably increases the fiber-resin adhesion and the composite shear strength.

The initial etching experiments suggested that less severe etching conditions might be found which would not seriously decrease the flexural strength but which would still significantly improve the shear and compressive strengths. A second set of etching experiments was carried out with a solution temperature of 50 to 55°C and at immersion times of 0.5, 1, 2, and 5 minutes. Rings were wound from yarn lots numbers 1 and 3. The dependence of compressive and flexural strengths on yarn immersion time is shown in Figure 85 for both the first and second set of etching experiments. Again, a large increase in compressive strength was obtained, a result which is almost independent of length of immersion time and of the yarn lot used in the ring. The flexural strength results are more complicated. For yarn lots number 3 and number 4 etched at 50°C, the flexural strength decreased only slightly for up to 5 minutes of yarn immersion. On the other hand, an etch of 0.5 minute caused the flexural strength of yarn lot number 1 to decrease by 40 percent.

Similar experiments on the tensile strength of rings wound with etched yarn of lots numbers 1 and 3 confirmed the flexural strength results. For lot number 3, a 2-minute etch decreased the tensile strength by only approximately 10 percent, whereas for lot number 1, both 0.5 and 1 minute etches decreased the tensile strength by over 50 percent.

From these experiments, it appears that a suitable light etch may double the composite shear and compressive strengths and not decrease the tensile and flexural strengths by more than 5 to 10 percent. However, on some lots of yarn, a very light etch causes the tensile strength to decrease by 50 percent; thus much more must be learned about characterizing the yarn and the etching process before reliable results can be consistently achieved.
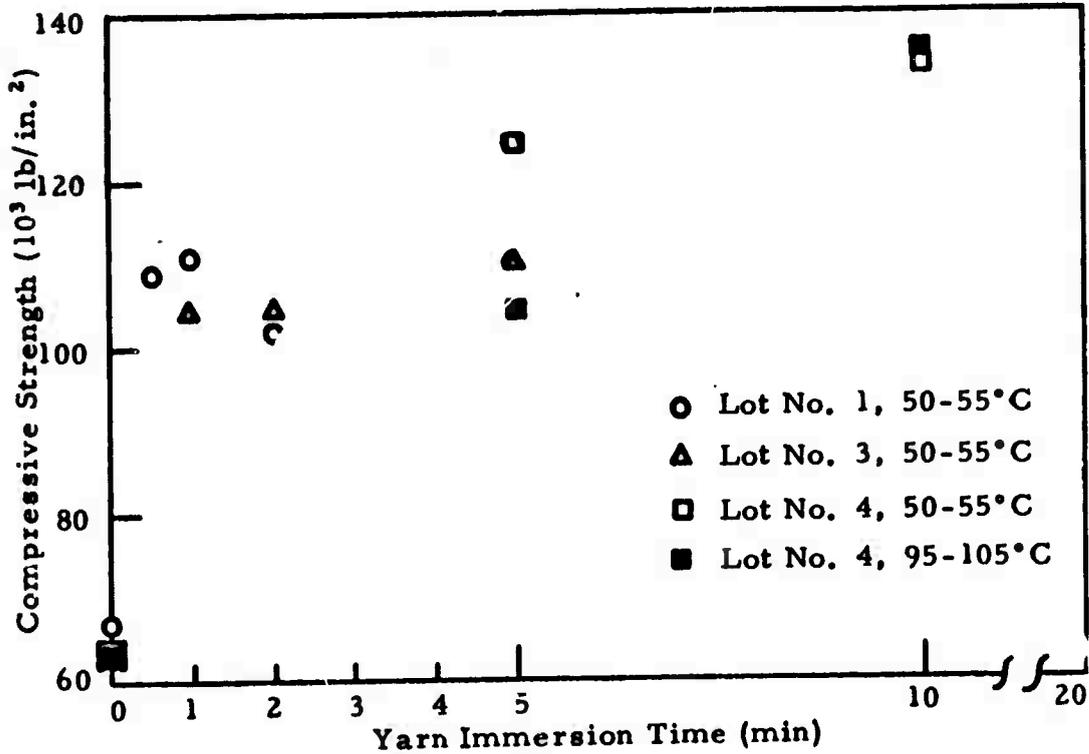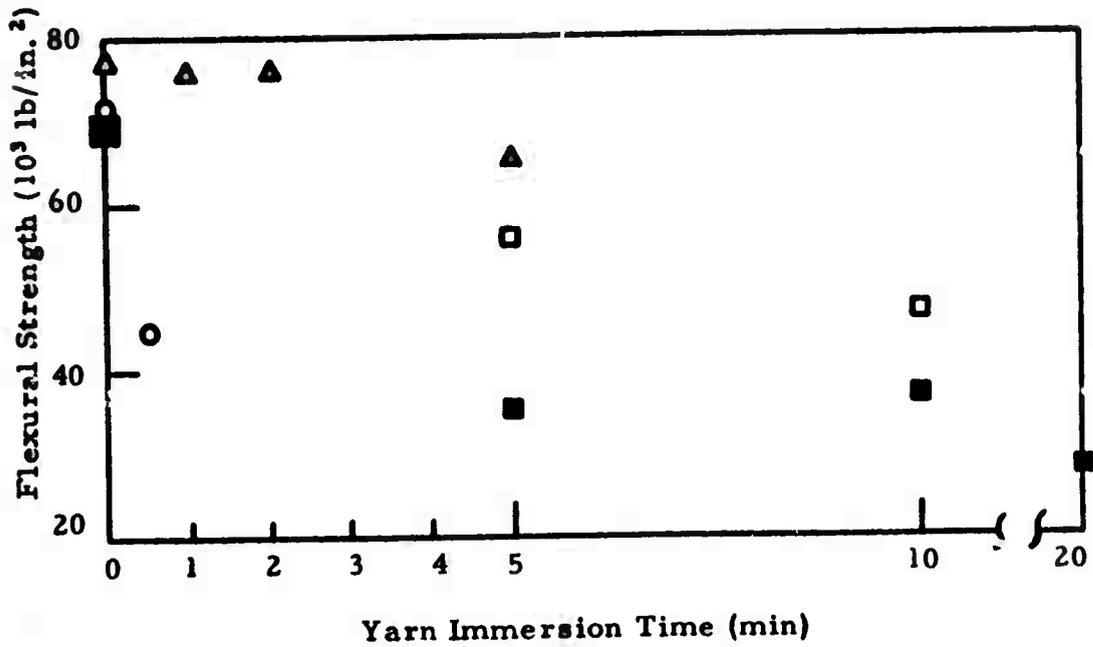
N-9482

Figure 85.   Flexural and Compressive Strengths of Resin Rings
Versus Etching Time of Yarn.

SECTION VII

MICROMECHANICS AND DESIGN DATA STUDIES FOR FIBER COMPOSITES

Improved structural design can be achieved in many ways including advancements in optimization techniques, introduction of new materials and design concepts, and improved methods of structural analysis. Although the development of new materials and design concepts possess the greatest payoff, a complete understanding of material behavior and limitations is a prerequisite to any efficient design. The full potential of both the material and the design may never be realized if the practicing engineer is not provided with reliable design data.

In order to improve the understanding of the behavior and limitations of carbon fiber composites, the following projects were undertaken. In Section VII A the current status of stiffness predictions for filamentary composites is discussed, and an approach is outlined for analytically predicting composite stiffnesses by using computer-simulated random models. An examination of test methods and possible improvements for the experimental determination of design data is described in Section VII B. Studies of three-dimensional photoelastic models of filamentary composites are reported in Section VII C. The initial effort has been to determine curing stresses and fiber end effects. A comparison of predicted unidirectional properties of composites fabricated from various constituents is given in Section VII D. Finally, a procedure for determining bidirectional composite properties from a series of tests on pressure bottles is presented in Section VII E.

A. Prediction of Stiffness Properties
(Professor Kicher, Case Institute)

1. Introduction

The design of efficient fiber composites requires the availability of accurate means of analyses which predict such behavioral quantities as stresses, strains and displacements. The displacements predicted by the analysis are then compared to the limiting values to determine if the design adequately performs its function. The analytically predicted stresses and strains are used in conjunction with some accepted failure criterion to determine if the material is sufficient to support the loads. Design situations for which minimum weight consideration are important generally result in thin structural elements and must also be analyzed for failure in one or more modes of buckling.

Typical of light weight structures for aerospace applications are the class of stiffened shell structures, which are in service presently. For these metal shells, buckling can occur in a gross manner or in any one of the elements of stiffener or skin. While fiber shells will be different in structural concept buckling considerations should also be included in any minimum weight design study. Therefore, it is imperative that accurate analytical tools for buckling failure predictions be available before any optimization study can proceed.

Stiffness properties, which are the basic data for stress, strain, displacement and buckling analyses, therefore are given a high priority. In the design of conventional metal structures the prediction of stiffness properties is rather straightforward since the material is isotropic. However for fiber composites the prediction of stiffness properties is more complicated but the designer can now specify the design of the material in addition to the more traditional parameters controlling size and configuration. The development of a capability to determine optimum designs must be based on reliable analyses which in turn must have as data accurate stiffness properties.

2. Mathematical Models for Stiffness Properties

Empirical representations of stiffnesses for fiber composites based on experimental data is impractical for all but the simplest cases of optimum design studies. The inclusion of pertinent parameters leads to a prohibitive number of specimens to be tested. The development of rational bases for mathematical prediction of these data is the most feasible approach as has been shown by studies on glass-fiber, epoxy composites. The application of these concepts to carbon fiber composites started with a study of the published theories.

The prediction of the modulus in the direction of the fibers for a unidirectional composite has been based on the well-known Rule of Mixtures:

$$E_L = E_f - (E_f - E_m) V_M \qquad \text{(VII A-1)}$$

where

E_f = fiber modulus

E_m = matrix modulus

V_m = percent matrix by volume

This relationship can be developed from simple strength of materials concepts[39] based on the assumption of uniform strain, i.e., each constituent carries a load proportional to its stiffness. It can also be developed from the more rigorous bounding approach based on energy principles[40] assuming a parallel model as an upper bound. Finally it can be developed in a more sophisticated manner and then reduced as a simple approximation[41] to a more exact theory. Other improvements in this relation have been attempts to account for misalignment[42].

The prediction of other elastic constants, such as (1) the major Poisson's ratio, ν_{LT}, (2) the transverse modulus, E_T, and (3) the shear modulus, G_{LT}, has not resulted in such simple relations. In fact, the relative location of the fibers seems to play an important role in the predictions. For example,

-160-

Table XVII gives a summary of the transverse modulus E_T and the shear modulus G_{LT} for various mathematical models based on a volume ratio of 40 percent matrix, a fiber modulus $E_f = 10.6 \times 10^6$ psi, and matrix modulus $E_m = 0.5 \times 10^6$ psi.

TABLE XVII

COMPARISON OF TRANSVERSE AND SHEAR MODULI CALCULATED BY DIFFERENT MODELS

Model		$E_T(10^6 psi)$	$G_{LT}(10^6 psi)$
Netting Analysis[39]		0.0 to 0.5	0.185
Series of Fiber and Matrix[40]		1.16	0.313
Hexagonal Array[41]		1.35	0.400
Random[42]	Fibers Isolated	1.35	0.400
	Fibers Touching	2.20	1.280
Strips of Circular Fibers[43]		1.98	0.480
Periodic Rectangular Array[44]		2.00	1.870
Random Packing[45]		1.65	0.347
Parallel Model of Fiber & Matrix[40]		---	1.750

Omitting the results for netting analysis, the transverse modulus is seen to vary from 1.16×10^6 to 2.20×10^6 for the various mathematical models. A photomicrograph of the cross section will show that the fibers assume none of the proposed regular packing models but rather a random distribution. Therefore the observed spread of the experimental data is probably due to the variations of manufacturing rather than to the packing of the fibers. Using a truly random set of fiber packing models, it is thought that the analytical transverse modulus will have a pronounced mean and a small standard deviation.

3. Experimental Data and Correlation

Attempts to correlate the analytical prediction using the above models with experimental results have enjoyed moderate success. The best correlation is between the longitudinal modulus E_L and the Rule of Mixtures. The prediction of E_T and G_{LT} does not enjoy the same experimental substantiation. Several empirical coefficients intended to give a rational basis for modifying the analytical curves have been introduced. For example, Tsai has suggested the use of a factor k to account for misalignment. Adaptation of this coefficient to the Rule of Mixtures would lead to

$$E_L = k [E_f - (E_f - E_m) V_m]$$ (VII A-2)

Efforts to account for the relative locations of fibers have lead to the following two theories:

Contiguity factor, $C^{(43)}$ - The coefficient C assumes a value of zero for isolated filaments and unity for contiguous filaments. The experimental data fits between a band for $C = 0.0$ and $C = 0.4$.

Mean Fiber spacing, $R^{(45)}$ - To account for the random spacing of fibers the use of the coefficient R has been suggested, where

$$R = \frac{D}{S} = \frac{4}{\pi} V_f = 1.275 V_f$$ (VII A-3)

where

D   =   filament diameter

S   =   average fiber spacing

V_f =   percent fibers by volume

This approach of smearing a random distribution of fibers by using some equivalent coefficient appears to give spurious results. Therefore, an approach using random models and in some way accounting for the location of the fibers should give more meaningful results.

4. Random Models

A computer program has been developed which generates models with randomly distributed fibers. There are two input parameters which control the proximity of fibers and have been used to generate models with packing densities up to 75 percent by volume of fibers. Figure 86 shows a plot of a typical set of results where the packing density of fibers is 54 percent by volume. This model could then be used to determine a contiguity coefficient C, the mean fiber spacing R or finally the elastic constants could be found directly for this model. Obviously a closed form solution for the model would be difficult if not impossible. Therefore some numerical approach will have to be used. If the computer developed model were analyzed using either a finite difference scheme or a discrete element matrix method, coefficients representing the gross elastic constants could be found.

The computer program was developed to simulate the winding process and is based on the assumption that the handling of fibers in a yarn or roving condition is only a manufacturing device. Once the resin impregnated composite is cured, association of fibers with various yarns or rovings is impossible. An x-y coordinate system is defined such that the x axis points along the direction of winding advancement, while the y axis points in the direction of increasing thickness. The x coordinate of the center of the
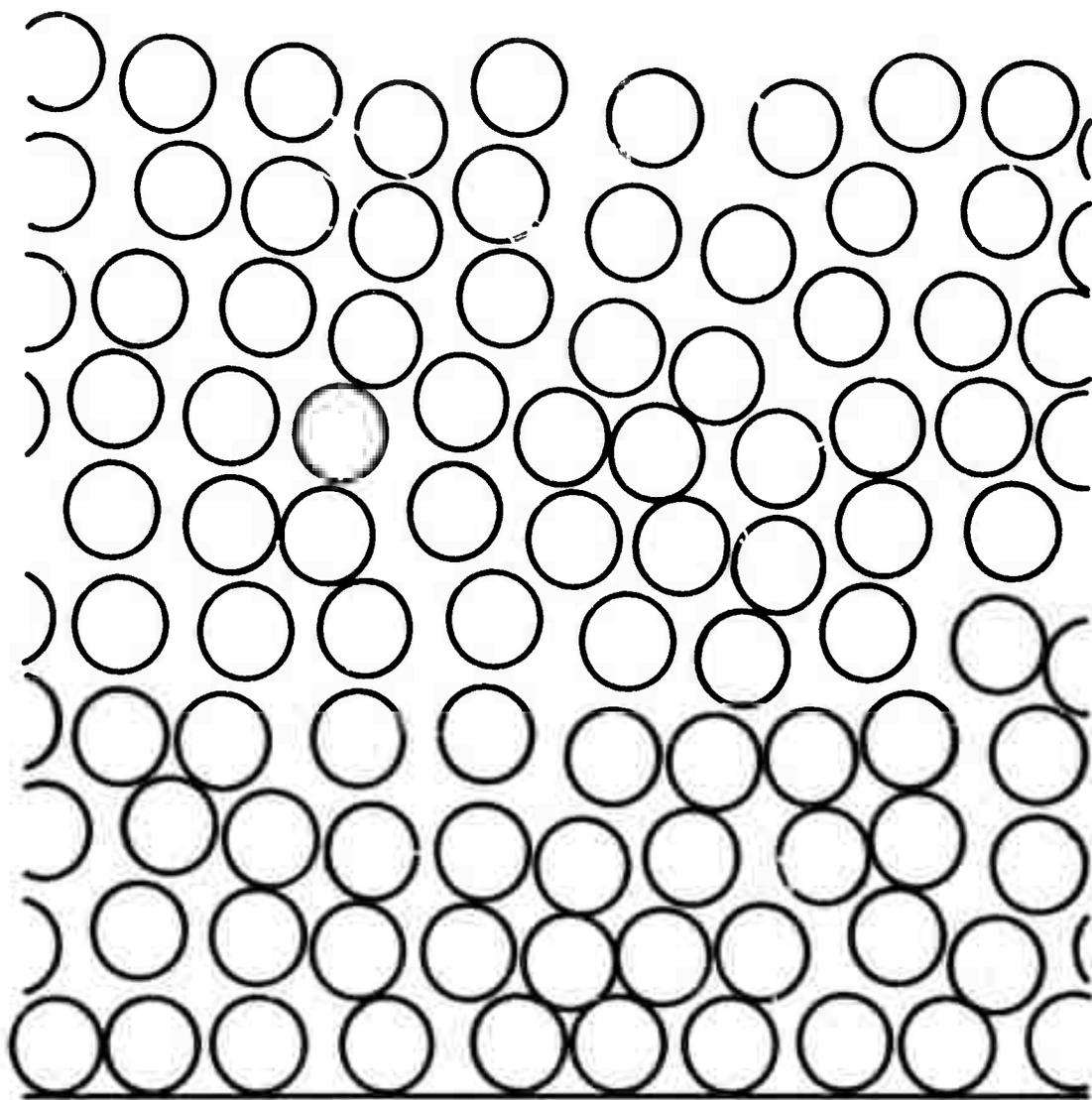
Figure 86. Computer Simulated Random Packing.

i^{th} fiber must be at least 2R away from i's left adjacent neighbor but less than 4R else another fiber could occupy the vacant space. In summary then

$$x^{i-1} + 2R \leq x^i \leq x^{i-1} + 4R \qquad \text{(VII A-4)}$$

Using a standard computer routine to generate random numbers, N, between zero and unity the following can be written

$$x^i = x^{i-1} + 2R + N_1 \left(\frac{2R}{C_1}\right) \qquad \text{(VII A-5)}$$

where C_1 is a proximity coefficient indicating how close the fiber is placed to the geodesic. If the process is advancing too fast for the geodesic, C_1 will assume a small value. If the wing advancement is slow compared to the geodesic C_1 will be large.

The y coordinate is determined in a similar manner, once the row of fibers adjacent to the mandrel is laid down. For this first row, it is assumed that all the y coordinates of the centers are R. Thereafter the fibers are moded vertically (x^i = constant) such that the center of the nearest fiber below is at a distance greater than 2R but less than 4R. Again if the fibers were further than 4R apart, the possibility of another fiber occupying this space arises. In summary then the distance between vertically adjacent fibers, L is bounded by

$$2R \leq L \leq 4R \qquad \text{(VII A-6)}$$

Again using a standard computer routine to generate random numbers, N_2, between zero and unity, the following can be written

$$L^i = 2R + N_2 \left(\frac{2R}{C_2}\right) \qquad \text{(VII A-7)}$$

The parameter C_2 is a proximity coefficient indicating the winding tension. If the winding tension is high the value of C_2 will be high. Typical running times for the generation of each model has been approximately 15 seconds. Voids in the packing could be introduced by using an additional random number generator to determine the presence or absence of a particular fiber. In addition voids could be introduced by allowing the fibers to be laid down at a distance greater than 4R from its neighbors. However, strict control over the void content would not be possible using this latter scheme.

In addition to the random location of fibers, these same ideas could be applied at random distribution of fiber diameters, for, say, glass fibers which may vary as follows

$$R_L \leq R_i \leq R_u \qquad \text{(VII A-8)}$$

The cross section of a carbon fiber cannot be assigned a single radius to identify its shape. However if for each carbon fiber cross section a minimum and maximum radius (see Figure 87) were assigned using a random number generator, then the location of fiber centers could be determined. The constraint on the location of the fiber center would be more complicated and would look like the following: (See Figure 88)

$$x^{i-1} + R^i_{min} + R^{i-1}_{max} \leq x^i \qquad \text{(VII A-9)}$$

and

$$x^{i-1} + R^i_{max} + R^{i-1}_{min} \leq x^i \qquad \text{(VII A-10)}$$

where now the x coordinate must satisfy both constraints. Similar expressions can be developed for the distance between vertically adjacent fibers for the solution of the y coordinate. The total area occupied by that fiber must be between πR_{min}^2 and πR_{max}^2, therefore the fiber area A_i could be expressed as

$$A_i = \pi R_{min}^2 + \pi N_3 (R_{max}^2 - R_{min}^2) \qquad \text{(VII A-11)}$$

These models will be used to determine the effects of packing on the elastic constants, particularly E_T and G_{LT}. Methods of matrix structural analysis using two and three dimensional finite elements readily lend themselves to such calculation. There is also a possibility of developing specialized finite elements that contain a reinforcing element. A study of these techniques is currently underway for this purpose and will also be used for microstress analysis to numerically study the failure mechanisms of fiber composites. Estimates of the mean and the standard deviation of the elastic constants will be made. Relatively low values for the standard deviation will indicate that the scatter in the experimental data is not due to the fact that the real composite assumes drastically different packing arrangements. This then could lead to the identification of a mathematically representable standard model which best represents the composites.
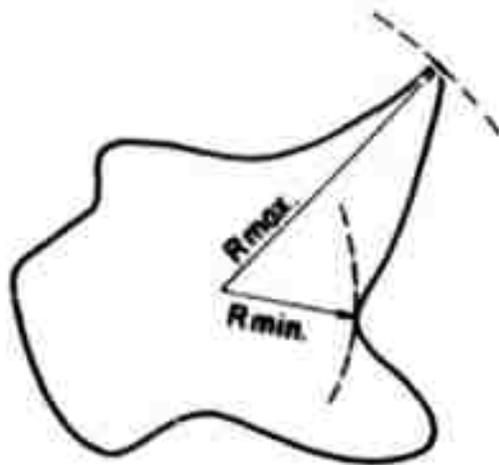
Figure 87. Hypothetical Cross Section of a Carbon Fiber.
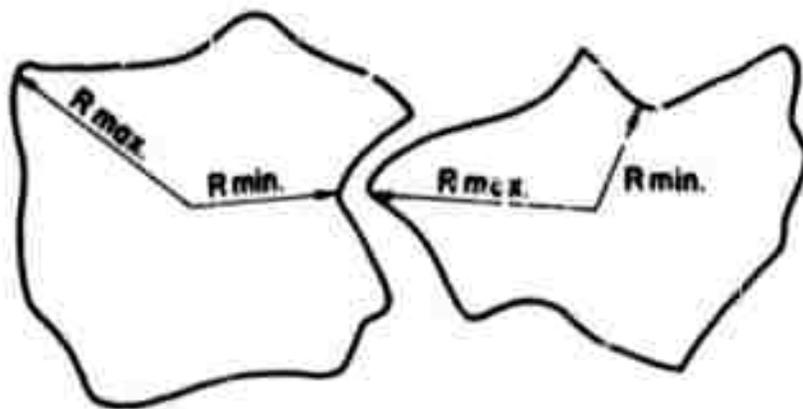
Figure 88. Location of Fiber Centers for Carbon Composites.

B. Test Methods for Design Data
(Professors Goble and Kicher and Mr. F. Campbell, Case Institute)

A study of existing test methods for filamentary composites was initiated by examining the split D test, which is a standard test for determining tensile properties of unidirectional composites. It has been shown through experimental data that the stresses in the NOL ring vary radially due to the bending at the split and circumferentially due to both bending and friction.

A photoelastic investigation will attempt to determine the effects of stress concentrations in the NOL ring at the split separating the two halves of the test fixture, and the distribution of stress in the circumferential stress distribution will also be studied.

In order to carry-out this photoelastic study on the split D test for NOL rings, a special fixture had to be built. Figue 89 shows the split D fixture with a photoelastic ring in place. This fixture, which was not designed for testing fiber composite rings, allows a maximum of area for photoelastic observation in the polariscope. Figure 90 shows the loading frame used in the polariscope with the photoelastic NOL ring in place on the special split D fixture. Finally Figure 91 shows the NOL ring in the polariscope. The observed variations in the NOL ring are the isochromatics, lines of constant difference between principal stresses. The results obtained thus far are limited but indicate that the method of fabrication used has produced a photoelastic test specimen with an irregular inside surface. These irregularities show up as surface stress concentrations in the polariscope. An improved method of fabricating test specimens will have to be developed before the experimental study can proceed.

At the same time, the development of a new test fixture for determining the tensile data on unidirectional rings has continued. The goals specified for the design are as follows:

(1) uniformly distributed stresses,
(2) accessible for visual observation, and
(3) loaded in any Universal Testing Machine.

The basic concept of a proposed design which achieves these goals is to load the ring with an internal contact pressure produced through the Poisson's expansion of a longitudinally compressed rubber insert. Figure 92 shows the parts of a test fixture which is based on this concept. In the lower portion of the figure are the rubber insert, a carbon NOL ring and two constraining rings used to insure uniform loading on the specimen. Figure 93 shows the assembled test fixture in the foreground and the load fixture (inverted) in the background. Finally, Figure 94 shows the assembled fixture with the loading head in place. This fixture is then placed in a universal testing machine and loaded in compression. Due to the Poisson's expansion of the rubber, the NOL ring is loaded in tension. Experimental results are not yet available for discussion or evaluation.

Figure 91

Photoelastic Pattern
in an NOL Ring.

Figure 90

Loading Frame.

Figure 89

Split D Fixture for
Photoelastic Investigation.
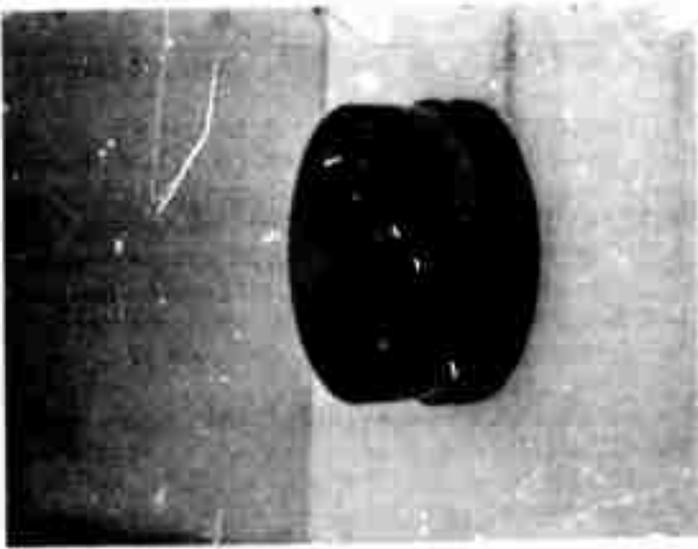
Figure 94

Assembled Tensile
Test.
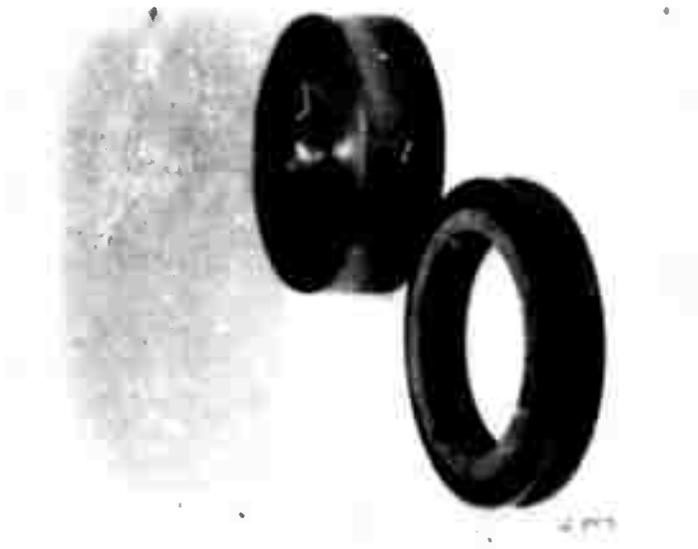
Figure 93

Tensile Test Showing Rubber
Insert, Carbon Ring and Steel
Retainer Rings.
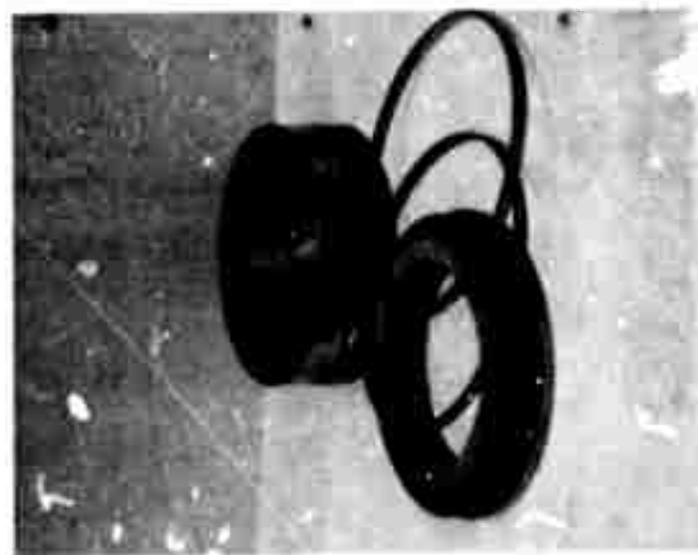
Figure 92

Tensile Test
Components.

C. Three Dimensional Photoelastic Model of Filamentary Composite
      (Professor Wright and Mr. D. Weitzenhof, Case Institute)

The object of this research is to develop a technique for accurately determining the stresses caused by loads applied to filamentary composite systems. This study will be done using three-dimensional photoelastic models, since all effects of loading and geometry may not be present in two-dimensional models. Unfortunately, three-dimensional models also have their shortcomings, the most important of which are the apparent stresses introduced by the stress freezing cycle into the two-component system. This problem is the major subject of this report.

The research program includes several types of models to be tested and analyzed. These models will be compared and their results correlated. Two dimensional models will be used to determine the general stress distributions. Three-dimensional models of similar configurations will then be analyzed to give the exact stress distribution for a given case.

1. Test Method

The test method used is the technique of stress freezing. This utilizes an epoxy material (Hysol 4290 in this case) which, when loaded, heated to 270°F, and cooled slowly, retains part of the strains induced by the applied load. This heating, unfortunately, causes differential expansion between the aluminum fiber and the epoxy matrix. The induced strains show up as fringe patterns which must be deleted from loaded models so that actual stresses may be calculated.

Other difficulties involved with the photoelastic models are (1) the mottling of the material (the wavy lines in the photographs of isochromatic patterns), which can be eliminated by using a higher quality material and (2) cast-in strains, which can be removed by annealing the material for several hours at 270-280°F.

The two-and three-dimensional models under consideration are: (1) unloaded single fiber model (Figure 95), (2) loaded single fiber model (Figure 96), and (3) loaded and unloaded multiple fiber models. All of the above studies will be completed using fibers of various shapes.

The loading fixture for the three-dimensional models is shown in Figure 97. The loading set-up including the model is shown in Figure 98. The structure surrounding the model is the thermostatically controlled oven. The loading fixture assures pure tensile loading through a ball joint shown in Figure 97. The tensile load, P, will be about 150 lbs.

2. Mathematical Analysis

The method of analysis used is quite simple. The equilibrium equation in three-dimensions for Cartesian coordinates is
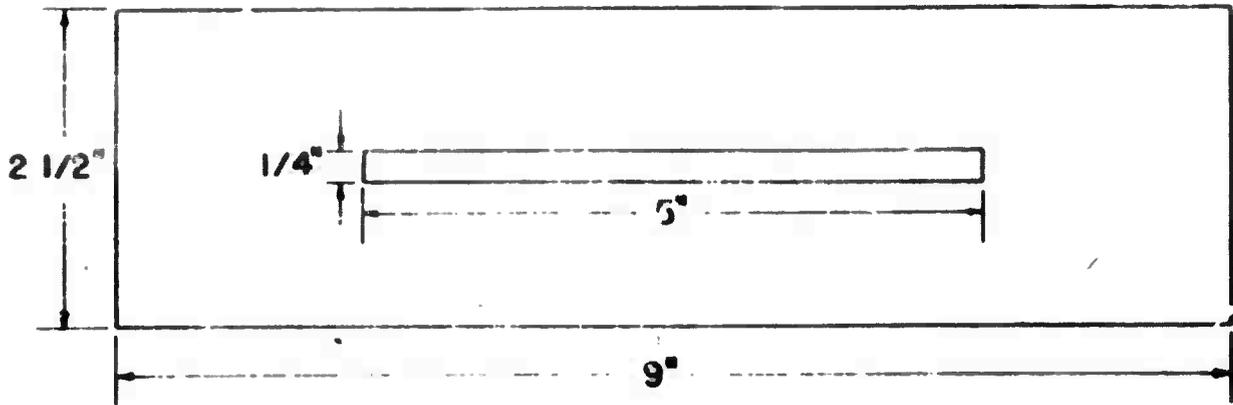
Figure 95. Unloaded Single Fiber Model.

(SCALE – 1/2" : 1")

1/4" DIA

2 1/2"
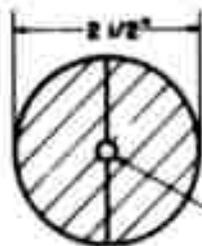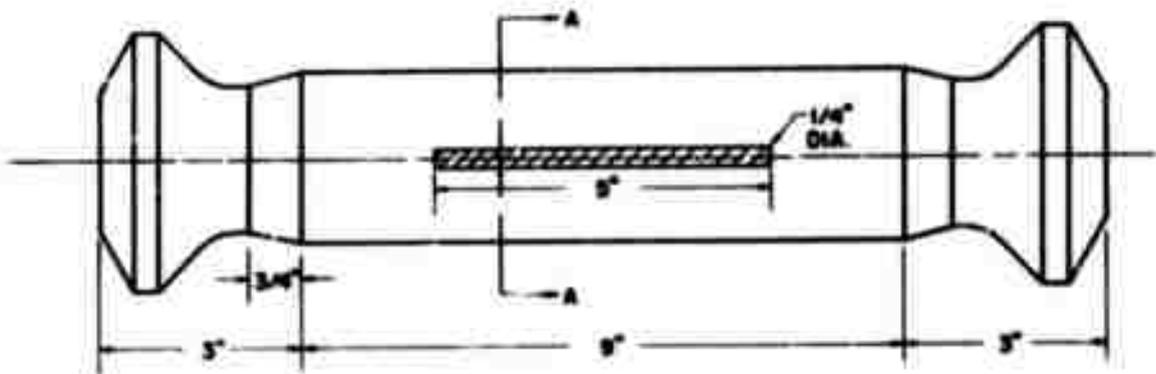
1/4" DIA. ALUMINUM ROD

SECTION A-A

Figure 96. Loaded Single Fiber Model.

Figure 98

Stress Freezing Apparatus in
Thermostatically Controlled Oven.
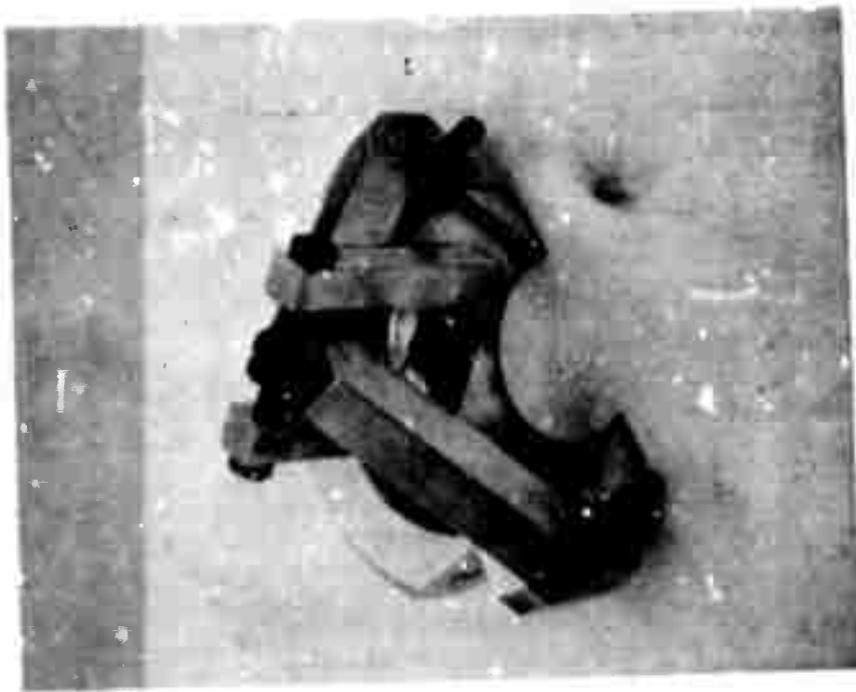
Figure 97

Loading Fixture and
Ball Joint Assembly.

$$\frac{\partial \sigma_x}{\partial x} + \frac{\partial \tau_{xy}}{\partial y} + \frac{\partial \tau_{xz}}{\partial z} = F \qquad \text{(VII C-1)}$$

where F, the body forces, are zero in this case. This equation is modified for use in photoelastic analysis to

$$\frac{\Delta \sigma_x}{\Delta x} + \frac{\Delta \tau_{xy}}{\Delta y} + \frac{\Delta \tau_{xz}}{\Delta z} = 0 \qquad \text{(VII C-2)}$$

or

$$\Delta \sigma_x = - \left(\frac{\Delta \tau_{xy}}{\Delta y} + \frac{\Delta \tau_{xz}}{\Delta z} \right) \Delta x \qquad \text{(VII C-3)}$$

The shear stresses τ are easily calculated from the fringe number and the iso-clinic angles at the point in question. A starting point is selected where both of the stresses are known, say at a corner where both stresses (σ_x and σ_y) are zero. The data are then taken at a set of points leading to the point in question. The actual calculations will be done on the Univac 1107 computer.

Slices were taken from the unloaded three-dimensional model, and photographs were made of the photoelastic patterns. The position of the slices is shown in Figure 99.

Slice No. 1 is shown in Figures 100 and 101. In Figure 100, the aluminum fiber is still in position. In Figure 101, it has been removed from the matrix. It can be seen in Figure 101 that before the aluminum rod was removed, the maximum number of fringes was about eleven. After removal of the inclusion, the number of isochromatic fringes dropped to about eight. With a photoelastic constant of 1.35 psi-in/fringe, the value of the maximum shear stress with fiber included was

$$\tau_{max} = \frac{11}{0.231} \times \frac{1}{2} \times 1.35 = 32.2 \text{ psi}$$

With the fiber removed, the maximum shear was

$$\tau_{max} = \frac{8}{0.231} \times \frac{1}{2} \times 1.35 = 23.4 \text{ psi}$$

The ripples along the fiber were caused by uneven bonding. The dotted line is the zero order fringe. Mottling effects can be seen along the edge of the slice.
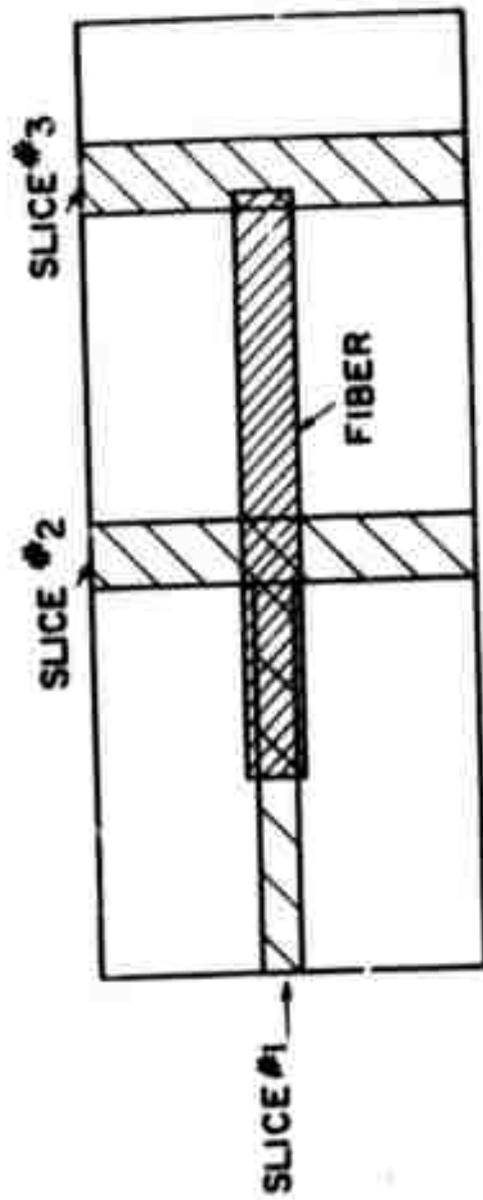
Figure 99. Slice Configuration.

Figure 101

Isochromatic Pattern Slice No. 1
with Fiber Removed, Slice Thickness
0.231 inch.

Figure 100

Isochromatic Pattern Slice No.
1 with Fiber Intact, Slice
Thickness 0.231 inch.

Slices No. 2 and No. 3 are quite similar. Figures 102 and 103 show the 0° and 45° isoclinics respectively from both slices. The symmetry of the isoclinic patterns shows that the expected symmetry of a symmetrical model under symmetrical loading actually exists. The disturbances present in these photoelastic patterns are caused by the mottling effect and do not influence the stresses in the undisturbed portions of the slices. The isochromatic patterns are also somewhat similar as shown in Figures 104 through 107.

Figure 104 shows the isochromatic pattern in Slice No. 2 after the fiber was removed. However, edge effect stresses were present. To eliminate these, the model was dried at 150°F for several days. The result is shown in Figure 105. One of the fringes has disappeared, and the resultant shear stress was

$$\tau_{max} = \frac{1}{0.252} \times \frac{1}{2} \times 1.35 = 2.68 \text{ psi}$$

Figure 106 shows the isochromatic pattern resulting when Slice No. 3 with the fiber present was photographed. Figure 107 shows the same view with the aluminum fiber removed. The maximum shear stress present here was

$$\tau_{max} = \frac{1}{0.134} \times \frac{1}{2} \times 1.35 = 5.0 \text{ psi}$$

The irregularities present in this supposedly radially symmetric system were caused by the non-uniform thickness of the epoxy glue used to join the aluminum fiber to the epoxy matrix. The thicker sections of the glue softened and absorbed part of the temperature-induced strains.

At this time, results are just beginning to be obtained and they represent only a small portion of the planned study. Many more models remain to be constructed, tested and analyzed. From the results obtained thus far it can be concluded that in general the temperature-induced stresses along the length of the fiber are quite low; however, at the ends, the stresses are about an order of magnitude greater.
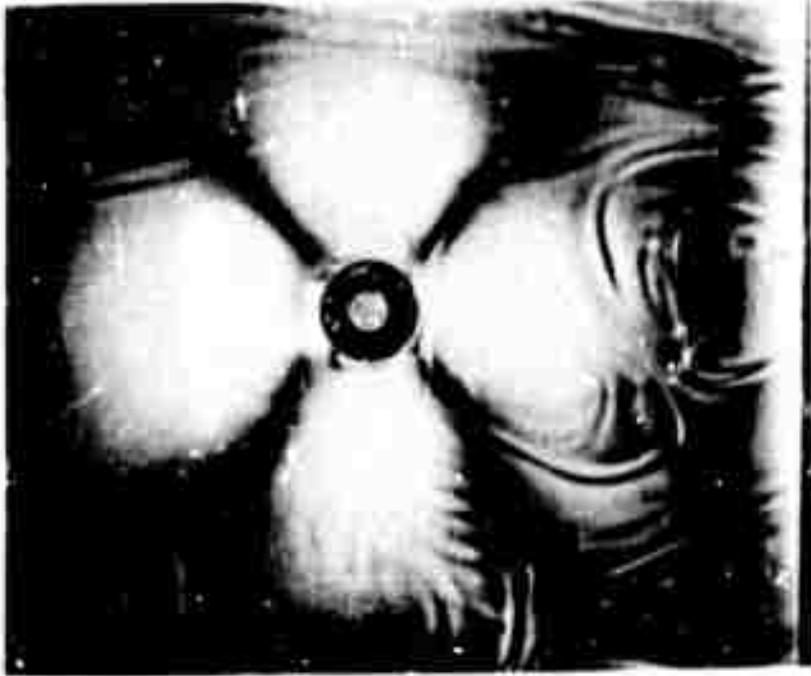
Figure 103

45° Isoclinic, Slice Nos. 2 and 3, fiber removed.
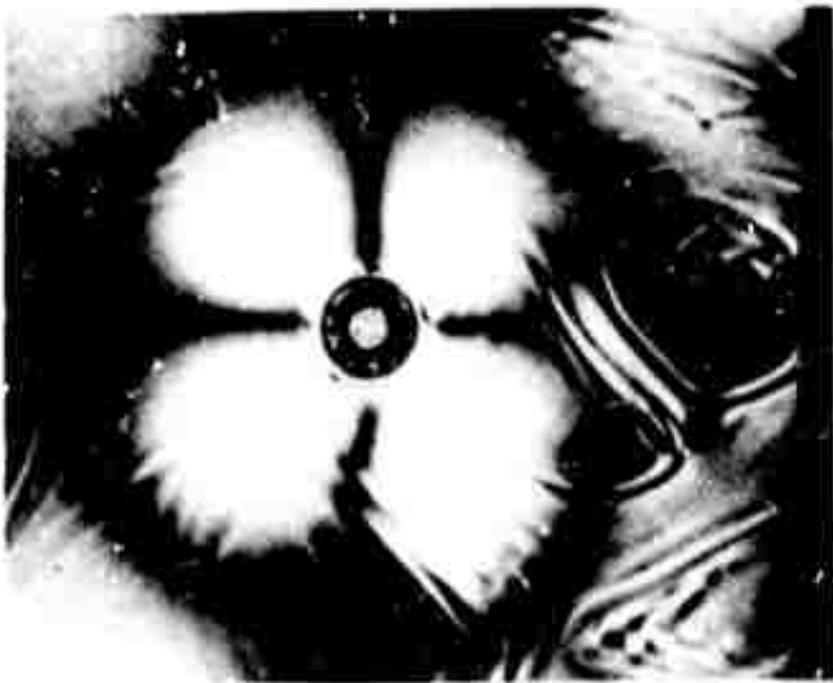
Figure 102

Zero Degree Isoclinic, Slice Nos. 2 and 3, fiber removed.
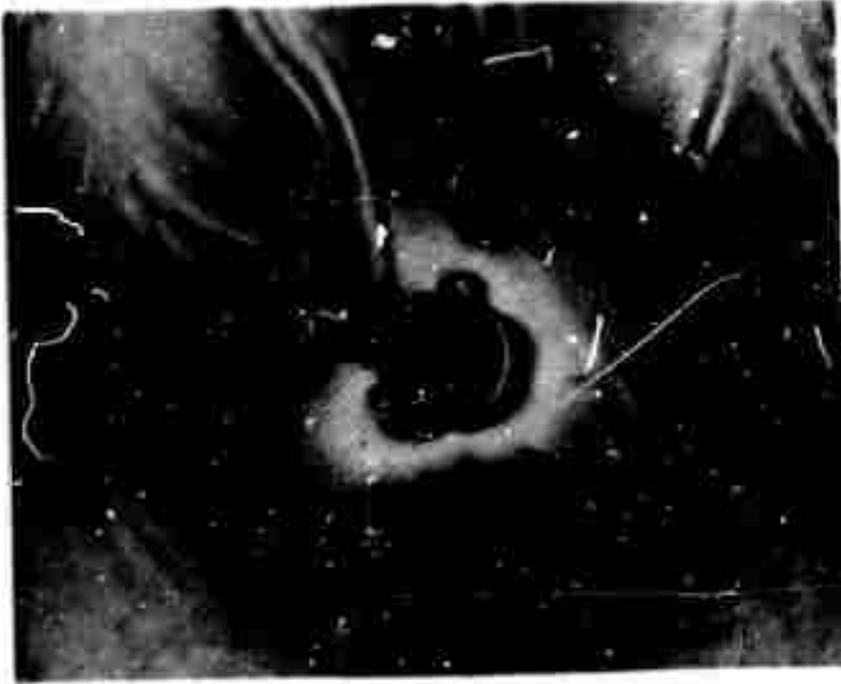
Figure 105

Isochromatic Pattern Slice No. 2
with Fiber Removed After Drying.

Figure 104

Isochromatic Pattern Slice No.
2 with Fiber Removed, Slice
Thickness 0.252 inch.

-178-

Figure 107

Isochromatic Pattern Slice No. 3 with Fiber Removed, Slice Thickness 0.134 inch.

Figure 106

Isochromatic Pattern Slice No. 3 with Fiber Intact, Slice Thickness 0.134 inch.

D. Theoretical Comparison of Unidirectional Composites
   (D.P. Hanley. Bell Aerosystems)

Theoretical estimates were made of the principal mechanical properties of various unidirectional fiber reinforced composites. The objectives of making these calculations were three-fold: (1) to generate data on the performance expected of the newer classes of composite materials, (2) to utilize the approximate data in preliminary design of the representative component, and (3) to determine the magnitude of variability in composite properties as a function of the constituents and distribution within the composite.

Table XVIII summarizes approximate performance comparisons from this study for six composite materials: glass/resin, boron/resin, and carbon/resin, aluminum, titanium, and nickel matrices. The equations used apply to uniaxial tensile loading and are based on Ekvall's model (45).

Table XIX presents in more detail the influence of fiber/matrix composition and content on composite tensile properties. Table XX gives the input properties of component materials upon which Tables XVIII and XIX were based.

The tremendous potential of the carbon fiber and carbon composites using low density matrices is clearly evident in Figure 108. This figure shows the superposition of data from Tables XIX and XX on recent data from Texaco which compared the specific strength and moduli of conventional structural materials (steel, Al, Ti, Mg) with boron, beryllium, and E-glass. Interestingly, it is seen in Figure 108 that a linear relation between σ/ρ and E/ρ is observed for many of the filament materials and composites. This fact may be of use in later synthesis work to assist automated material selection studies. Significant conclusions at this time based upon the unidirectional composite performance estimates are:

(1) The strengths of the carbon/metal matrix composites will be about the same as present day glass/resin composites and greater than those expected of boron/resin composites.

(2) By far the lowest density structural composite of those considered will be the carbon/resin combination.

(3) The principal composite moduli with carbon or boron and either resin or metal matrices will be increased 5 to 6.5 times that of current glass/resin composites. (The carbon/nickel composite, having the highest modulus, is also the most dense).

(4) Use of carbon or boron fibers with resins will yield composites which have 4.5 times the anisotropy of current glass/resin systems. Using metal matrices and the high-modulus fibers, the anisotropy of the composites will only be 20 to 30 percent of that of the current glass/resin systems.

(5) Modulus/density ratios will be increased by a factor of 7.5 with the use of carbon fibers in place of glass. Increases up to 30 percent will correspondingly be achieved in composite strength/weight ratios.

(6) Plastic deformation in metal matrices surrounding carbon fibers will be encountered under tensile loads applied in the direction of the fibers. Under transverse tensile loads, the matrix strain magnification effect with carbon

TABLE XVIII

APPROXIMATE THEORETICAL COMPARISONS
OF UNIAXIAL COMPOSITES

Strength

Carbon/Ti }	270,000 psi
Glass/resin }	
Carbon/Al }	260,000
Carbon/Ni }	
Carbon/resin	230,000
Boron/resin	195,000

Density

Carbon/resin	0.049 lb/in.^{3}
Carbon/Al	0.065
Glass/resin	0.075
Boron/resin	0.077
Carbon/Ti	0.089
Carbon/Ni	0.116

Longitudinal Modulus

Carbon/Ni	52×10^6 psi
Carbon/Al	47
Carbon/Ti	46
Carbon/resin	40
Boron/resin	39
Glass/resin	8

Anisotropy Ratio (E_L/E_T)

Carbon/resin }	28
Boron/resin }	
Glass/resin	6.2
Carbon/Al	1.8
Carbon/Ti	1.5
Carbon/Ni	1.1

Shear Modulus

Carbon/Ni	18.2×10^6 psi
Carbon/Ti	12.7
Carbon/Al	10.4
Carbon/resin }	
Glass/resin }	0.6
Boron/resin }	

Modulus/Density

Carbon/resin	820×10^6 in.
Carbon/Al	720
Carbon/Ti	520
Boron/resin	510
Carbon/Ni	450
Glass/resin	110

Strength/Density

Carbon/resin	4.7×10^6 in.
Carbon/Al	4.0
Glass/resin	3.6
Carbon/Ti	3.0
Boron/resin	2.5
Carbon/Ni	2.3

TABLE XIX

THEORETICAL PERFORMANCE COMPARISON OF IDEAL UNIAXIAL COMPOSITES

Composite	Matrix Content V_m, V_m	Longitudinal Modulus (E_L)	Transverse Modulus (E_T)	Shear Modulus (G_{LT})	Anisotropy Ratio (E_L/E_T)	Transverse Reinforcement Factor (E_T/E_m)	Density (ρ)	Long Mod to Density Ratio (E_L/ρ)	Transverse Poisson's Ratio (ν_{LT})	Matrix Stress Magnification Factor (E_mT/E_f)	Load Carried by Fibers	Composite Strength	Composite Strength to Density Ratio
Glass/Resin	11.65* 31.25 / 36.5 / 47.5	18 x 10⁶ / 9.2 / 6.9	3.03 x 10⁶ / 1.24 / 1.01	0.75 x 10⁶ / 0.40 / 0.37	4.3 / 5.2 / 6.7	3.1 / 2.7 / 1.9	0.086 / 0.075 / 0.068	125 x 10⁶ / 110 / 100	0.25 / 0.25 / 0.26	33 / 7.5 / 4.4	93.5 / 91.3 / 86.8	311,000** / 283,000 / 213,000	3.65 x 10⁶ / 3.87 / 3.18
Boron/Resin	11.7* / 36.2 / 45.5	50 / 39 / 31	2.28 / 1.40 / 1.03	0.95 / 0.50 / 0.37	21 / 28 / 30	4.3 / 2.3 / 1.9	0.084 / 0.077 / 0.070	580 / 510 / 440	0.23 / 0.30 / 0.31	120 / 9.7 / 4.7	99.7 / 99.8 / 99.4	326,000 / 191,000 / 136,000	3.85 / 2.56 / 2.0
Graphite/Resin	18.2* / 36.2 / 48.6	47 / 40 / 33	2.28 / 1.44 / 1.11	0.95 / 0.52 / 0.46	21 / 28 / 30	9.5 / 3.5 / 2.2	0.051 / 0.048 / 0.044	926 / 825 / 690	0.28 / 0.28 / 0.31	120 / 11.4 / 5.2	99.1 / 98.6 / 98.4	279,000 / 231,000 / 193,000 CTI	5.55 / 4.75 / 4.06
Graphite/Aluminum	34.6* / 60 / 64.3	48 / 47 / 43	63 / 35 / 33	11.5 / 10.4 / 9.3	1.7 / 1.3 / 1.3	3.3 / 2.6 / 2.2	0.062 / 0.063 / 0.066	780 / 728 / 620	0.26 / 0.27 / 0.37	6 / 5.3 / 4.1	92.3 / 94.3 / 92.0	24,000 279,000 / 23,000 261,000 / 21,400 251,000	4.50 / 4.01 / 3.85
Graphite/Titanium	44.5* / 65 / 72	50 / 48 / 47	37 / 35 / 27	13.2 / 12.7 / 11.2	1.5 / 1.3 / 1.3	3.4 / 3.0 / 2.7	0.074 / 0.088 / 0.095	665 / 525 / 420	0.26 / 0.23 / 0.32	2.9 / 3.1 / 2.7	92.3 / 90.0 / 84.6	198,000 226,000 / 178,000 263,000 / 169,000 252,000	2.73 / 2.95 / 2.57
Graphite/Nickel	46.5* / 70 / 80	54 / 53 / 49	39 / 46 / 44	19.1 / 18.2 / 18.4	1.1 / 1.1 / 1.1	1.5 / 1.3 / 1.1	0.110 / 0.113 / 0.117	490 / 450 / 310	0.26 / 0.29 / 0.31	1.3 / 1.3 / 1.7	87.9 / 83.6 / 73.0	32,000 262,000 / 50,000 261,000 / 47,000 225,000	2.38 / 2.26 / 1.91

*Values correspond to minimum amount of matrix in perfectly packed square fiber array; $V_f = 0.785$, $V_m = 0.215$.

**Strength based on tensile fiber failure at values given in Table XX. Respective matrix stress levels are for the three systems: 13,000 psi, glass/resin; 2500 psi, xcron/resin; and, 1930 psi graphite/resin.

***Strength based on elastic limits of matrices from Table XX. Respective fiber stress levels for these three systems are: 223,000 graphite/Al; 223,000 graphite/Ti; and 52,000 graphite/Ni).

-182-

TABLE XX

REPRESENTATIVE COMPONENT MATERIAL INPUTS FOR COMPOSITE EVALUATION

	Moduli		Density	Strength	ν
	Tensile	Shear			
Graphite	60×10^6 psi	24×10^6 psi	0.0523 lb/in.^{3}	350,000 psi	0.25
Boron	60	24	0.095	300,000	0.25
Nickel	31	11	0.322	30,000	0.41
Titanium	15.5	6.5	0.163	80,000	0.19
Glass (S)	12.5	5.1	0.092	400,000	0.22
Aluminum	10	4	0.100	5,000	0.31
Epoxy	0.5	0.18	0.0435	20,000	0.38

NOTE: Data are considered representative based on the literature; values of G & ν are assumed for graphite and boron. All values given are for room temperature conditions and nominal strain rates.
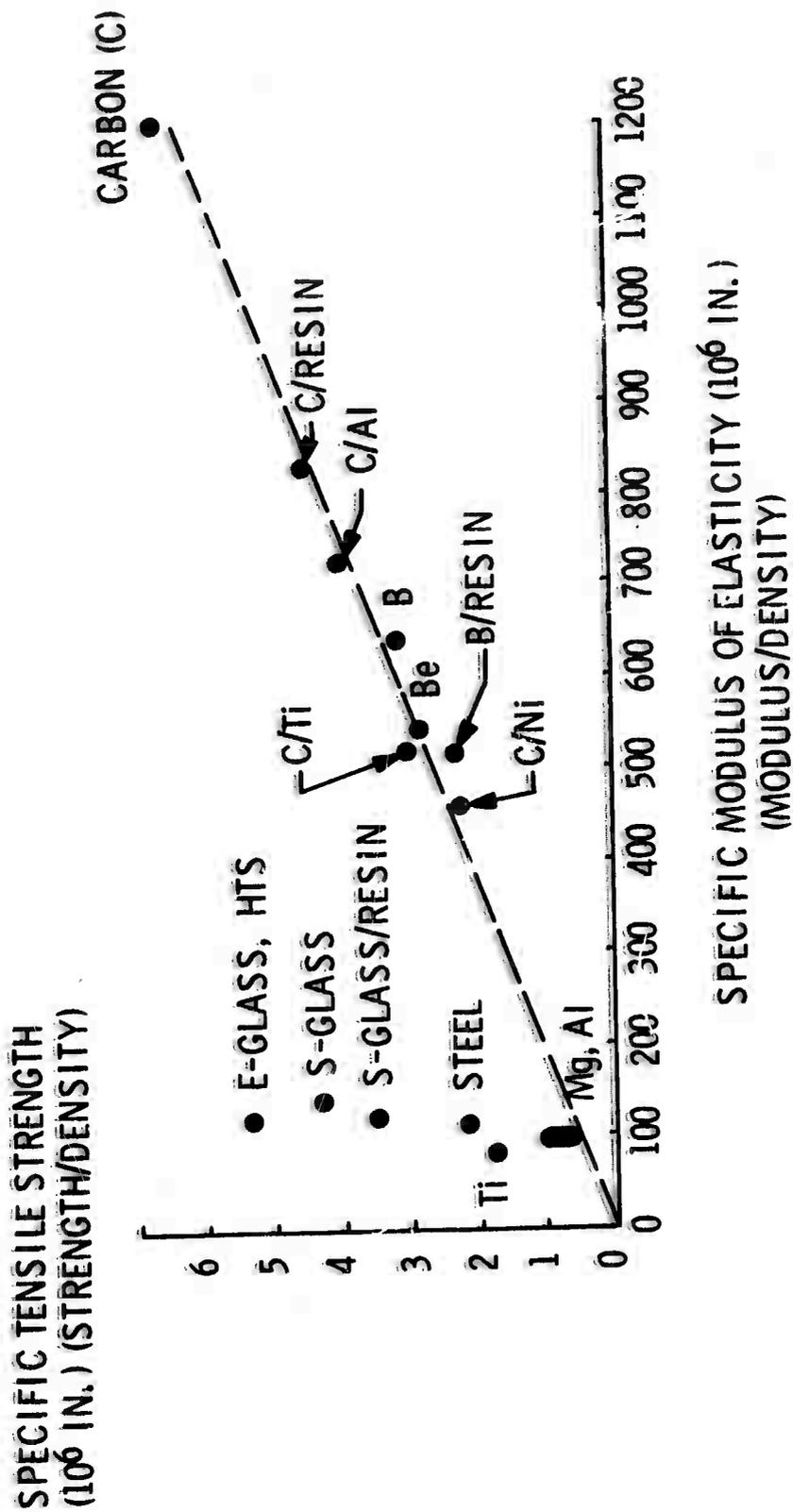
Figure 108. Specific Strengths and Moduli of Selected Fibers and Composites.

and/or boron resin composites will be greater than with glass/resin; with metal matrices and carbon or boron fibers, the effect will be less.

E.   Procedure for Determining Bidirectional Composite Properties
(D.P. Hanley, Bell Aerosystems)

Approximately midway through this reporting period the performance estimates as described above were obtained for the uniaxial behavior of unidirectional fiber reinforced composites. In working toward an extension of this work to predict the biaxial performance behavior of bidirectional composites, a new approach was developed for determination of engineering design properties.*

The novel feature of the approach is to measure the ratio of longitudinal/hoop strains in pressurized cylinders wound at three different helix angles as described later and to use these ratios to solve an elementary system of simultaneous equations for the composite material design moduli. The basic unidirectional properties of the laminate may then be deduced. This is particularly significant since the unidirectional properties are difficult to obtain reliably and accurately through direct experimentation. Indeed there are difficulties as well in the theoretical prediction of unidirectional properties** which may be circumvented with the new approach.

The theoretical basis for the tests is outlined below; advantages of the concept and projected results are described in the subsequent sections.

The well-known orthotropic strain-stress relationships for a symmetrically wound fiber-reinforced cylinder are

$$\epsilon_1 = S'_{11}\,\sigma_1 + S'_{12}\,\sigma_2$$

$$\epsilon_2 = S'_{12}\,\sigma_1 + S'_{22}\,\sigma_2 \qquad\qquad \Bigg\}\quad \text{(VII E-1)}$$

$$\gamma_{12} = S'_{66}\,\tau_{12}$$

---

* The author acknowledges the contributions of J.H Nourse in the field of composite materials mechanics. In particular, Mr. Nourse first suggested (in July 1964) the concept upon which this work is based. At that time, he was a Consultant to the Hercules Powder Company, Allegany Ballistics Laboratory under U.S. Navy Subcontract No. 111, NOrd 16640 and the author was contract technical monitor.

** Of the four independent constants required to characterize the orthotropy of a unidirectional laminate (E_L, E_T, G_{LT}, and ν_{LT}) only E_L and ν_{LT} may be calculated with reasonable agreement (on the order of 10-20%) between the various theories and experiment. Large discrepancies (factors of 2 to 3) exist between the various theories in predicting E_T and G_{LT}. Unfortunately, most experimental data are scattered over this range and the designer is pretty much then left "up in the air". To complicate design problems further, no theories have yet been advanced to predict composite properties with noncircular fibers such as carbon.

where the 1 and 2 directions correspond to the hoop and longitudinal directions and the bidirectional compliances are related to the moduli by

$$
\begin{aligned}
S'_{11} &= C'_{22}/\Delta \\
S'_{12} &= -C'_{12}/\Delta \\
S'_{22} &= C'_{11}/\Delta \\
S'_{66} &= 1/C'_{66}
\end{aligned}
\qquad \text{(VII E-2)}
$$

and

$$
\Delta = C'_{11} C'_{12} - C'^{2}_{12}
$$

If the cylinder is loaded as a closed-end pressure vessel,

$$
\sigma_1 = 2\sigma_2 \qquad \text{(VII E-3)}
$$

and

$$
\begin{aligned}
\frac{\epsilon_1}{\sigma_1} &= \frac{1}{2\Delta}\,(2\,C'_{22} - C'_{12}) \\[2mm]
\frac{\epsilon_2}{\sigma_1} &= \frac{1}{2\Delta}\,(C'_{11} - 2\,C'_{12})
\end{aligned}
\qquad \text{(VII E-4)}
$$

Thus the ratio of strains is

$$
n = \frac{\epsilon_2}{\epsilon_1} = \frac{C'_{11} - 2\,C'_{12}}{2\,C'_{22} - C'_{12}} \qquad \text{(VII E-5)}
$$

Consider now the four principal material constants (C_{11}, C_{12}, C_{22} and C_{66}, the generalized restrained unidirectional moduli) in the transformation relations

$$
\begin{aligned}
C'_{11} &= C_{11}\sin^4\alpha + 2\,(C_{12} + 2\,C_{66})\cos^2\alpha\,\sin^2\alpha + C_{22}\cos^4\alpha \\
C'_{12} &= C_{12}(\cos^4\alpha + \sin^4\alpha) + (C_{11} + C_{22} - 4\,C_{66})\cos^2\alpha\,\sin^2\alpha \\
C'_{22} &= C_{11}\cos^4\alpha + 2\,(C_{12} + 2\,C_{66})\cos^2\alpha\,\sin^2\alpha + C_{22}\sin^4\alpha \\
C'_{66} &= C_{66}(\cos^2\alpha - \sin^2\alpha)^2 + (C_{11} + C_{22} - 2\,C_{12})\cos^2\alpha\,\sin^2\alpha
\end{aligned}
\qquad \text{(VII E-6)}
$$

A simple torsion test on a hoop wound cylinder ($\alpha = 90°$) yields directly the constant C_{66} (= τ_{12}/γ_{12}) as the last above equation verifies. Substituting the three previous equations in the strain ratio relation yields

$$n = \frac{DC_{11} + EC_{12} + FC_{22} + G}{HC_{11} + IC_{12} + JC_{22} + K} \qquad \text{(VII E-7)}$$

where the constants are given by

$$D = \sin^4\alpha - 2\cos^2\alpha\,\sin^2\alpha$$

$$E = 2\left[\cos^2\alpha\,\sin^2\alpha - (\cos^4\alpha + \sin^4\alpha)\right]$$

$$F = \cos^4\alpha - 2\cos^2\alpha\,\sin^2\alpha$$

$$G = 12\,C_{66}\cos^2\alpha\,\sin^2\alpha = K$$

$$H = 2\cos^4\alpha - \cos^2\alpha\,\sin^2\alpha$$

$$I = 4\cos^2\alpha\,\sin^2\alpha - (\cos^4\alpha + \sin^4\alpha)$$

$$J = 2\sin^4\alpha - \cos^2\alpha\,\sin^2\alpha$$

$\qquad$ (II E-8)

Now, if the measurements are made of the strain ratios (n_1, n_2, n_3) from three cylinders wound each at a different helix angle (α_1, α_2, α_3), the remaining three principal material constants (C_{11}, C_{12}, and C_{22}) are given by the solution of three simultaneous equations upon substitution of the respective values in the above strain ratio equation.

Having determined the C_{ij}'s as outlined, the basic unidirectional material properties may be determined from

$$E_L = \frac{C_{11}\,C_{22} - C_{12}^2}{C_{22}} \qquad \nu_{LT} = \frac{C_{12}}{C_{22}}$$

$$E_T = \frac{C_{11}\,C_{22} - C_{12}^2}{C_{11}} \qquad \nu_{TL} = \frac{C_{12}}{C_{11}}$$

$$G_{LT} = C_{66}$$

$\qquad$ (VII E-9)

In that the "law of mixtures" has been adequately substantiated in the prediction of longitudinal composite properties, this fact used in connection with the pressurized cylinder test enables the fiber modulus and Poisson's ratio to be determined without actually performing tensile and torsion tests on the fiber, i.e.,

$$E_f = \frac{E_L - V_m E_m}{1 - V_m}$$

$$\nu_f = \frac{\nu_{LT} - V_m \nu_m}{1 - V_m}$$

(VII E-10)

This should be an interesting method of determining average "delivered fiber modulus" since gage length effects, grip yielding and delicate fiber tensile testing procedures are eliminated. In the case of noncircular fibers, this also seems a useful approach to determining an effective Poisson's ratio. It is assumed in both of the above equations that the matrix material has generally well characterized engineering properties (modulus and Poisson's ratio) in contrast to fibers being newly developed.

Although recognizing cost to be a somewhat greater factor in the proposed test compared to conventional "coupon" and plate testing, advantages to be gained are:

(1) More nearly homogeneous stress fields are obtained with minimized discontinuities and less complicated boundary conditions than are encountered with flat specimens.

(2) The test specimen is representative of the form and fabrication processes of filament wound structural configurations which is often not the case with flat specimens. Requirements for specimen machining are also eliminated.

(3) The test yields directly engineering (tensile) design properties independent of internal micromechanics. The test can also be adapted to determining compressive properties by conducting external pressurization tests.

(4) By virtue of the relatively simple theoretical problem formulation, the test should provide data more suitable for statistical analysis than is permitted with many of the current mathematical models.

(5) The biaxial test is sensitive to the onset of the matrix yielding or crazing and appears potentially capable of treating the nonlinear regime and nonconservative behavior.

Calculations have been made to determine the engineering "reasonableness" of the approach suggested. Intuitively, one might expect, for a given composite material, that at certain winding angles, the strains likely to be encountered would be quite small. This fact, along with inaccuracies in measuring small strains, could thus give rise to relatively large errors in the strain ratio $\underline{n}$ and thereby seriously affect the determination of material constants.

To examine the above possibilities, normalized strains were calculated for pressurized cylinders wound (hypothetically) at angles from zero to $90°$. A graphite fiber/resin system was assumed with the following properties.

-188-

$$E_f = 60 \times 10^6 \text{ psi}$$

$$E_m = 0.5 \times 10^6$$

$$\nu_f = 0.25$$

$$\nu_m = 0.38$$

$$W_m = 30 \text{ percent}, \quad V_m = 34.2 \text{ percent}$$

Using Ekvall's model, which accounts for matrix constraint, (in the interest of simplified computation), the following constants were determined:

$$E_L = 39.8 \times 10^6 \text{ psi} \qquad\qquad C_{11} = 40.0 \times 10^6 \text{ psi}$$

$$E_T = 2.33 \times 10^6 \qquad\qquad C_{12} = 0.69 \times 10^6$$

$$G_{LT} = 0.52 \times 10^6 \qquad\qquad C_{22} = 2.34 \times 10^6$$

$$\nu_{LT} = 0.295 \qquad\qquad C_{66} = 0.52 \times 10^6$$

$$\nu_{TL} = 0.0173$$

Strains for the cylinders are shown in Figure 109. These curves are recognized to be approximate by virtue of the model used, but they illustrate the peculiar behavior of orthotropic composites; viz., for certain winding angles in pressurized cylinders there can be a negative axial strain accompanied by a positive hoop strain. The data also explain, in part, why engineers are often distrustful of experimental strain measurements, for example, variations of ± several degrees in winding angle can account for significant discrepancies in strain magnitude and sign.

Note that the "balanced" design winding angle ($\alpha = 56°$) based on orthotropic analysis ($\epsilon_1 = \epsilon_2$) is quite close to the ideal netting analysis ($\sigma_1 = 2\sigma_2$) balanced angle of 54.75°. For glass/resin composites, the former analysis predicts values in excess of 60°. Thus, the higher modulus fibers tend to improve agreement with the netting prediction because they more nearly satisfy the fundamental assumption of inextensibility used in netting analysis. An obvious limitation of the latter analytical technique is, however, that strains can not be calculated.

In the theory pertaining to Figure 109, it was explicitly assumed that the composite exhibits linear elastic behavior. With fiber reinforced/resin composites, however, crazing or yielding may be encountered, which implies that theory is good only up to the "knee" in the composite stress-strain curve. It is suggested now that by conducting experiments and recording data at various levels up to ultimate burst pressure, the C_{ij} engineering "constants" may be determined for any condition in the composite without regard for the internal mechanism of degradation. Thus, the "elastic" constants C_{ij} and C_{ij} could be specified as functions of the level of loading. This approach appears promising with regard to eventually predicting nonconservative
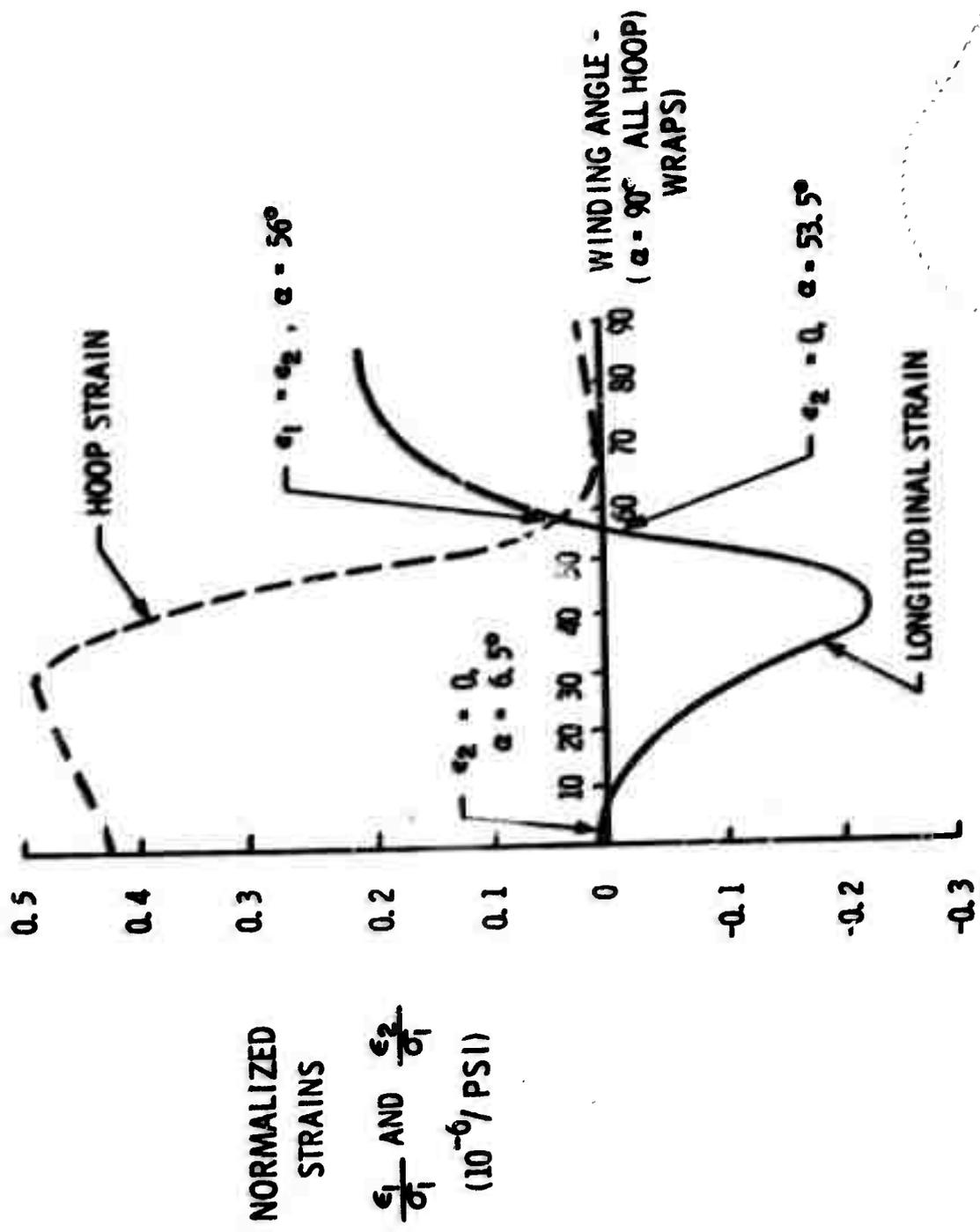
Figure 109. Theoretical Strains in Wound Graphite Fiber/Resin Composite Cylinders - Effect of Winding Angle

material behavior. With pressure cycling tests from zero to various levels of pressurization and unloading, it is believed possible to obtain functional expressions of the constants for engineering design use.

Figure 110 shows that appreciable differences may exist in the C_{ij} moduli depending upon the degree of matrix "effectiveness" in the composite. For the curves labeled "matrix effective" it is assumed that linear orthotropic behavior applies whereas for the curves labeled "matrix ineffective" it is considered that there is no transverse reinforcement, i.e., $E_T = \nu_{LT} = \nu_{TL} = 0$. The proposed method of determining gross engineering material properties may thus be able to provide a quantitative measure of the degree of crazing or nonlinearity in a wound structure by comparing experimental data with the two mathematically ideal extremes of matrix behavior: effective and completely ineffective.
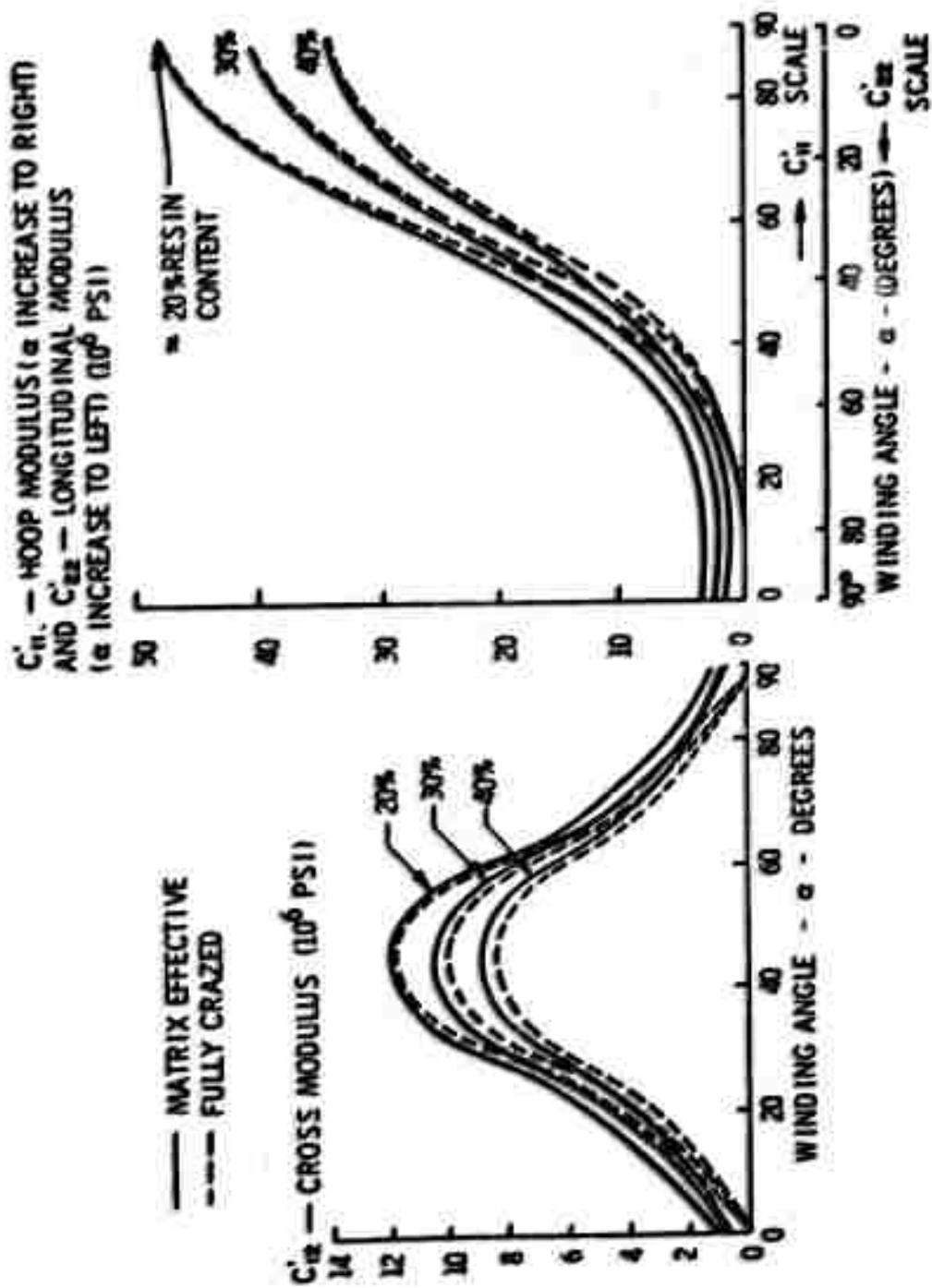
Figure 110. Graphite/Resin Composite Material Behavior

SECTION VIII

MATERIALS RESEARCH ON CARBON-FIBER, METAL-MATRIX COMPOSITES

Carbon-fiber, metal-matrix composites have a wide range of potential applications, as shown by Table III in Section IV. The technology of metal-matrix composites is far behind that of resin-matrix composites; thus, the initial studies of carbon-fiber, metal-matrix composites must be on basic questions of wetting and infiltration techniques. The literature relevant to carbon-fiber, metal-matrix composites is reviewed in Section VIII A. Preliminary experiments on pressure infiltration and wettability are discussed in Section VIII B. Because of the urgent need for a light-weight, stiff material, the major emphasis of the work to date has been on aluminum matrix composites with several types of coated carbon fibers; this work is reported in Section VIII C. Although aluminum matrix composites have been made, their properties were not exceptional due to the formation of intermetallics or poor fiber-metal adhesion. Studies of nickel matrix composites are given in Section VIII D. Carbon fibers can be electroclad with nickel by several techniques; and nickel matrix composites, prepared by hot pressing the coated fibers, have shown good fiber distribution and densities less than 3.5 g/cm³. In Section VIII E, work on lower-modulus matrix composites using tin and a cupro-nickel alloy is described.

A. Literature Review
        (R. V. Sara, Union Carbide)

Although considerable effort is being expended at the present time on the development of useful filament-based composites, the general emphasis has been on oxide whiskers, glass fibers, metal wires, and the metalloids such as boron and silicon carbide. An attempt at reinforcing metals with carbon fibers was made by Armour Research Foundation[46] and by investigators at the Battelle Memorial Institute.[47] In their studies with Al, Al-4 percent Cu, and 50 percent Cu-50 percent Ni alloys, Armour observed that the ultimate tensile strengths fell considerably short of expectations. These results were partially attributed to difficulty in obtaining high-density composites with good fiber distribution. Battelle attempted to fabricate a nickel composite by electrocladding and hot pressing, but the nickel coatings spalled during the thermal treatment.

Since the early efforts by the Armour Research Foundation, the necessary conditions for optimizing the mechanical properties in composites have been established more clearly. These considerations should include factors such as minimum fiber damage during fabrication, uniform distribution and orientation in the matrix, fiber length greater than that giving a critical fiber length-to-diameter ratio, fiber modulus of elasticity greater than that of the matrix, and maximum fiber-matrix bonding without excessive reaction at the interface. According to Sutton,[48] mechanical properties are optimized to a greater degree if the matrix metal is molten

during fabrication and particularly if the liquid phase readily wets the fiber surfaces. The degree of wetting, bonding, and chemical reaction between fiber and metal can be controlled to a certain extent through use of a suitable coupling agent.

Applying these considerations to carbon filaments, one learns from the available phase diagrams that a number of interesting composite systems are handicapped by features such as intermediate compounds or high carbon solubility. Specifically, the ductile metals aluminum, titanium, and nickel have considerable appeal as matrix components for a variety of reasons; but each is thermodynamically unstable in the presence of carbon. One would expect that attempts to infiltrate these metals into carbon filament networks would result in conversion of the fibers to either Al_4C_3 or TiC or that they would dissolve in nickel. A number of metals exist which are compatible with carbon (e. g. , copper or silver); but, for reasons of cost, refractoriness, oxidation resistance, density, etc. , none has the immediate appeal of aluminum, titanium, and nickel.

If molten metal is to be infiltrated effectively into a network of carbon filaments, a near-zero contact angle between the two components is desirable. Published studies on the wettability of graphite by various metals are relatively scarce. The most comprehensive effort on this problem appears in the Russian literature. [49] The Russian results concur with experience gained at this laboratory and also with isolated reported data on metal-to-carbon adhesion. [50,51] These studies indicate that usually the metals which do not form compounds with carbon do not wet a carbon surface. Conversely, the elements which are compound formers are observed to be adherent to graphite. In particular, when transition elements which are compound formers with carbon are alloyed with elements such as copper, tin, and silver, the contact angle decreases sharply.

The above generalizations indicate that the opportunity exists for wetting carbon fibers with aluminum and titanium but not with nickel. Experience has shown that aluminum and titanium readily wet graphite only when there is the formation of Al_4C_3 and TiC, respectively. Carbon filaments subjected to infiltration by these metals would undoubtedly be damaged as a result of these reactions. On the other hand, nickel is known not to wet graphite extensively and conceivably would dissolve the fibers. A possible method for alleviating the difficulties just cited would be the use of a coupling agent between the carbon fiber and metal matrix. Consequently, a considerable portion of the work described in succeeding sections was devoted to cladding fibers with a material which is readily wetting and nonreactive with the matrix metal. This approach was applied principally to aluminum studies.

The possibility of using hot pressing as a fabricating technique has also been investigated. This approach is worthy of consideration because the fibers are electrically conductive and, consequently, are capable of being electroclad with a variety of metals. This method has particular appeal for the more refractory metals, where one could envision considerable difficulty in isolating a coupling agent which is not only chemically compatible

with the fiber but also stable in the presence of a high melting metal. Such is the case for nickel: a coupling material is not known at present which fulfills the requirements for infiltrating this high melting metal.

B. Preliminary Experiments
(R. V. Sara, Union Carbide)

Several screening-type studies were conducted to study the chemical reactivity and wettability of carbon fibers relative to several metal matrices. Essentially, these experiments consisted of pressure infiltrating aluminum into a fiber network and also of qualitatively assessing the degree of wetting by supporting the as-received fibers in pure molten nickel, copper, and copper with varying alloy ingredients.

In the absence of Al_4C_3 formation, aluminum does not wet graphite; and, without wetting, the infiltration of aluminum into an oriented graphite fiber network requires significant external pressures to offset the capillary forces. Sutton[52] has calculated that a pressure of approximately 25 lb/in.^{2} is requires to force molten nickel into the capillaries formed by 50 volume percent of 8 micron diameter sapphire fibers. The capillary diameters, volume fraction of fibers, and wettability of the sapphire-nickel system are similar to the conditions of the carbon-aluminum system; therefore, similar infiltration pressures are to be expected.

Ram

Aluminum

Perforated Graphite Capsule with 50% Fibers

Graphite Insert
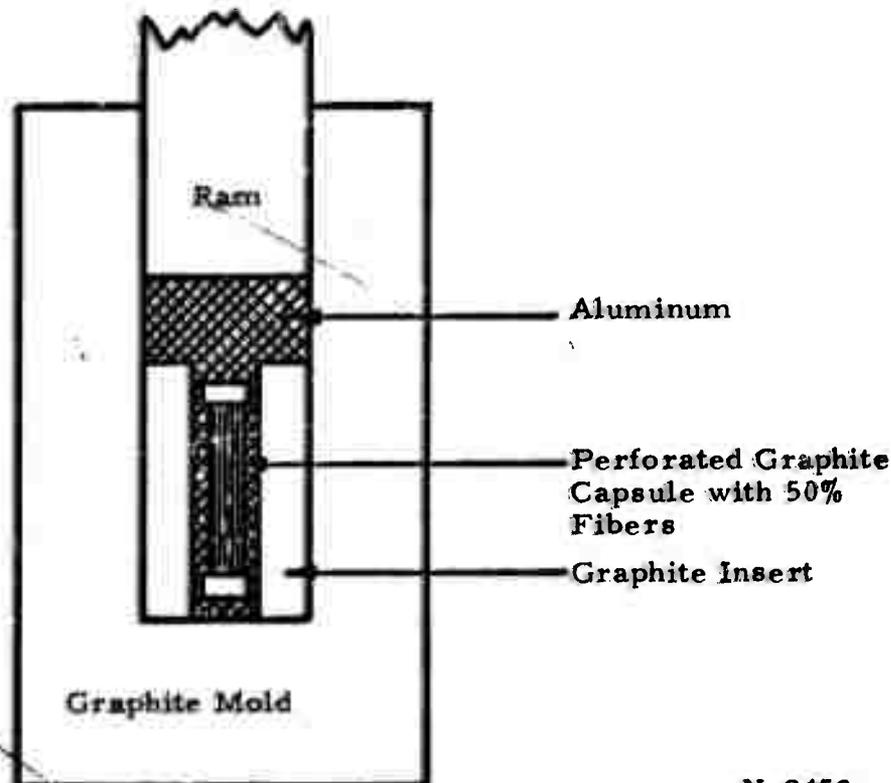
Graphite Mold

N-9450

Figure 111. Mold Configuration for Pressure Infiltration of Aluminum around Graphite Filaments.
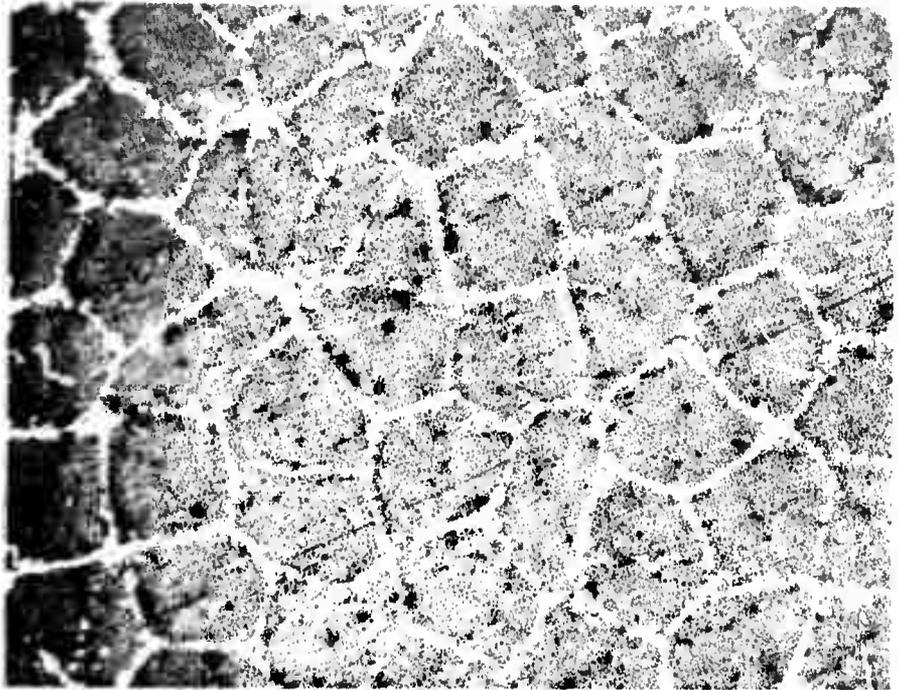
N-9693

Figure 112. Pressure Infiltrated Aluminum around Plies of
Graphite Yarn. 50X.

The feasibility of generating a composite by pressure infiltration was
evaluated by charging a graphite capsule with 50 volume percent fibers and
positioning the capsule in a graphite mold as shown in Figure 111. The
mold was inductively heated in vacuum to 750°C before force was applied
to the graphite piston. Two experiments were conducted in this manner
with pressures of 360 and 1080 lb/in.^{2} applied to the aluminum and main-
tained through the cooling cycle. Figure 112 indicates the degree of
infiltration achieved at 360 lb/in.^{2} The aluminum metal was forced into
spaces 20 to 30 μ wide formed at the ply junctures. The islands (plies)
containing approximately 720 filaments were not infiltrated. At the higher
pressure, results were even less satisfactory, for the filaments were
forced even closer together leaving no demarcation zone between the plies.

These results indicate that the calculated infiltration pressures are low.
Before this approach can be evaluated as a method for preparing a
composite, an experimental arrangement is needed capable of confining the
molten aluminum more effectively than the simple piston mold shown in
Figure 111. Improvements in the contact angle and surface tension of the
metal would contribute to the success of this approach.

Copper is known not to wet graphite, but additions to this metal have markedly changed the contact angle. A simple experimental arrangement was devised to screen alloying additions which might be considered in future infiltration experiments. Fibers supported in Cu and Cu alloys containing 1.4 and 2.75 weight percent Ti, Ir, Rh, TiSi (high silicon eutectic composition), and CaSi were heated to 1350°C in vacuum for five minutes. The noble metal additives had little effect on the wetting of the fibers at this temperature, but the others did. Bonding between the metal and the graphite components exposed to the melt was evident for additions of Ti, TiSi, and CaSi; unfortunately, the fibers went into solution.

Both Ti and Si are often used as additives for coupling metals to graphite. The function of these elements evidently is to form a carbide interface which is wetted more readily by the metal. The screening studies described above indicate that extremely small quantities of either Ti or Si ($\ll 1.0$ weight percent) would have to be considered in future studies to avoid the damaging effects of carbide formation or solution of the fibers. An unknown at this point is the extent of reaction or carbide formation which could be tolerated on the fiber surface before property degradation commences.

A similar experiment was performed with pure nickel as the candidate matrix component. The metal was heated in vacuum just to the point of melting and then chilled rapidly by quickly shutting off the heater power. Metallographic studies of the nickel revealed complete solution of the fibers and subsequent precipitation as spheroidal graphite.

These preliminary experiments indicated that a coupling agent would be necessary for pressure infiltration of aluminum around networks of carbon filaments. Also, for a nickel matrix, a less drastic fabrication technique would have to be used than that of direct infiltration.

C. Aluminum Matrix Studies.
        (R. V. Sara, Union Carbide)

Most of the effort connected with incorporating graphite fibers into an aluminum matrix was concerned with cladding the fibers with a coupling agent which is wet more readily by the aluminum than are the fibers. Particular attention was given to the interfacial region between the coupling agent and aluminum, since aluminides are inherently brittle, leading to the weakening of the composite structure. Emphasis was placed on metallic coupling agents, since these are subject to electrodeposition, which is a more effective cladding process for the conductive fibers than are other techniques such as vapor deposition.

The first coupling agent evaluated was TiC because literature data[53] inferred that TiC is compatible with and wetted by aluminum, a rare characteristic for most materials. The TiC coatings were prepared by exposing the carbon fibers to a H_2-$TiCl_4$ gaseous mixture at a temperature of 1000°C. The fibers were separated and cemented on a "C" form to assure uniform deposition. Metallographic studies revealed that complete

coverage (Figure 113) could be achieved after exposing the fibers to
H_2-TiCl_4 for 60 minutes. The carbide coating depicted in Figure 113 is
approximately 0.2 μ in thickness. The X-ray diffraction studies of the TiC
lattice parameter indicate a C/Ti atom ratio of 0.55, a value which denotes
a very carbon-deficient lattice.
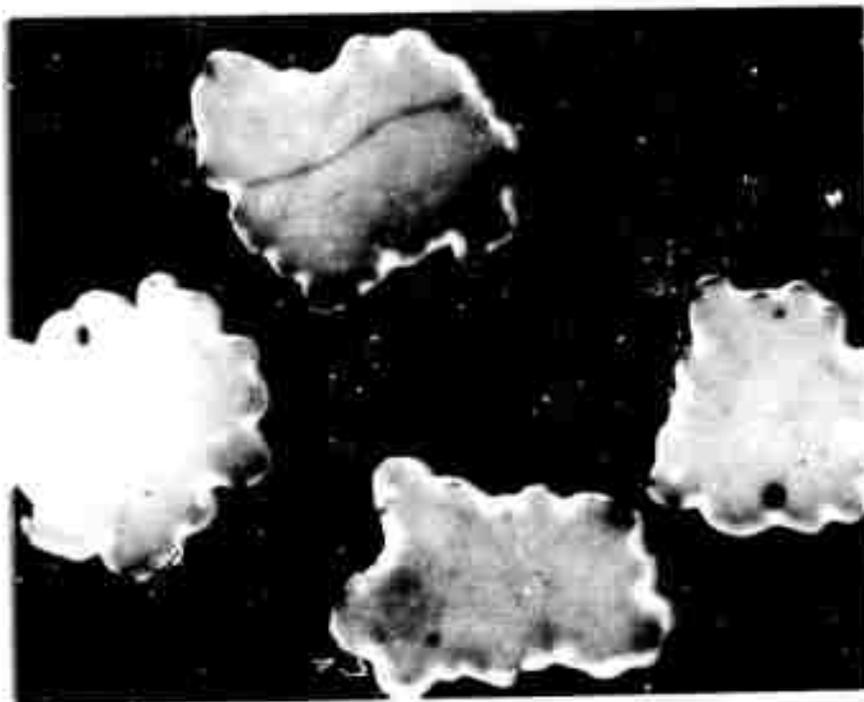
N-8008

Figure 113. TiC-Coated Fibers. 2000X. Enlarged
100 Percent for Reproduction.

Strength and modulus of elasticity values determined for a series of
carbon fibers exposed for varying time to $TiCl_4$ vapors are shown in
Table XXI. The "as-received" fibers provided the highest tensile strength.
After pretreatment exposure to hydrogen at 1000°C for 30 minutes,
(common to all specimens) but with no exposure to $TiCl_4$ atmosphere, the
fiber strength decreases approximately 20 percent. This change is
believed due to further pyrolysis. Complete carbide coverage reduced
the tensile strength by a factor of four, although the cross-sectional area
remained unchanged. This behavior is similar to that which takes place
when filaments such as boron[54] or glass[55] are weakened because of
surface reactions. The decrease in strength is thought to be due to
notch effects.

TABLE XXI

EFFECT OF TiC ON CARBON FIBER MECHANICAL PROPERTIES

Exposure Time min	Tensile Strength lb/in.^{2}	Modulus of Elasticity 10^6 lb/in.^{2}
As Received	124,000	5.9
0	102,300	5.1
15	45,800	3.5
30	42,100	7.1
60	29,400	6.4

The infiltration procedure was to maintain a vacuum of 10^{-5} to 10^{-6} torr until the desired temperature was attained, after which argon was back-filled into the vessel until nearly atmospheric pressure (25 inches Hg) was reached. The TiC-coated fibers to be infiltrated were contained in a quartz tube which could be immersed into the molten aluminum (99.9 percent purity) at the desired time. A vacuum line to the quartz tube contained a calibrated Nupro metering valve which provided precision control and reproducibility of the aluminum infiltration rate.

Infiltration attempts with the TiC-coated fibers at temperatures below 1250°C resulted in extensive channeling of the aluminum, a result which is indicative of poor wetting between the melt and fiber coating. Therefore, a series of experiments was conducted to determine the spreading behavior of aluminum on TiC. A TiC coating was formed on a highly polished substrate of high density graphite by the same process employed for the fibers. Pellets of high purity aluminum were heated in contact with this deposit to 1000°, 1150°, 1390°, and 1410°C in an argon atmosphere. An experiment was also conducted at 1000°C in vacuum. In argon, the contact angle below 1250°C is substantially greater than 90 degrees, with wetting taking place at the higher temperatures. In vacuum, a contact angle smaller than 90 degrees is encountered at temperatures as low as 1000°C. The inability to infiltrate aluminum into the TiC-coated fibers below 1250°C is explained by the absence of wetting at these temperatures in an argon atmosphere. These results concur with those reported by Russian investigators,[56] who noted a contact angle of 118 degrees between aluminum and TiC at 700°C in an atmosphere of argon. The highly stable oxide film which forms on aluminum has a profound effect on the wetting capabilities of this metal. This fact was recognized by Wall and Milner[57] who observed spreading to occur only after the aluminum oxide film had been mechanically punctured or degraded by chemical or vacuum methods.

At infiltration temperatures above 1250°C, channeling of the aluminum was not encountered. The cross section of a composite formed by infiltration above 1250°C is shown in Figure 114. The periphery of each fiber was observed to undergo hydrolysis, a condition which probably resulted from solution or decomposition of the TiC barrier material and subsequent formation of Al_4C_3. This behavior was also evident in the specimens used for contact angle measurements and particularly in those cases where wetting was encountered.
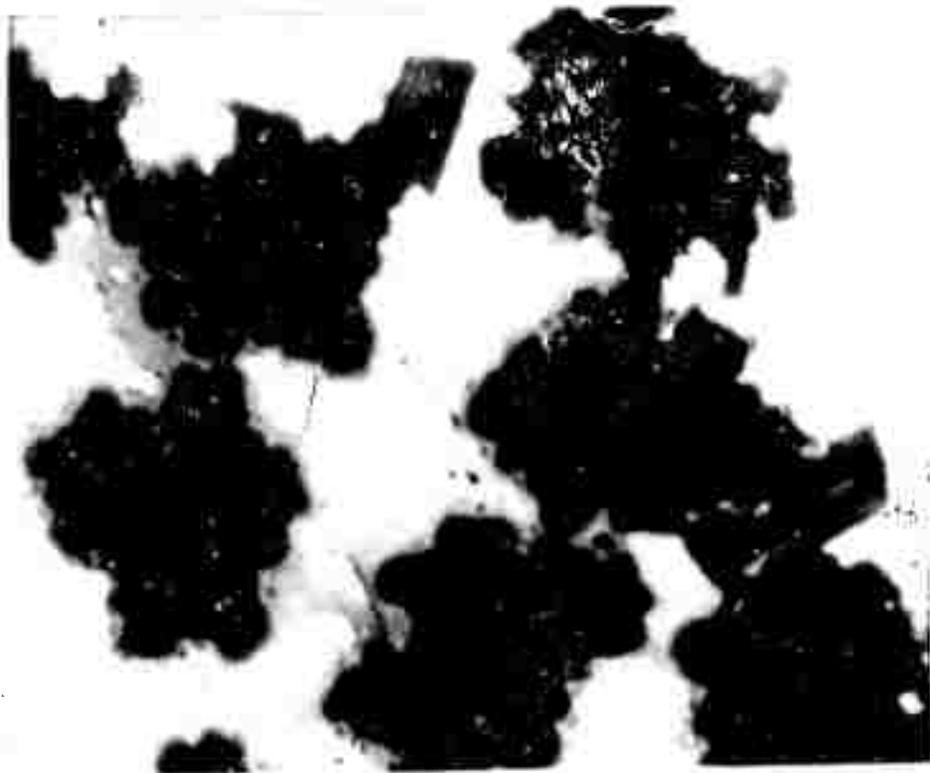
Figure 114. TiC-Coated Fibers Infiltrated with Aluminum.
2000X. Enlarged 100 Percent for Reproduction.

The reactivity of the monocarbides with aluminum is further exemplified by the results shown in Figure 115. The substrate in this instance is NbC. The presence of Al_4C_3 was again suggested by the extensive hydrolysis which had occurred in the large reaction zone depicted in Figure 115.

The studies conducted on several monocarbides for ultimate use as coupling agents between the carbon fiber and aluminum matrix indicate that their potentialities are limited both because wettability is not enhanced to the degree indicated in the literature and also because their
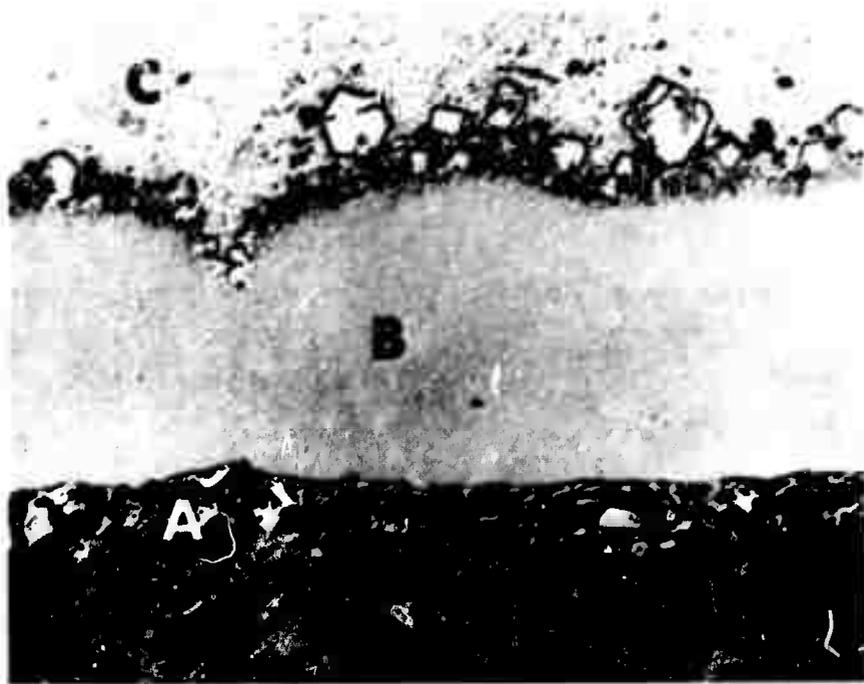
Figure 115. NbC-Al Reaction Zone after Two Minutes at 1000°C
in Vacuum: A. NbC, B. Reaction Zone, C. Al.
250X.

chemical reactivity with aluminum results in the formation of Al_4C_3. A possible exception to the latter generalization is TaC: it has been reported[58] that TaC can be synthesized from the elements in an aluminum matrix.

A study was made of the contact angle and reaction of aluminum with a number of metals and with TiB_2 and $TiSi_2$. The metals included Ti, Cr, Mo, Ta, Nb, W, Ni, Cu, and Ag. The evaluation was made after the substrate and piece of aluminum were heated at 1000°C in vacuum for several minutes. Either complete spreading or essentially zero contact angles was observed for Ti, Nb, Ta, and TiB_2. For the remaining substrates, the contact angle was approximately 30 degrees. No metallographic evidence could be obtained which suggested that reaction had occurred between TiB_2 and Al. For $TiSi_2$, although the results are less certain, they indicate that this material is significantly more stable in the presence of aluminum than are the metals.

The metal substrates were eroded by aluminum to varying degrees and, in a relative manner, signified which metal, when applied to the fibers as

Figure 116. Ta-Al Reaction Zone after Two Minutes at 1000°C
in Vacuum: A. Ta, B. Al. 250X.
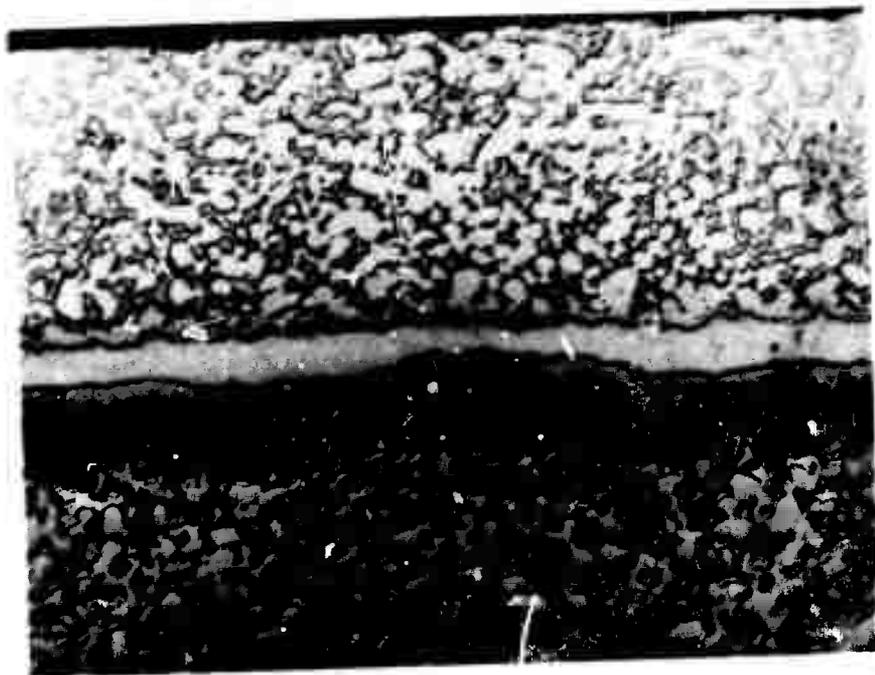
Figure 117. Ti-Al Reaction Zone after Two Minutes at 1000°C
in Vacuum: A. Ti. 250X.

a coating, would function best as an infiltration aid. Ideally, the metal coating should not react with the molten aluminum, since a brittle intermetallic phase could adversely affect the strength of the composite. Extensive solubility of the coupling metal in the matrix is undesirable, since a high solubility would dissolve the coating. In view of these considerations, tantalum appears superior to the other metal coating candidates considered in this study. The photomicrograph in Figure 116 reveals that a narrow and coherent reaction zone exists between tantalum and aluminum. The photomicrograph in Figure 117 for titanium, which is typical of the other metals, shows the extensive reaction which prevailed, resulting in depletion of about 0.003 inch of titanium substrate. The feature which distinguishes tantalum from most of the remaining metals studied in this program is the apparent absence of an Al_3M type phase, one example of which is shown dispersed throughout the aluminum in Figure 117.

Exploratory studies with tantalum as a coupling agent were extended to include aluminum infiltration around networks of 0.005-inch diameter tantalum wires. The objective of this study was to determine the infiltration conditions required for a negligible reaction zone at the aluminum-tantalum interface. At a bath temperature of 1000°C, aluminum is readily infiltrated into the wire network without need for precautionary wire cleaning procedures. After fifteen seconds at temperature, the thickness of the reaction zone is about two microns (see Figure 118). For infiltration at temperatures near the melting point of aluminum (~700°C), vacuum cleaning of the tantalum wires at 1500°C was necessary. Wires infiltrated at the very low temperature did not exhibit a reaction zone (see Figure 119).
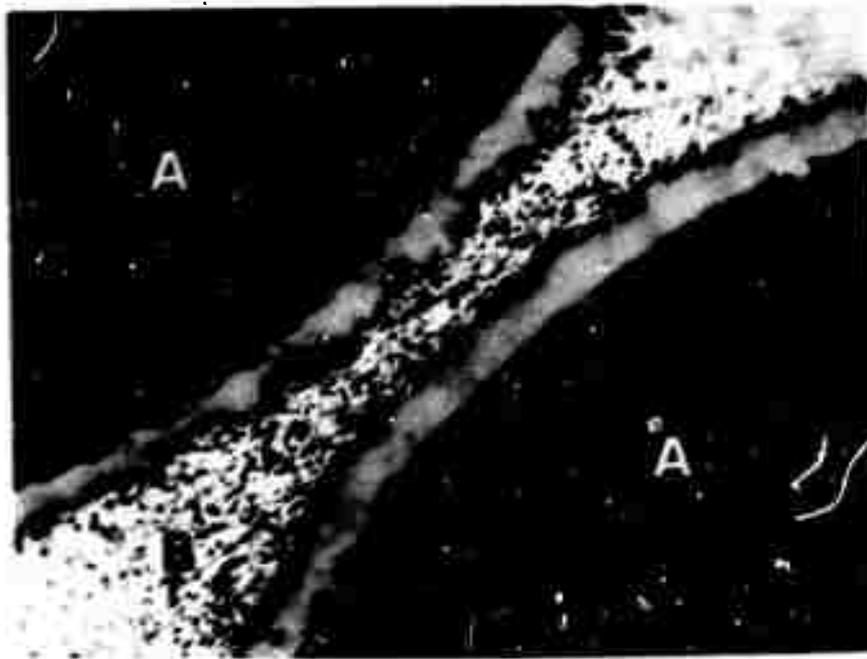
N-8617

Figure 118. Reaction Zone Around Ta Wires Infiltrated with Aluminum at 1000°C: A. Ta wires, B. Al. 2000X.

-203-
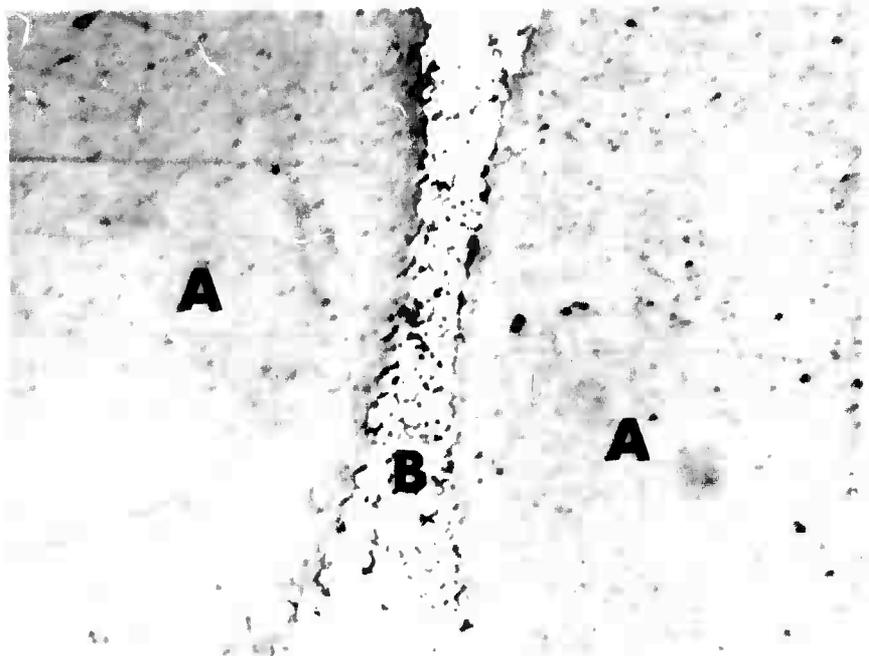
Figure 119. Ta Wires Infiltrated with Aluminum at 700°C:
A. Ta Wires, B. Al. 2000X.
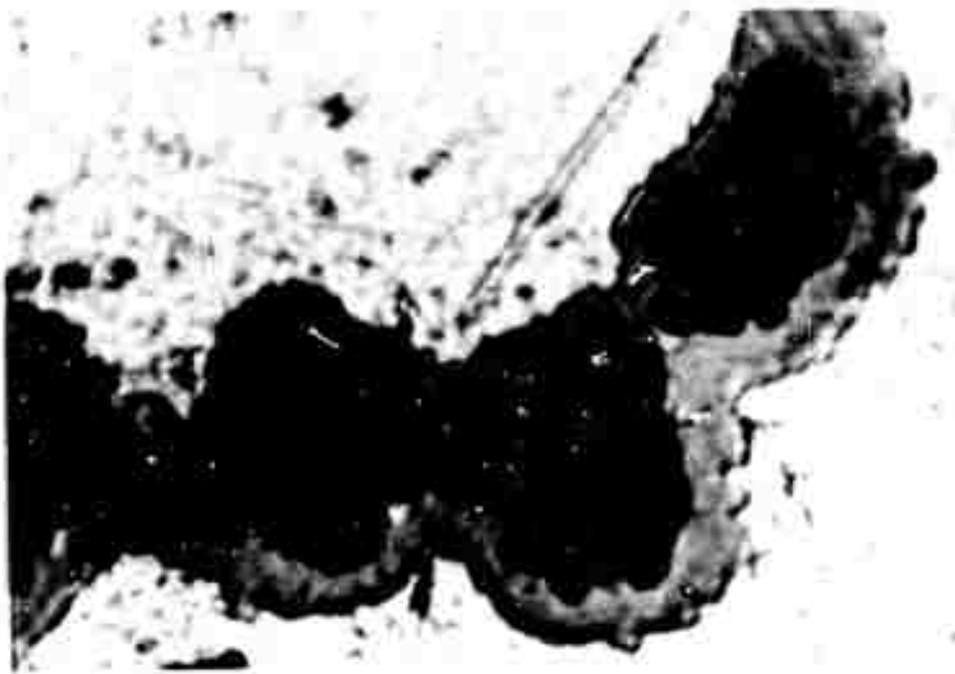
Figure 120. Tantalum-Coated Fibers Infiltrated with Aluminum.
2000 X. Enlarged 100 Percent for Reproduction.

Carbon fibers were coated with tantalum by a fused salt process. Although the process is capable of yielding a high-purity deposit, repeated attempts to achieve a uniform coating on all the fibers were without success. The poor wetting between the molten salt bath and the carbon fibers resulted in the cladding of only the peripheral fibers of the yarn with tantalum. Nevertheless, infiltration studies on these poorly plated fibers confirmed results achieved with the wires. Figure 120 reveals the absence of reaction at the aluminum-tantalum interface. These results imply that tantalum has great potential as a coupling agent by virtue of its chemical compatibility with both fiber and metal matrix under infiltration conditions. Preparations are currently being made for the deposition of thin tantalum films by sputtering techniques. This technique is superior to that used in the thermal decomposition of the halides in that there is less possibility of carbide formation and, possibly, the tantalum-graphite bond strength may be greater.

Nickel, copper, and silver were investigated as coupling agents because they can be easily electrodeposited. Attention was given to determining minimum infiltration times and temperatures in order to reduce the amount of reaction zone.

Nickel, in particular, received attention, since this metal functioned well in the aluminum infiltration experiments reported by Sutton;[59] procedures were developed during this program for electrodepositing reasonably uniform coatings from a $NiSO_4$-H_3BO_3 bath on all the filaments within a multiply yarn. Nickel also has the advantage of lower density compared to tantalum and silver.

Nickel coatings were deposited on the fibers to a thickness of one to two microns; the fiber diameter is about eight microns. Initial infiltration studies were conducted using the quartz tube and vacuum procedure described previously. Vacuum drawing of the molten metal into a tube containing the oriented fibers often resulted in channeling. The molten metal, more often than not, would seek the easiest path available (capillaries with the largest diameters), thereby leaving many of the fibers untouched by the metal. A method was devised which produced test specimens superior to those achieved by the vacuum drawing procedure. In principle, the technique consists of submerging a sealed, outgassed, and evacuated graphite capsule containing the oriented fibers below the molten metal surface. The previously evacuated vessel enveloping the molten metal system is back-filled with inert gas to approximately one atmosphere, thereby forcing liquid metal through a number of small holes in the graphite capsule. This method eliminates the channeling of aluminum within the capsule which prevailed in earlier studies and permits exercising greater control of the infiltration time.

With this modified infiltration method, very satisfactory specimens were achieved in terms of density and fiber distribution, as shown in Figure 121. However, it was not possible to avoid Al_3Ni formation, as evidenced by the photomicrograph in Figure 122, even though particular
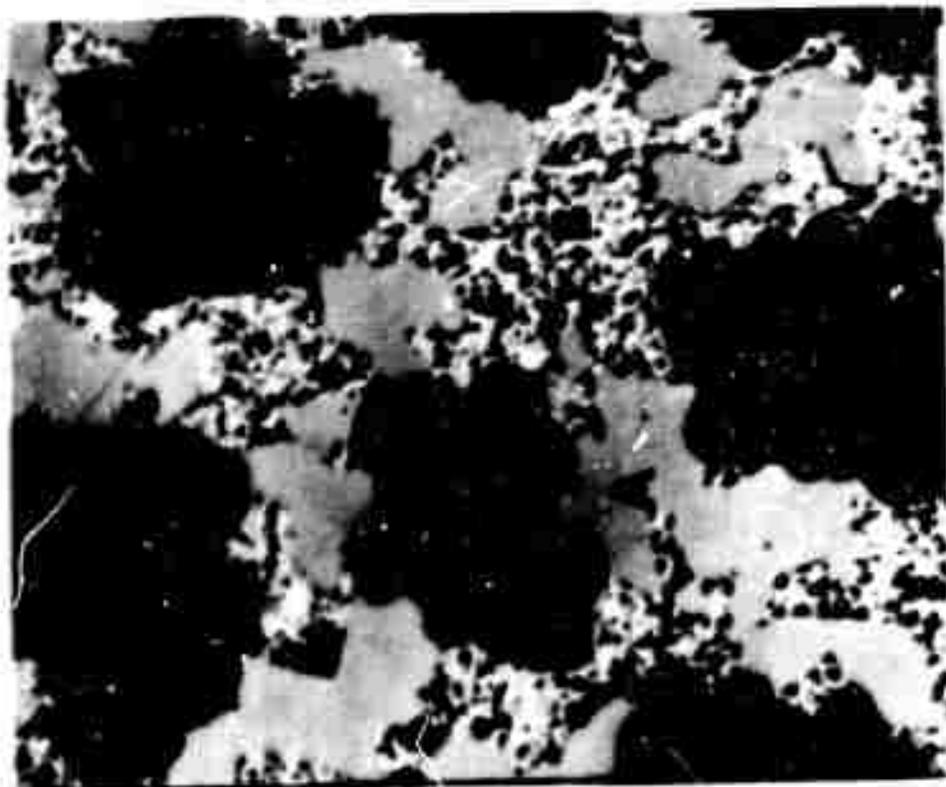
N-9320

Figure 122. Nickel-Coated Fibers Infiltrated with Aluminum Depicting: A. Al₃Ni; B. Al. 2000X. Enlarged 100 Percent for Reproduction.
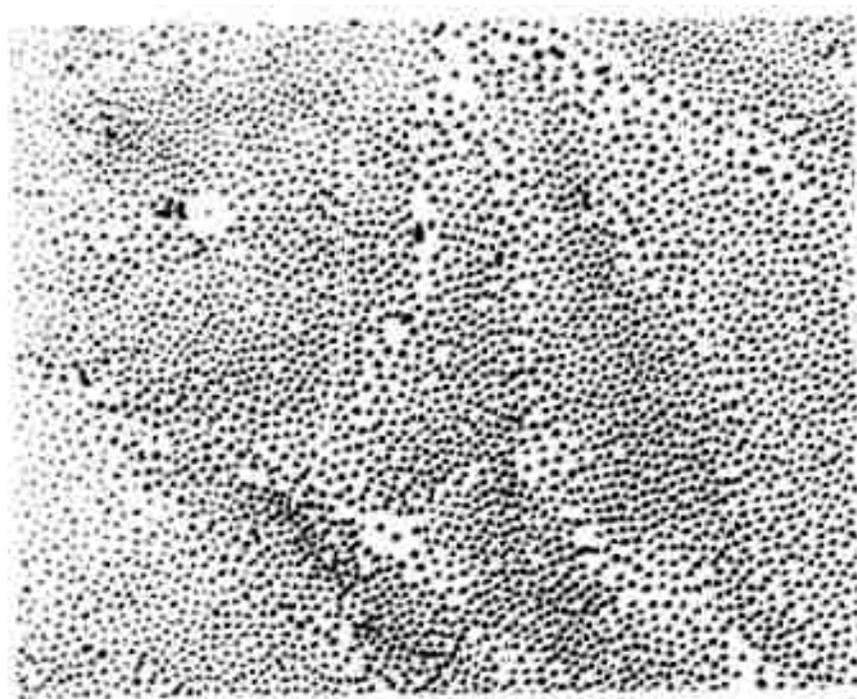
N-9319

Figure 121. Nickel-Coated Fibers Infiltrated with Aluminum. 150X.

consideration was given 'o the absolute minimum in melt temperature and infiltration time (six seconds). Pure aluminum and the alloys 4043 and 2011 were considered as part of this study, but each provided the same end product. It is possible that Sutton also encountered Al_3Ni formation, but his sputtered nickel coatings evidently provided less opportunity for migration of the intermetallic phase into the matrix than that depicted in Figure 122.

Typical results for an aluminum composite containing about 40 volume percent fibers were: density, 2.7 g/cm^3; modulus of elasticity, 20 x 10^6 $lb/in.^2$; and tensile strength, 26,500 $lb/in.^2$ The fibers are characterized by a modulus of 34.5 x 10^6 $lb/in.^2$ and a tensile strength of 200,000 $lb/in.^2$ It is difficult to compare composite values with theoretical values because of contributions from Al_3Ni.

Silver was studied briefly as an infiltration aid for aluminum principally because the phase diagram depicts an extensive solubility range of silver in aluminum (around 38 atomic percent) at the solidus temperature. This phase diagram configuration provides an opportunity for creating an intermetallic-free matrix. Another favorable aspect is that the Ag_3Al_2 phase occurs at a relatively high Ag concentration, a situation which favors a smaller volume of intermetallic in the aluminum if reaction should occur. The obvious obstacle in this system is dewetting if the silver coating should dissolve too rapidly in the aluminum.

An aqueous silver cyanide bath was used to deposit a thin coating of silver on the fibers. First attempts at deposition resulted in the coating of only approximately 75 percent of the fibers; and, after infiltration with aluminum, approximately this same fraction of the fibers was incorporated in the matrix. The photomicrograph in Figure 123 does not reveal the prior existence of silver around the fibers because of the alloying of the silver with the matrix. The small areas of gray phase in the photomicrograph are Ag_3Al_2. A second experiment conducted with more uniformly coated fibers was altered to include a one-minute equilibration period at the infiltration temperature. This equilibration period was an attempt to homogenize the alloy and deplete the matrix of Ag_3Al_2. These objectives were achieved, but most of the fibers were dewetted and regrouped as clusters of uninfiltrated fibers.

Copper was also studied as a coupling agent. However, the copper-aluminum system does not possess a solubility range as wide as that of silver. This phase diagram difference for the two systems is also reflected in the extent of intermetallic formation observed in infiltrated specimens. Aluminum infiltrated around copper-coated fibers resulted in the formation of considerable quantities of Al_3Cu, a behavior very similar to that for nickel-coated fibers.
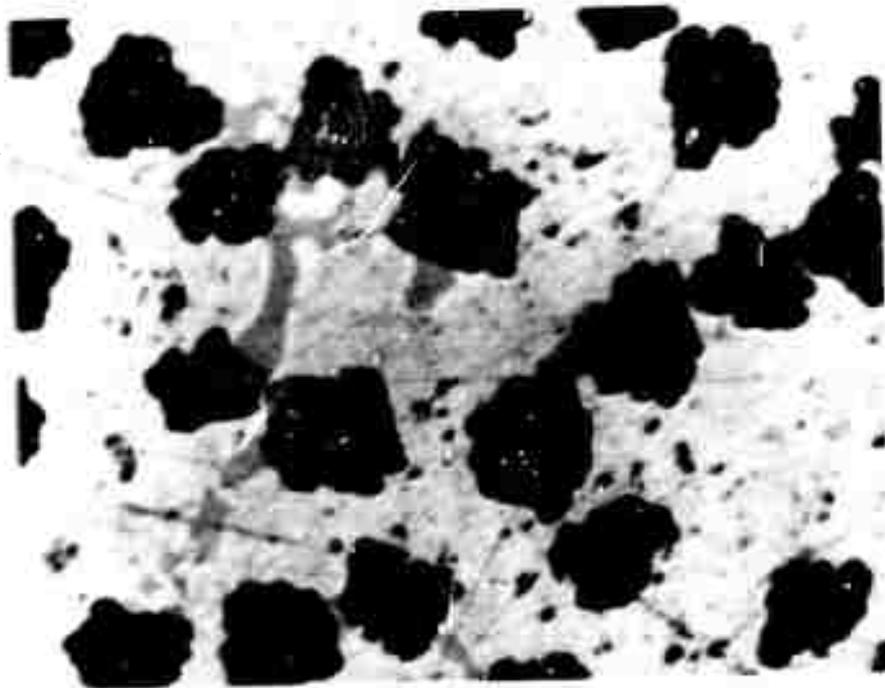
Figure 123. Silver-Coated Fibers Infiltrated with Aluminum.
2000X.

D. Nickel Matrix Studies
(R. V. Sara and R. Didchenko, Union Carbide)

Early in this program, an electroless method was developed for depositing nickel around multifilament strands of carbon yarn on a continuous basis. Initial attempts to obtain a suitable deposit by straight-forward electroless plating failed; but when the fiber was made cathodic in a standard electroless nickel bath, a sufficiently uniform deposit of nickel could be obtained. The thickness of the deposit could be regulated to some extent by varying the current and the rate at which the fiber was passing through the solution. The nickel-coated fibers were formed into test specimens measuring 10 cm long, 6 mm wide, and 3 to 4 mm thick by hot pressing at 750°C and 2000 lb/in.^{2} A number of specimens showed areas of delamination where the nickel deposit was very thin around the fibers (approximately one micron or less).

For comparative purposes, additional test bars were prepared from the pure matrix material under similar sintering conditions. The density of these test bars was 6.8 g/cm^3; the composite density was 3.5 to 4.5 g/cm^3. Tensile strength measurements were made at room temperature and 650°C, and the results are given in Table XXII. The best composite

TABLE XXII

TENSILE STRENGTH OF CARBON-FIBER,
NICKEL-MATRIX COMPOSITES

Material	Tensile Strength (lb/in.^{2}) 25°C	650°C
Unreinforced Electroless Nickel	15,000	4,000
Reinforced with Carbon Fibers	34,900	>18,500

samples broke at the grips in the high temperature test. The actual tensile
strength is, therefore, higher than the reported value. These preliminary
results indicate a significant fiber strengthening effect, particularly at
650°C. Since fiber densities were not measured, the fiber stress at
fracture is not known.

The electroless nickel is actually a nickel-phosphorus alloy (our
deposits contain around 5 percent phosphorus), the mechanical properties
of which are not so good as those of pure nickel. Therefore, in subsequent
work, an electrolytic process based on nickel sulfate-boric acid was used.

Carbon fibers with an average modulus of elasticity of 34.5×10^6 lb/in.^{2}
and tensile strength of 200,000 lb/in.^{2} were electroclad with varying
thicknesses of nickel and hot pressed in vacuum at 900°C for one hour under
various applied loads. The bar specimens measured one inch long, one-
eighth inch wide, and approximately one-sixteenth inch thick. Five
specimens were prepared for brief studies of such aspects as fiber loading,
forming pressure, and, in one instance, fibers having a greater fiber
modulus and tensile strength. The results of these studies are summarized
in Table XXIII. The moduli were determined from sonic measurements,

TABLE XXIII

PHYSICAL AND MECHANICAL PROPERTIES
OF CARBON-FIBER, NICKEL-MATRIX COMPOSITES

Sample	Forming Pressure lb/in.^{2}	Apparent Density g/cm^3	Young's Modulus 10^6 lb/in.^{2}	Shear Modulus 10^6 lb/in.^{2}	Tensile Strength lb/in.^{2}	Volume Percent Fibers
A	2250	3.47	21.6	---	40,500	61.1
B	2250	4.15	26.3	3.20	49,700	48.0
C	4500	4.84	28.6	4.01	48,800	55.5
D	6750	4.81	28.8	4.07	47,300	55.5
E	2250	3.48	33.8	2.80	43,300	---

and the tensile strengths were obtained from dogbone-shaped specimens having a one-centimeter gauge length. The ends of the dogbone were cemented with epoxy into fixtures to facilitate gripping on the Instron instrument. The fiber-loading figures noted above are based on the number of fibers charged into the mold, their cross-sectional area, and the formed specimen cross-sectional area. The fiber-loading values will be corroborated by means of chemical analytical results. The chemical analysis will also provide a means for establishing more precisely the composite theoretical density.

The fibers used in preparing samples A and E were electroplated in the same manner. The fibers used in samples B, C, and D were also plated similarly but with a larger cross-sectional area of nickel than in A and E.

Specimens A and E, prepared and tested first in this series, provided moduli and strengths much lower than the rule-of-mixtures values. For example, specimen A should have had a Young's modulus of 32×10^6 lb/in.^{2} and a strength of about 150,000 lb/in.^{2}; specimen E (made from fibers having a modulus of 53.4×10^6 lb/in.^{2} and a tensile strength of 330,000 lb(in.^{2}) should have been characterized by a modulus of approximately 44×10^6 lb/in.^{2} and strength of 230,000 lb/in.^{2} Microstructures revealed porosity at the junctures of the coated fibers and prompted a study of the influence of forming pressure on density and mechanical properties. When the pressure was doubled to 4500 lb/in.^{2}, the porosity problem was solved, but the modulus and strength were still below theoretical values. An even higher forming pressure produced no density or microstructural change and did not significantly affect the mechanical properties.

A study was made of the fibers to detect if property degradation was taking place as a consequence of the plating operation. In particular, fibers plated with nickel were stripped of the coating with diluted HCl. These fibers did provide lower property values: modulus of 28.6×10^6 lb/in.^{2} and strength of 178,000 lb/in.^{2} The cause for these changes has not been established conclusively, but the sulfate ion in the plating solution is suspect in that it will form interlaminar compounds with graphite. With this lower modulus value for the fibers, the theoretical value of the modulus is very nearly achieved in the high density composite (specimens C and D), but the revised (lower) theoretical strength is not achieved. The low composite strength may be due, in part, to the fact that the fiber modulus is less than that of the matrix. The microstructure for sample D, showing fiber orientation normal to the applied forming pressure, is depicted in Figure 124. This figure indicates that some fiber breakage has occurred, but the aspect ratios are still quite large. Furthermore, the nickel was effectively forced between the broken ends of the fibers and nullified potential void areas. Figure 125 shows a cross-sectional view of composite D which indicates very little fiber-fiber contact and verifies the high degree of densification discussed previously. No reaction was evident in microstructures at the nickel-fiber interface, but this result does not preclude the possibility of carbon diffusion occurring which might degrade one or both constituents in the composite.

Figure 124. Horizontal Section of Carbon-Fiber,
Nickel-Matrix Composite. 250X.
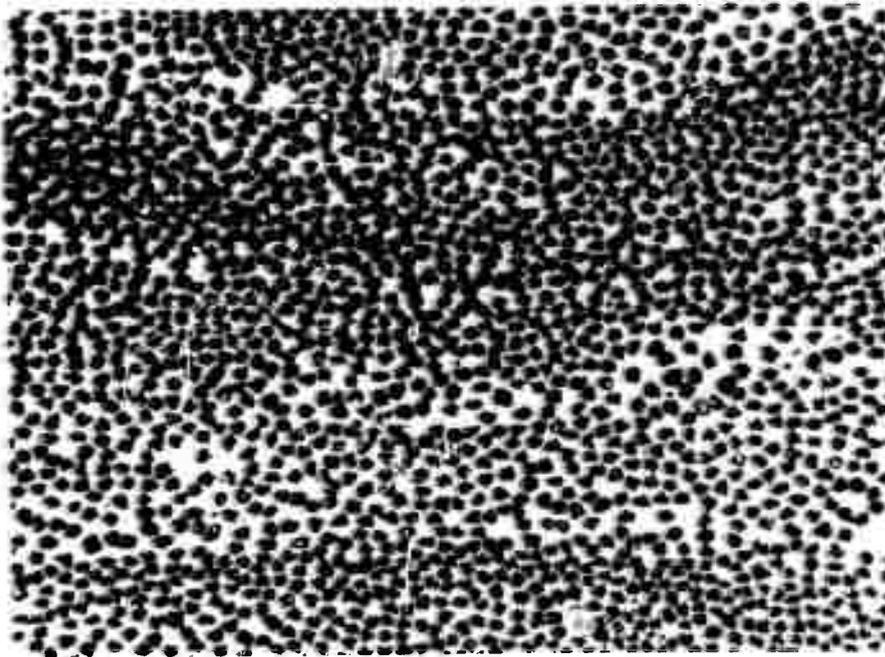
Figure 125. Cross Section of Carbon-Fiber,
Nickel-Matrix Composite. 250X.

This study will be extended on this composite system to include variables such as forming pressures and temperatures, fiber loading, fiber modulus, chemical compatibility, and bonding. A knowledge of the effect of these variables is essential for optimizing the composite properties.

E. Other Metal Matrix Studies
(R. V. Sara, Union Carbide)

Studies on two composite systems with low-modulus matrices were initiated primarily to assess the strengthening which might be realized if a more favorable relationship existed between the fiber and matrix moduli. The first of these composites included tin, which has a modulus of 7.75 x 10^6 lb/in.^{2} and a tensile strength of approximately 4000 lb/in.^{2} The nickel coated fiber network after infiltration with tin was practically pore free. The density was 5.52 g/cm^3, and the fiber loading was approximately 33.5 volume percent. A cross-sectional view of this infiltrated composite is shown in Figure 126. Measurements revealed that tin was strengthened by a factor of twelve (47,400 lb/in.^{2}), and the modulus was increased twofold to 16.2 x 10^6 lb/in.^{2} The measured modulus corresponds to the theoretical value, whereas only 75 percent of the theoretical strength was realized.
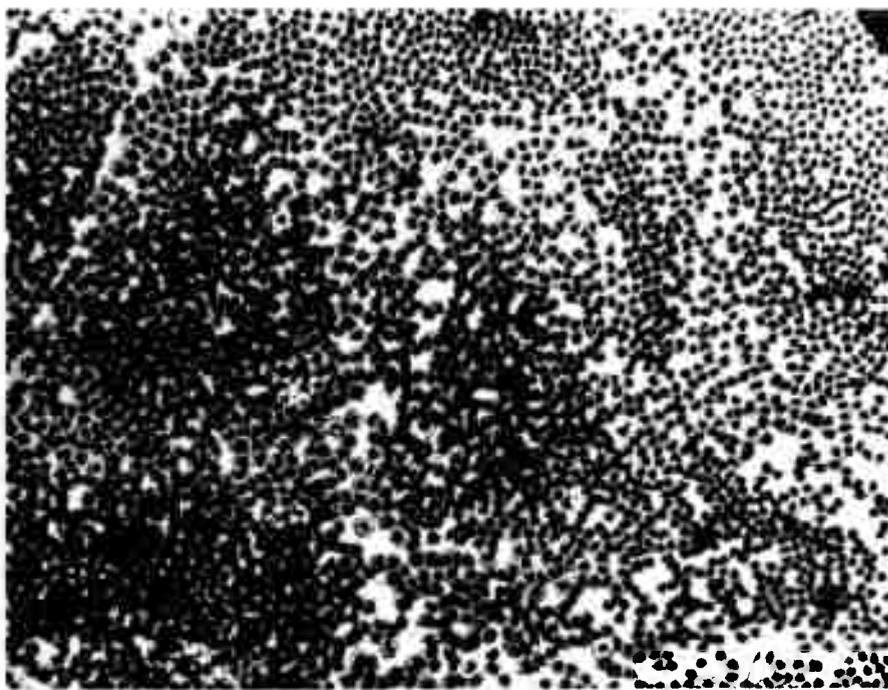
N-9696

Figure 126. Cross Section of Carbon-Fiber, Tin-Matrix Composite. 150X.
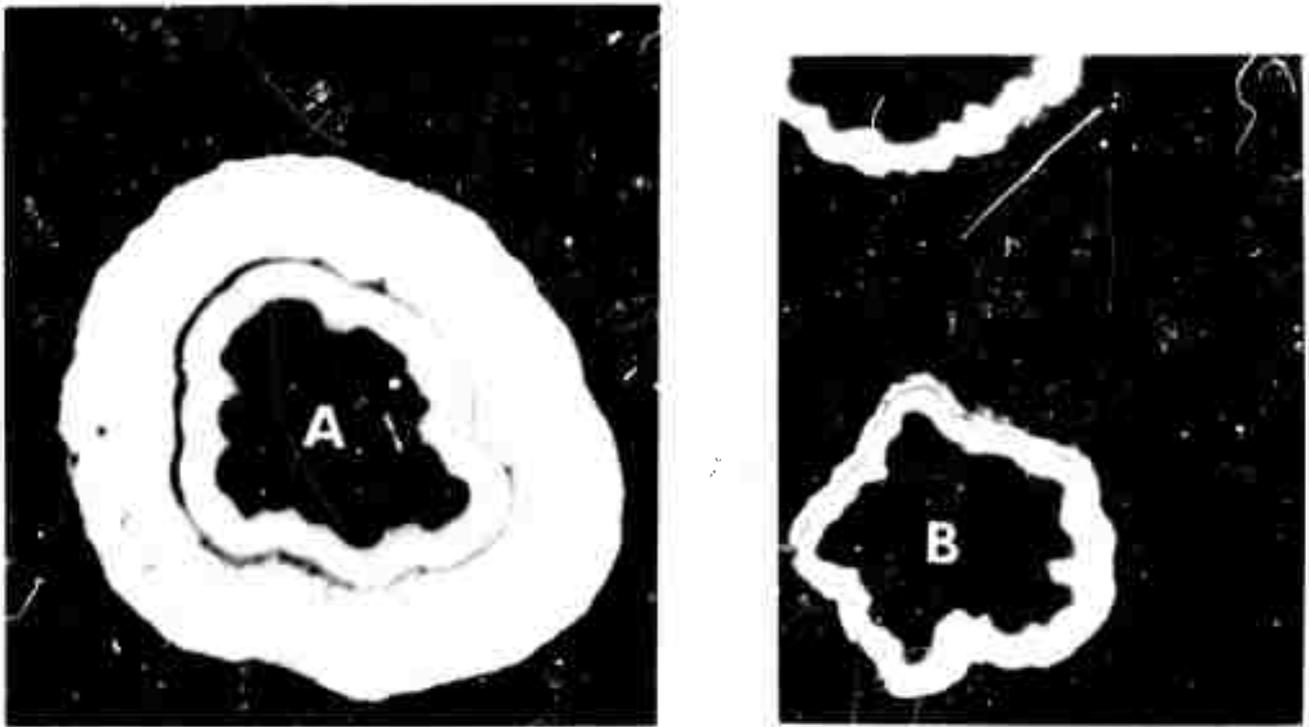
Figure 127. Nickel-Copper Coatings on: A. Peripheral Carbon Fiber,
B. Inner Fibers. 2000X. Enlarged 100 Percent for
Reproduction.

In the other composite considered in this phase study, the nickel-matrix
modulus was decreased by alloying with copper ($E = 18 \times 10^6$ lb/in.^{2}). The
cupro-nickel matrix was formed by first electrocladding the fibers with
nickel and then with copper. The low throwing power of the copper sulfate
bath resulted in heavier plating on the peripheral fibers (Figure 127a) and
less on fibers deeper within the yarn (Figure 127b). The plated fibers
were compacted in a manner paralleling that used for Sample B in Table
XXIII. Even though the copper was not deposited uniformly, the total mass
of metal deposited was comparable with Sample B. The fabricated Ni-Cu
composite showed slight delamination tendencies which did not prevail in
composites B, C, or D. This delamination is due to sparse concentrations
of metal in certain regions of the composite. A density of 4.60 g/cm^3 was
determined for the specimen. Microstructures revealed that alloying was
complete and densification was good in regions containing ample metal.
The modulus of elasticity and tensile strength were 26.9 x 10^6 lb/in.^{2} and
55,800 lb/in.^{2}, respectively. These measurements cannot be compared
with theoretical values because of variation in the alloy composition, but
the strength is the highest realized to date for a carbon-fiber composite.
The fracture for this specimen is shown in Figure 128. The splintered
appearance is probably due to the occurrence of areas which possess very

poor shear strengths due to metal deficiency. The fracture pattern was less irregular for the pure nickel composites which had less porosity and better metal distribution (see Figure 129), a pattern which is similar to that of Sample D in Table XXIII. It is expected that higher copper-nickel composite strengths will be obtained by decreasing the porosity and improving the metal distribution.
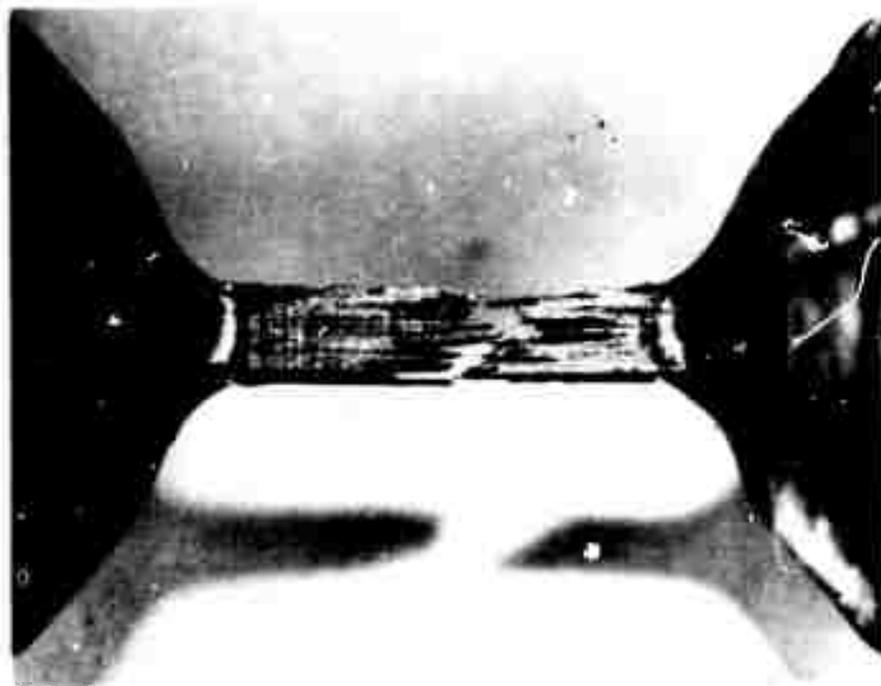
N-9698

Figure 128. Fracture Pattern for Carbon-Fiber, Cupro-Nickel-Matrix Tensile Specimen.

N-9699
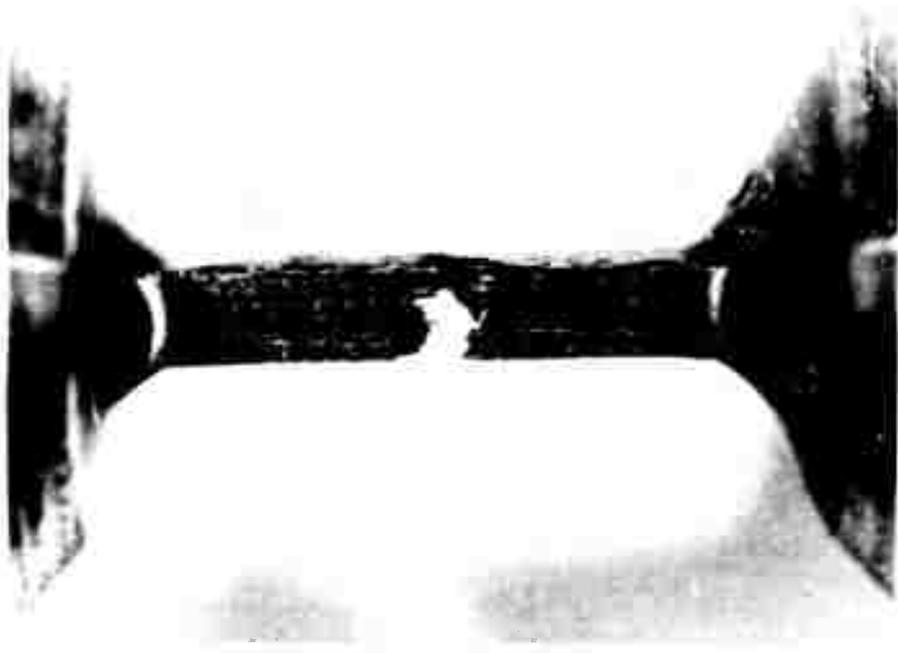
Figure 129. Fracture Pattern for Carbon-Fiber,
Nickel-Matrix Tensile Specimen.

SECTION IX

ADVANCED ANALYSIS AND SYNTHESIS STUDIES

The effective use of composite materials in high performance structural systems depends upon realistic behavior prediction and efficient design procedures. Analyses and criteria to be used in guarding against failure of composite material structures are complicated by the anisotropic and nonlinear material properties exhibited by these materials. In many applications the geometric configurations involved will be complex structural arrangements with irregular mechanical and thermal loadings and with severe discontinuities. The studies reported in this section are directed toward obtaining improved methods for structural analysis and automated optimum design.

In Section IX A the use of an incremental complementary energy formulation as a means of dealing with nonlinear multiaxial stress analysis problems is discussed. In Section IX B the selection and generation of modern optimization capabilities is reported. The inherent complexity of the analyses and failure criteria on which synthesis of composite material structural systems must rest emphasizes the importance of having available efficient optimization procedures which make effective use of information available from previous design cycles. In Section IX C the extension of discrete element methods of structural analysis to include anisotropy is presented. Finite element methods of structural analysis are known to be particularly useful in dealing with complex and irregular structural arrangements fabricated from essentially isotropic materials, and this feature is expected to carry over to anisotropic materials. The scope of the finite element formulations reported is such that material and geometric nonlinearities can be treated in the future using iterative computational procedures. In Section IX D the extension to anisotropic material of a rather general transient temperature distribution analysis capability is reported. This thermal analysis program will be applicable to both particulate and fibrous composite systems, provided the material can be considered quasi-homogeneous. All of the studies reported in Section IX can be expected to contribute to the overall goal of being able to rationally design an optimum structure and material simultaneously.

A. **Nonlinear Multiaxial Stress Analysis**
        (Professor Schmit and Mr. E. Rybicki, Case Institute)

Multiaxial stress analysis including material nonlinearity is a difficult problem of growing importance. Mendelson (Reference 60) has studied various plane stress problems for isotropic strain hardening materials. The plan of attack in this study calls for first trying out an incremental complementary energy approach on some of the isotropic problems studied by Mendelson and then extending this work to orthotropic nonlinear materials subject to multiaxial stress distributions.

The incremental complementary energy approach will be described in terms of a plane stress problem. The change in the complementary energy density Δu_c between stress distribution state $Q-1$ (σ_{xQ-1}, σ_{yQ-1}, σ_{xyQ-1}) and stress distribution state $Q(\sigma_{xQ}$, σ_{yQ}, $\sigma_{xyQ})$ can be expressed as follows

$$\Delta u_c = \int_{\sigma_{xQ-1}}^{\sigma_{xQ}} \varepsilon_x \, d\sigma_x + \int_{\sigma_{yQ-1}}^{\sigma_{yQ}} \varepsilon_y \, d\sigma_y + \int_{\tau_{xyQ-1}}^{\tau_{xyQ}} \gamma_{xy} \, d\tau_{xy} \qquad \text{(IX A-1)}$$

Stress distribution state $(Q-1)$ is associated with load level $Q-1$ and it is assumed to be known. Stress distribution state Q is associated with load level Q arrived at by incrementing upward from load level $(Q-1)$. The stress distribution state Q is unknown and is to be determined. The stress-strain temperature relations are assumed to be of the form

$$\varepsilon_x = \frac{\sigma_x}{E} - \nu \frac{\sigma_y}{E} + \alpha \, \Delta T + \sum_{q=1}^{Q-1} \Delta \varepsilon_x^{(q)P} + \Delta \varepsilon_x^{P} \qquad \text{(IX A-2)}$$

$$\varepsilon_y = \frac{\sigma_y}{E} - \nu \frac{\sigma_x}{E} + \alpha \, \Delta T + \sum_{q=1}^{Q-1} \Delta \varepsilon_y^{(q)P} + \Delta \varepsilon_y^{P} \qquad \text{(IX A-3)}$$

$$\gamma_{xy} = \frac{\tau_{xy}}{G} + \sum_{q=1}^{Q-1} \Delta \gamma_{xy}^{(q)P} + \Delta \gamma_{xy}^{P} \qquad \text{(IX A-4)}$$

In Equations IX A-2 and IX A-3 the first two terms are the elastic strain, the third term is the thermal strain, the fourth term is the accumulated plastic strain components from the first $Q-1$ load increments, and the fifth term represents the incremental plastic strain component. In Equation IX A-4 the first term is the elastic shear strain, the second term the accumulated plastic shear strain components from the first $Q-1$ load increments, and the third term represents the incremental plastic shear strain component. The incremental plastic strain components are assumed to be given by the Prandtl-Reuss relations

$$\Delta\varepsilon_x^p = (\sigma_x - \frac{1}{2}\sigma_y)\frac{\Delta\bar{\varepsilon}^p}{\bar{\sigma}} \qquad \text{(IX A-5)}$$

$$\Delta\varepsilon_y^p = (\sigma_y - \frac{1}{2}\sigma_x)\frac{\Delta\bar{\varepsilon}^p}{\bar{\sigma}} \qquad \text{(IX A-6)}$$

$$\Delta\gamma_{xy}^p = 3\tau_{xy}\frac{\Delta\bar{\varepsilon}^p}{\bar{\sigma}} \qquad \text{(IX A-7)}$$

where $\Delta\bar{\varepsilon}^p$ is the incremental equivalent plastic strain and the equivalent stress $\bar{\sigma}$ is defined as follows

$$\bar{\sigma} = (\sigma_x^2 - \sigma_x\sigma_y + \sigma_y^2 + 3\tau_{xy}^2)^{1/2} \qquad \text{(IX A-8)}$$

The basic assumption of the incremental strain theory is that the equivalent stress $\bar{\sigma}$ and the equivalent strain $\bar{\varepsilon}$ are related in the same manner as the uniaxial stress-strain curve of the material. Note that the initial tangent modulus and the equivalent plastic strain $\bar{\varepsilon}_p$ uniquely define a value of the equivalent stress $\bar{\sigma}$. Thus the equivalent stress $\bar{\sigma}$ can be expanded in a Taylor series about the (n-1) stress state, that is

$$\bar{\sigma} = \bar{\sigma}_{n-1} + \left(\frac{d\bar{\sigma}}{d\bar{\varepsilon}^p}\right)_{n-1}\Delta\bar{\varepsilon}^p + \ldots \qquad \text{(IX A-9)}$$

neglecting higher order terms and solving for $\Delta\bar{\varepsilon}^p/\bar{\sigma}$ yields

$$\frac{\Delta\bar{\varepsilon}^p}{\bar{\sigma}} = \left(1 - \frac{\bar{\sigma}_{n-1}}{\bar{\sigma}}\right)\left(\frac{d\bar{\varepsilon}^p}{d\bar{\sigma}}\right)_{n-1} \qquad \text{(IX A-10)}$$

For a linear strain hardening material (see Figure 130)

$$\bar{\varepsilon}^p = (\bar{\sigma} - \bar{\sigma}_0)\frac{1}{E}\left(\frac{1-m}{m}\right) \qquad \text{(IX A-11)}$$

and

$$\frac{d\bar{\varepsilon}^p}{d\bar{\sigma}} = \frac{1}{E}\left(\frac{1-m}{m}\right) \qquad \text{(IX A-12)}$$

from which it follows that

-218-

$$\bar{\epsilon}^P = \left(\frac{\bar{\sigma} - \bar{\sigma}}{mE} \right) - \left(\frac{\bar{\sigma} - \bar{\sigma}_0}{E} \right)$$
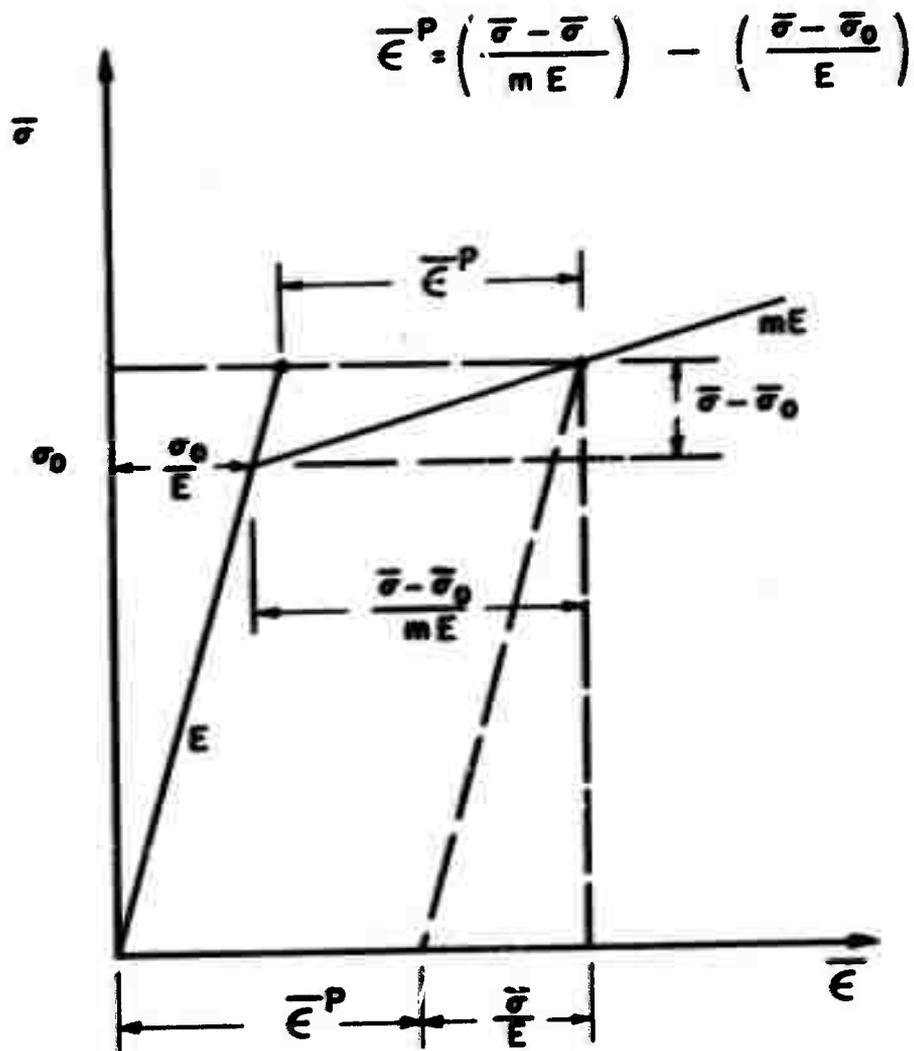
Figure 130. Linear Strain Hardening.

$$\frac{\Delta \bar{\epsilon}_p}{\bar{\sigma}} = [\frac{1}{E}(\frac{1-m}{m})] [1 - \frac{\bar{\sigma}_{n-1}}{\bar{\sigma}}] \qquad (\text{IX A-13})$$

For Ramberg Osgood type strain hardening material (see Figure 131)

$$\bar{\epsilon}^p = K (\frac{\bar{\sigma}}{E})^n \qquad (\text{IX A-14})$$

and it can be shown that

$$\frac{\Delta \bar{\epsilon}_p}{\bar{\sigma}} = [\frac{Kn}{\bar{\sigma}} (\frac{\bar{\sigma}}{E})^n]_{n-1} [1 - \frac{\bar{\sigma}_{n-1}}{\bar{\sigma}}] \qquad (\text{IX A-15})$$

It is important to establish that the behavior between stress state (n-1) and stress state n is conservative. This behavior is conservative if there is no net change in the complementary energy as a result of going from stress state n-1 to stress state n and then back to stress state n-1. Stated in equation form the behavior stress state n-1 and stress state n is conservative if

$$\oint_{\sigma_{n-1}}^{\sigma_0} d u_c + \oint_{\sigma_0}^{\sigma_{n-1}} d u_c = \oint d u_c = 0 \qquad (\text{IX A-16})$$

where

$$d u_c = \epsilon_x d\sigma_x + \epsilon_y d\sigma_y + \gamma_{xy} d\tau_{xy} \qquad (\text{IX A-17})$$

Let

$$\bar{F} = \epsilon_x \bar{i} + \epsilon_y \bar{j} + \gamma_{xy} \bar{k} \qquad (\text{IX A-18})$$

and denoted

$$d\bar{R} = d\sigma_x \bar{i} + d\sigma_y \bar{j} + d\tau_{xy} \bar{k} \qquad (\text{IX A-19})$$

Then substituting Equations IX A-18 and IX A-19 into Eq. IX A-17 and Equation IX A-17 into Eq. IX A-16 gives
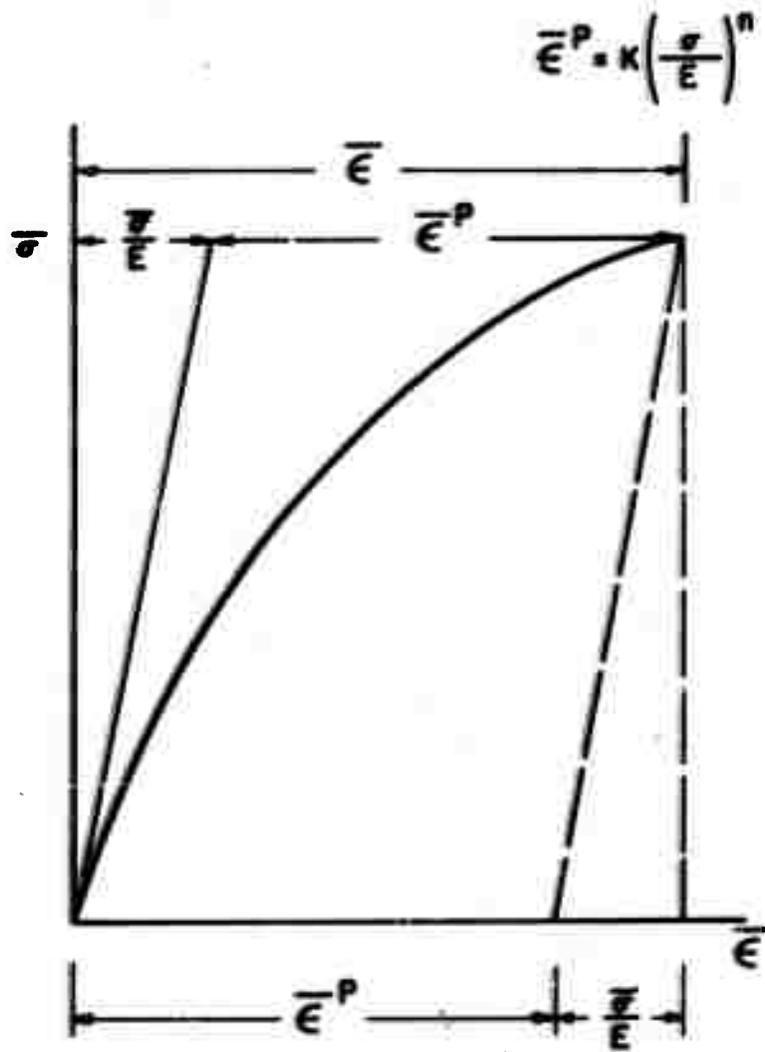
Figure 131. Ramburg Osgood Strain Hardening.

$$\oint du_c = \oint \overline{F} \cdot d\overline{R} = 0 \qquad \text{(IX A-20)}$$

But by Stokes Theorem it follows that

$$\oint \overline{F} \cdot d\overline{R} = \iint (\nabla \times \overline{F}) \cdot \overline{n} \, dS \qquad \text{(IX A-21)}$$

and from Equation IX A-21 it follows that Equations IX A-20 and IX A-16 will be satisfied if $\nabla \times \overline{F} = 0$, and this requirement

$$\nabla \times \overline{F} = \begin{vmatrix} \overline{i} & \overline{j} & \overline{k} \\ \dfrac{\partial}{\partial \sigma_x} & \dfrac{\partial}{\partial \sigma_y} & \dfrac{\partial}{\partial \tau_{xy}} \\ \varepsilon_x & \varepsilon_y & \gamma_{xy} \end{vmatrix} = 0 \qquad \text{(IX A-22)}$$

yields the following conditions

$$\frac{\partial \gamma_{xy}}{\partial \sigma_y} = \frac{\partial \varepsilon_y}{\partial \tau_{xy}}$$

$$\frac{\partial \gamma_{xy}}{\partial \sigma_x} = \frac{\partial \varepsilon_x}{\partial \tau_{xy}} \qquad \text{(IX A-23)}$$

$$\frac{\partial \varepsilon_x}{\partial \sigma_y} = \frac{\partial \varepsilon_y}{\partial \sigma_x}$$

It can be shown that the stress-strain relations represented by Equations IX A-1, IX A-2, and IX A-4 satisfy the conservative behavior conditions Equation IX A-23 therefore the incremental complementary energy density Δu_c (see Equation IX A-1) is independent of the path taken to arrive at stress state Q from stress state $Q-1$. This is true for both the linear strain hardening case or the Ramberg-Osgood type of strain hardening material.

The incremental complementary energy density can be expressed as function of the unknown stress state Q by substituting Equation IX A-2, IX A-3, and IX A-4 into Equation IX A-1. For the case of linear strain hardening the result is

$$\Delta u_c = \frac{1}{2E} \left[\sigma_{xQ}^2 + \sigma_{yQ}^2 - 2\nu \sigma_{xQ} \sigma_{yQ} + 2(1+\nu) \tau_{xyQ}^2 \right.$$

$$- \sigma_{xQ-1}^2 - \sigma_{yQ-1}^2 + 2\nu \sigma_{xQ-1} \sigma_{yQ-1} - 2(1+\nu) \tau_{xyQ-1}^2 \left. \right]$$

$$+ \left(\sum_{q=1}^{Q-1} \Delta\epsilon_x^{(q)P} \right) (\sigma_{xQ} - \sigma_{xQ-1}) + \left(\sum_{q=1}^{Q-1} \Delta\epsilon_y^{(q)P} \right) (\sigma_{yQ} - \sigma_{yQ-1})$$

$$+ \left(\sum_{q=1}^{Q-1} \Delta\gamma_{xy}^{(q)P} \right) (\tau_{xyQ} - \tau_{xyQ-1})$$

$$+ (\alpha\Delta T)_Q (\sigma_{xQ} + \sigma_{yQ}) - (\alpha\Delta T)_{Q-1} (\sigma_{xQ-1} + \sigma_{yQ-1}) \qquad \text{(IX A-24)}$$

$$+ \frac{1-m}{2mE} (\bar{\sigma}_Q - \bar{\sigma}_{Q-1})^2$$

The method of solution being explored using this incremental complementary energy approach can now be outlined. Let the structure be subdivided into K regions or zones of volume V_k. Then the total incremental complementary energy $\Delta \Pi_c$ may be expressed as follows

$$\Delta \, \Pi_c \; = \; \sum_{k=1}^{K} \; [\int_{V_k} \Delta \, u_c \; dV_k] \; - \; \int_{S_2} (\overline{u} \, X + \overline{v} \, Y) \; dS_2 \qquad \text{(IX A-25)}$$

where the second term on the right hand side of Equation IX A-25 introduces the influence of prescribed displacement boundary conditions $(\overline{u}, \overline{v})$ over the S_2 portion of the boundary. In each region V_k the stress function $\psi^{(k)}(x,y)$ can be represented by the products of one dimensional Hermite interpolation formulas (Reference 61). Note that the stresses depend upon the stress function ψ in the following manner:

$$\sigma_x \; = \; \frac{\partial^2 \psi}{\partial y^2} ; \qquad \sigma_y \; = \; \frac{\partial^2 \psi}{\partial \sigma^2} ; \qquad \tau_{xy} \; = \; - \frac{\partial^2 \psi}{\partial x \, \partial v} \qquad \text{(IX A-26)}$$

Using second order Hermite interpolation formulas (hyperosculatory) the approximate representation for the stress function in the k th region can be expanded in the form of a series which will involve a total of thirty-six unknowns. Executing the integration over the volume

$$\int_{V_k} \Delta \, u_c \; dV_k$$

give the contribution of the k th region to the incremental complementary energy and summing over the K regions gives the incremental complementary energy for the entire system. At the boundaries between the regions stresses are matched exactly thus reducing the number of independent unknowns. At external boundaries prescribed stress boundary conditions can be assigned by specifying the values of appropriate unknowns. The basic unknowns in this formulation may be viewed as participation coefficients in the series approximations for the $\psi^{(k)}(x,y)$. Minimization of the incremental complementary energy with respect to the independent participation coefficients will yield a solution for the stress state η. It is expected that the unconstrained minimization techniques reported in Section IX B-2 can be effectively applied to this class of nonlinear stress analysis problems.

B. Selection and Generation of Synthesis Procedures
(Professor Fox and Mrs. Pankush, Case Institute)

1. Introduction

In order to carry out the various optimization tasks throughout the project it is necessary to have a selection of synthesis techniques available. This portion of the work has two major goals: first to develop a solid base of experience with methods available in the recent litera- ture and with possibilities for new methods in relation to the specific optimization problems involved in this project, and second to generate an actual operational capability in terms of computer programming that can be used for part of the synthesis work. These techniques, in varying degrees, can be generalized and developed into a modularized set of computer routines to be used as necessary for optimization problems. By and large, the methods which will be described in this section are available in the literature as mathematical programming methods for nonlinear programming problems.

Many design problems can be stated in the following form:

Find the vector, $\vec{D}$, of design variables such that a func- tion $F(\vec{D})$, called the objective function, is minimized (or maximized) subject to a system of constraints on the design variables as follows:

$$g_j(\vec{D}) \leq 0 \qquad\qquad j = 1, 2, \ldots, m \qquad (IX\ B-1)$$

where the constraint functions $g_j(\vec{D})$ represent the design restrictions such as stress limitations, temperature limitations, an upper or lower bound on a design variable itself and so on. Generally speaking, in most real design problems the $g_j(\vec{D})$ are very complicated functions and in fact in the usual sense are not really functions at all but the result of a complicated analysis of some engineering design. They are, however, functions in the sense that there are rules for determining their value given the argument $\vec{D}$. When the problem is stated in this way it is implicit that an analysis must be executed in order to determine the values of the functions $g_j(\vec{D})$.

Another way of stating the same problem which is valid for many engineering situations is as follows. Define a vector $\vec{X}$ which is the concatenation of the vector of design variables and a vector of behavior variables, that is

$$\vec{X} = (\vec{D}, \vec{Y}) = (D_1, D_2, \ldots, D_n, Y_1, Y_2, \ldots, Y_k) \qquad (IX\ B-2)$$

where the Y_i are behavior quantities such as stress, displacement, temperature, etc. The problem can now be stated as follows:

Find the $\vec{X}$ such that the function $F(\vec{X})$ is minimized and such that the following constraints are satisfied:

$$g_j(\vec{X}) \leq 0 \qquad j = 1, 2, \ldots, m \qquad \text{(IX B-3)}$$

$$\ell_p(\vec{X}) = 0 \qquad p = 1, 2, \ldots, n \qquad \text{(IX B-4)}$$

where the functions $g_j(\vec{X})$ are as before and the new equality constraints represent the analysis of the engineering design.

The system of equations $\ell_p(\vec{X}) = 0$ may be, in a linear structural analysis problem, the following matrix equation

$$L(\vec{X}) = K\vec{Y} - \vec{P} = 0 \qquad \text{(IX B-5)}$$

in which K, the stiffness matrix, is a function of the design variables, $\vec{D}$, and the displacements, $\vec{Y}$, are the behavior variables. Thus the two modes of statement of the synthesis problem differ in that in the first instance the analysis is assumed to be performed as a subsidiary function to solving the design problem and the problem statement contains only inequality constraints. In the second instance the analysis is an integral part of the design problem and is performed at the same time values for the design variables are sought which optimize the design. Thus this latter statement of the design problem contains equality constraints in the form of the $\ell_p(\vec{X}) = 0$. The first form of problem statement is perhaps the more natural to engineering, however it has been discovered that the latter form often has advantages which make it useful in certain applications.

A rough means of categorizing the available methods for solving these problem is to break them down into two general categories: the unconstrained methods and the constrained methods. Either of the methods is applicable in theory to both formulations of the synthesis problem. In the constrained methods both the equality and inequality constraints are handled directly by considering them as inviolable limits on the design variables. In the unconstrained methods a new function is formulated which incorporates contributions from both the objective function and from penalties representing increases in the function value proportional in some way to the violations of the constraints. These functions are then minimized and their minima tend successively to the solution of the constrained minimization problem. A brief description of two unconstrained formulations is presented later in this section.

2. Unconstrained Minimization Algorithms

Central to the unconstrained methods are algorithms for finding the minimum of a function of many variables without considering constraints. Generally speaking, all of the practical methods are iterative. Consider a function $\phi(\vec{X})$ which is to be minimized. An iteration process can proceed as follows

$$\vec{X}^{q+1} = \vec{X}^q + \alpha_q \vec{S}^q \qquad \text{(IX B-6)}$$

in which the $q+1^{th}$ iterate is determined from the qth iterate by the addition of a scalar multiple of a vector $\vec{S}^q$. The various schemes for unconstrained minimization differ essentially in the ways in which the directions $\vec{S}^q$ are generated and by ways in which the scalar multiples α_q are determined. A simple relaxation scheme, for example, is one in which the $\vec{S}^q$ are successively

$$\vec{S}^1 = (1, 0, 0, \ldots, 0),$$

$$\vec{S}^2 = (0, 1, 0, 0, \ldots, 0),$$

$$\vec{S}^3 = (0, 0, 1, 0, \ldots, 0),$$

$$\vdots \qquad\qquad \text{(IX B-7)}$$

$$\vec{S}^n = (0, 0, \ldots, 0, 1)$$

$$\vec{S}^{n+1} = (1, 0, 0, \ldots, 0)$$

$$\vdots$$

A method of this type is also often called a univariate method. Even with the simple relaxation method there are still a wide variety of possibilities for the α_q. For example, the α_q may be taken to be a small predetermined quantity which is kept constant until its use no longer produces decreases in ϕ or it may be changed on an ad hoc basis as the iteration process progresses. Perhaps the most common rationale for modern methods is to choose α_q such that $\phi(\vec{X}^q + \alpha \vec{S}^q)$ is minimized. We will denote the α which minimizes the $\phi(\vec{X}^q + \alpha \vec{S}^q)$ as α^*. This latter method of choosing the α is ordinarily the most efficient method and is in every case the method chosen for work on this project.

An efficient improvement of the simple univariate methods has been developed by Powell (Reference 62). This method has been programmed and a description of the algorithm follows.

Select for an initial set of directions the univariate directions, i.e. the elements of the qth direction, $\vec{S}^q$, are

$$s_i^q = \delta_{qi} \qquad \begin{array}{l} q = 1, 2, \dots, n \\ i = 1, 2, \dots, n \end{array} \qquad \text{(IX B-8)}$$

as in Equations IX B-7. Denoting the starting point for an iteration sequence as $\vec{X}^1$ compute $\vec{X}^2, \vec{X}^3, \dots, \vec{X}^{n+1}$ as

$$\vec{X}^{q+1} = \vec{X}^q + \alpha * \vec{S}^q \qquad q = 1, 2, \dots, n \qquad \text{(IX B-9)}$$

Then compute the direction vector from $\vec{X}^1$ to $\vec{X}^{n+1}$ and denote it as $\vec{S}^{n+1}$

$$\vec{S}^{n+1} = \vec{X}^{n+1} - \vec{X}^1 \qquad \text{(IX B-10)}$$

and compute the $n+2^{th}$ iterate as

$$\vec{X}^{n+2} = \vec{X}^{n+1} + \alpha * \vec{S}^{n+1} \qquad \text{(IX B-11)}$$

Finally revise the direction set by

$$\vec{S}^{q-1} = \vec{S}^q \qquad q = 2, 3, \dots, n+1 \qquad \text{(IX B-12)}$$

and repeat the steps given by Equations IX B-9 through IX B-12. This last step (Equation IX B-12), discards the current direction $\vec{S}^1$ and places $\vec{S}^{n+1} = \vec{X}^{n+1} - \vec{X}^1$ into the set. The advantage of this is that this latter vector contains better information on the direction of decreasing function value than do the univariate directions. In Reference 62 a more sophisticated method is given for selecting the vector to be discarded. This method has also been programmed as part of this work.

A surprising feature of the Powell method is the fact that is is quadratically convergent. This means that if the function $\phi(\vec{X})$ is a quadratic function in the variables the method will converge in n steps, where n is the number of variables involved. Of course most of the functions arising from synthesis problems are of higher order than quadratic; however, the property of quadratic convergence is extremely advantageous because as the minimum of the problem is approached the function becomes more nearly approximatable by a quadratic and the method accelerates to the minimum. The programmed versions of these methods have been tested on a variety of functions and these theoretical conclusions have in fact been verified. Powell's method has the

advantage that it does not require any information of the function at any
iteration other than the function value at particular points tested. This
is an advantage in the sense that other information, in particular first
partial derivatives with respect to the x_i, need not be determined. However,
in terms of length of computations and number of iterations required to
obtain a minimum, Powell's method is less efficient than the higher order
methods which do involve partial derivatives of the function.

The simplest of the higher order methods was originated with Cauchy
(Reference 63) and is called the gradient method or steepest descent method.
This technique involves an iteration in which the $\vec{S}^q$ is merely the negative
of the gradient of the function ϕ, $\nabla\phi$. This method in itself is not very
efficient but forms the conceptual basis for a large class of relatively
new methods which are extremely efficient in terms of their convergence
rates. The methods of this category are often referred to as Conjugate
Direction Methods and are also quadratically convergent. They have an
additional advantage over Powell's method in that they are more stable
against round-off error as the iteration process proceeds. In many cases
the computational effort involved in computing the derivatives is made up
for by the reduced number of iterations required. Two methods of this
category have been programmed under this project.

The first of these was developed by Fletcher and Reeves (Reference
64) and operates in the following way. Select a starting vector
$\vec{X}^1$ and set $\vec{S}^1 = - \nabla\phi\,(\vec{X}^1)$. Denote $\nabla\phi(\vec{X}^q)$ as $\vec{G}^q$ and iterate as follows

$$\text{compute} \qquad \beta_q = (\vec{G}^q)^2/(\vec{G}^{q-1})^2 \qquad\qquad\qquad \text{(IX B-13)}$$

$$\text{and} \qquad \vec{S}^q = -\vec{G}^q + \beta_q\,\vec{S}^{q-1} \qquad\qquad\qquad \text{(IX B-14)}$$

$$\text{and} \qquad \vec{X}^{q+1} = \vec{X}^q + \alpha^*\,\vec{S}^q \qquad\qquad\qquad \text{(IX B-15)}$$

It can be proven rigorously that this method, apart from rounding errors, is
guaranteed to locate the minimum of any quadratic function of n variables in
at most n iterations. The proof is involved and for the purposes of this
description is should suffice to note that each direction used in the itera-
tion process contains a contribution from every previous direction. The
proportion of each of the preceeding directions which is contained in this
"carry over direction" is dependent upon the ratio of the square of the
lengths of the gradients of the function at each of the points in the itera-
tion. Thus, the direction in a sense accumulates information about the form
of the function as the iteration process proceeds. This method has been
tested on several non-quadratic functions and its efficiency has been found
to be quite high. Occasionally however since the accumulated information
in the direction vector is subject to round-off error, it is necessary to
clear this information out periodically and begin to accumulate new information.

Various criteria are used in determining the point in the iteration process when the $\vec{S}^{q-1}$ in Equation IX B-14 must be set equal to zero. For problems with many variables it is generally necessary to reset this vector to zero after n iterations. For extremely large problems, for example on the order of 300 to 600 variables, it may be necessary to reset the accumulated direction vector to 0 in as few as n/2 iterations.

Probably the most powerful of the gradient type methods is that developed by Davidon (Reference 65) and further explained by Fletcher and Powell (Reference 66). This method operates as follows:

Select a starting point $\vec{X}^1$ and choose any positive definite symmetric matrix H_1 and compute

$$\vec{X}^{q+1} = \vec{X}^q + \alpha^* \vec{S}^q \qquad (IX\ B-16)$$

where

$$\vec{S}^q = -H_q \vec{G}^q \qquad (IX\ B-17)$$

and

$$H_q = H_{q-1} + \frac{\vec{\sigma}^q \vec{\sigma}^{qT}}{\vec{\sigma}^{qT} \vec{y}^q} - \frac{H_{q-1} \vec{y}^q \vec{y}^{qT} H_{q-1}}{\vec{y}^{qT} H_{q-1} \vec{y}^q} \qquad (IX\ B-18)$$

where

$$\vec{\sigma}^q = \vec{X}^q - \vec{X}^{q-1} = \alpha^* \vec{S}^{q-1} \qquad (IX\ B-19)$$

and

$$\vec{y}^q = \vec{G}^q - \vec{G}^{q-1} \qquad (IX\ B-20)$$

3. One Dimensional Minimization

As was mentioned earlier, in all of these methods the technique of determining α is to choose it in such a way that the ϕ $(\vec{X}^q + \alpha \vec{S}^q)$ for that particular iteration is minimized. There are several alternative ways of doing this. First of all, the function may be assumed to be quadratic in the direction $\vec{S}^q$. This in general is a fairly good assumption and becomes better and better as the minimum of the function is approached, as is evident from examining a Taylor series expansion of a function about the minimum. With this assumption the function value tested at three distinct points can be used to generate the coefficients of the quadratic and the minimum of the quadratic may be determined and used as an approximation to the minimum of the actual function. Thus, if it is assumed that

$$\phi(\vec{X}^q + \alpha \vec{S}^q) = a + b\alpha + c\alpha^2 \qquad \text{(IX B-21)}$$

and the three values of ϕ, ϕ_1, ϕ_2, and ϕ_3 corresponding to say $\alpha = 0, 1/2,$ and 1 are available then

$$a = \phi_1$$

$$a + \frac{b}{2} + \frac{c}{4} = \phi_2 \qquad \text{(IX B-22)}$$

$$a + b + c = \phi_3$$

From which

$$a = \phi_1$$

$$b = -3\phi_1 + 4\phi_2 - \phi_3 \qquad \text{(IX B-23)}$$

$$c = 2\phi_1 - 4\phi_2 + 2\phi_3$$

The value of α^* is estimated by setting

$$\frac{d}{d\alpha} \phi(\vec{X}^q + \alpha\vec{S}^q) = b + 2c\alpha = 0$$

which yields

$$\alpha^* = -\frac{b}{2c} \qquad \text{(IX B-24)}$$

or

$$\alpha^* = \frac{-3\phi_1 + 4\phi_2 - \phi_3}{4(\phi_1 - 2\phi_2 - \phi_3)}$$

A better fit can be obtained in many cases by assuming that the function is cubic in the direction $\vec{S}^q$ and evaluating the function and its derivative in the direction $\vec{S}^q$ with respect to α at two points and using this information to generate the coefficients of a cubic. As with the quadratic the minimum of the cubic is taken as an approximation to the minimum of the actual function.

Thus the assumption

$$\phi(\vec{X}^q + \alpha \, \vec{S}^q) = a + b\alpha + c\alpha^2 + d\alpha^3 \qquad \text{(IX B-26)}$$

is made and the four quantities ϕ_1, ϕ_1', ϕ_2 and ϕ_2' are evaluated where

$$\phi_1 = \phi(\vec{X}^q + \alpha_1 \, \vec{S}^q) \qquad \text{(IX B-27)}$$

$$\phi_2 = \phi(\vec{X}^q + \alpha_2 \, \vec{S}^q) \qquad \text{(IX B-28)}$$

$$\phi_1' = \vec{S}^T \nabla\phi \, (\vec{X}^q + \alpha_1 \, \vec{S}^q) \equiv \left.\frac{d\phi}{d\alpha}\right|_{\alpha=\alpha_1} \qquad \text{(IX B-29)}$$

$$\phi_2' = \vec{S}^T \nabla\phi \, (\vec{X} + \alpha_2 \, \vec{S}^q) \equiv \left.\frac{d\phi}{d\alpha}\right|_{\alpha=\alpha_2} \qquad \text{(IX B-30)}$$

This information can be used to evaluate a, b, c and d from

$$a + b\,\alpha_1 + c\,\alpha_1^2 + d\,\alpha_1^3 = \phi_1$$

$$a + b\,\alpha_2 + c\,\alpha_2^2 + d\,\alpha_2^3 = \phi_2 \qquad \text{(IX B-31)}$$

$$b + 2c\,\alpha_1 + 3d\,\alpha_1^2 = \phi_1'$$

$$b + 2c\,\alpha_2 + 3d\,\alpha_2^2 = \phi_2'$$

from which

$$\alpha^* = \alpha_1 - \left(\frac{\phi_1' + w - z}{\phi_1' - \phi_2' + 2w}\right) (\alpha_1 - \alpha_2) \qquad \text{(IX B-32)}$$

where

$$z = 3\left(\frac{\phi_1 - \phi_2}{\alpha_1 - \alpha_2}\right) + \phi_2' - \phi_1' \qquad \text{(IX B-33)}$$

and

$$w = (z^2 - \phi_2{'} \; \phi_1{'})^{1/2} \qquad\qquad \text{(IX B-34)}$$

Both the quadratic and cubic estimation schemes have been programmed in a modular form and either can be used in conjunction with any of the four previously described minimization routines. Both of these methods may at a particular step in the iteration process produce poor estimates of the location of the minimum of the function. This situation can be detected by testing the dot product between the gradient of the function, $\nabla\phi$, at the estimated minimum point and the direction S^q. If the point is the minimum of the function then the dot product should be equal to zero, and its deviation from zero can be used as a test or criterion for goodness of fit.

4. Unconstrained Formulations

At this point a brief description of two formulations for converting the constrained minimization problems stated above into unconstrained minimization problems is appropriate. Methods of this class are often called penalty function formulations for reasons which will become obvious.

A powerful method for handling problems of the first form (inequality constraints only) was developed by Carroll (Reference 67) and further expanded by Fiacco and McCormick (Reference 68). In this formulation a new function ϕ is created as follows

$$\phi(\vec{X}) = F(\vec{X}) - r \sum_{j=1}^{m} 1/g_j(\vec{X}) \qquad\qquad \text{(IX B-35)}$$

where r is an arbitrary positive constant. If the function ϕ is minimized for a particular choice of the parameter r, starting the iterative process from a point $\vec{X}^1$ for which $g_j(\vec{X}^1) < 0$, then the $\vec{X}_{min}(r)$ will also satisfy $g_j(\vec{X}_{min}(r)) < 0$. The smaller r is, the closer $\vec{X}_{min}(r)$ can approach the solution: $F(\vec{X}) \to$ min such that $g_j(\vec{X}) \leq 0$. The "penalty function" $- r \sum_{j=1}^{m} 1/g_j$ serves to insure that the constraints will be satisfied as the minimum of F is sought. The smaller r is chosen the less the "penalty" interferes with the true minimum of F; on the other hand small values of r produce functions, ϕ, which are difficult to minimize hence a sequential reduction process is used. Starting with a feasible point, $\vec{X}^1$ (i.e. $g_j(\vec{X}^1) < 0$), and a large value of r, denoted r_1, ϕ is minimized.

The resulting point $\vec{X}_{min}(r_1)$ is then used as the starting point for a minimization of with $r = r_2 < r_1$. The process is repeated until $F[\vec{X}_{min}(r)]$ can no longer be reduced. There are refinements of the method which estimate even better starting points than this and these have proved to be quite useful.

This attack on the optimization problem is more a formulation than it is an algorithm and as such very little can be done in the way of producing programming before the fact. However several simple example problems have been solved in order to establish a base of experience with the method. Generally this testing has shown the formulation to be viable however, if it is necessary to go into the lower ranges on r, the most powerful of the minimizers (Fletcher-Powell) is required.

A formulation which is applicable to the second form of optimization problem was developed by Schmit and Fox (References 69,70). This method makes use of the bracket function as a penalty function. The bracket function is defined as

$$
<t> = \begin{cases} t & t \geq 0 \\ \\ 0 & t < 0 \end{cases} \qquad (\text{IX B-36})
$$

A function is constructed as

$$
\phi(\vec{X}) = \sum_{p=1}^{\Omega} [\ell_p(\vec{X})]^2 + \sum_{j=1}^{m} <g_j(\vec{X})>^2 + <F(\vec{X}) - F_G>^2 \qquad (\text{IX B-37})
$$

where F_G is a goal for the objective function. If the minimum of ϕ is zero then the point $\vec{X}_{min}(F_G)$ corresponds to a design and its correct analysis which satisfies the inequality constraints and has a value of the objective function less than or equal to F_G. Optimization is accomplished by successively lowering the value of F_G until a choice is made for which $\phi[\vec{X}_{min}(F_G)] \neq 0$. In this way the optimum is ultimately bracketed by two successive choices of F_G. The method is described in depth in References 69 and 70.

As with the Fiacco-McCormick formulation it is not practical to attempt to preprogram the draw-down method described above. Needless to say a base of experience has been established for this formulation during its development.

5. Constrained Methods

A class of constrained or direct methods which is being implemented is known as methods of feasible directions (Reference 71). The programming for these algorithms is well along but not complete at this writing.

The concept involved in these methods when applied to the first form of problem statement is that the iterative procedure

$$\vec{X}^{q+1} = \vec{X}^q + \alpha \vec{S}^q \qquad \text{(IX B-38)}$$

must produce an $\vec{X}^{q+1}$ for which $g_j(\vec{X}^{q+1}) \leq 0$. This places restrictions directly upon the choice $\vec{S}^q$ and α. If at $\vec{X}^q$ the functions $g_j(\vec{X}^q) < 0$ for all j, then $\vec{S}^q$ can be taken as $-G^q$ and α taken either as the value α^* if no $g_j (\vec{X}_{min}^{q+1}) > 0$ or otherwise the value nearest to α^* that does not cause violations. This usually causes $g_j(\vec{X}^{q+1}) = 0$ for some set of values of j denoted as a set J_c. The constraints whose indices are in J_c are termed bound or active constraints. When a point in the iteration is encountered for which some $g_j = 0$ then $\vec{S} = - \vec{G}$ will not generally be a direction in which further redesign can be made.

A direction called a useable-feasible direction is one for which

$$S \cdot \vec{q}_j \leq 0 \qquad\qquad j \in J_c \qquad \text{(IX B-39)}$$

$$S \cdot \vec{G} \leq 0 \qquad\qquad\qquad \text{(IX B-40)}$$

where $\vec{q}_j = \nabla g_j (\vec{X}^q)$.

The direction is one in which, locally, the function F can be reduced without violating the constraints. A method of feasible directions is actually any method for locating such a direction.

A formulation which is useful for obtaining a "good" useable-feasible direction is:

Find an $\vec{S}$ and a scalar σ such that

$$(i) \quad \vec{S} \cdot \vec{q}_j + \theta_j \sigma \leq 0 \qquad j \in J_c \qquad \text{(IX B-41)}$$

$$(ii) \quad \vec{S} \cdot \vec{G} + \alpha \leq 0 \qquad\qquad \text{(IX B-42)}$$

(iii) a normalization requirement is satisfied

$$\text{example} \quad |\vec{S}| < 1 \qquad\qquad \text{(IX B-43)}$$

$$\text{and} \qquad \sigma \to MAX$$

where θ_j are arbitrary positive constants. $\sigma_{max} > 0$ corresponds to a "best" useable-feas ble direction; if $\sigma_{max} = 0$ then the point $\vec{X}^q$ is a local optimum.

The above "direction finding problem" is itself an inequality constrained optimization problem but it is considerably simpler than the source problem and may even be a linear programming problem depending upon the choice of Requirement iii.

The basic logic and programming for this method are being developed but the central section of coding involving the computation of g_j and $\vec{q}_j$, which are the heart of the problem technically, depend upon the specific problem and must be developed on an ad hoc basis.

C. Discrete Element Structural Analysis Methods
(Dr. R. Mallett, E. Helle, Dr. R.H. Gallagher, Bell Aerosystems)

The high stiffness, high strength and low density of advanced composite materials make them attractive for a variety of structural applications. The geometric configurations of interest vary widely depending upon the application. Most involve complex structural arrangements, and boundary conditions, nonuniform loadings, and gross discontinuities. Furthermore, many composite material systems exhibit brittle behavior which requires a high degree of accuracy in the prediction of stresses, particularly in localized regions of high stress concentration. It is obvious that classical analytical solutions cannot adequately cope with the diversity of structural configurations and types of loading involved. Therefore, it is necessary to employ an analysis method which has great flexibility of application with respect to configurational forms, loading, and boundary conditions. The discrete element matrix method satisfies these requirements and, therefore, was chosen for the structural analysis of representative components.

At the outset of the program a very strong general structural analysis capability based on the discrete element technique, existed for isotropic materials. The present research program has been directed toward extension of this existing analysis capability to accommodate anisotropic materials. It is important to note that the attractiveness of composites as structural materials stems, in large part, from the controllable variability of their anisotropy, stiffness, and strength. The same considerations also represent major sources of increased complexity introduced into design problems by the use of composite materials. The use of high stiffness composites serves to amplify the significance of geometric nonlinearity in the thin-shell problem class; important applications also exist in which high stress levels induce significant material nonlinearity. The scope of the formulation developed is such that these material and geometric nonlinearities can be treated using iterative computational procedures.

The importance of the requirements discussed above is emphasized by a description of the particulate representative component analysis problem. The component is basically a short thick axisymmetric structure. Various geometric configurations such as the one shown in Figure 132 were examined. All candidate configurations were irregular with respect to any coordinate system. Environmental conditions were represented by nonuniform pressure and thermal loadings. Attention was focused on designs of uniform material type. However, significant variations in properties due to temperature effects were included. Further complexity was introduced by the need for analyzing several different sets of boundary conditions.

The description of the throat insert design problem, together with the complexities of the fiber reinforced shell design problem, clearly indicates that practical analysis requirements transcend specific problem oriented formulations. Thus development of analysis methods contributes to the overall program objectives in a number of ways. Most importantly, the analysis capabilities play a major role in the design of composite components for structural applications. Completed portions of the analysis capability have already been employed in this connection during the design studies of the JTA representative (see Section V H). As a second benefit, development and application of the analysis capability serves to point out areas of
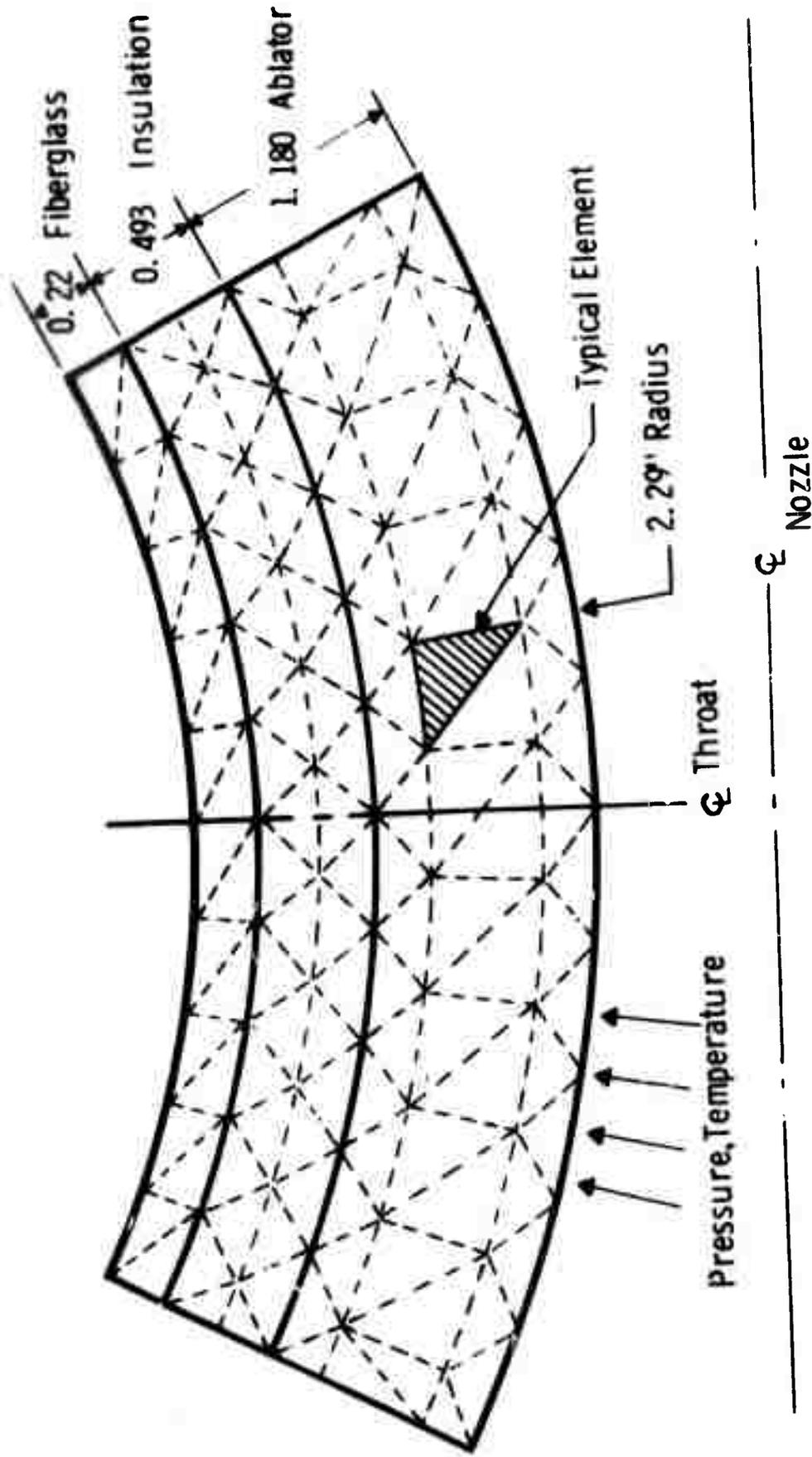
Figure 132. LEM Engine Thrust Chamber
Throat Area Element Idealization.

structural mechanics which merit consideration in university course work and research. It is pertinent to note that this widespread trend in the aerospace industry toward general purpose discrete element structural analysis capabilities, which Bell has pioneered, have been recently reflected in university curricula. Ultimately, in the scope of the present program, analysis capability will find important application in defining material property goals for composite materials development.

1. Principles of Discrete Element Systems

The discrete element approach to structural analysis may be consistently developed within the framework of continuum mechanics variational methods. Therein, discretization of a continuum can be designed to facilitate construction of admissible displacement functions. The physical model so constructed may be equivalently viewed as an assemblage of discrete structural elements connected such that interelement continuity is maintained. It is this latter view point which permits broad generality of the method. Development of the concept has enabled the systematic analysis of large complex structures viewed as assemblies of elementary components. Relation of the method to continuum mechanics allows the use of well-known convergence criteria in interpreting predicted behavior.

To illustrate the principles of the discrete element method, a representative problem solved at Bell using the general purpose program for structures of isotropic materials is briefly described. Figure 133 presents a physical model employed for an Apollo heat shield analysis. The thickness of the shell is variable due to scalloping and the shell configuration is irregular. Both rigid and elastic supports are provided. A varying distribution of pressure is applied over only a portion of the surface. These variations are accounted for in the discrete element idealization since the structure description is referenced to individual elements. The shell shape and element grid-work illustrate the applicability of triangular and quadralateral thin shell elements of arbitrary shape. It is particularly important to note the distribution of grid points which pro de refinement of the representation in regions of complex behavior. Variations in materials, geometry, loading, and boundary conditions are all considered in defining the grid patterns. Experience in defining gridworks enables a reduction in the selection of degrees of freedom without a corresponding loss of accuracy, thereby permitting economics in computer setup and run-time.

2. Theory

A complete mathematical representation of a discrete element is, within the scope of the research program, taken to consist of algebraic expressions for the following matrices:

(a) Stiffness $[K]$

(b) Incremental Stiffness $[N]$

(c) Pressure Load $\{F_P\}$

(d) Thermal Load $\{F_T\}$

(e) Prestrain Load $\{F_\epsilon\}$, and

(f) Stress $[S]$, $\{s\}$

VARYING THICKNESS SANDWICH SHELL

IMPACT PRESSURES

B. ANALYSIS MODEL

AXIS OF SYMMETRY

180 ELEMENTS

C. ELEMENT GRIDWORK

APOLLO COMMAND MODULE

HEAT SHIELD

WATER

A. DESCENT CONDITIONS
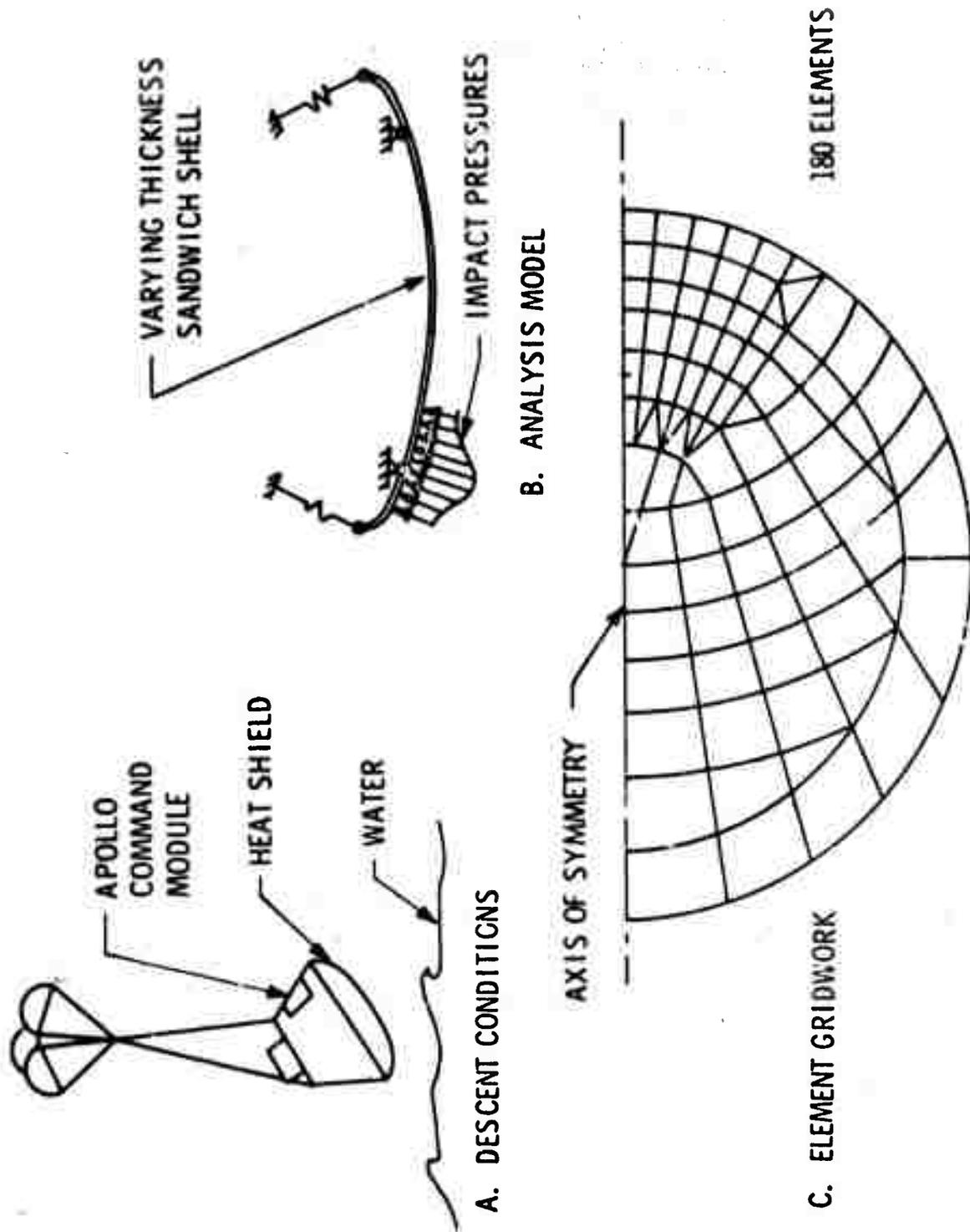
Figure 133. Apollo Heat Shield.

These matrices arise in the stationary conditions of the element potential energy except for the stress matrices which stem directly from the element stress-displacement relations.

The potential energy functional mathematical model of a discrete element is discretized into a finite number of degrees of freedom herein through the assumption of displacement function mode shapes. The selection of these displacement functions warrants careful consideration since they serve as a basis for all element response characteristics. Displacement functions must be complete up to the order of truncation, embody all rigid body modes, and provide for interelement continuity in order to allow valid use of established convergence criteria.

The assumed displacement functions for an element may be written symbolically as

$$\{ U(\ ) \} = [B(\ )] \{ \beta \} \tag{IX C-1}$$

The coefficients $\{ \beta \}$ in the assumed modes are referred to as "field coordinate" displacement degrees of freedom. These field coordinates afford considerable simplification in the development of algebraic expressions for the energy functions; however, in order to apply physical boundary conditions to an element it is convenient to transform to element boundary or grid point degrees of freedom:

$$\{ \beta \} = [\Gamma_{\beta q}] \{ q \} \tag{IX C-2}$$

Having constructed the displacement mode shapes and selected the grid point degrees of freedom, the derivation of the element matrices is pursued by forming the element potential energy.

The element potential energy is defined as

$$\pi_P = \frac{1}{2} \lfloor \epsilon(\ ) \rfloor [E] \{ \epsilon(\ ) \} - T(\ ) \lfloor \epsilon(\ ) \rfloor [E] \{ \alpha \}$$
$$- \lfloor \epsilon(\ ) \rfloor [E] \{ \epsilon_i(\ ) \} - W \tag{IX C-3}$$

where the notation employed is as follows:

$T(\ )$ is the temperature relative to ambient temperature

$\{ \alpha \}$ is the thermal coefficients of expansion

$\{ \epsilon(\ ) \}$ is the strain

$\{ \epsilon_i(\ ) \}$ is the prestrain, and

$[E]$ is the coefficient matrix in the generalized Hooke's law, i.e.,

$$\{ \sigma(\ ) \} = [E] \{ \{ \epsilon(\ ) \} - \{ \epsilon_i(\ ) \} - T(\ ) \{ \alpha \} \}$$

Introducing the assumed displacement functions into the linear strain-displacement relations for an element yields the strains expressed in terms of the field coordinates

$$\{\epsilon(\ )\} \quad [D(\ )]\{\beta\} \tag{IX C-4}$$

Substitution of this relation into the potential energy function and expanding the external work yields

$$\pi_p \quad \int_V (\tfrac{1}{2}\lfloor\beta\rfloor[D(\ )]^T[E][D(\ )]\{\beta\}$$
$$-T(\ )\lfloor\beta\rfloor[D(\ )]^T[E]\{\alpha\} \tag{IX C-5}$$
$$-\lfloor\beta\rfloor[D(\ )]^T[E]\{\epsilon_i(\ )\})\,dv$$
$$-\int_R (\lfloor\beta\rfloor[B(R)]^T\{p(\ )\}\ )\,dR$$

Carrying out the indicated integration and introducing the previously described transformation from field coordinate displacement degrees of freedom to selected grid point displacement degrees of freedom the final form of the linear potential energy is obtained,

$$\pi_p \quad \tfrac{1}{2}\lfloor q\rfloor[K]\{q\} - \lfloor q\rfloor\{F_T\} - \lfloor q\rfloor\{F_\epsilon\} - \lfloor q\rfloor\{F_p\} \tag{IX C-6}$$

where the element matrices are

$$[K] \quad \int_V [\Gamma_{\beta q}]^T [D(\ )]^T [E][D(\ )][\Gamma_{\beta q}]\,dv \tag{IX C-7}$$

$$\{F_T\} \quad \int_V T(\ )[\Gamma_{\beta q}]^T [D(\ )]^T [E]\{\alpha\}\,dv \tag{IX C-8}$$

$$\{F_\epsilon\} \quad \int_V [\Gamma_{\beta q}]^T [D(\ )]^T [E]\{\epsilon_i(\ )\}\,dv \tag{IX C-9}$$

$$\{F_p\} \quad \int_R [\Gamma_{\beta q}]^T [B(R)]^T \{p(\ )\}\,dR \tag{IX C-10}$$

One additional element matrix that is not shown above the incremental stiffness matrix $[N]$ which is needed in nonlinear problems, has not as yet been defined in meaningful symbolic matrix notation.

The element stress matrices are supplementary matrices which stem directly from the governing stress-displacement relation.

$$\{\sigma(\ )\} \quad [E][D(\ )][\Gamma_{\beta q}]\{q\} - [E]\{\epsilon_i(\ )\}$$
$$-T(\ )[E]\{\alpha\} \tag{IX C-11}$$

Particularization of this relation to specific points yields the stress matrices, i.e.,

$$\{\sigma\} \quad [S]\{q\} - \{s\} \tag{IX C-12}$$

The variational viewpoint taken thus far is carried forward into the assembly of the individual element representations to form the mathematical model of the total structure. The structure mathematical model is constructed simply by effecting a nonconformable sum of element matrices to connect adjacent elements. Structure

compatibility requirements are thereby satisfied in the assembly process. Equilibrium is established by solving the resulting governing matrix equation for the displacement unknowns. Stresses are then determined from the displacement solution.

It is important to note that the mathematical description developed for a structure is referenced to the individual discrete elements. It is this separation of the mathematical description from the structure mathematical model formed by assembly that accounts for the broad applicability of discrete element analysis capabilities. Applicability is limited only by the suitability of the discrete elements available for the structural idealization.

3. Analysis Capabilities

Development of analysis methods was directed toward extending Bell's general purpose capability to deal with anisotropic materials and advanced structures. A linear analysis capability for thick-walled axisymmetric structures has been accomplished through the introduction of the set of orthotropic ring discrete elements shown in Figure 134.

This set of axisymmetric discrete elements includes plane strain ring and core elements. Linear radial displacement assumed modes were employed for these one dimensional models. Cylindrically orthotropic material properties were considered. A linearly varying radial temperature profile over the elements was assumed in order to provide piecewise approximation of actual thermal loading. Stress matrices were included which yield predictions of stress at element midpoints.

These plane strain elements are suitable for the analysis of long thick-walled or solid axisymmetric structures without significant axial variations in geometry and applied loading. In addition, these plane strain elements are useful for conducting efficient preliminary analyses of more general cases.

A triangular cross-section ring and a corresponding core element were included to enable realistic idealization of thick-walled and solid axisymmetric structures with significant axial variations. As in the case of the plane strain elements, linear displacement functions were assumed. Stiffness, thermal load, and stress matrices were provided in this element representation.

The triangular cross-section element is very versatile. The arbitrary cross-section shape enables precise idealization of any axisymmetric thick-walled configuration. As an example, this element alone was sufficient for the refined analyses conducted in the design of the particulate composite throat insert component discussed in Section V H. A typical configuration and gridwork employed in this design process is illustrated in Figure 135. The component was subjected to the pressure and thermal loads given in Figure 61. Predicted stress behavior is presented in Figures 136 through 138. Two general characteristics of these stress results merit comment. First, predicted stress intensities are extremely high at the throat center inside face of the nozzle and decrease rapidly in both radial and axial directions. The unreasonably high predicted stresses suggest that it may be essential to include nonlinear material behavior in the analysis.

PLANE STRAIN RING

CORE ELEMENT

TRIANGULAR RING
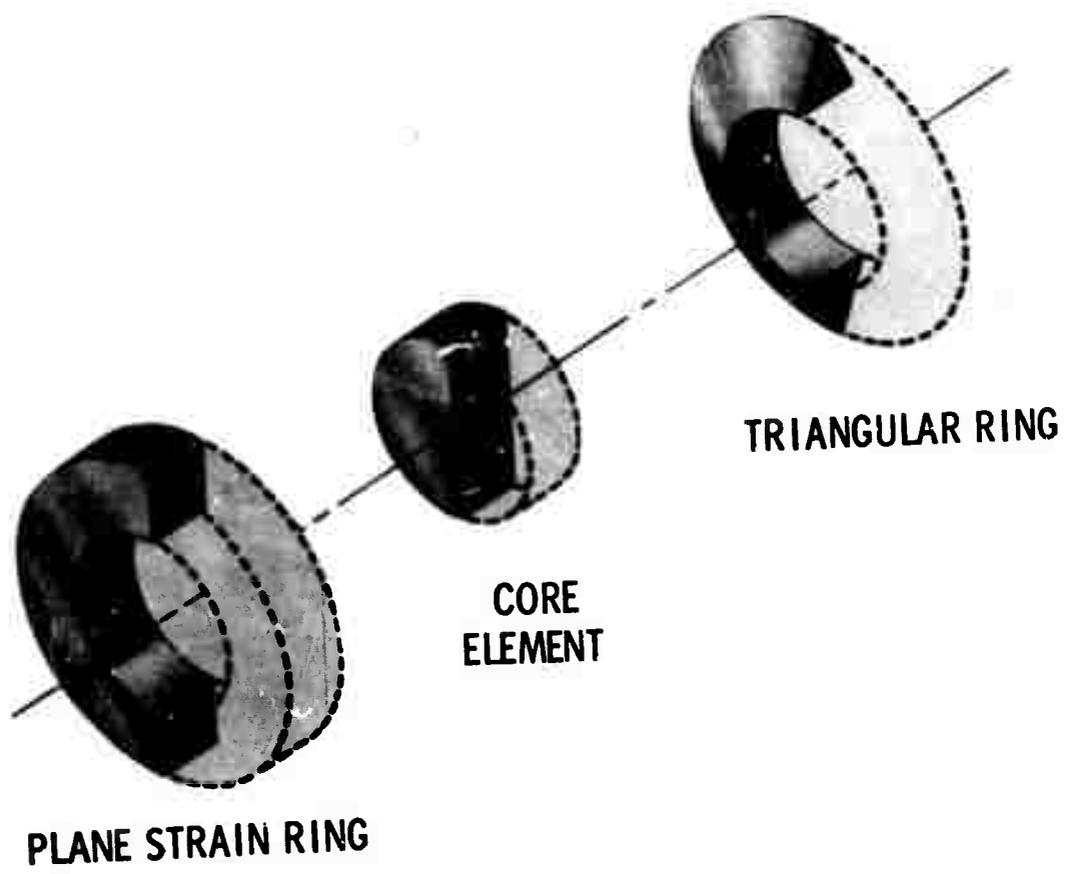
Figure 134.   Discrete Elements for Analysis of Thick
Axisymmetric Structures.

GAS FLOW
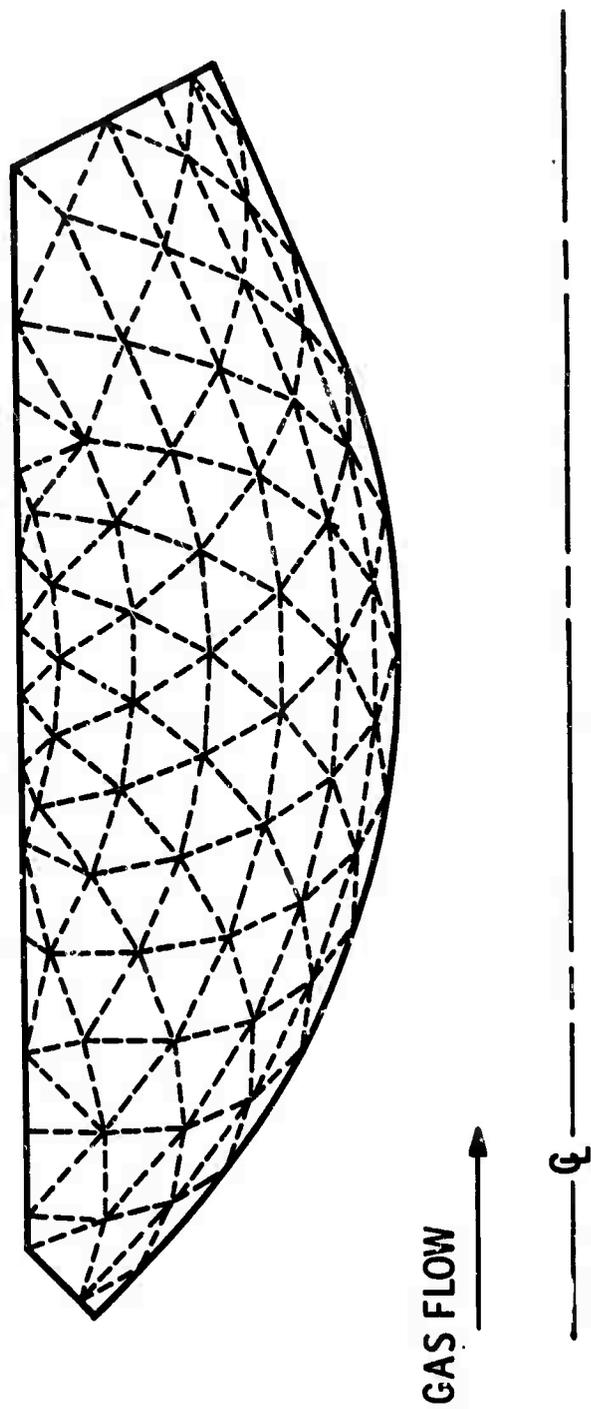
Figure 135. Rocket Throat Insert Idealization.
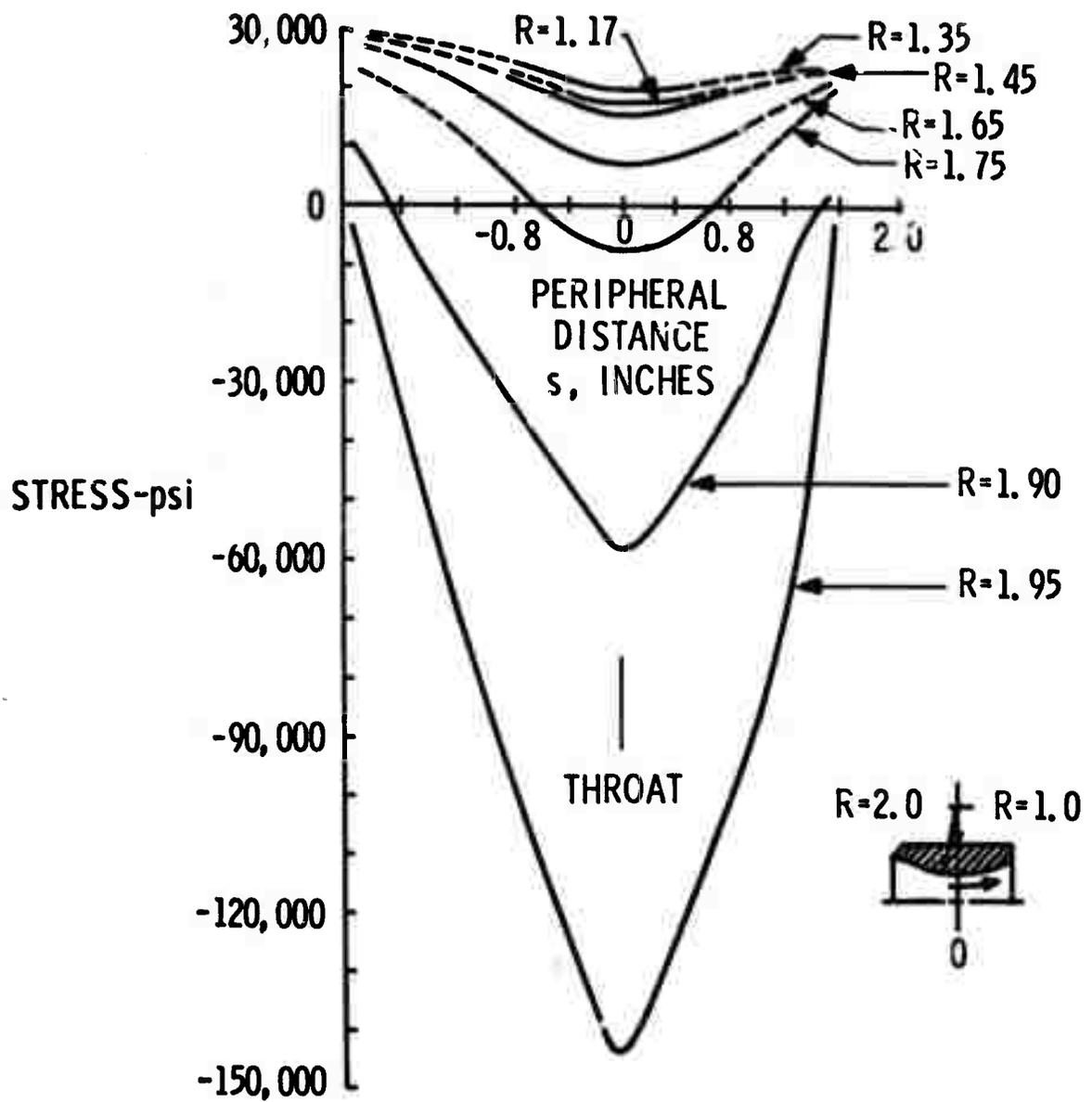
Figure 136. Circumferential Stresses in Rocket Throat Insert, 2.0
Seconds After Ignition, Non Uniform Wall Thickness.
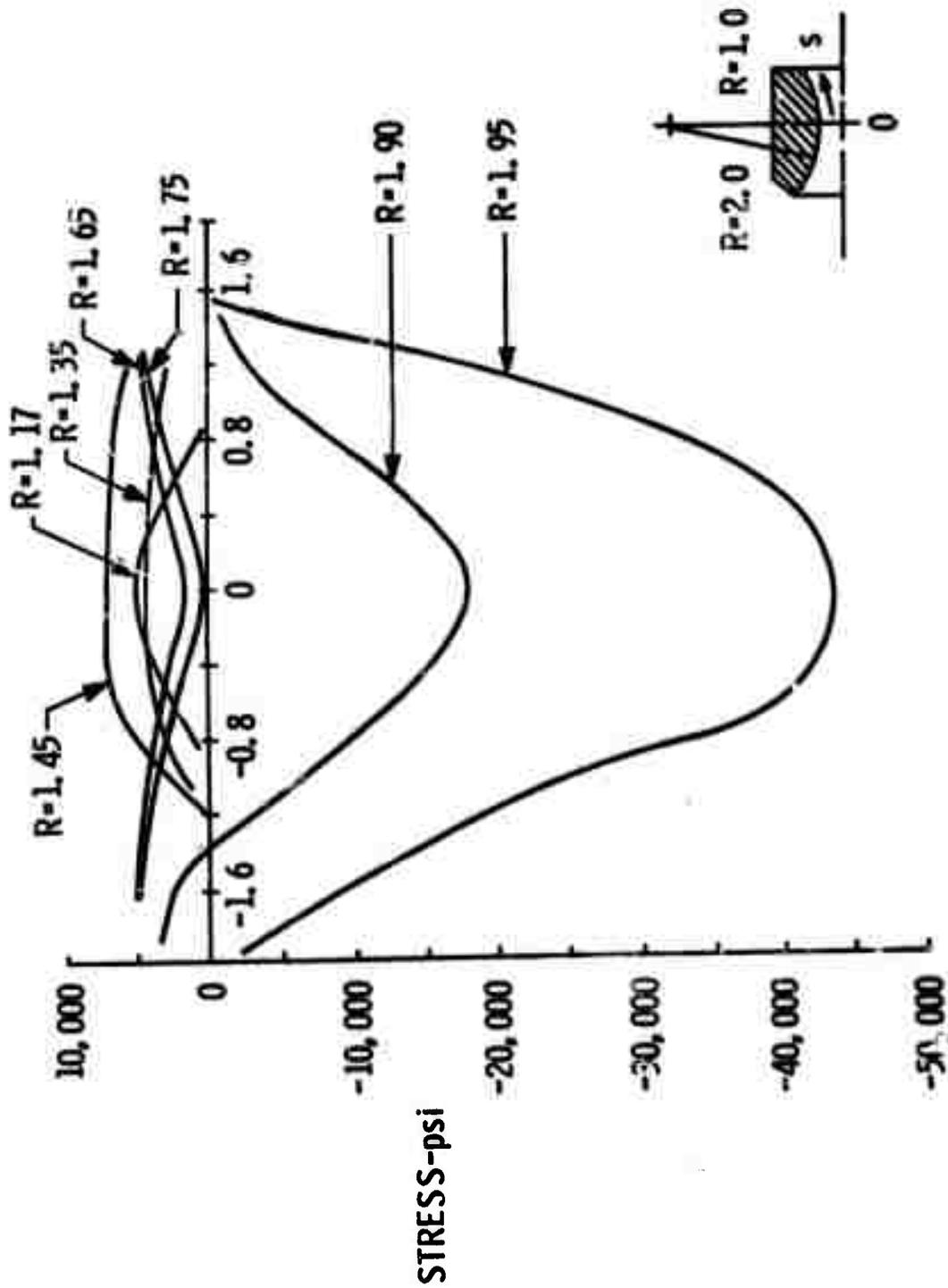
Figure 137. Axial Stresses in Rocket Throat Insert, 2.0 Seconds After Ignition, Non Uniform Wall Thickness.
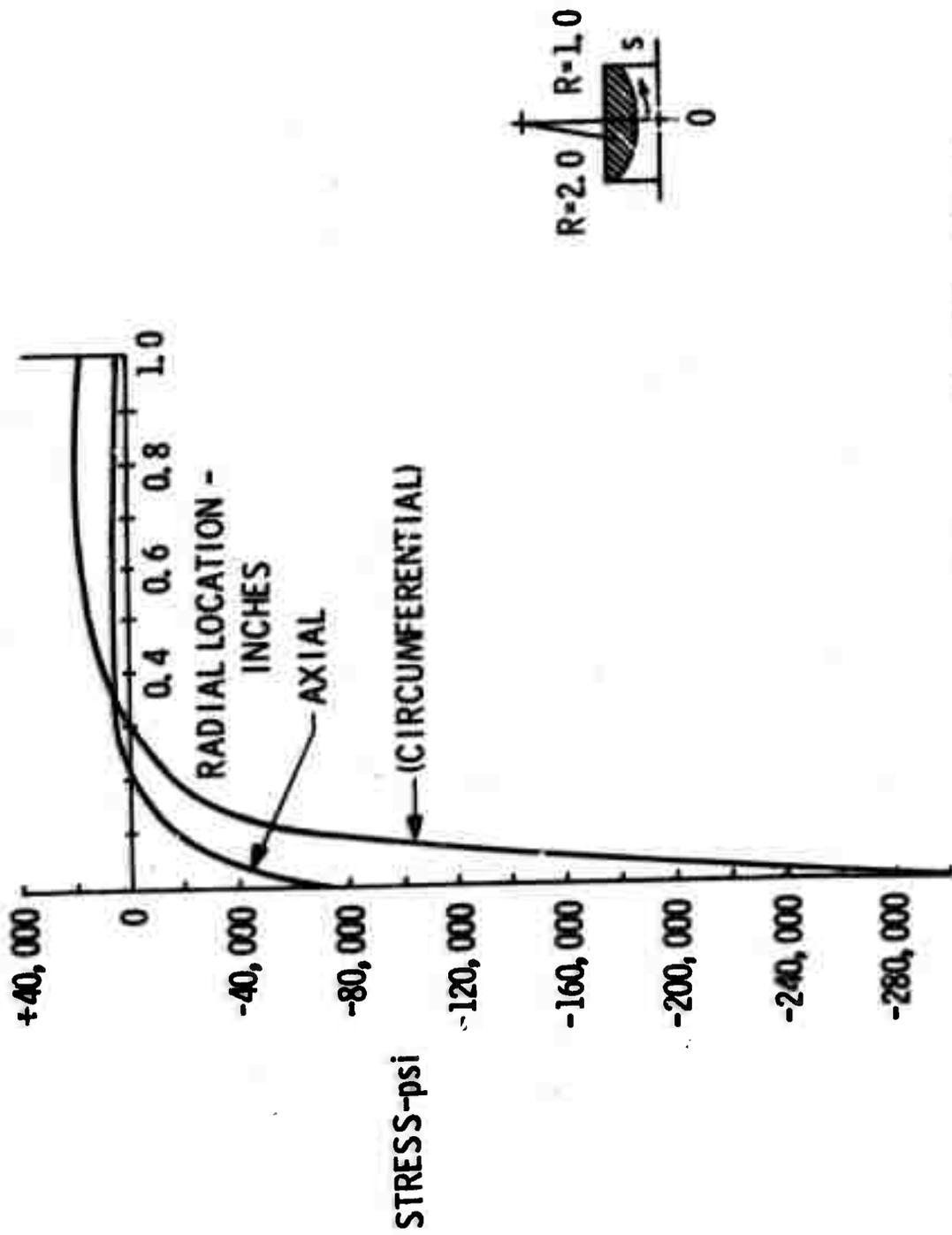
Figure 138. Axial and Circumferential Stresses at Throat Diameter, 2.0 Seconds After Ignition, Non Uniform Wall Thickness.

Secondly, it is important to note the tensile stress state induced along the outer face of the insert. This is potentially a design constraint since the tensile strength of the material is a fraction of the compressive strength. Additional applications of the triangular cross-section ring elements are given in Section V H.

Three orthotropic thin-shell discrete elements are being developed to extend the analysis capability to deal with fiber reinforced composite structural components. The first of these thin-shell elements, shown in Figure 139, is an axisymmetric toroidal ring element. This ring element will allow smoothly continuous idealization of thin axisymmetric structures with axial variations in loading. An osculatory membrane displacement function and a hyperosculatory transverse displacement function have been employed. The excess number of degrees of freedom associated with these displacement mode assumptions will provide economy of the total number of degrees of freedom in structure idealizations and also serve to minimize stress interpretation problems. Stiffness, pressure load, thermal load, prestrain load, and stress matrices were formulated for this element representation. It is anticipated that this element will be employed in extending material selection synthesis concepts to accommodate discrete element analysis techniques. Orthotropic triangular and quadrilateral thin shell discrete elements have been selected to enable effective polygonal idealization of arbitrary fiber reinforced composite thin-shell structures. The representation formulated for this set of elements includes stiffness, incremental stiffness, pressure load, prestrain load, thermal load, and stress matrices.

The discrete elements just described were selected for use in this program based on a considerable background of experience in structural analysis and design in equivalent applications using isotropic materials. These orthotropic discrete element representations together with the linear structural analysis computational procedure form a sound basis for evaluating the structural performance of composite materials. Having established this basis, the next step will be to generalize the computational procedures to deal with composite structures characterized by significant material and geometric nonlinearity.

A further important projected effort will be devoted to structural synthesis. It is anticipated that weight optimizations will be conducted for large scale structures with fixed material specifications. Best materials can then be suggested based on an interpretation of several fixed material optimizations. A secondary conceptual structural synthesis developmental effort is planned to incorporate material selection design variables within the automated portion of the design cycle. The nature of this effort will be guided by the results of the feasibility studies conducted at Case.

D.   Thermal Analysis Methods
        (M. Janis, Bell Aerosystems)

The study of anisotropic effects on heat transfer dates back to 1832 when Duhamel (72) first developed a mathematical theory on heat conduction in crystals. The modern treatment is due to Stokes (73) and more recently Wooster (74). However, despite a long history of analytic treatment the absolute principle thermal conductivities are today still unknown for most noncubic crystals. Unfortunately, the development of polycrystalline and filamentary composite materials has compounded the difficulties
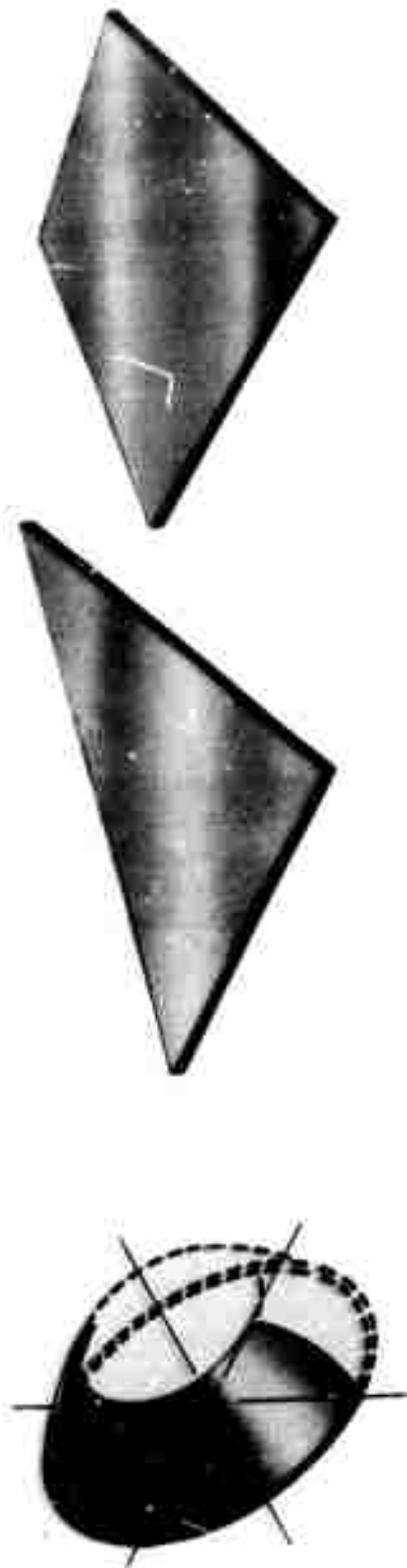
Figure 139. Discrete Elements for Analysis of Thin Shell Structures.

involved in the analytical prediction of thermal properties for these classes of materials. Thus it would seem reasonable that increased effort should be directed toward development of analytic and/or experimental techniques for the determination of the required properties. It should be noted, however, that simplified models have been employed (75, 76) recently to predict the thermal properties of some classes of fiber reinforced composite materials.

1. Theory

Most of the general theory of conduction in anisotropic media applies equally well to the conduction of heat and of electricity. Experiment has shown that in an isotropic conductor the flow, whether of heat or electricity, across a unit area in a unit time is proportional to the gradient of temperature or potential in the direction of the flow.

For an isotropic material the above relation between heat flow and potential may be expressed,

$$\dot{q} = k \frac{d\theta}{dr} \qquad (IX\ D\text{-}1)$$

where $\dot{q}$ is the amount of heat crossing unit area A perpendicular to the direction of flow in unit time, k is a constant known as the conductivity, $d\theta/dr$ is the temperature gradient; $\dot{q}$ and $d\theta/dr$ are vector quantities which can be resolved into components parallel to the three mutually perpendicular axes

$$\dot{q}_i = k \frac{d\theta}{dx_i} \quad (i = 1, 2, 3) \qquad (IX\ D\text{-}2)$$

Extension of these relations to anisotropic materials is given by

$$\dot{q}_i = k_{ij} \frac{d\theta}{dx_j} \ (i, j = 1, 2, 3) \qquad (IX\ D\text{-}3)$$

which equation assumes that each component of the flow is a linear function of the potential gradient components. Thus in the general case of anisotropy there are nine conductivity constants.

From the form of the equations it is seen the k_{ij}'s are the components of a second order tensor and the individual values depend on the orientation of the reference axes relative to the principle material axes. The number of constants required to define the thermal conductivity for an isotropic material is, of course, one since $k_{11} = k_{22} = k_{33}$ and all other terms are zero. For a transversly isotropic material, there are two constants and for an orthotropic material three constants are required, i.e., k_{11}, k_{22}, and k_{33}. If the principle axes of the material are not orthogonal, then it is required to specify six constants (symmetrical array) to define the thermal conductivity of a given material. However, since a heat transfer computation routine has been developed to consider general anisotropy, the difficulties are associated only with defining the thermal conductivity for input to the general solution.

2. Computation Technique

Many numerical techniques have been developed over the years which may be employed to compute the transient heat transfer through complex structural systems. However, the method most familiar to Bell Aerosystems is that of Dusinberre (77) which has been found easier to apply than many of the other techniques.

The method consists of dividing the space and time domains into discrete intervals and approximating the dependent variable, i.e., temperature, at a given location in terms of the temperatures at other locations. This is done using the first few terms of a Taylor series expansion, as given below.

$$T_{i,\,t+\Delta t} = T_{i,\,t} + \Delta t \frac{dT_i}{dt} + \frac{\Delta t^2}{2} \frac{d^2 T_i}{dt^2} \tag{IX D-4}$$

Experience has indicated that the second order term may be neglected unless extreme accuracy is required near the initiation of integration. The first order term is obtained by solving the energy balance, i.e.,

$$\frac{dT_i}{dt} = \frac{1}{mC_{P_i}} \left[\sum_{j=1}^{N} \bar{k}_{ij} \frac{A_{ij}}{r_{ij}} (T_j - T_i) \right]$$

$$+ \sum_{j=1}^{N} A_i F_{ij} (T_j^4 - T_i^4) \tag{IX D-5}$$

$$-\sigma \Delta s_i \epsilon_i T_i^4 + \dot{q}_{B.C.}$$

on the basis of the current temperatures. It should be noted that all material properties are considered temperature dependent; the nomenclature in the above equation not previously defined is as follows:

m	=	mass
C_p	=	specific heat
$\bar{k}_{ij}$	=	mean conductivity between two arbitrary i, j points
A_{ij}	=	cross sectional area between i, j points
r_{ij}	=	path length between i, j points
$A_i F_{ij}$	=	radiation interchange between i, j points
σ	=	Stefan-Boltzman material constant
ΔS_i	=	external surface area of element
ϵ_i	=	surface emissivity

The thermal conductivity in the above equation refers to a specific direction and is obtained by matrix multiplication of the conductivity tensor by the unit vector along

the directed line from the ith to the jth location in the physical system. The term $q_{B.C.}$ represents a variety of time or temperature dependent boundary conditions which may be imposed if required.

The structure temperatures at the start of each interval are defined by those at the close of the preceding interval and the solution subsequently progresses from initial conditions to completion.

The computation technique described above was incorporated into a computer program for conducting transient heat transfer analyses of anisotropic media. The program is written in Fortran IV for an IBM 7090 digital computer and solutions may be obtained for as many as 450 locations in a three-dimensional physical system. The program accounts for internal conduction and radiation interchange (limited to 2000 interchange factors), as well as radiative dissipation to the environment, and a variety of time or temperature dependent boundary conditions. The initial temperature distribution may be completely arbitrary and the thermal properties, i.e., thermal capacity and emittance, are assumed temperature dependent. The thermal conductivity is assumed dependent on both temperature and direction. The program is very efficient and solves the transient temperatures for a relatively detailed discrete element idealization of a rocket nozzle throat insert (Figure 140) in approximately 26 x real time. The solution for a similar rocket nozzle throat insert obtained with Bell's general thermal analyzer program, which does not handle the more general thermal anisotrophy as developed under the current program, on an IBM 7090 computer ran 27.6 x real time.

The data print-out includes the input which save core space as well as transient temperature and heat flows at specified locations in the system. If desired, the output temperature data may be recorded on tape for automatic plotting.

3. Results

As a check of the new thermal analysis program, its results were compared with results from a previously available program which approximately represents transversely isotropic materials. The JTA throat insert was studied to determine the effect of anisotropy on the temperature transients incurred subsequent to ignition. The insert configuration and the idealization employed in the thermal analysis are shown in Figure 140. Because of the steep temperature gradient expected at the gas-solid interface, a nonuniform finely divided grid was employed.

Element thermal characteristics were based on temperature dependent material behavior. JTA composite material properties from the literature were used and thermal loading conditions were as defined in Section IV B.

The thermal studies were conducted on the basis of a perfectly insulated external surface. (During the first few seconds of operation, the temperature distributions are essentially independent of the external boundary condition). Transient temperatures were determined during the first two seconds of operation and typical results are shown in Figure 141. The radial temperature distribution at the minimum throat diameter and the axial temperature distributions at various depths from the inner
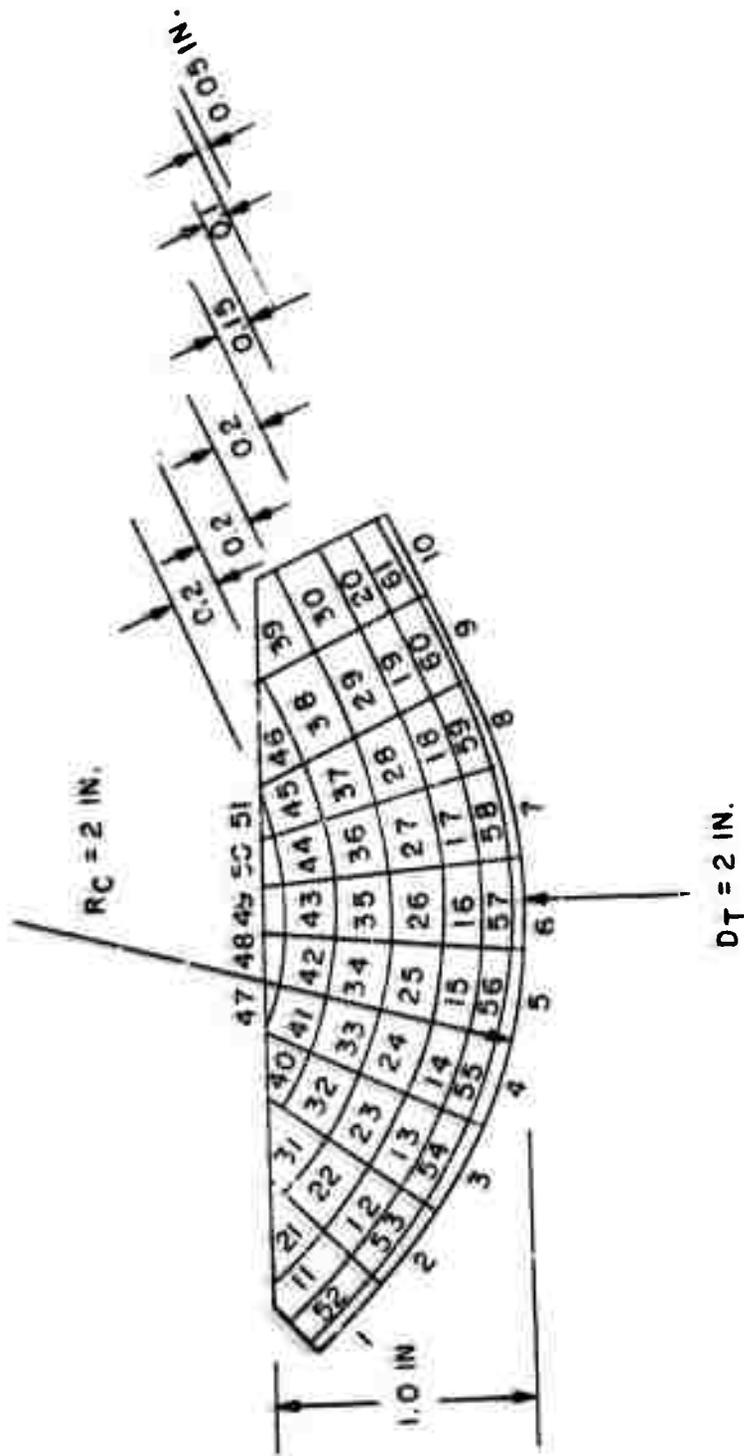
Figure 140.   Heat Transfer Model of Throat Insert.

N$_2$O$_4$/50-50, 0/F=2
2 inch Throat Dia., 500 psia Chamber Pressure
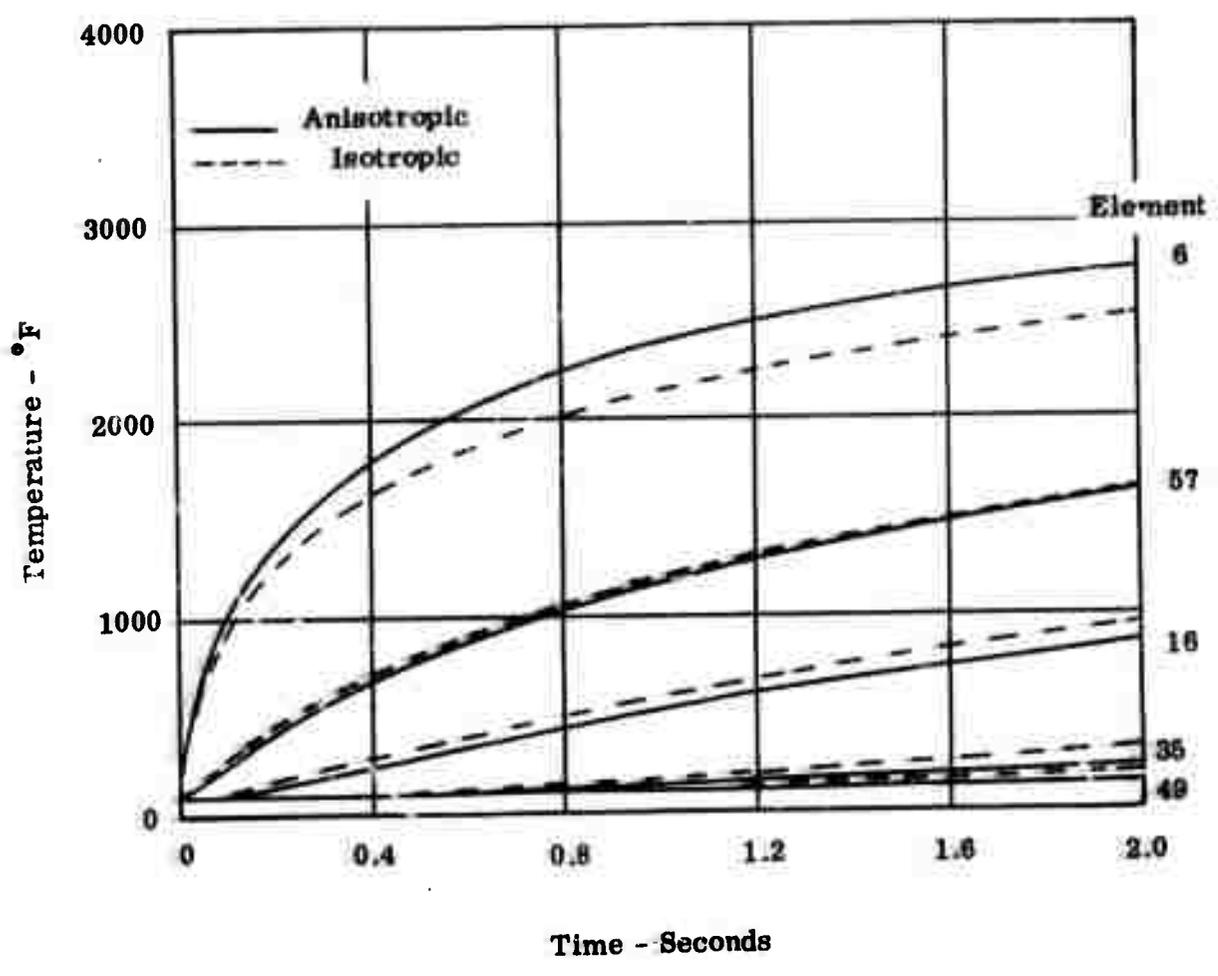
Figure 141. Transient Temperature of Throat Insert.

surface at two seconds after engine ignition are shown in Figures 142 and 143, respectively. Isotherms in the insert two seconds after ignition are shown in Figure 144.

Superimposed on Figures 141 and 142 are results for an isotropic insert having "with grain" properties. It is evident that significant differences in the transient temperatures result from the influence of material anisotropy.

It is of interest to compare the results of the new computer program with those obtained during a previous investigation of JTA throat inserts as reported in Section V H. The solutions differ only in the technique used to account for directional dependence of the thermal conductivity, i.e., the previous study made use of the analogy between thermal conductivity and resistance to approximate the directional dependence whereas anisotropy is exactly accounted for in the study reported herein through the use of the thermal conductivity as a tensor.

A comparison of the temperatures at the end of a 2 second firing at specified locations in the insert is presented in Table XXIV. The maximum absolute deviation is approximately 1.6% and occurs at the downstream extremity of the insert. It should be noted, however, that the close agreement shown is believed fortuitous and is thought to be related to the choice of material; i.e., JTA composite exhibits an almost constant ratio of principal conductivities over a large range of temperature and is transversly isotropic as well thus, allowing the uncoupling of the heat flow equations. For other classes of composites, the new computer program allows an improved representation of thermal anisotropy.

TABLE XXIV

COMPARISON OF PREDICTED INSERT TEMPERATURES
AFTER FIRING 2 SECONDS

	Temperatures		
Element Location	This Study $^{\circ}F$	Section V H $^{\circ}F$	Deviation $^{\circ}F$
1	1711.3	1679.1	-32.2
6	2759.7	2766.2	+ 6.5
10	1767.1	1731.3	-35.8
49	148.37	150.89	+ 2.52
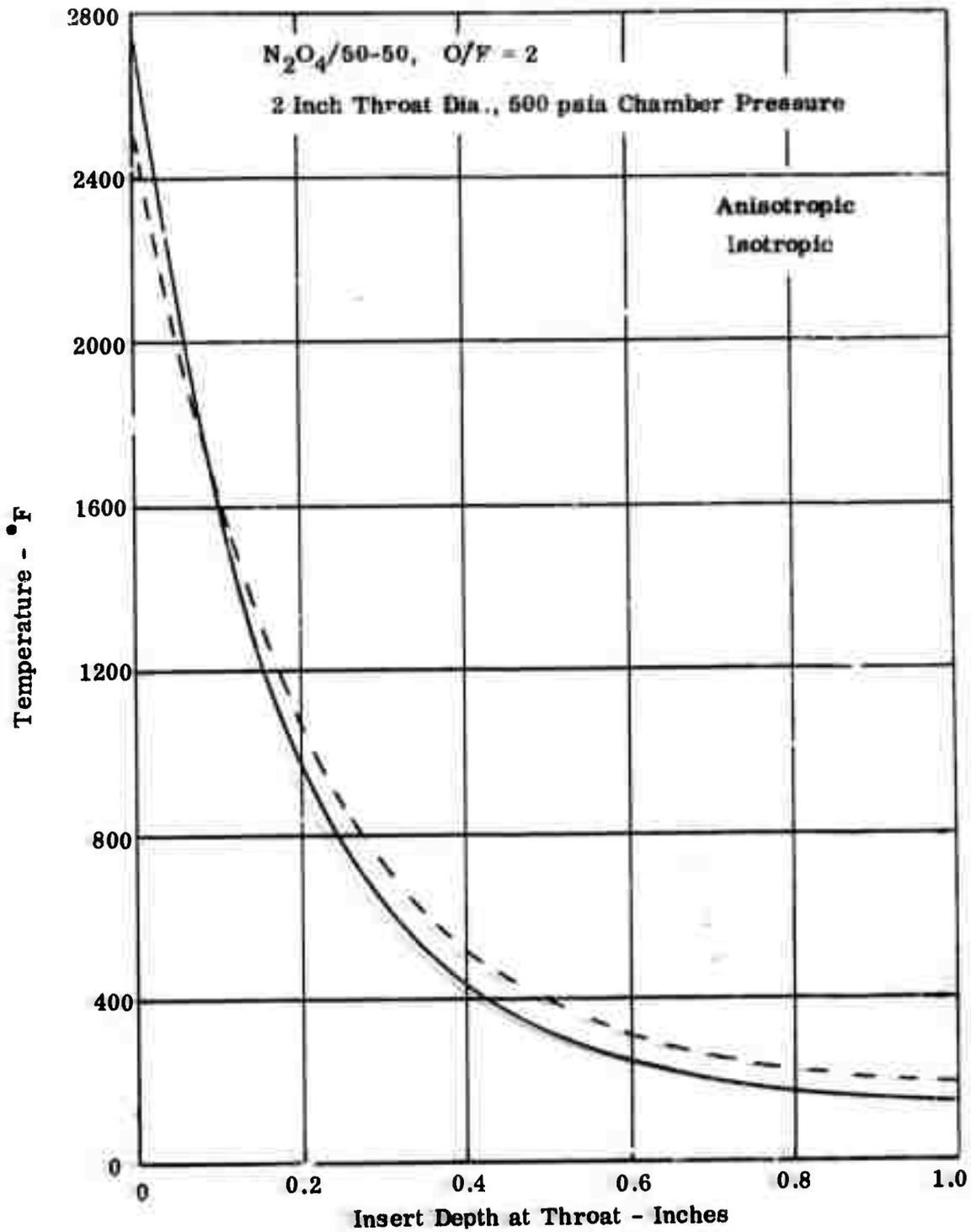
Figure 142. Insert Temperatures at Throat 2 Seconds after Ignition.

Figure 143. Axial Temperature Distribution at Various Depths from Inner Surface of JTA Throat Insert 2 Seconds after Ignition.

$N_2O_4/50$-$50,O/F = 2$
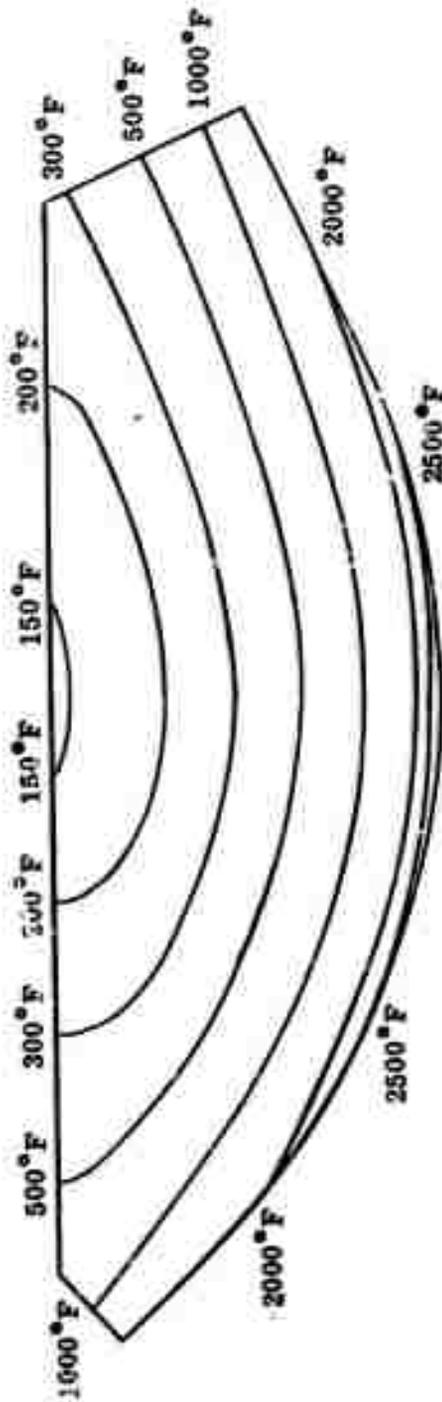
2 Inch Throat Dia., 500 psia Chamber Pressure

Figure 144. Throat Insert Temperature Distribution 2 Seconds after Ignition.

SECTION X

FIBER COMPOSITE AIRFRAME COMPONENT

A representative fuselage section was selected for study as the first representative component to utilize the carbon-fiber, resin-matrix composite material. Preliminary design studies (Section X A) indicate significant weight advantages for the carbon composite material and suggest a structural configuration consisting of stringers and rings to stabilize the fuselage skin. Preliminary approaches were defined with respect to attachment design concepts (Section X B) and structural testing (Section X C).

A.   Fuselage Preliminary Design Studies
      (D. P. Hanley, A. Krivetsky, and J. Witmer, Bell Aerosystems)

For purposes of preliminary study, the nominal dimensions and proportions of the fuselage section as shown in Figure 2 were established as $D_1 = 24$ inches, $D_2 = 22$ inches and $L = 48$ inches. An examination of the load-geometry parameters (M is the applied moment and d is the shell diameter) for aerospace vehicles indicates that the structural loading index $(M/d^3)^{1/3}$, lies generally in the range between 1.5 and 5.0, where the upper limit is somewhat on the high side[78].

With an assumed value of 4.0 for the structural loading index and the geometry of the fuselage section established in Figure 3, the maximum section bending moment can then be calculated. The bending moment may then be transformed into an equivalent axial loading (i.e. producing the same maximum stress in the section) by utilizing the expression:

$$N = 4M/\pi d$$

The advantage of converting moment into an equivalent axial loading is due to the fact that more information is available on compression panels with various types of reinforcement than is available for equivalent cylinders in bending. The panel data provide the overall instability criteria necessary for minimum weight investigations. These considerations apply primarily to isotropic materials of construction.

In general, analytical studies of structural efficiency and/or minimum weight are based on idealized structures. Such studies do not consider limitations such as minimum practical thicknesses, distances between stiffening elements that are dictated by fabrication methods, and discontinuities in the structure that may arise from load concentrations and/or mechanical fastenings between sections of an entire structure.

Recognizing these idealizations and using the above described design approach, preliminary minimum weight estimates of the fuselage structure for several materials and several types of shell construction were estimated as presented in Figure 145. The conical configuration in these calculations was approximated for simplicity in the analysis as a circular cylinder (24 inch diameter by 48 inch long). With an $(M/d^3)^{1/3} = 4.0$, the corresponding axial compression loading is 1955 lb/in. which value is seen to be well bracketed by the range of data shown in Figure 3 for many aerospace applications.

Titanium

$$\rho = 0.163 \text{ lb/in.}^3$$

$$E = 15 \times 10^6 \text{ psi}$$

Ring Stiffened Shell

    Ring Spacing = 12 in.

Stringer - Ring Shell

    Ring Spacing = 2.9 in.

Weight = 1.33 psf

$\bar{t} = 0.057$ in.

Weight = 0.61 psf

$\bar{t} = 0.026$ in.

Fiberglass Composite

Ring Stiffened Shell

$$\rho = 0.08 \text{ lb/in.}^3$$

$$E_L = 8.0 \times 10^6 \text{ psi} \quad G_{LT} = 0.48 \times 10^6 \text{ psi}$$

$$E_T = 1.3 \times 10^6 \text{ psi} \quad \nu_{LT} = 0.28$$

Weight = 1.20 psf

$\bar{t} = 0.104$ in.

Graphite/Resin Composite

Ring Stiffened Shell

$$\rho = 0.05 \text{ lb/in.}^3$$

$$E_L = 40 \times 10^6 \text{ psi} \quad G_{LT} = 0.52 \times 10^6 \text{ psi}$$

$$E_T = 1.5 \times 10^6 \text{ psi} \quad \nu_{LT} = 0.29$$

Weight = 0.86 psf

$\bar{t} = 0.119$ in.

Circular Cylinder - 24 in. Dia. x 48 in. Long

Loading = 1955 lb/in. $(M/d^3)^{1/3} = 4.0$ (Room Temperature)

Figure 145. Preliminary Minimum Weight Concepts of Circular Cylinders.

Using titanium at room temperature as an example material, the skin-stringer-ring shell shows an appreciable weight advantage (0.61 psf) over a ring-stiffened shell (1.33 psf), but it also illustrates the relatively thin gages that must be used to achieve lightweight design with a conventional material and monolithic construction.

Following a similar approach[79] for a ring-stiffened shell, the graphite fiber/resin composite material shows a decided advantage (0.86 psf) over the fiberglass (1.20 psf); the difference between titanium (1.33 psf) and fiberglass (1.20 psf) can be considered small.

Since the titanium skin-stringer-ring configuration indicated a considerable weight saving over a plain ring-stiffened shell, it can be assumed that similar stiffening advantages would result with the use of a graphite fiber/resin material in the skin-stringer-ring configuration. Derivations of the required structural efficiencies to prove this will indeed be complex because of the orthotropic material characteristics. An estimate of 0.4 to 0.5 psf would appear reasonable though for the idealized graphite fiber ring-stringer-shell composite, which would represent a 20 to 30% weight saving over the idealized titanium shell.

Although the preliminary minimum weight design approaches show considerable promise for the graphite fiber/resin composite, further analytical effort is required to define the structural design. The need for an improved specification of the elastic constants used in the anlysis is recognized.

Further study is also being made in the following areas: comparative performance evaluations of idealized isotropic and orthotropic shells of various designs (ring, stringer, ring-stringer stiffened, and sandwich constructions) as functions of loading intensity, structure size, and material properties; ring/stringer intersections; methods of joining the stiffeners and skin; minimum practical skin thicknesses; and provisions for attachments and/or test adapters.

Since the preliminary design work conducted to date has only considered an axial loading equivalent to a typical bending moment intensity, additional work is also required to define analysis procedures and minimum weight design concepts for orthotropic shells subjected to combined loads.

B.   Attachment Design Concepts
      (D. P. Hanley, Bell Aerosystems)

Final design of the representative fuselage component will require consideration of macro-discontinuity stress problems related to attachments, ring/stiffener/shell intersections, and other areas as described in Section X A.

Work was therefore initiated during this period to determine ultimately the impact of attachment hardware weight penalties on overall structure performance.

The more immediate goals of this program phase have been: (1) to identify problems associated with various design approaches and (2) to apply some of the more creative design approaches in a practical manner to the fuselage component.

A review and general organization of design problems associated with attachments and gross discontinuities in fiber reinforced composite structures has been accomplished. Design problem areas were categorized as follows: (1) stress concentrations due to penetrations (holes, cut-outs, etc.) in plates and shells; (2) discontinuity stresses associated with shell junctures; (3) methods of reinforcing plates and shells; and (4) methods of attaching thin-walled finite-length shell elements (such as filament wound hollow beams, cylinders, etc.) to one another, to conventional shell elements, or to testing fixtures. Modes of failure considered for these applications were primarily strength and instability. Very little work has been reported on fatigue failure modes.

Within the above categorization of problem areas and based on a review of significant work in the field, the following general observations were made:

(1) Much of the previous work in the field features ponderous and imprecise methods of analysis which are based on gross simplifications of material behavior, structure geometry, and loading conditions.

(2) There are available methods of predicting stress concentration effects around penetrations in homogeneous orthotropic media. These are useful in qualitatively establishing the reinforcement required to locally strengthen the composite.

(3) Analysis of locally reinforced regions (around holes, junctures, etc.) in composite structures is at best very approximate because the nature of inter-and intralaminar shear stress behavior is not well defined. This area in particular is deserving of attention because of potentially significant weight savings in structures (in certain applications on the order of 30% of the total structure weight may be due to reinforcements).

(4) Several major obstacles which have hindered determination of gross discontinuity stresses in structures have been: (a) the lack of adequate data characterizing orthotropic materials (directional moduli, strengths, etc.) and (b) the tremendous amount of calculation required to analyze composite structures. These are being rapidly overcome with increasing attention in the field to both materials and computer-based design methods.

(5) Considerably more information is available on design concepts for attachments of and to composite structures than is available on their performance and relative comparisons.

Considering the above points, the present research is being directed toward designing and analyzing a single structure which involves (to a progressively more realistic degree) major elements in each of the identified problem areas. Because of the analytical complexities involved, it is anticipated that this can only be done within the scope of this effort in an approximate manner. In this respect the idealized fuselage component represents many of the elements of discontinuity stress problems in advanced structures--ring/stringer/shell intersections, attachments, and concern for penetrations -- and will, therefore, serve to generate specific but broadly applicable design techniques.

C. Structural Testing of Fiber Composite Components
   (D. P. Hanley and J. Witmer, Bell Aerosystems)

Testing activity on fiber composite components at Bell is expected to consist of: (1) tests of simple components and (2) tests of the representative components. To date, only tentative test plans have been formulated.

With respect to simple components, tentative specifications were formulated for a filament wound cylinder test program to measure directly the four plane stress orthotropic elastic constants as discussed in Section VII E. Specimen design, materials, geometry, fabrication, inspection, assembly, testing, and data analysis parameters were identified. Some consideration has also been given to the testing of a limited number of stiffened panels but plans have not been completed.

Tests of the representative fuselage component have been qualitatively defined to simulate bending, torsion, and heating environments. A series of tests are planned to apply bending and torsion separately and in combination in order to obtain stress distribution data with which to compare theoretical predictions. Loading will be established to avoid damage to the component once crazing thresholds, etc. are defined from the simple component tests. Limited tests will be conducted to measure thermal stresses. The fuselage section will then be loaded to failure under simulated design conditions which will most likely include a combination of bending, torsion, and heating.

REFERENCES

1. Union Carbide Corporation, National Carbon Company, Research and Development on Advanced Graphite Materials - Oxidation Resistant Graphite Base Composites, by K. J. Zeitsch and J. M. Criscione, WADD TR 61-172, Vol. XXX, (April 1964), (AF33(616)-6915).

2. A. Naidai, Theory of Flow and Fracture of Solids, Vol. I, (McGraw-Hill Book Company, New York, 1950), pp. 353-359.

3. W. J. Parker, R. J. Jenkins, C. P. Butler, and G. L. Abbott, "Flash Method of Determining Thermal Diffusivity, Heat Capacity, and Thermal Conductivity," J. Appl. Phys. 32, 1679-1684 (1961).

4. Union Carbide Corporation, National Carbon Company, Research and Development on Advanced Graphite Materials - Survey and Analytical Representation of the Measurements of the Specific Heat of Graphite, by G. B. Spence, WADD TR 61-72, Vol. XLI, (November 1963), (AF33(616)-6915).

5. Battelle Memorial Institute (Columbus), Refractory Ceramics of Interest in Aerospace Structural Applications -- A Materials Selection Handbook, by J. R. Hague, J. F. Lynch, A. Rudnick, F. C. Holden, and W. H. Duckworth, RTD-TDR-63-4102 (1963), p. 55, (AF33(657)-8326).

6. A. Goldsmith, T. E. Waterman, and H. J. Hirschhorn, Handbook of Thermophysical Properties of Solid Materials, Vol. III: Ceramics, (MacMillan Company, New York, 1961), p. 925.

7. IIT Research Institute, Physical Properties of Refractory Materials, IITRI-G6001-9, Quarterly Report No. 3 on AF33(615)-3028, (December 1, 1965, to February 28, 1966).

8. IIT Research Institute, Physical Properties of Refractory Materials, IITRI-G6001-6, Quarterly Report No. 2 on AF33(615)-3028, (August 1 to November 30, 1965).

9. A. E. H. Love, A Treatise on the Mathematical Theory of Elasticity, 4th ed. (Dover, New York, 1927).

10. I. S. Sokolnikoff, Mathematical Theory of Elasticity, 2nd ed. (McGraw-Hill Book Company, New York, 1956).

11. J. E. Dorn, "Stress Strain Rate Relations for Anisotropic Plastic Flow," J. Appl. Phys. 20, 15-20 (1949).

12. Rodney Hill, Mathematical Theory of Plasticity, (Oxford University Press, London, 1950).

REFERENCES (Cont'd)

13. R. Hill, "A Theory of Yielding and Plastic Flow of Anisotropic Metals," Proc. Roy. Soc. 193, 281-297 (1948).

14. J. E. Griffith and W. M. Baldwin, "Failure Theory for Generally Orthotropic Materials," Proceedings of the 1st Southeastern Conference on Theoretical and Applied Mechanics, (Plenum Press, New York, 1963), pp. 410-420.

15. J. Boschat, "Une Generalisation du Critere de Tresca Pour Les Milieux Anisotropes," These Universite de Grenoble (1962).

16. W. Weibull, "The Statistical Theory of Strength of Materials," The Royal Swedish Institute for Engineering Research, Proceedings No. 151, (1939).

17. O. K. Salmassy, et al., Behavior of Brittle State Materials, WADC Technical Report 53-15, Parts I and II, (June 1955).

18. F. M. Anthony, et al., Investigation of Feasibility of Utilizing Available Heat Resistant Materials for Hypersonic Leading Edge Applications, WADC Technical Report 59-744, Vols. I - VIII, (January 1961).

19. F. M. Anthony, et al., Selection Techniques for Brittle Materials - Evaluation of ZrB-MoSi as a Structural Refractory Ceramic Body, AFML-TR-65-209 (September 1965).

20. R. L. Barnett, et al., The Behavior and Design of Brittle Structures, AFFDL-TR-65-165 (September 1965).

21. W. Weibull, "A Statistical Distribution Function of Wide Applicability," Journal of Applied Mechanics 18, 293-297 (September 1951).

22. R. L. Barnett, Review of Structural Design Techniques for Brittle Components under Static Loads, Armour Research Foundation Report No. 8259 (May 1963).

23. R. Sedlacek and F. A. Halden, "Method for Tensile Testing of Brittle Materials," Rev. Sci. Inst. 33, 298-300 (1962).

24. G. E. Forsythe and W. R. Wasaw, Finite Difference Methods for Partial Differential Equations, (John Wiley and Sons, Inc., 1960), pp. 101-107.

25. C. T. Wang, Applied Elasticity, (McGraw-Hill Book Company, Inc., 1953), pp. 70-76.

REFERENCES (Cont'd)

26. D. R. Bartz, "A Simple Equation for Rapid Estimation of Rocket Nozzle Convective Heat Transfer Coefficients," Jet Propulsion 27, 49-51 (January 1957).

27. F. M. Anthony, et al., "Selection Techniques for Brittle Materials," (Research Toward the Evaluation of JTA Graphite as a Structural Refractory Ceramic Body), First Quarterly Progress Report, No. 2178-900601, (February 1966).

28. R. Bacon, A. A. Pallozzi, and S. E. Slosarik, "Carbon Filament Reinforced Composites," Proc. 21st Annual Tech. Conf., SPI Reinforced Plastics Division, (Soc. of the Plastics Industry, Inc., New York, 1966), Sec. 8-E.

29. R. Nelson Smith, "Chemistry of Carbon-Oxygen Surface Compounds," Quart. Rev. (London) 13, 287-305 (1959).

30. W. P. Harkins and H. K. Livingston, "Energy Relations of the Surfaces of Solids," J. Chem. Phys. 10, 342-56 (1942).

31. R. N. Wenzel, "Resistance of Solid Surfaces to Wetting by Water," Ind. Eng. Chem. 28, 988-994 (1936); "Surface Roughness and Contact Angle," J. Phys. and Colloid Chem. 53, 1466-1467 (1949).

32. A. W. Adamson, Physical Chemistry of Surfaces, (Interscience Publishers, Inc., New York, 1960), p. 5.

33. B. Derjaguin, "Theory of the Distortion of a Plane Surface of a Liquid by Small Objects and Its Application to the Measurement of the Contact Angles of Thin Filaments and Fibres," Compt. rend. acad. sci. URSS 51, 519-22 (1946).

34. W. H. Anderson, "The Solution of Simultaneous, Ordinary Differential Equations Using a General Purpose Digital Computer," Comm. of the ACM 3, 355-60 (1960).

35. E. W. Washburn, "The Dynamics of Capillary Flow," Phys. Rev. 57, 273-83 (1921).

36. R. L. Peek, Jr. and D. A. McLean, "Capillary Penetration of Fibrous Materials," Ind. and Eng. Chem. 6, 85-90 (1934).

37. P. W. Erickson, I. Silver, and H. A. Perry, Jr., "Proposed NOL Ring Test Method for Parallel Glass Roving Reinforced Plastics: Evaluation of Chemical Finishes," NAVORD Report No. 5680, (July 1, 1957).

REFERENCES (Cont'd)

38. American Society for Testing and Materials, Standards, Part 26, Plastics-Specifications, ASTM Designation: D2291-64T, "Tentative Recommended Practice for Fabrication of Ring Test Specimens," p. 461.

39. L. B. Greszczuk, "Elastic Constants and Analysis Methods for Filament Wound Shell Structures," Douglas Aircraft Company Report SM-45849 (January 1964).

40. B. Paul, "Prediction of Elastic Constants of Multi-Phase Materials," Trans. AIME 218, 36-41 (1960).

41. B. W. Rosen, N. F. Dow, and Z. Hashin, Mechanical Properties of Fibrous Composites, NASA CR-31, (April 1964).

42. S. W. Tsai, Structural Behavior of Composite Material, NASA CR-71, (July 1964).

43. L. B. Greszczuk, Theoretical and Experimental Studies on Properties and Behavior of Filamentary Composites, Douglas Aircraft Company, Paper No. 3550, (February 1966).

44. S. W. Tsai, "A Method of Analysis of Filamentary Structures," in American Society of Mechanical Engineers, Filament Structures Technology. Proceedings of 6th Annual Technical Symposium..., (December 1965) pp. 114-25.

45. J. C. Ekvall, "Elastic Properties of Orthotropic Monofilament Laminates," ASME Paper No. 61-AV-56, January 26, 1961 (an improved treatment of Ekvall's work, not included in the analysis of this report, may be found in: J. C. Ekvall, "Structural Behavior of Monofilament Composites," Sixth AIAA Structures and Materials Conference, Palm Springs, California, April 5-7, 1965).

46. Armour Research Foundation, Fiber Reinforced Metals and Alloys, NOW-61-0555C, (Final Report), (May 1962), (AD 276,620).

47. Battelle Memorial Institute, Development of Carbon Filament Reinforced Composite Materials, NOW-65-0615C, (Bimonthly Progress Report No. 3), (January 1966).

48. W. H. Sutton and J. Chorne', (General Electric Company), Development of Composite Structural Materials for High Temperature Applications, NOW-64-0540, (Seventeenth Progress Report), (September 1964), (AD 452,881).

REFERENCES (Cont'd)

49. Yu. V. Naidich and G. A. Kolesnichenko, "Investigation of the Wetting of Diamond and Graphite by Molten Metals and Alloys. III. The Wetting of Diamond Crystals," Soviet Powd. Met. and Metal Ceramics 3, 191-5 (1964).

50. M. Humenik, Jr. and W. D. Kingery, "Metal-Ceramic Interactions. III. Surface Tension and Wettability of Metal-Ceramic Systems," J. Am. Ceram. Soc. 37 (1) 18-23 (1954).

51. S. Weiss, "The Promotion of Wetting and Brazing," Ph.D. Thesis, (M.I.T., 1965).

52. W. H. Sutton, J. Chorne', A. Gatti, and E. Sauer, Development of Composite Structural Materials for High Temperature Applications, NOW-60-0465-d, (Final Report), (February 1965), (AD 461,357).

53. C. E. Ransley, "The Application of the Refractory Carbides and Borides to Aluminum Reduction Cells," in Extractive Metallurgy of Aluminum, Vol. 2, Aluminum, Gary Gerard, Editor, (Interscience Publishers, New York, 1963) pp. 487-507.

54. J. A. Alexander, Research on Filament-Metal Matrix Composite Materials, AF33(615)-3155, (Second Quarterly Progress Report), (January 1966).

55. D. Cratchley, "Experimental Aspects of Fibre-Reinforced Metals," Met. Reviews 10 (37), 79-144 (1965).

56. G. V. Samsonov, Plenum Press Handbooks of High-Temperature Materials, No. 2 Properties Index, (Plenum Press, New York, 1964), p. 290.

57. A. J. Wall and D. R. Milner, "Wetting and Spreading Phenomena in a Vacuum," J. Inst. Metals 90, 394-402 (1962).

58. D. A. Robbins, Paper presented at Symposium on Physical Chemistry of Metallic Solutions and Intermetallic Compounds, National Physical Laboratory, Teddington, England (1958).

59. W. H. Sutton, (General Electric Company), Research on Fiber-Reinforced Composites, Technical Information Series R66SD2, (January 1966).

60. Alexander Mendelson, "Solutions of Some Plane Thermal and Crack Problems for Strain-Hardening Materials," Ph.D. Thesis, Engineering Thesis Advisor: Dr. R. H. Scanalan, Case Institute of Technology, (1965).

REFERENCES (Cont'd)

61. F. K. Bogner, R. L. Fox, and L. A. Schmit, Jr., "The Generation of Interelement-Compatible Stiffness and Mass Matrices by the Use of Interpolation Formulas," presented at the Conference on Matrix Methods in Structural Mechanics, October 26-28, 1965, Wright-Patterson Air Force Base, Ohio.

62. M. J. D. Powell, "An Efficient Method for Finding the Minimum of a Function of Several Variables without Using Derivatives," Computer Journal 7, 155-162 (1964).

63. A. L. Cauchy, "Mode Generale Pour la Resolution des Systems d'Equations Simultanees," Compt. Rend. 25, 536 (1847).

64. R. Fletcher and C. M. Reeves, "Function Minimization by Conjugate Gradients," Computer Journal 7, 149-154 (1964).

65. W. C. Davidon, Variable Metric Method for Minimization, A.E.C. Res. and Dev. Rept. ANL-5990, (1959).

66. R. Fletcher and M. J. D. Powell, "A Rapidly Convergent Descent Method for Minimization," Computer Journal 6, 163-168 (1963).

67. C. W. Carroll, "The Created Response Surface Technique for Optimizing Nonlinear Restrained Systems," Operations Research 9, 169 (1961).

68. A. V. Fiacco and G. P. McCormick, "The Sequential Unconstrained Minimization Technique for Nonlinear Programming, A Primal Dual Method," Mgt. Science 10, 360-366 (January 1964).

69. L. A. Schmit and R. L. Fox, "An Integrated Approach to Structural Synthesis and Analysis," AIAA Journal 3, 1104 (1965).

70. R. L. Fox and L. A. Schmit, "Advances in the Integrated Approach to Structural Synthesis," Journal of Spacecraft and Rockets 3, 858-867 (June 1966).

71. G. Zoutendijk, Methods of Feasible Directions, (American Elseview Publishing Co., Inc., New York, 1960).

72. J. Duhamel, Ecole Polytechnique. J. Paris 13, Cah. 21 356 (1832).

73. G. C. Stokes, Cambridge and Dublin Math. J. 6, 215-38 (1851).

74. William Alfred Wooster, Textbook on Crystal Physics, (Cambridge, 1949).

75. J. D. Thornburgh and C. D. Pears, "Prediction of the Thermal Conductivity of Filled and Reinforced Plastics," ASME Paper 65-WA/HT-4, contributed by Heat Transfer Division for presentation at the Winter Annual Meeting of the ASME, Chicago, Illinois, (November 7-11, 1965).

REFERENCES (Cont'd)

76. Longin B. Greszczuk, "Thermoelastic Properties of Filamentary Composites," (Amer. Inst. Aeronautics and Astronautics) <u>AIAA 6th Structures and Materials Conf.</u>, (1965), pp. 285-90.

77. G. M. Dusinberre, <u>Heat Transfer Calculations by Finite Differences</u>, (International Textbook Company, Scranton, Pennsylvania, 1961).

78. A. Krivetsky, <u>Minimum Weight Design of Shells in Bending</u>, Bell Aircraft Corporation, Report No. 7-58-2952-5, (October 18, 1958).

79. N. F. Dow and B. W. Rosen, "Structural Efficiency of Orthotropic Cylindrical Shells Subjected to Axial Compression," AIAA Journal, <u>4</u>, 481-485 (March '966).

BLANK PAGE

DOCUMENT CONTROL DATA - R&D

(Security classification of title, body of abstract and indexing annotation must be entered when the overall report is classified)

1. ORIGINATING ACTIVITY (Corporate author)	2a. REPORT SECURITY CLASSIFICATION
Union Carbide Corporation, Case Institute of Technology, and Bell Aerosystems Company	Unclassified
	2b. GROUP

3. REPORT TITLE

Integrated Research on Carbon Composite Materials

4. DESCRIPTIVE NOTES *(Type of report and inclusive dates)*

Annual Report   May 17, 1965 to May 16, 1966

5. AUTHOR(S) *(Last name, first name, initial)*

Union Carbide Corporation, Carbon Products Division, in Association with Case Institute of Technology and Bell Aerosystems Company, a Textron Company

6. REPORT DATE	7a. TOTAL NO. OF PAGES	7b. NO. OF REFS
October 1966	271	79

8a. CONTRACT OR GRANT NO.	9a. ORIGINATOR'S REPORT NUMBER(S)
AF 33(615)-3110	
b. PROJECT NO. ARPA Order No. 719	
c. Program Code No. 5950	9b. OTHER REPORT NO(S) *(Any other numbers that may be assigned this report)* AFML-TR-66-310, Part I
d.	

10. AVAILABILITY/LIMITATION NOTICES This document is subject to special export controls and each transmittal to foreign governments or foreign nationals may be made only with prior approval of the Nonmetallic Materials Division, Air Force Materials Laboratory, Wright-Patterson Air Force Base, Ohio 45433

11. SUPPLEMENTARY NOTES	12. SPONSORING MILITARY ACTIVITY
	Air Force Materials Laboratory Research & Technology Division Wright-Patterson AFB, Ohio

13. ABSTRACT   Both resin and metal matrix composites with high modulus carbon fibers are being developed. Chemical etchants which roughen the fiber surface have approximately doubled the compressive strength of resin rings. Contact angle and wicking rate tests are used to evaluate surface treatments. Various coatings (best: Ta) improve wetting with aluminum, but brittle intermetallic phases degrade composite properties. Nickel matrix composites have near theoretical modulus and 1/2 theoretical strength. The effect of random fiber spacing on calculated composite moduli is being studied. Curing stresses and stress concentrations at fiber ends have been measured photoelastically. Improved test concepts have been formulated for uni- and bidirectional composites. Discrete element methods of structural analysis, a transient temperature analysis capability, and a statistical theory of strength have been extended to include material anisotropy. New structural synthesis algorithms are being investigated. Work is reported on a method for nonlinear, multiaxial stress analysis. Preliminary minimum weight estimates have been made for a fiber composite component representative of a fuselage section. The use of structural synthesis methods to select the best material from within a class of materials is being investigated on a series of particulate composites similar to grade JTA. Material property data, analyses of a hollow cylinder and a flat plate, and the design of a rocket throat insert are reported.

DD FORM 1 JAN 64 **1473**

KEY WORDS	LINK A		LINK B		LINK C	
	ROLE	WT	ROLE	WT	ROLE	WT
1. Composites, 2. Intermediate Modulus Graphite Fibers, 3. Micromechanics, 4. Component Design, 5. Plastic Matrix 6. Metal Matrix, 7. Mechanical Properties, 8. Discrete Element Analysis, 9. Nonlinear Structural Analysis, 10. Structural Synthesis						

INSTRUCTIONS

1. ORIGINATING ACTIVITY: Enter the name and address of the contractor, subcontractor, grantee, Department of Defense activity or other organization (corporate author) issuing the report.

2a. REPORT SECURITY CLASSIFICATION: Enter the overall security classification of the report. Indicate whether "Restricted Data" is included. Marking is to be in accordance with appropriate security regulations.

2b. GROUP: Automatic downgrading is specified in DoD Directive 5200.10 and Armed Forces Industrial Manual. Enter the group number. Also, when applicable, show that optional markings have been used for Group 3 and Group 4 as authorized.

3. REPORT TITLE: Enter the complete report title in all capital letters. Titles in all cases should be unclassified. If a meaningful title cannot be selected without classification, show title classification in all capitals in parenthesis immediately following the title.

4. DESCRIPTIVE NOTES: If appropriate, enter the type of report, e.g., interim, progress, summary, annual, or final. Give the inclusive dates when a specific reporting period is covered.

5. AUTHOR(S): Enter the name(s) of author(s) as shown on or in the report. Enter last name, first name, middle initial. If military, show rank and branch of service. The name of the principal author is an absolute minimum requirement.

6. REPORT DATE: Enter the date of the report as day, month, year; or month, year. If more than one date appears on the report, use date of publication.

7a. TOTAL NUMBER OF PAGES: The total page count should follow normal pagination procedures, i.e., enter the number of pages containing information.

7b. NUMBER OF REFERENCES: Enter the total number of references cited in the report.

8a. CONTRACT OR GRANT NUMBER: If appropriate, enter the applicable number of the contract or grant under which the report was written.

8b, 8c, & 8d. PROJECT NUMBER: Enter the appropriate military department identification, such as project number, subproject number, system numbers, task number, etc.

9a. ORIGINATOR'S REPORT NUMBER(S): Enter the official report number by which the document will be identified and controlled by the originating activity. This number must be unique to this report.

9b. OTHER REPORT NUMBER(S): If the report has been assigned any other report numbers (either by the originator or by the sponsor), also enter this number(s).

10. AVAILABILITY/LIMITATION NOTICES: Enter any limitations on further dissemination of the report, other than those imposed by security classification, using standard statements such as:

(1) "Qualified requesters may obtain copies of this report from DDC."

(2) "Foreign announcement and dissemination of this report by DDC is not authorized."

(3) "U. S. Government agencies may obtain copies of this report directly from DDC. Other qualified DDC users shall request through

_____."

(4) "U. S. military agencies may obtain copies of this report directly from DDC. Other qualified users shall request through

_____."

(5) "All distribution of this report is controlled. Qualified DDC users shall request through

_____."

If the report has been furnished to the Office of Technical Services, Department of Commerce, for sale to the public, indicate this fact and enter the price, if known.

11. SUPPLEMENTARY NOTES: Use for additional explanatory notes.

12. SPONSORING MILITARY ACTIVITY: Enter the name of the departmental project office or laboratory sponsoring (paying for) the research and development. Include address.

13. ABSTRACT: Enter an abstract giving a brief and factual summary of the document indicative of the report, even though it may also appear elsewhere in the body of the technical report. If additional space is required, a continuation sheet shall be attached.

It is highly desirable that the abstract of classified reports be unclassified. Each paragraph of the abstract shall end with an indication of the military security classification of the information in the paragraph, represented as (TS), (S), (C), or (U).

There is no limitation on the length of the abstract. However, the suggested length is from 150 to 225 words.

14. KEY WORDS: Key words are technically meaningful terms or short phrases that characterize a report and may be used as index entries for cataloging the report. Key words must be selected so that no security classification is required. Identifiers, such as equipment model designation, trade name, military project code name, geographic location, may be used as key words but will be followed by an indication of technical context. The assignment of links, rules, and weights is optional.